Doctoral Thesis

Thesis Title

Creation of Low Frictional Nanointerface

for Water Lubrication System with Stainless Steel

Department of Mechanical Systems Engineering

Graduate School of Engineering,

TOHOKU UNIVERSITY

Kenta Akagami

指 導 教 員	足立　幸志　　教授
研究指導教員	
審 査 委 員 （○印は主査）	○　足立　幸志　教授 1　小川　和洋　教授　2　祖山　均　教授

Tohoku University

Graduate School of Engineering

Creation of Low Frictional Nanointerface for Water Lubrication System with Stainless Steel

（ステンレス鋼を用いた水中摩擦システムのための低摩擦界面創成）

A Dissertation Submitted for Degree of Doctor of Philosophy (Engineering)

Department of Mechanical Systems Engineering

by

Kenta Akagami

January 14, 2020

Creation of Low Frictional Nanointerface for Water Lubrication System with Stainless Steel

Kenta Akagami

Abstract

Reducing energy consumption around the world is an urgent issue. Water is a clean lubricant that can exhibit low friction due to its low viscosity. Widespread use of the lubrication system using water is important for energy conservation. In this study, the possibility of a water lubrication system using stainless steel, which is used as a general machine component was investigated. The surface of stainless steel has a passive film made of chromium oxide (Cr_2O_3), which is known to prevent bulk material corrosion. The targets of thesis are to create the low frictional nanointerface on stainless steel and to propose the design guidelines of water lubrication system with stainless steel.

In chapter 1, the author summarized the importance of tribology and water lubrication system based on previous study. In addition, the author described that the use of stainless steel is an effective solution to the current water lubrication problem.

In chapter 2, the friction properties between stainless steels were investigated. This friction pair expressed a coefficient of friction of about 0.3-1.0. It has been shown that the amount of wear increases as the product of initial contact pressure and sliding velocity increasing. Both worn surfaces of stainless steel even under low sliding velocity and initial contact pressure were seized and that water lubrication between stainless steels was impossible are clarified. As a first step in improving water lubrication properties using stainless steel, to control the adhesion of stainless steel itself was proposed.

In chapter 3, silicon carbide and silicon nitride, represented by silicon-based ceramics with a potential of water lubrication systems, were used as a mating material of stainless steel in order to adhere stainless steel itself. Using the silicon-based ceramics, the low and stable friction coefficient was exhibited, and the wear volume was decreased rather than the combination between stainless steel and itself. However, these combinations still exhibit higher friction than the current SiC/SiC combination. The wettability of the wear track on SiC disk and the wear scar on AISI 304 ball was improved. The improvement of hydrophilicity was caused by sliding between silicon-based ceramics and stainless steel. The improvement of the hydrophilicity of the wear surface on stainless steel was considered to be the key to the construction of a water lubrication system using stainless steel.

In chapter 4, diamond-like carbon (DLC) coating was used as stainless steel counterparts in order to adhere stainless steel itself, similar to silicon-based ceramics. DLC coating has a potential as tribo-material in water. By introduce of DLC coating as a mating material of AISI 304, the improvement of tribological properties were confirmed. It was clarified that running-in depends on the value which the contact pressure divided by sliding velocity. When the area where the transfer film is not seen is dominant, the friction

coefficient of 0.07 or less is exhibited with running-in. In order to exhibit running-in, the transfer of carbon from DLC coating onto stainless steel and the suppression of the oxidation of iron, which is the bulk material of stainless steel need. From a cross-sectional image of the area where the transfer film is not formed, it was revealed that the existence of nanolayer consisting of chromium and oxygen with a thickness of about 20 nm, on the wear scar stainless steel. Based on the fact that the passive film of ordinary stainless steel has a thickness of 1 to 3 nm, that this passive film was self-formed during friction is clarified.

In chapter 5, in order to clarify the transfer mechanism of carbon from DLC coating onto stainless steel, the author developed an ESEM-tribo system equipped with a mechanism that allows observation and analysis without exposing the friction surface on the ball specimen to the atmosphere. By purging water vapor into the chamber of an environmental scanning electron microscope (ESEM), a friction test in a humid environment is possible. In the low humidity environment of <0.5% RH, a transfer film mainly composed of carbon was formed on the stainless steel. However, in the humidity environment of 0.5% RH or higher, the formation of the transfer film was suppressed in the wear scar was observed. These results indicate that the moisture in the environment has a role in suppressing the formation of transfer film, so that the critical amount of water existed. However, the fact that carbon is transferred in water suggests that even in water, water film was broken out and carbon was transferred at the order of the real contact point.

In chapter 6, based on the results of the previous chapters, in order to improve the water lubrication property of stainless steel, SiC-DLC coating was introduced newly as the mating material of stainless steel making use of the results of Chapters 3 and 4. SiC-DLC coating was produced by a plasma-enhanced chemical vapor deposition (PE-CVD) method and DC magnetron co-sputtering of SiC target simultaneously. By introduce of SiC-DLC coating, there was the expansion of the sliding condition where the running-in was exhibited compared with the tribo-pair of stainless steel and DLC coating. When the combination between stainless steel and SiC-DLC coating showed low friction in the boundary lubrication regime, a passive film containing chromium and oxygen in addition to silicon was self-formed on stainless steel, and the film was hydrophilic. Furthermore, by introducing SiC into DLC coating, the hydrophilicity of the coating itself due to friction was improved compared to DLC coating. Therefore, in order to use stainless steel in a water lubrication system, it has been found that it is necessary to draw out the potential as a sliding material in water by self-forming a hydrophilic nanolayer derived from a passive film on the stainless steel.

In chapter 7, the general conclusions were described

Table of Contents

Chapter 1
Introduction

1.1 Background

Since the industrial revolution, human beings have started to use fossil fuels, while living with rich science and technology advances. It is known that the global warming caused by an increase in the consumption of CO_2 and disasters such as storms and droughts that are expected to be caused by global warming frequently occur [1]. In 2007, global CO_2 emissions were 2.9×10^4 kg, but if new power generation methods aren't developed and environmental policies aren't implemented, emissions are expected to continue increasing to 4.0×10^4 kg in 2030. In fact, the breakdown of global CO_2 emissions in 2007 is as follow [2]:

-40% for power generation;
-22% for industry activities;
-24% for transportation;
-10% for buildings.

The IEA presents a 2DS scenario reflecting the 2009 Copenhagen Accord's acceptance of "the scientific view that the increase in global temperature should be below 2°C". The 2DS is consistent with a 50% chance of limiting future global average temperature increases to 2°C by 2100. IEA shows the important technology for achieving the 2DS scenario as shown in Fig. 1-1[3]. The graph shows the difference between when the CO_2 increases according to the baseline and when the 2DS scenario is achieved. In the case of 2DS, the total CO_2 emissions are below 1.0×10^4 kg. According to their report, the most influential technology is expected to use energy efficiency because energy-efficient technologies dominate the cumulative CO_2 emissions reductions achieved in the power generation, industry activity, buildings and transport sectors for achieving the 2DS vision. Then, what kind of methods to improve energy efficiency is examined using a passenger car as an example.

The following results are based on the assumption that the vehicle is driven by the following passenger car shown in Fig. 1-2.

–13,000 km annual mileage

–60 km/h average speed

– Average-road driving

–300 g/kWh fuel efficiency at 12 kW engine power

–2.5 kg CO2 emissions per liter fuel consumed

It is estimated that about 33% of the energy obtained from fossil fuels is consumed as friction loss [4] (See Fig. 1-2). In other words, it solves various problems related to friction and wear of the surrounding transportation means including automobiles, but as a result, it reduces the use of fossil fuel and leads to the conservation of the global environment.

In this way, the tribology that deals with friction and wear is the research field which holds the key to improving energy efficiency. Tribology is defined as “the science and technology of interacting surfaces in relative motion and of related subjects and practices” [5]. Performance, reliability and durability of machines are determined by tribological performance. Therefore, the improvement if tribological performance which leads to efficient use of resources is expected to greatly contribute to the solution of global energy problems.

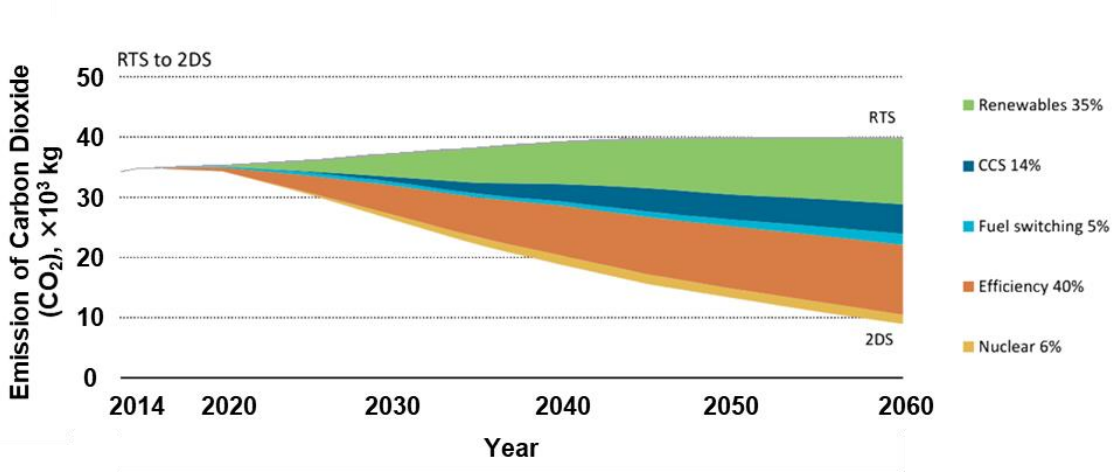

Fig. 1-1 Global CO_2 emissions reductions by technology field [3].

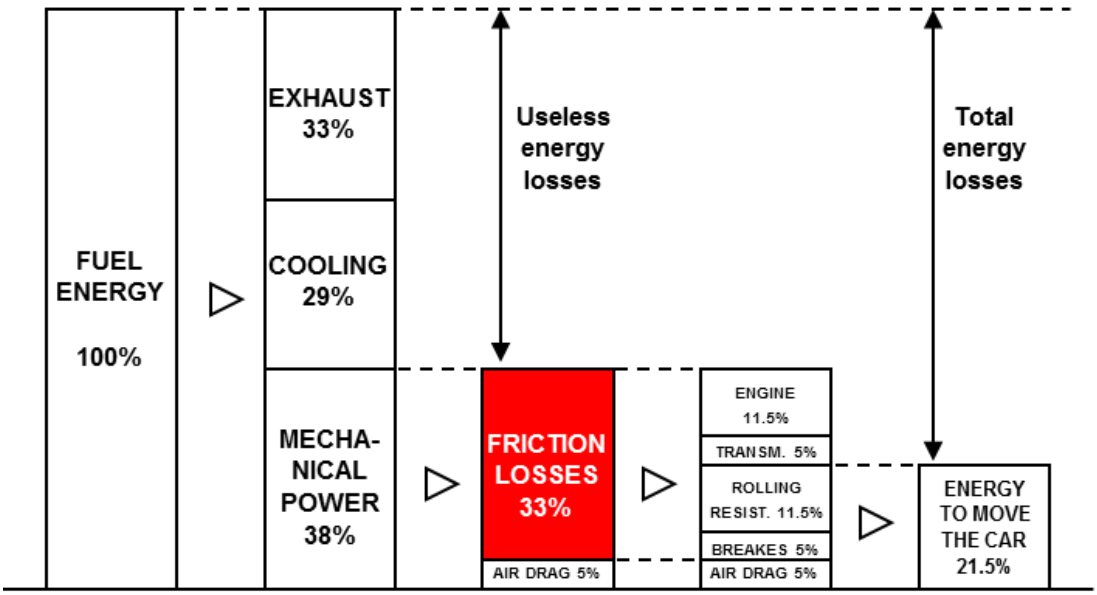

Fig. 1-2 Breakdown of passenger car energy consumption [4].

1.2 Potential of low viscosity fluids as lubricant

In order to reduce friction loss, it is effective to reduce friction in the hydrodynamics lubrication regime where many machine products are usually used. The hydrodynamics lubrication regime represents one of the contact states between the two surfaces. In order to explain this contact condition theoretically, Stribeck derived a function of contact pressure and sliding velocity for constant oil temperature as follows:

$$G = \frac{\eta V}{P_m} \tag{1.1}$$

$$\mu = \frac{F}{W} \tag{1.2}$$

where η [Pa・s], V [m/s], P_m [Pa], F [N] and W [N] are the viscosity of lubricant, the sliding velocity, the average contact pressure, friction force and vertical load, respectively. Figure 1-3 shows schematic image of Stribeck curve. Stribeck curve shows friction coefficient as a function of G which indicates the thickness of lubricant oil film relatively. Lubrication state is divided into hydrodynamic lubrication, mixed lubrication and boundary lubrication. A decrease in the value of G which indicates that the lubricant film is thinner causes increasing the contacts between two surfaces. In other words, the lower value of G means that the harder formation of lubricant film with sufficient thickness. An increase in the value of G which indicates that the formed lubricant film is thicker causes the support between two surfaces by lubricant. Since the shear resistance of the fluid is proportional to the viscosity of the fluid, the use of a low viscosity fluid contributes to low friction in the hydrodynamics lubrication regime. Therefore, a friction system using low-viscosity fluid is effective for reducing friction loss.

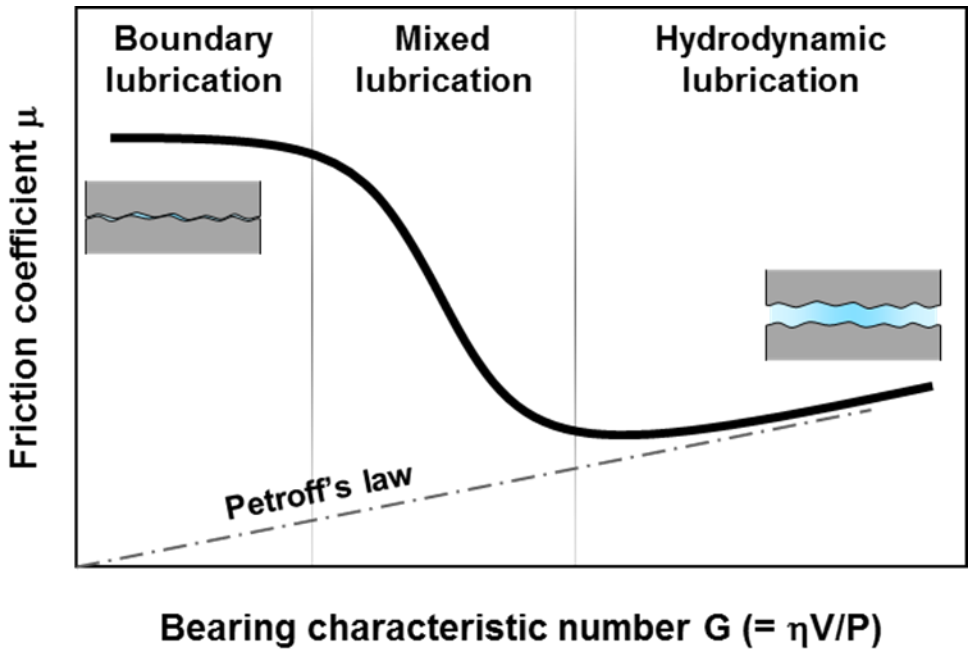

Fig. 1-3 Schematic image of Stribeck curve.

1.3 Water lubrication with silicon-based ceramics

It is known that water is low viscosity fluid. When the viscosity at 40 ºC is compared with common automobile engine oil (5W-30) with low viscosity at low temperatures, the viscosity of engine oil is 57.7 mPa·s [6] and the viscosity of water is 0.653 mPa·s.

Since 1985, Tomizawa and Fischer have reported friction and wear properties of silicon nitride (Si_3N_4) and silicon carbide (SiC) in water [7], [8]. They found that sliding of self-mated Si_3N_4 in water gives quite low friction coefficient ($\mu < 0.002$). It was clarified that hydrodynamic lubrication can be obtained when Si_3N_4 slides against Si_3N_4 or SiC in water. Sugita et al. showed that ($SiO_2 \cdot xH_2O$) hydrate was formed on the wear surface when friction was applied while dripping water on Si_3N_4 [9].

The lubrication characteristics of water vary greatly depending on the ceramic material [10-13]. It shows the change of friction coefficient when Si_3N_4 and SiC are rubbed with water shown in Fig. 1-4 [14], [15]. Si_3N_4 initially exhibits a friction coefficient higher than 0.8, but decreases rapidly immediately. In contrast, SiC initially shows lower values than Si_3N_4, but the subsequent decline is gradual and occurs rapidly after a period of time. The friction coefficient after reaching the steady friction region shows a very low value of 0.01 or less. This process is called running-in process. In other words, running-in is required for achieving low friction in water. During running-in process, it has reported that the average contact pressure decreases, the specific wear rate becomes quietly small, and the shape of wear particles change shown in Fig. 1-5 [16], [17]. It has been recognized that chemical wear of silicon-based ceramics in water which exhibits low friction is quite important.

Following these reports, water lubrication with silicon-based ceramics is thought to form chemical products on the worn surface by the following tribochemical reaction.

$$Si_3N_4 + 6H_2O \rightarrow 3SiO_2 + 4NH_3 \quad (1.3)$$

$$SiC + 2H_2O \rightarrow SiO_2 + CH_4 \quad (1.4)$$

Although SiC and Si_3N_4 are difficult to cause oxidation reaction in the static state, it has been found that the following hydrothermal reactions occur under high temperature and pressure conditions of 1000 °C and 10-100 MPa, respectively [18], [19]. Nevertheless, Sugita et al. confirmed the formation of an amorphous SiO_2, layer and a hydrated SiO_2, layer on polished surface on Si_3N_4 at normal temperature under friction conditions [9]. This amorphous SiO_2 has a low adhesion strength with the bulk material, so it is easy to remove as friction progresses, and the worn surface gradually smoothes to repeat its generation and removal. After this process, it moves to the hydrodynamics lubrication regime and exhibits develops low friction in water.

In addition, it has also been proposed that OH groups tend to be terminated on the surface of amorphous SiO_2 and, because of their hydrophilicity, contribute to the realization of hydrodynamics lubrication region through water at the friction interface.

$$SiO_2 + 2H_2O \rightarrow Si(OH)_4 \quad (1.5)$$

$$SiO_2 + nH_2O \rightarrow SiO_2 \cdot n(H_2O) \quad (1.6)$$

Advantages of using water as a lubricant are not only low viscosity, but also low cost, cleanness, abundance of resources and environment friendly. Therefore, water lubrication system is regard as an eco-friendly and environmentally friendly lubrication system. In constant, water has a problem of low load capacity because of its low viscosity. It is easy to cause the solid contact, show the friction coefficient rising rapidly [20] (Fig. 1-6).Therefore, low load capacity is an issue for water lubrication systems. In order to improve the characteristic of load capacity, a method to control the tribochemical reaction on the friction surface has been studied in previous studies. To realize the smoothing of the friction surface and the formation of the hydrate SiO_2 gel layer be in advance, the load is applied every 200 N until the rate of change of the friction coefficient is within 5% [21]. This process is called running-in method. Increasing the normal load of the running-in method to 400 N, it was found that the load regime that exhibited low friction was increased and the load capacity was improved of SiC/SiC in water. The results of evaluating the running-in method from a view point of chemical effect are Fig. 1-7 and Fig. 1-8 [22-24]. Comparison of the running-in method with the normal load of 200 N and 400 N results showed that the surface free energy improved most and the hydrophilization progressed at 400 N. Furthermore, the effect of hydrophilicity on the liquid film was obtained by resonance shear apparatus, which is effective for analyzing the behavior of a nanometer-thick liquid sandwiched between solids (Fig. 1-9) [25]. From this result, it can be seen that the load required to approach the surface distance D = 1.0 nm increases about 20 times when the contact angle of water decreases from 49° to 22°. These results show the possibility of increasing the load supported by water between the two surfaces by improving the hydrophilicity of the friction surface. Water lubrication system using self-mated SiC is known to form amorphous nano-thick layer which consists of silicon, carbon and oxygen when low friction appears in water (Fig. 1-10) [26], [26]. It became clear that the low load capacity of the water lubrication system can be improved by actively controlling the tribochemical reaction between water and silicon.

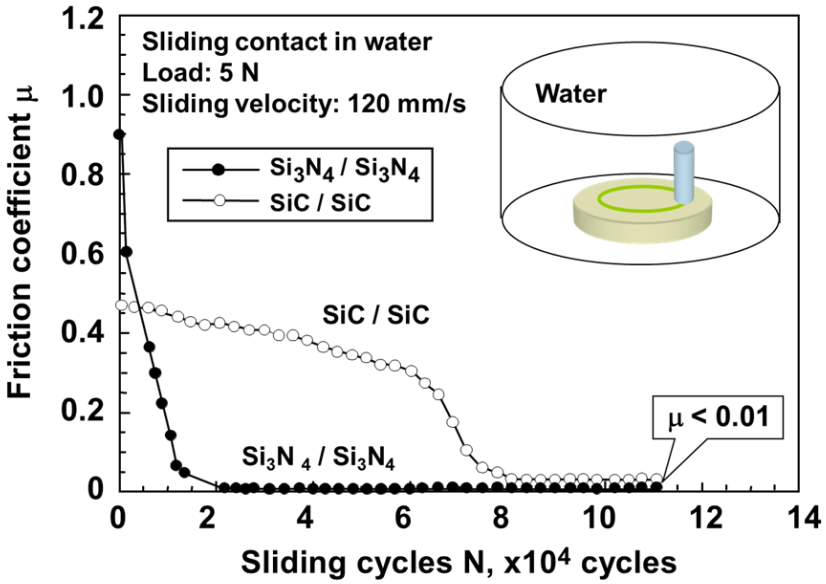

Fig. 1-4 Variation of friction coefficient of Si_3N_4 and SiC with sliding cycles under water lubrication [14], [15].

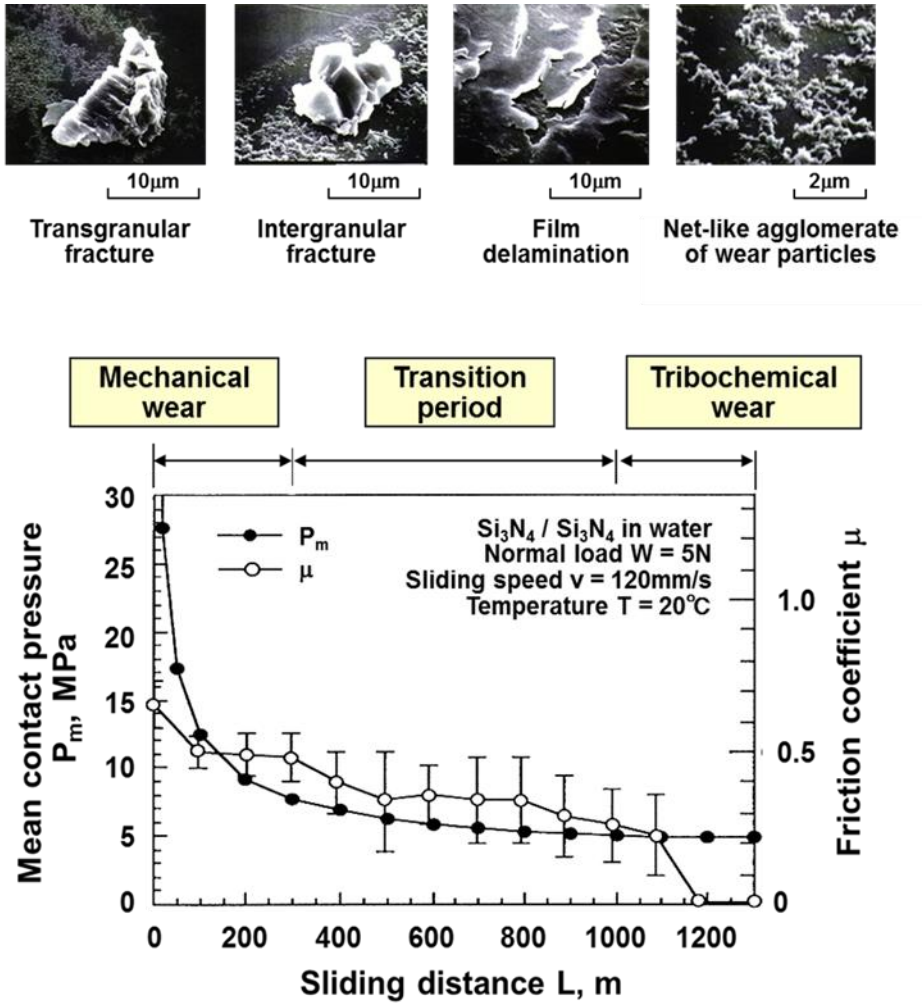

Fig. 1-5 Friction coefficient and mean contact pressure of Si_3N_4 slid against Si_3N_4 in water and SEM images of wear particle [16], [17].

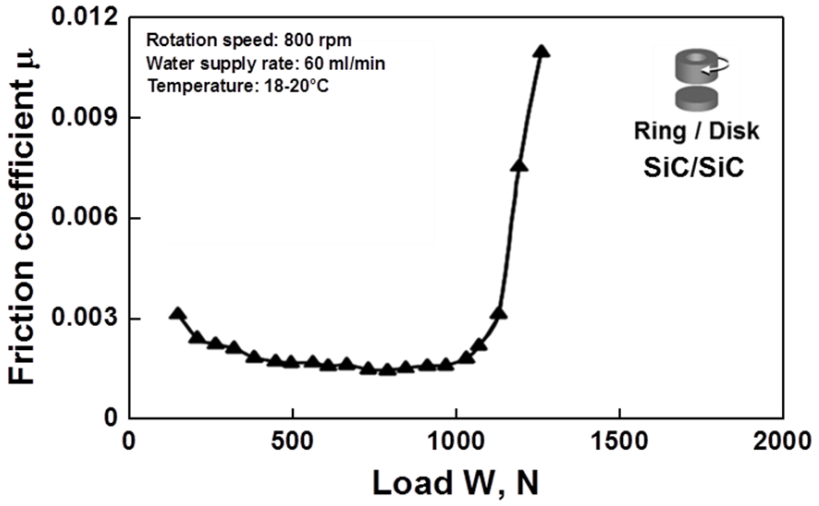

Fig. 1-6 Increase suddenly of friction coefficient in water [20].

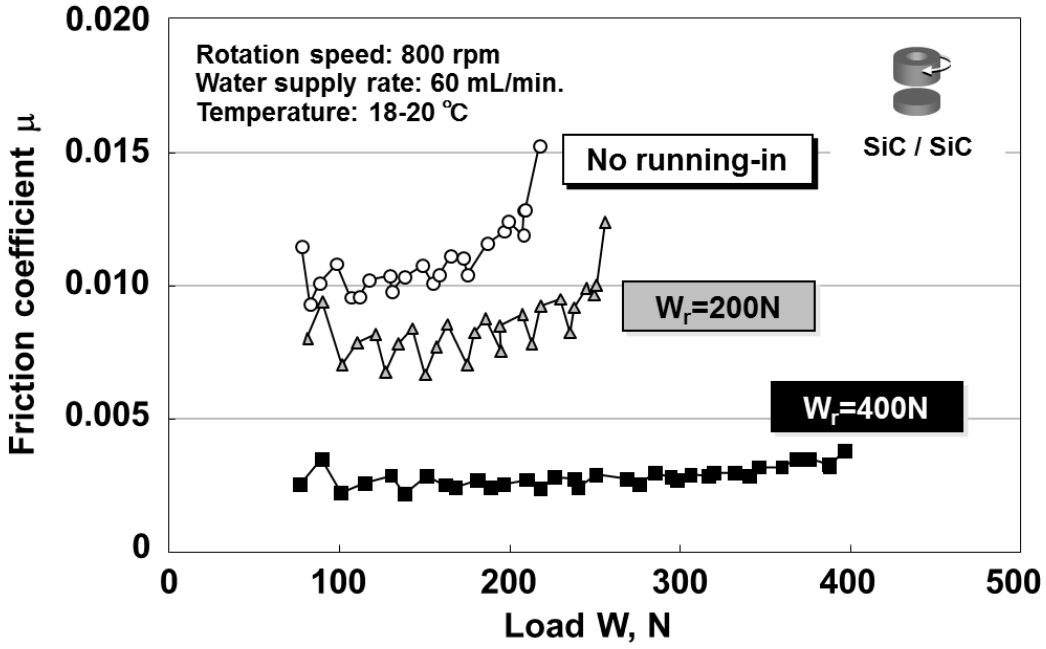

Fig. 1-7 Effect of running-in loads on friction properties of SiC/SiC in water [22].

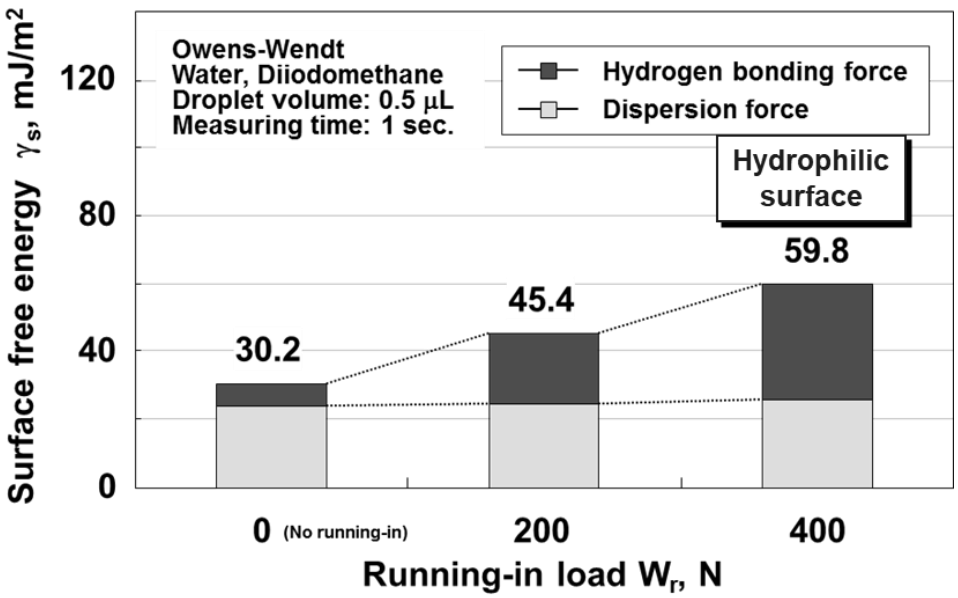

Fig. 1-8 Effect of running-in loads on surface wettability of worn surface of SiC [22].

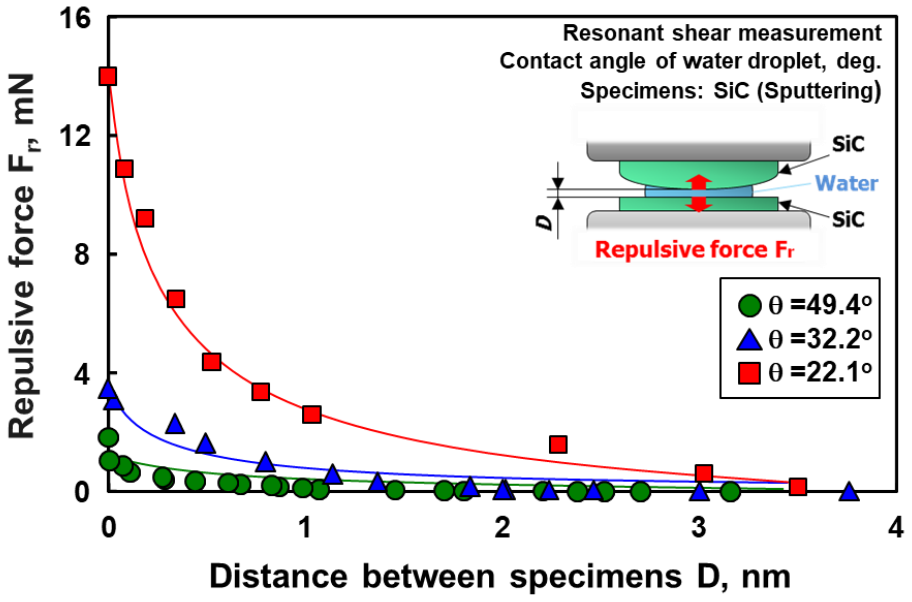

Fig. 1-9 Relationship between repulsive force and distance of SiC with difference water contact angle [23].

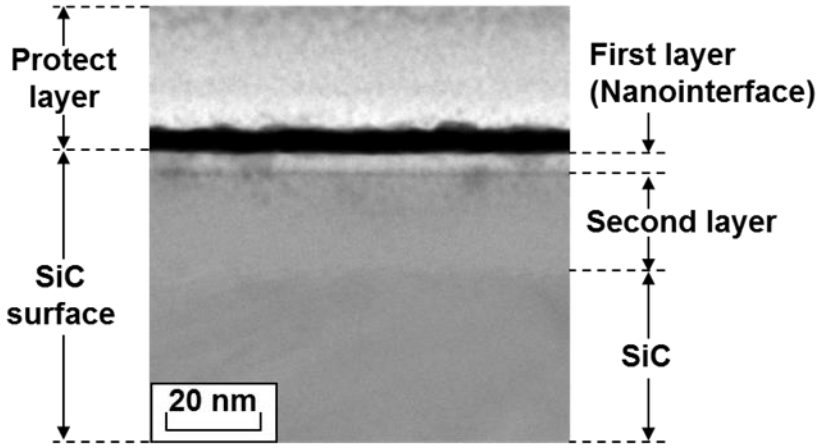

	C (at.%)	O (at.%)	Si (at.%)
First layer	36.1	36.7	27.2
Second layer	52.3	0.0	46.7
SiC	52.8	0.0	47.2

Fig. 1-10 Cross-sectional image of worn surface of textured SiC and the ratio of chemical composition of each point [25].

1.4 Possibility for water lubrication with stainless steel

As mentioned above, water lubrication system is expected because it exhibits low friction and contributes to friction loss reduction. In fact, water lubrication systems are used in air compressors, turbines for hydroelectric power generation, and mechanical seals for automobiles. A mechanical seal for water pump etc. is used to prevent the coolant from leaking from the gap between the pump body and the shaft shown in Fig. 1-11 [27]. The mechanical seal consists of two rings: a rotating ring mounted on the shaft and a fixed ring mounted on the pump housing. The rotating ring rotates with the shaft and slides while maintaining clearance of with the locking ring. As a material of the sliding part, ceramics such as silicon carbide and alumina are often used for the rotating ring, and a carbon material is often used for the fixing ring. However, a wide range of water lubrication applications have not yet been achieved.

The reasons for limitations on sliding materials. Materials often used in water lubrication systems include ceramic materials such as Si_3N_4, SiC, and alumina (Al_2O_3), and resin materials [28]. Figure 1-12 shows a map arranged by Ashby et al [31]. This map indicates that ceramic materials generally have sufficient strength, but their fracture toughness values are low and tend to break. The severe fractures occur due to pores and grain boundaries present inside the bulk material and cracks near the surface introduced during the machining process because ceramics material is a sintered material. In constant, Figure 1-12 indicates that the resin material has a high fracture toughness value, which absorbs stress and resists cracking but has low strength too. Therefore, these materials have the characteristic that they are difficult to process due to fractures dependent on pores, grain boundaries, and cracks near the surface. Because of high processing cost, ceramic materials are not widely used in the manufacture of mechanical parts. However, metal materials are easy to process and widely used as mechanical materials. Use of metal material as sliding materials for water lubrication systems is expected to lead to further applications of water lubrication systems. In particular, stainless steel is expected to be used in water lubrication systems because of its corrosion resistance to water [32-35]. Stainless steel protects the bulk material by being covered with a passive film made of chromium oxide and prevents the whole from corrosion [36-39]. Taking advantage of the characteristics of corrosion resistance, its use in seawater environment [41],[41] and in vivo[43], [43] are being studied. In fact, unlubricated linear sliding bearing using stainless steel as a tribo-material have been developed [44].

The benefit of expanding the water lubrication system would be a clean environment such as a food factory or a semiconductor factory. There are sliding parts of mechanical equipment such as transfer machines and processing machines used in such factories, and lubrication is required. Grease is used as a

lubricant to dislike dust generation and outgassing, but the grease is a liquid lubricant or other liquid lubricant with a thickener additive uniformly mixed. It has higher viscosity and lower fluidity than lubricating oil. Therefore, it has the disadvantage of high shear resistance. If a highly-robust water lubrication system could be constructed, it would be expected to replace conventional grease with water to increase energy efficiency and contribute to unmanned factories for longer life. Regarding unmanned factories, the impact is expected to be large in Japan, where the working population is decreasing year by year.

If it is possible to use stainless steel having various possibilities as a sliding material of a water lubrication system that develops low friction, it is expected that the water lubrication system can be widely spread. And furthermore, the friction reduction brought about by the water lubrication system with stainless steel will contribute to the realization of an energy saving society.

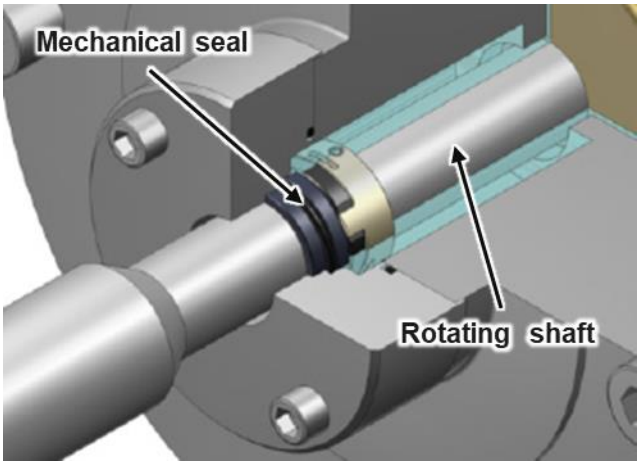

(a) Overview of mechanical seal

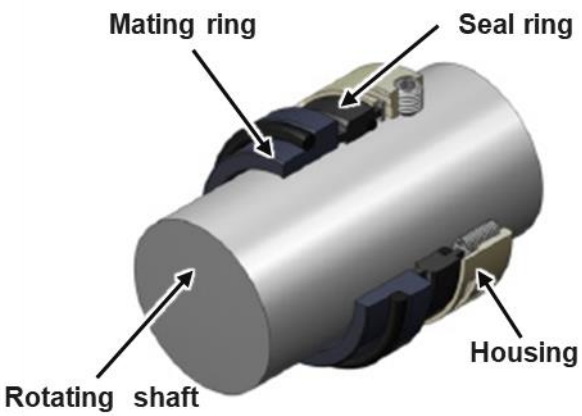

(b) Structure of mechanical seal

Fig. 1-11 Illustration images of mechanical seal used in water pump [27].

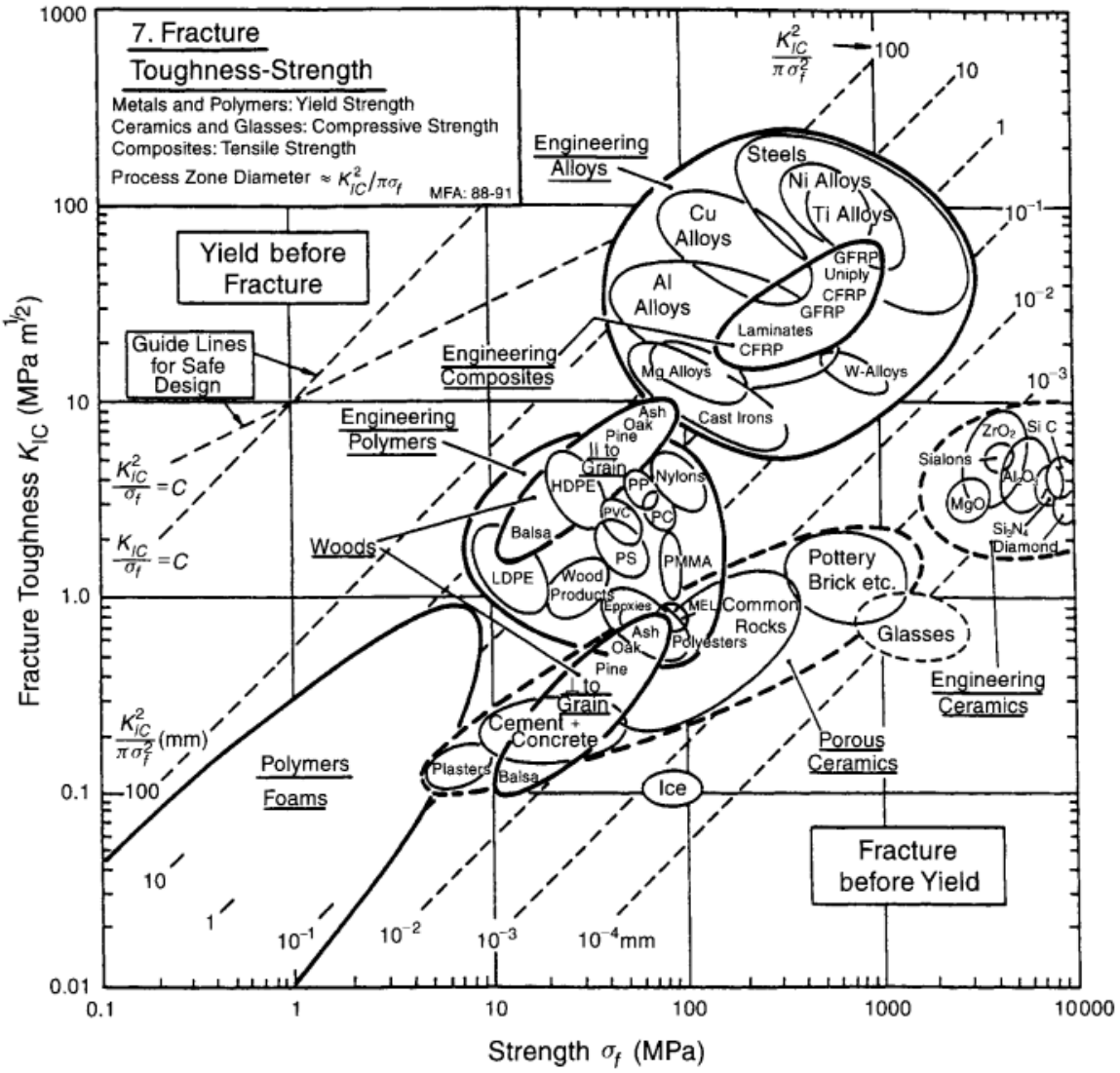

Fig. 1-12 Relationship between fracture toughness and strength for various classes of materials [31].

1.5 Objective and structure of this thesis

As seen in the previous section, the water lubrication system is expected to be a clean next generation lubrication system which enables to enormous cost savings and contributes to energy savings and resource savings. However, the water lubrication systems have not been widely used because of the limited sliding materials currently used. In order to expand the application of water lubrication systems, the construction of a water lubrication system using stainless steel, a general-purpose mechanical material, is desired.

Therefore, objective of this thesis is to create low frictional interface on stainless steel for water lubrication, then design guidelines of water lubrication system using stainless steel will be proposed. Figure 1-13 shows the Stribeck curve of the combination between SiC and itself in water. The evaluation of water lubrication using stainless steel is based on the frictional behavior between SiCs that has been used conventionally. The structure of the thesis is shown in Fig. 1-14. Contents of the chapters are described as follows:

Chapter 1 is the introduction, which proposes the objective of the thesis based on background of water lubrication system with silicon-based ceramics and previous studies.

Chapter 2 describes that friction properties between stainless steel and itself are investigated by ball-on-disk friction tester. Friction and wear properties of the combination of stainless steels is classified and the strategy for improvement of tribological properties is proposed.

Chapter 3 describes that the possibility of water lubrication system using stainless steel is clarified by introducing silicon-based ceramics such as Si_3N_4 and SiC as mating materials of stainless steel. As the result of chapter 2, SiC and Si_3N_4 which are stable chemically are used in order to prevent adhesion of stainless steel.

Chapter 4 describes the possibility of developing low friction in water was clarified by introducing diamond-like carbon (DLC) coating as mating material of stainless steel, and the low friction mechanism was discussed from the viewpoint of the hydrophilicity of the friction surface and the structure of the friction interface.

Chapter 5 describes the running-in process of the combination of stainless steel and DLC coating by the newly developed environmental scanning electron microscope (ESEM) tribo-system. The effectiveness of the ESEM tribo-system are shown by the friction test of tribo-pair of stainless steel and DLC coating conducted in an environment with varying relative humidity. ESEM tribo-system equipped with a mechanism that allows ex-situ observation of the wear surface of the ball without exposure to the

atmosphere is designed. In this chapter, the friction process in the initial state is focus on in order to clarify the transfer of carbon from DLC coating onto stainless steel.

Chapter 6 describes the potential of water lubrication system with stainless steel by newly introducing SiC-DLC coating. SiC-DLC coating is a new coating that uses DLC coating as a host matrix to support amorphous SiC structure making use of the results of chapters 3 and 4. The formation mechanism of low frictional surface on stainless steel is discussed to propose the design guidelines of water lubrication system using stainless steel in water.

Chapter 7 describes general conclusions of the thesis are summarized.

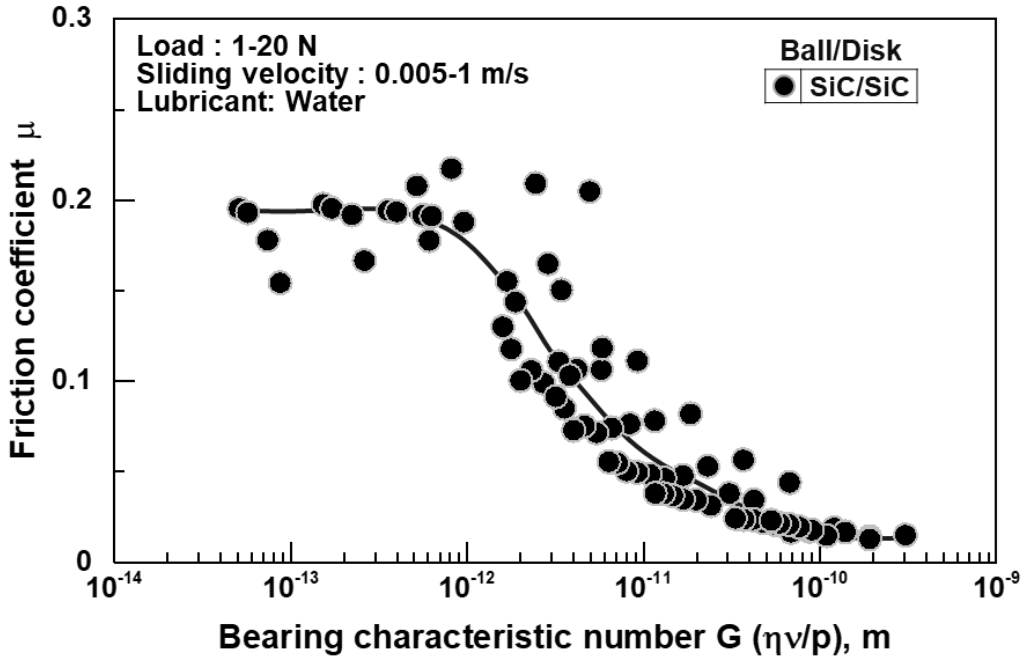

Fig. 1-13 Criteria of water lubrication system.

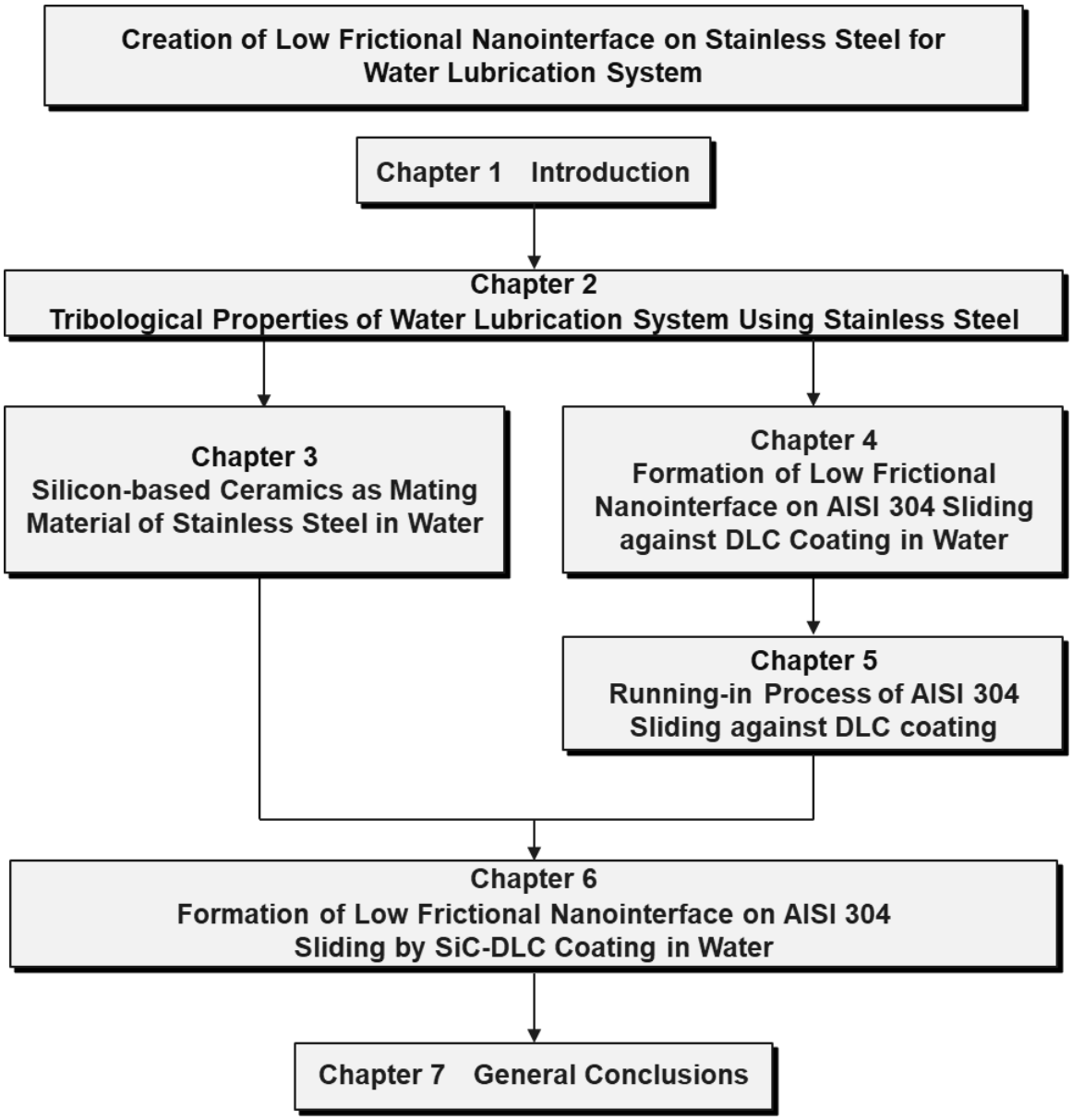

Fig. 1-14 Structure of this thesis.

References

[1] T. F. Stocker, S. K. Allen, V. Bex, P. M. Midgley, Climate change 2013 The physical science basis, working group I contribution to the fifth assessment report of the intergovernmental panel on climate change (2013) 159–254.

[2] International Energy Agency, Energy technology perspectives 2010 scenarios & strategies to 2050, International Energy Agency (IEA) Publications (2010) 67–99.

[3] International Energy Agency, Energy technology perspectives 2017 catalysing energy technology transformations Secure, International Energy Agency (IEA) Publications (2017) 49–112.

[4] K. Holmberg, P. Andersson, A. Erdemir, Global energy consumption due to friction in passenger cars, Tribology International, 47 (2012) 221–234.

[5] J. Peter, Lubrication (tribology), education and research: A report on the present position and industry's needs (1966) Paris.

[6] Technical deta sheet of Shell HELIX HX7 AJ 5W-30, Royal Dutch Shell PLC. (2012).

[7] T. E. Fischer, H. Tomizawa, Interaction of tribochemistry and microfracture in the friction and wear of silicon nitride, Wear, 105, 1 (1985) 29–45.

[8] H. Tomizawa, T. E. Fischer, Friction and wear of silicon nitride and silicon carbide in water: hydrodynamic lubrication at low sliding speed obtained by tribochemical wear, ASLE Transactions, 30, 1 (1987) 41–46.

[9] T. Sugita, U. Kanji, Material removal rubbing in water, Wear, 97 (1984) 1–8.

[10] K. H. Zum Gahr, Sliding wear of ceramic-ceramic, ceramic-steel and steel-steel pairs in lubricated and unlubricated contact, Wear, 133, 1 (1989) 1–22.

[11] R. S. Gates, S. M. Hsu, E. E. Klaus, Tribochemical mechanism of alumina with water, Tribology Transactions, 32, 3 (1989) 357–363.

[12] S. Sasaki, The effects of the surrounding atmosphere on the friction and wear of alumina, zirconia, silicon carbide and silicon nitride, Wear, 134, 1 (1989) 185–200.

[13] P. Andersson, Water-lubricated pin-on-disc test with ceramics, Wear, 154 (1992) 37–47.

[14] M. Chen, K. Kato, K. Adachi, The difference in running-in period and friction coefficient between self-mated Si_3N_4 and SiC under water lubrication, Tribology Letters, 11, 1 (2001) 23–28.

[15] M. Chen, K. Kato, K. Adachi, Friction and wear of self-mated SiC and Si_3N_4 sliding in water, Wear, 250, 1–12 (2001) 246–255.

[16] J. Xu, K. Kato, T. Hirayama, The transition of wear mode during the running-in process of silicon nitride sliding in water, Wear, 205, 1–2 (1997) 55–63.

[17] J. Xu, K. Kato, Formation of tribochemical layer of ceramics sliding in water and its role for low friction, Wear, 245, 1–2 (2000) 61–75.

[18] H. Yuko, Studies of tribochemical reactions of silicon based ceramics in water and alcohols and its applications to sliding and machining, National Institute of Advanced Industrial Science and Technology Mechanical Engineering Laboratory Report, 177 (1998) 1-74 (in Japanese).

[19] V. Presser, O. Krummhauer, K. G. Nickel, A. Kailer, C. Berthold, C. Raisch, Tribological and hydrothermal behaviour of silicon carbide under water lubrication, Wear, 266, 7–8 (2009) 771–781.

[20] X. Wang, K. Kato, K. Adachi, K. Aizawa, Loads carrying capacity map for the surface texture design of SiC thrust bearing sliding in water, Tribology International, 36, 3 (2003) 189–197.

[21] K. Adachi, T. Yokota, K. Kato, The running-in effect on friction properties of SiC in water, Proceedings of the Tribology Conference 2007 Autumn Saga, C36 (2007) 225–226 (in Japanese).

[22] K. Adachi, Nanointerface for superior tribological properties of silicon carbide in water, Proceedings of World Tribology Congress V, Torino, Italy (2013) 1096.

[23] K. Noguchi, M. Kasuya, M. Mizukami, K. Kurihara, K. Adachi, Control of solid-liquid interface for increasing load-carrying capacity of water lubrication system with silicon carbide, Proceedings of the Tribology Conference 2012 Spring Tokyo, B4 (2012) 73-74 (in Japanese).

[24] K. Noguchi, M. Kasuya, M. Mizukami, K. Kurihara, K. Adachi, The effect of structured-water on friction of silicon carbide in water, Proceedings of the Tribology Conference 2012 Autumn Muroran, F11 (2012) 399-400 (in Japanese).

[25] T. Hatta, K. Adachi, Formation of super-low friction interface by surface texturing in water lubrication, Proceedings of the Japan Society of Mechanical Engineers Tohoku Branch, Sendai, 51, 145 (2016) 87-88 (in Japanese).

[26] H. Sato, K. Adachi, Formation of nanointerface during running-in for low friction of silicon carbide in water, Proceedings of ITS-IFToMM 2017 & K-TIS 2017, Jeiu, Korea, T22-4 (2017) 151.

[27] Eagle Industry Co. LTD., Mechanical seals, https://www.ekkeagle.com/en/technology/mechanical/, (browsed at 2019 Nov. 20th).

[28] H. E. Guoren, Y. Guicheng, Friction and wear of poly(phenylene sulphide) carbon fibre composites: ii water lubrication, Wear, 116 (1987) 69–75.

[29] R. Prehn, F. Haupert, K. Friedrich, Sliding wear performance of polymer composites under abrasive and water lubricated conditions for pump applications, Wear, 259, 1–6 (2005) 693–696.

[30] C. P. Gao, G. F. Guo, F. Y. Zhao, T. M. Wang, B. Jim, B. Wetzel, G. Zhang, Q. H. Wang, Tribological behaviors of epoxy composites under water lubrication conditions, Tribology International, 95 (2016) 333–341.

[31] M. F. Ashby, Materials selection in mechanical design second edition, Butterworth-Heinemann (1999) 430–431.

[32] A. Iwabuchi, T. Tsukamoto, T. Shimizu, H. Yashiro, The mechanism of corrosive wear of an austenitic stainless steel in an aqueous electrolyte solution, Tribology Transactions, 41, 1 (1998) 96–102.

[33] S. Mischler, S. Debaud, D. Landolt, Wear-accelerated corrosion of passive metals in tribocorrosion systems, Journal of the Electrochemical Society, 145, 3 (1998) 750–758.

[34] B. Dumont, P. J. Blau, G. M. Crosbie, Reciprocating friction and wear of two silicon nitride-based ceramics against type 316 stainless steel, Wear, 238, 2 (2000) 93–109.

[35] P. Henry, J. Takadoum, P. Berçot, Tribocorrosion of 316L stainless steel and TA6V4 alloy in H_2SO_4 media, Corrosion Science, 51, 6 (2009) 1308–1314.

[36] V. Maurice, W. P. Yang, P. Marcus, XPS and STM investigation of the passive film formed on Cr(110) single-crystal surfaces, Journal of the Electrochemical Society, 141, 11 (1994) 3016–3027.

[37] V. Maurice, W. P. Yang, P. Marcus, XPS and STM study of passive films formed on Fe-22Cr(110) single-crystal surfaces, Journal of the Electrochemical Society, 143, 4 (1996) 1182–1200.

[38] V. Maurice, W. P. Yang, P. Marcus, X-ray photoelectron spectroscopy and scanning tunneling microscopy study of passive films formed on (100) Fe-18Cr-13Ni single-crystal surfaces, Journal of the Electrochemical Society, 145, 3 (1998) 909–920.

[39] R. Jung, H. Tsuchiya, S. Fujimoto, XPS characterization of passive films formed on type 304 stainless steel in humid atmosphere, Corrosion Science, 58 (2012) 62–68.

[40] J. Chen, Q. Zhang, Q. Li, S. Fu, J. Wang, Corrosion and tribocorrosion behaviors of AISI 316 stainless steel and Ti6Al4V alloys in artificial seawater, Transactions of Nonferrous Metals Society of China, 24, 4 (2014) 1022–1031.

[41] Y. Zhang, J.-Z. Wang, X.-Y. Yin, F.-Y. Yan, Tribocorrosion behaviour of 304 stainless steel in different corrosive solutions, Materials and Corrosion, 67, 7 (2016) 769–777.

[42] G. Perumal, A. Ayyagari, A. Chakrabarti, D. Kannan, S. Pati, H. S. Grewal, S. Mukherjee, S. Singh, H. S. Arora, Friction stir processing of stainless steel for ascertaining its superlative performance in bioimplant applications, ACS Applied Materials & Interfaces, 9, 42 (2017) 36615–36631.

[43] J. Saini, H. S. Arora, H. S. Grewal, G. Perumal, Excellent corrosion resistance of dual-phase bimodal stainless steel, 90, 5 (2019) 1–6.

[44] K. Hokkirigawa, K. Karube, M. Kubo, Y. Shirata, Development of new liner dry sliding bearing by using RB ceramics, Proceedings of the International Tribology Conference, Nagasaki 2000, II (2000) 845–849.

Chapter 2

Tribological Properties of Water Lubrication System Using Stainless Steel

2.1 Introduction

Water lubrication is expected in terms of reducing energy consumption and green technology. Therefore, to accelerate the widespread of water lubrication is desired. Stainless steel has a potential as a material that can

This thesis aims to create low frictional interface on the stainless steel and propose the design guidelines of water lubrication system using stainless steel.

As mentioned in the previous chapter, the bulk material of stainless steel is protected by a passive film composed mainly of Cr_2O_3 [1-4]. If this passive film is lost due to underwater friction, the bulk material is worn by corrosion as other ferrous materials. Therefore, keeping the passive film is a necessary condition for using stainless steel as a friction material for water lubrication systems. This means that the passive film must be maintained or self-formed.

In some cases, stainless steel has also been studied as a sliding material for marine vessels [5], [6]. In these previous studies, the combinations using stainless steel shows stainless steel is expected to have only corrosion resistance against seawater and show a friction coefficient of 0.4 or higher. In seawater compared to purified water, the friction coefficient tends to decrease due to the formation of soft corrosion products on stainless steel, but it is not as higher as that of the combination between SiCs.

In this chapter, the possibility of water lubrication system between stainless steel and itself is clarified and the strategy for achieving low friction using stainless steel in water is proposed.

2.2 Experimental details

2.2.1 Specimens

AISI 304 austenitic stainless steel (AISI 304) ball (8 mm in diameter) and disk (30 mm in diameter, 4 mm in height) were used as specimens. Overview of the AISI 304 ball and disk is shown in Fig. 2-1. Figure 2-2 shows the optical microscope images of AISI 304 ball and disk. A surface profile curve of disk

is shown in Fig. 2-3. The profile curve was measured with surface roughness meter (SURFCOM 1500DX, ACCRETECH). Arithmetic mean roughness is 4.7 nm. All specimens were sonicated by acetone and ethanol before the friction tests. Table 2-1 and Table 2-2 show chemical composition and physical properties of AISI 304.

2.2.2 Friction test apparatus

A ball-on-disk friction tester is shown in Fig. 2-4. Sliding friction is generated by pressing a ball specimen against a rotating disk specimen in water. The arm on which the ball specimen is mounted can rotate in the vertical direction around the pivot and in the tangential direction of the disk specimen. Load is applied with a deadweight attached to the arm. The friction force is obtained by measuring the force in the tangential direction of the disk specimen with a load cell.

2.2.3 Evaluation of wear of ball

Specific wear rate of ball ω_s [mm^3/Nm] was introduced to evaluate wear properties. Specific wear rate of ball was calculated as follows:

$$\omega_s = \frac{V}{W \cdot L} \qquad (2.1)$$

where V [mm^3], W [N] and L [m] are the wear volume of ball, normal load and sliding distance, respectively. Wear volume of ball was calculated assuming that the worn region is an ideal spherical cap (Fig. 2-5) and that wear scar of ball is an exact circle shape. The equations are as follows:

$$V = \frac{\pi h(3r^2 + h^2)}{6} \qquad (2.2)$$

$$h = R - \sqrt{(R^2 - r^2)} \qquad (2.3)$$

where R [mm], h [mm] and r [mm] are the radius of ball, the height of the cap and the radius of the wear scar, respectively. Radius of the wear scar which was measured by confocal microscopic images.

2.2.4 Initial contact pressure

Hertz contact pressure P_i [MPa] was introduced to show initial contact pressure. The hertz contact pressure is calculated as follows:

$$P_i = \frac{W}{\pi a^2} \qquad (2.4)$$

$$a = \left(\frac{3WR}{2E'}\right)^{1/3} \qquad (2.5)$$

$$\frac{1}{E'} = \frac{1}{2}\left(\frac{1-{v_1}^2}{E_1} + \frac{1-{v_2}^2}{E_2}\right) \qquad (2.6)$$

2.2.5 Friction test condition

Friction test was performed in purified water (Purified water, Daiwa Yakuhin Corporation) and sliding distance was set to 100 m. Load and sliding velocity were varied from 1 N to 10 N and from 0.01 m/s to 0.5 m/s, respectively. The water temperature was kept at 25°C constantly. Contact surface pressure was calculated from the dimeter of wear scar on ball specimen after friction test.

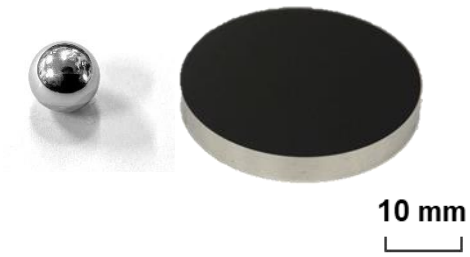

Fig. 2-1 Overview of the AISI 304 ball and disk.

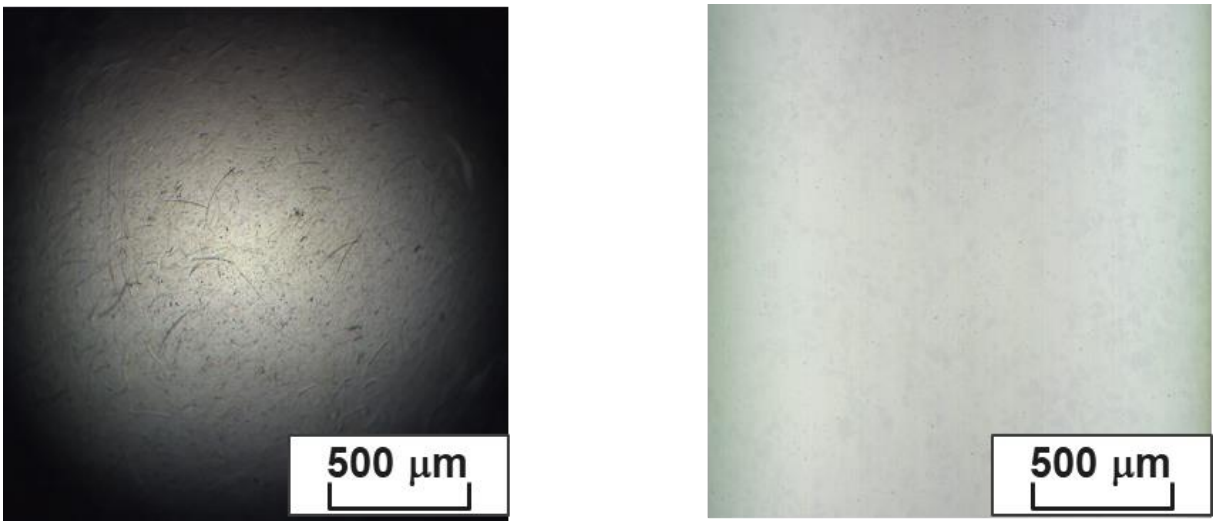

(a) AISI 304 ball

(b) AISI 304 disk

Fig. 2-2 Optical images of initial surface of (a) AISI 304 ball and (b) AISI 304 disk.

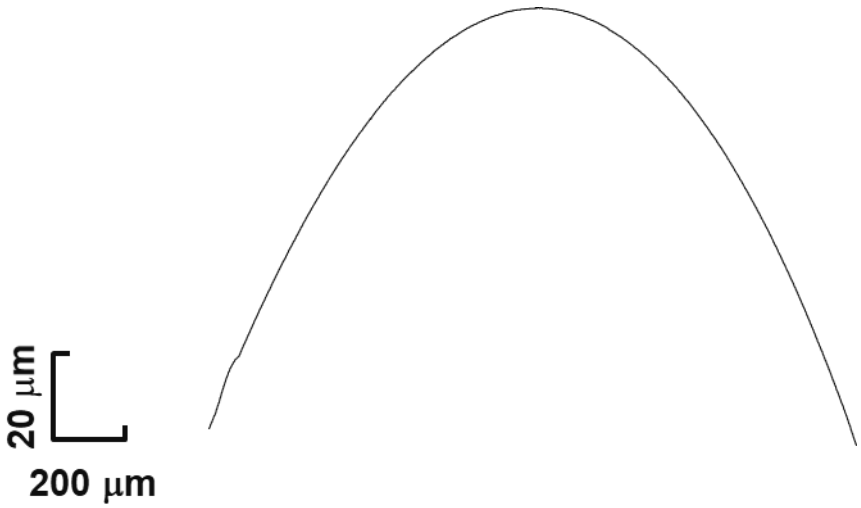

(a) AISI 304 ball

(b) AISI 304 disk

Fig. 2-3 Surface profile curves of (a) AISI 304 ball and (b) AISI 304 disk.

Table 2-1 Elemental composition in wt% of AISI 304 austenitic stainless steel.

Chemical composition wt.%							
C	Si	Mn	P	S	Ni	Cr	Fe
≤ 0.08	≤ 1.00	≤ 2.00	≤ 0.045	≤ 0.03	8.00- 10.5	18.0- 20.0	Bal.

Table 2-2 Mehcanical properties of AISI 304 austenitic stainless steel.

Density, kg/m^3	7930
Young's modulus, GPa	193
Poisson's ratio	0.43
Bending strength, MPa	520
Vickers hardness Hv, GPa	< 0.2
Thermal conductivity, W/m·K	16.3 (373.16 K)
Specific heat, kJ/(kg·K)	0.59

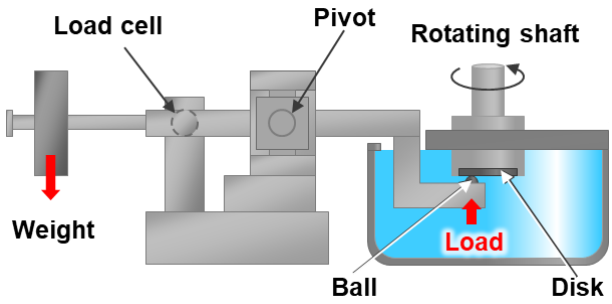

Fig. 2-4 Schematic illustration of ball-on-disk type friction apparatus.

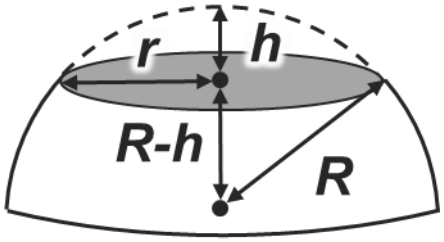

Fig. 2-5 Schematic diagram of worn ball specimen.

2.3 Experimental results and discussion

2.3.1 Friction behavior of stainless steel sliding against itself

Figure 2-7 shows friction properties of AISI 304/AISI 304 in water at load of 1 N and sliding velocity varied from 0.01 to 0.5 m/s. Figure 2-8 shows friction properties of AISI 304/AISI 304 in water at load of 5 N and sliding velocity varied from 0.01 to 0.5 m/s. Figure 2-9 shows friction properties of AISI 304/AISI 304 in water at load of 10 N and sliding velocity varied from 0.01 to 0.5 m/s. From these results, it can be seen that the friction coefficient continues to rise from the beginning and there is no condition that running-in behavior is exhibited in any load range and sliding velocity range. In particular, the friction behavior has large amplitude under sliding conditions of sliding velocity 0.2- 0.5 m/s.

Figure 2-10 shows optical microscope images of wear scar on AISI 304 ball slid against itself in water at normal load of 1 N and sliding velocity varied from 0.01 to 0.5 m/s. Figure 2-11 shows optical microscope images of wear scar on AISI 304 ball slid against itself in water at normal load of 5 N and sliding velocity varied from 0.01 to 0.5 m/s. Figure 2-12 shows optical microscope images of wear scar on AISI 304 ball slid against itself in water at normal load of 10 N and sliding velocity varied from 0.01 to 0.5 m/s. From these results, the wear scar diameter increases as the load increases. Many wear scars were formed parallel to the sliding direction, but the scaly transfer films were formed on the wear scars under conditions where frictional behavior has a large amplitude such as a sliding speed of 0.2-0.5 m/s occurs. Black wear particles that can be easily removed by rinsing with purified water is deposited around the wear scar. All wear scars basically had a metallic luster. When the sliding velocity is 0.2 m/s or 0.5 m/s, the area of wear scar is about four times as large as the other sliding velocity.

Relationship between friction coefficient and bearing characteristic number qualitatively showing the lubrication film thickness between the two surfaces is summarized in Fig. 2-13. AISI 304/AISI 304 shows the friction coefficient varied from 0.3 to 1.0 under various sliding conditions and does not depend on the relative thickness of the lubricating film. For reference, the friction coefficient of SiC/SiC is plotted. Thus, it can be understood how high the friction between AISI304 is.

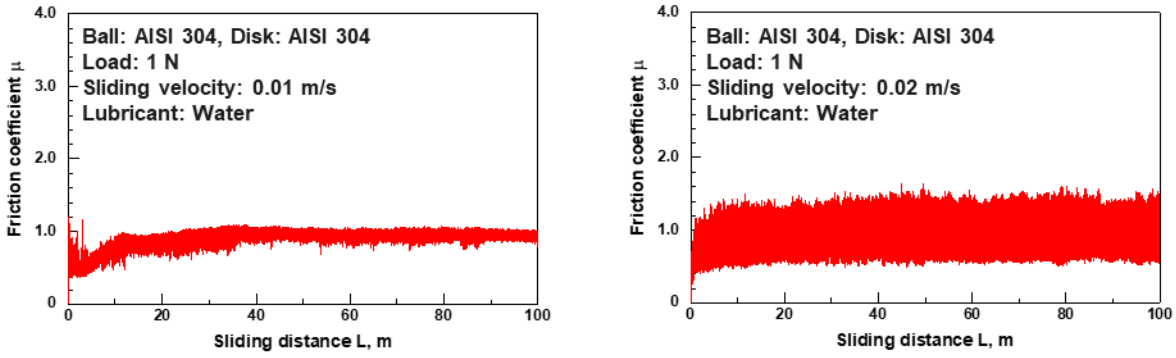

(a) 0.01 m/s

(b) 0.02 m/s

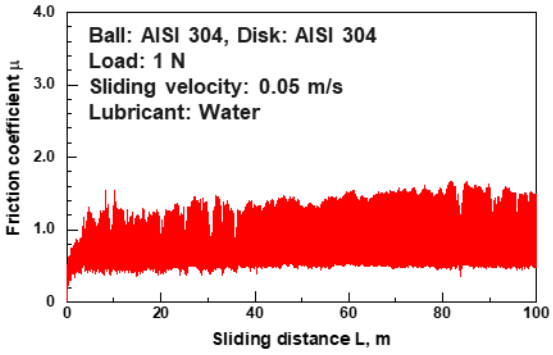

(c) 0.05 m/s

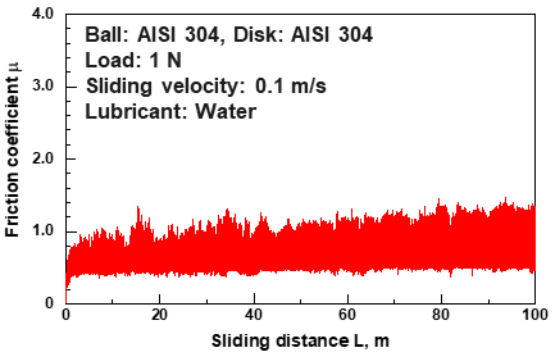

(d) 0.1 m/s

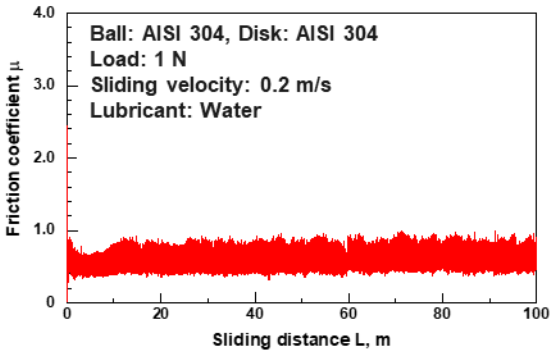

(e) 0.2 m/s

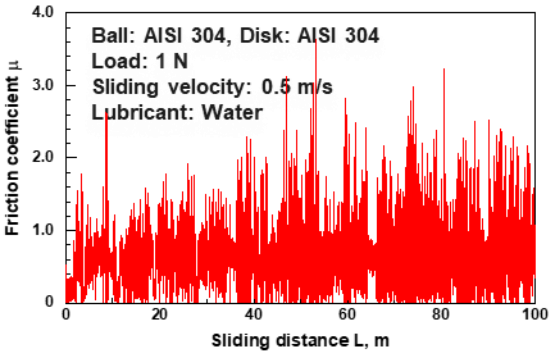

(f) 0.5 m/s

Fig. 2-7 Friction properties of AISI 304 sliding against itself in water at load 1 N and sliding velocity (a) 0.01 m/s, (b) 0.02 m/s, (c) 0.05 m/s, (d) 0.1 m/s, (e) 0.2 m/s and (f) 0.5 m/s.

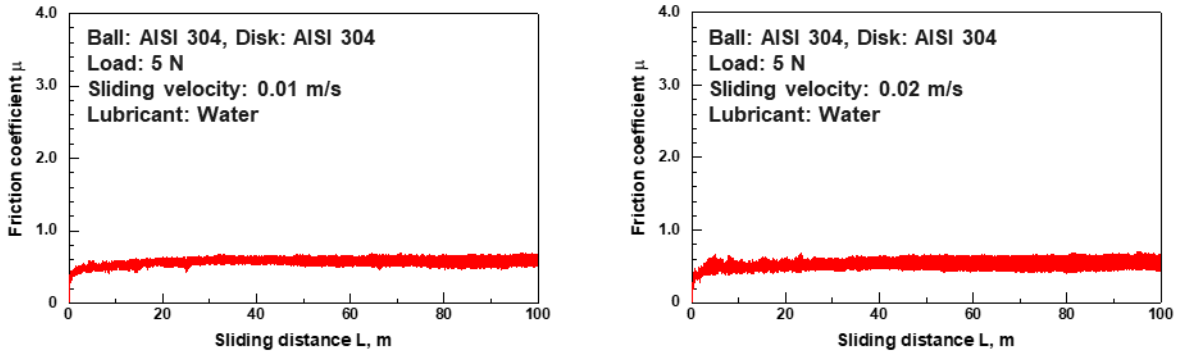

(a) 0.01 m/s

(b) 0.02 m/s

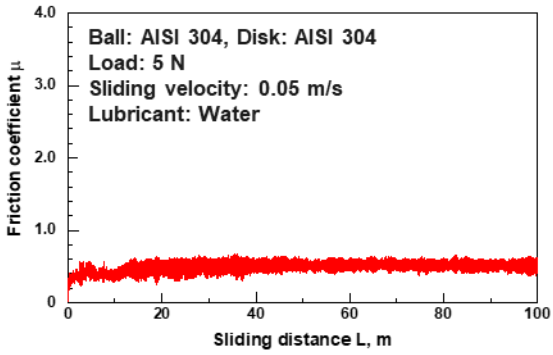

(c) 0.05 m/s

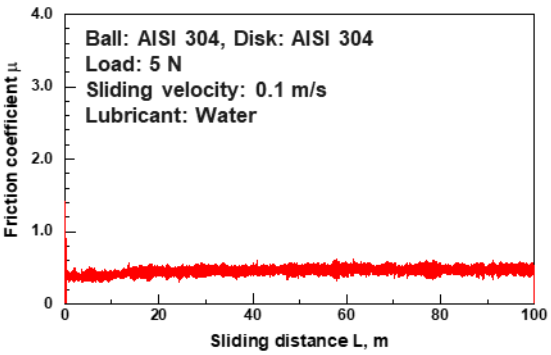

(d) 0.1 m/s

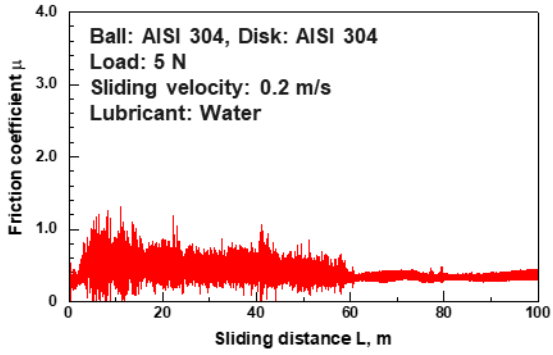

(e) 0.2 m/s

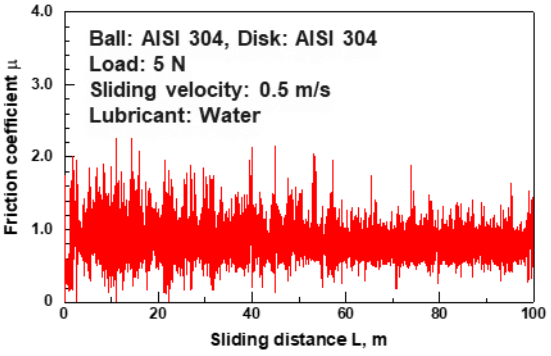

(f) 0.5 m/s

Fig. 2-8 Friction properties of AISI 304 sliding against itself in water at load 5 N and sliding velocity (a) 0.01 m/s, (b) 0.02 m/s, (c) 0.05 m/s, (d) 0.1 m/s, (e) 0.2 m/s and (f) 0.5 m/s.

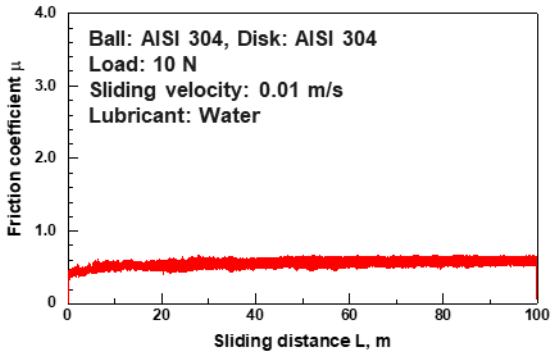

(a) 0.01 m/s

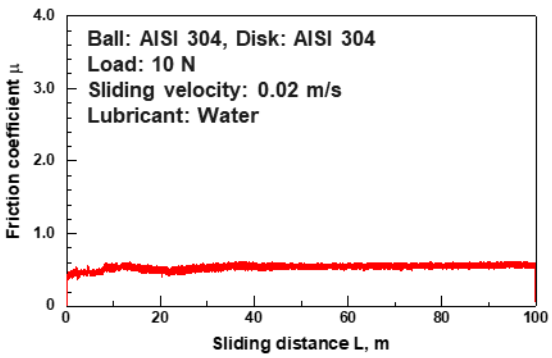

(b) 0.02 m/s

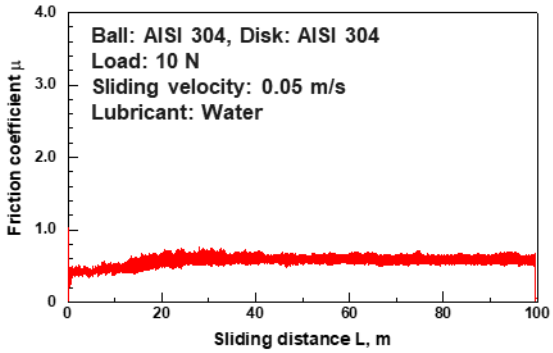

(c) 0.05 m/s

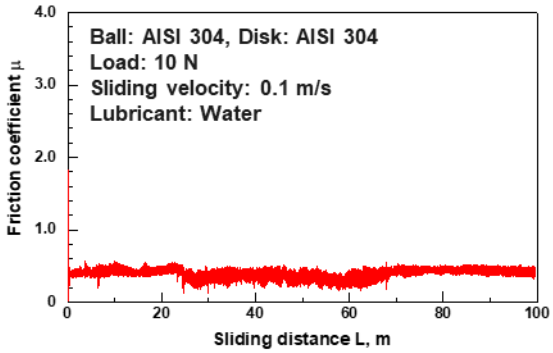

(d) 0.1 m/s

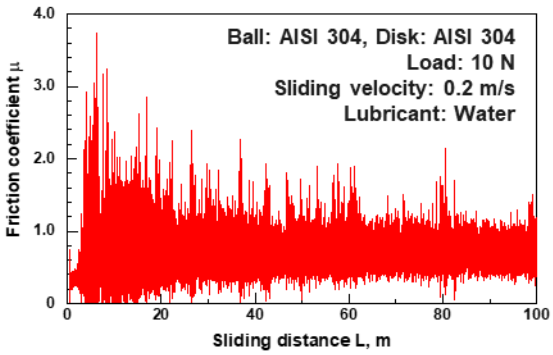

(e) 0.2 m/s

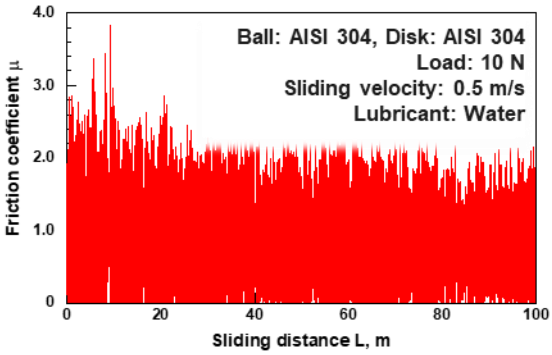

(f) 0.5 m/s

Fig. 2-9 Friction properties of AISI 304 sliding against itself in water at load 10 N and sliding velocity (a) 0.01 m/s, (b) 0.02 m/s, (c) 0.05 m/s, (d) 0.1 m/s, (e) 0.2 m/s and (f) 0.5 m/s.

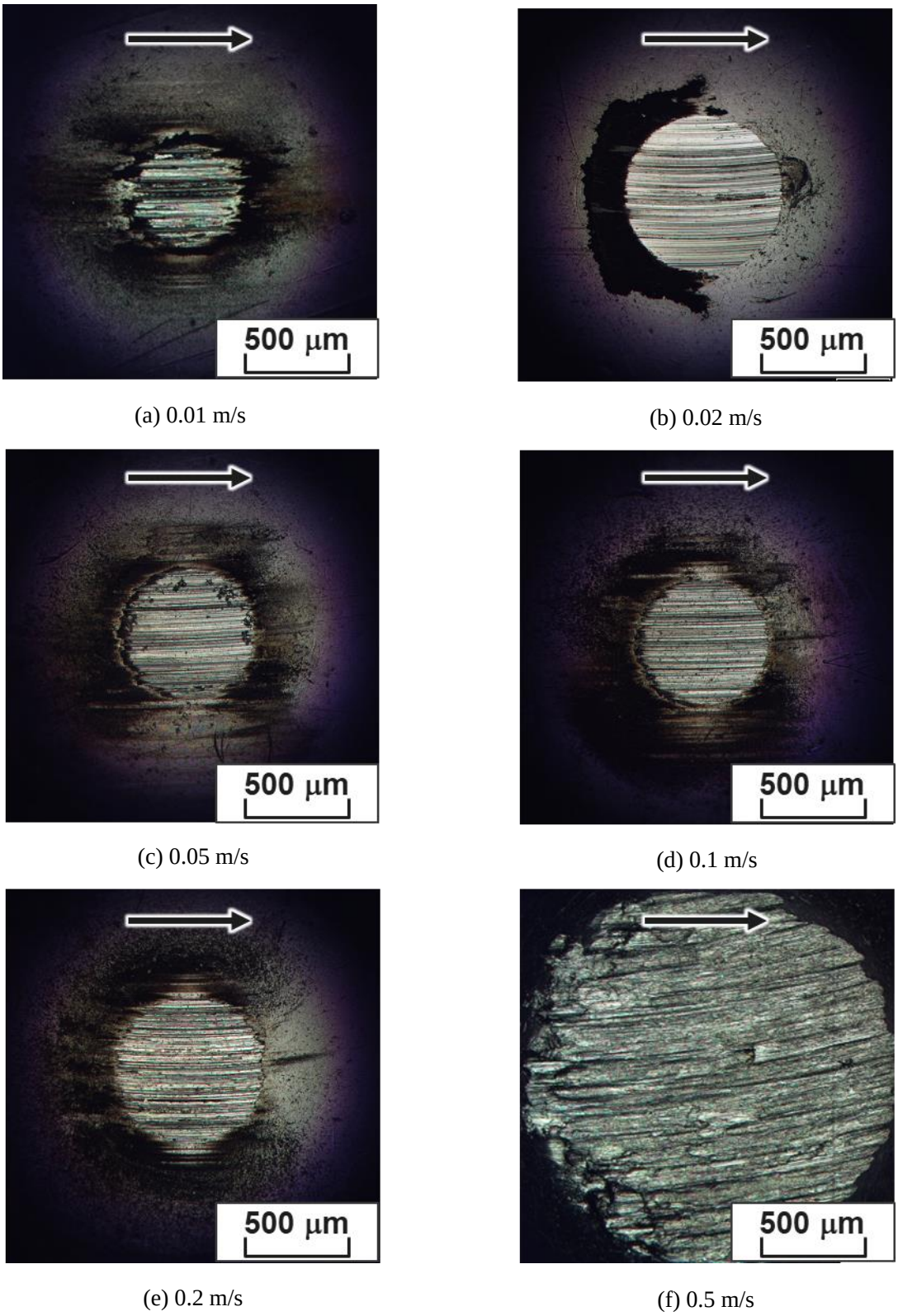

(a) 0.01 m/s (b) 0.02 m/s

(c) 0.05 m/s (d) 0.1 m/s

(e) 0.2 m/s (f) 0.5 m/s

Fig. 2-10 Optical microscope images of wear scar on AISI 304 ball sliding against itself in water at load 1 N and sliding velocity (a) 0.01 m/s, (b) 0.02 m/s, (c) 0.05 m/s, (d) 0.1 m/s, (e) 0.2 m/s and (f) 0.5 m/s. Blacks arrow indicate the sliding direction of disk material.

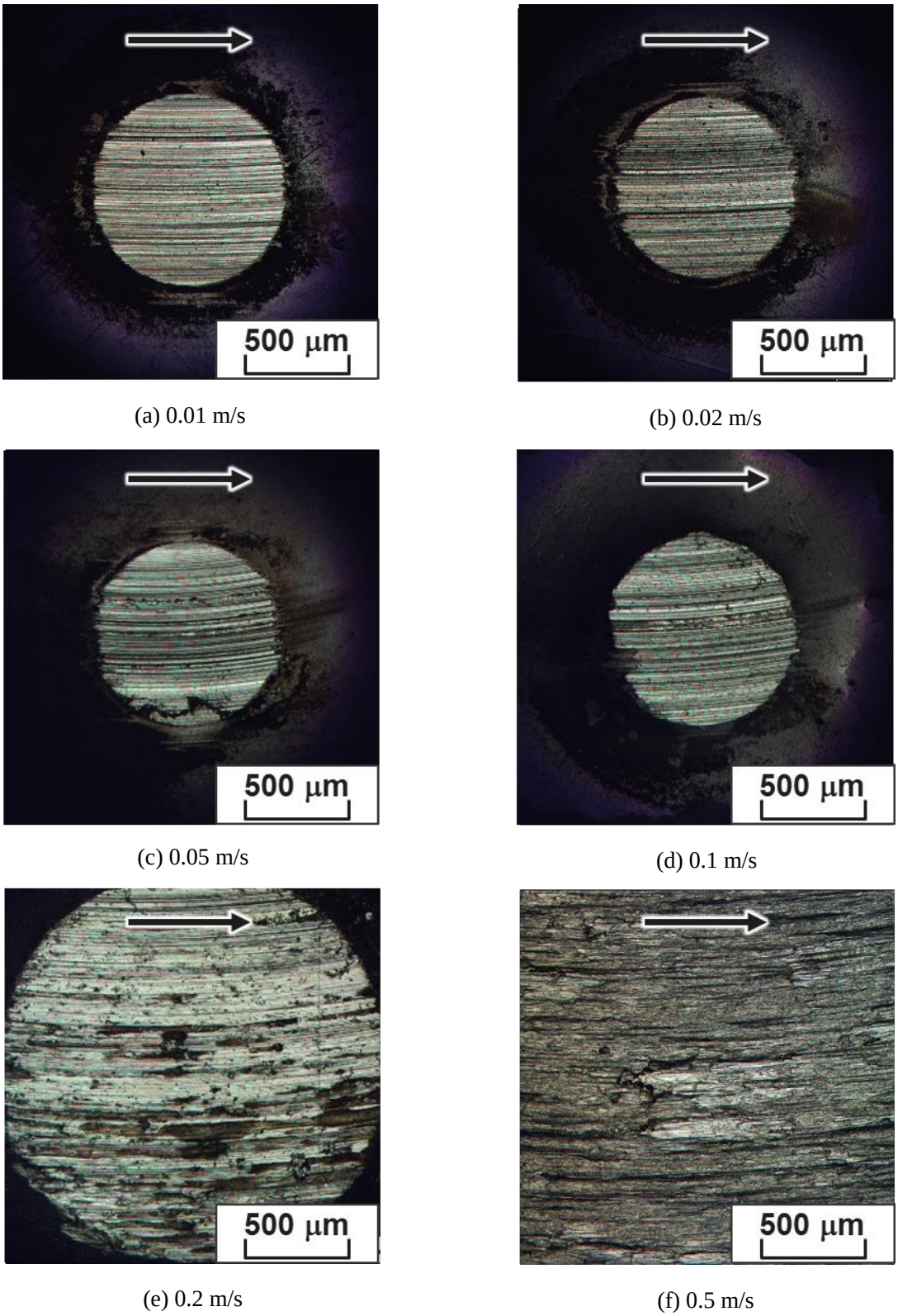

(a) 0.01 m/s (b) 0.02 m/s

(c) 0.05 m/s (d) 0.1 m/s

(e) 0.2 m/s (f) 0.5 m/s

Fig. 2-11 Optical microscope images of wear scar on AISI 304 ball sliding against itself in water at load 5 N and sliding velocity (a) 0.01 m/s, (b) 0.02 m/s, (c) 0.05 m/s, (d) 0.1 m/s, (e) 0.2 m/s and (f) 0.5 m/s.

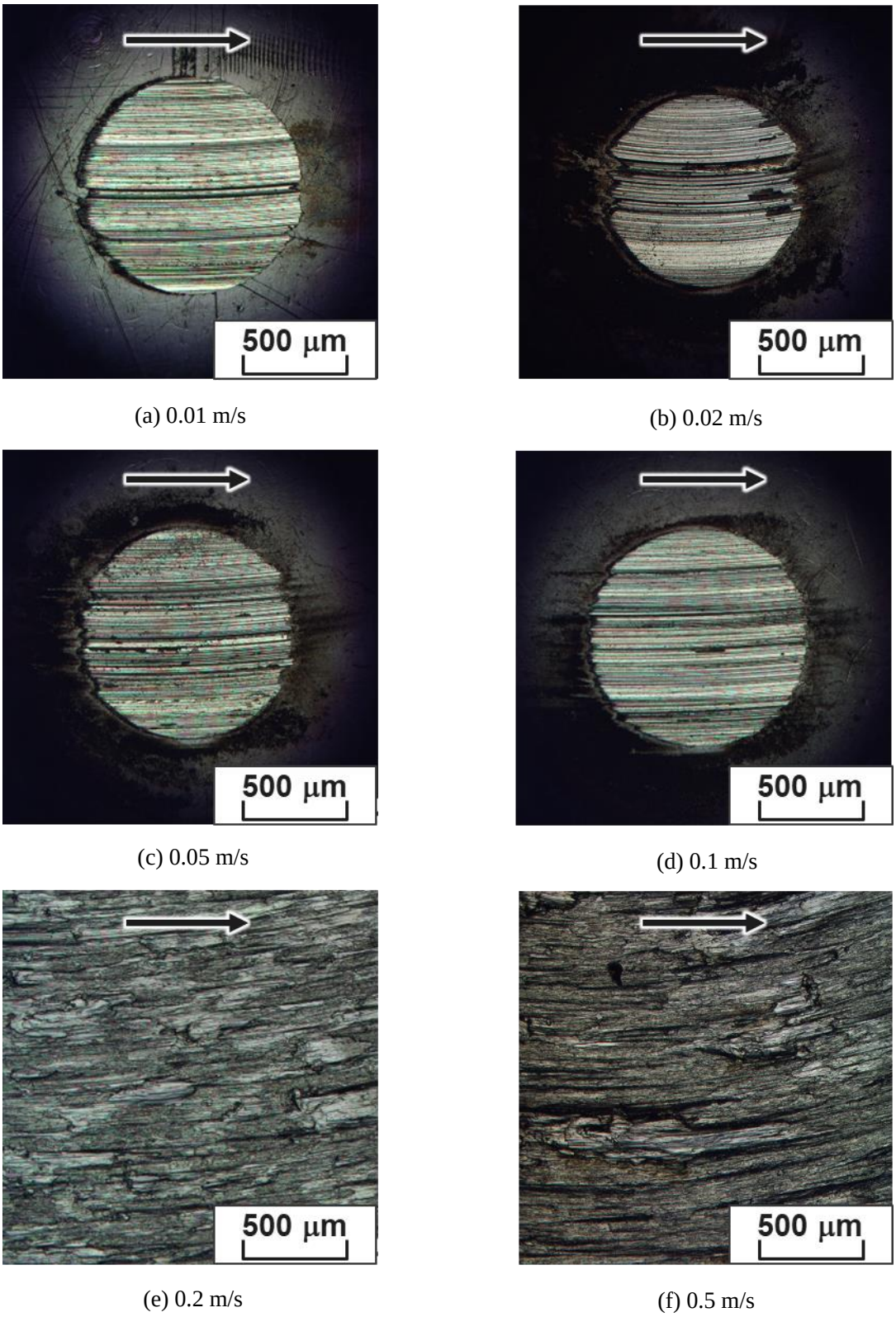

(a) 0.01 m/s (b) 0.02 m/s

(c) 0.05 m/s (d) 0.1 m/s

(e) 0.2 m/s (f) 0.5 m/s

Fig. 2-12 Optical microscope images of wear scar on AISI 304 ball sliding against itself in water at load 10 N and sliding velocity (a) 0.01m/s, (b) 0.02 m/s, (c) 0.05 m/s, (d) 0.1 m/s, (e) 0.2 m/s and (f) 0.5 m/s. Blacks arrow indicate the sliding direction of disk material.

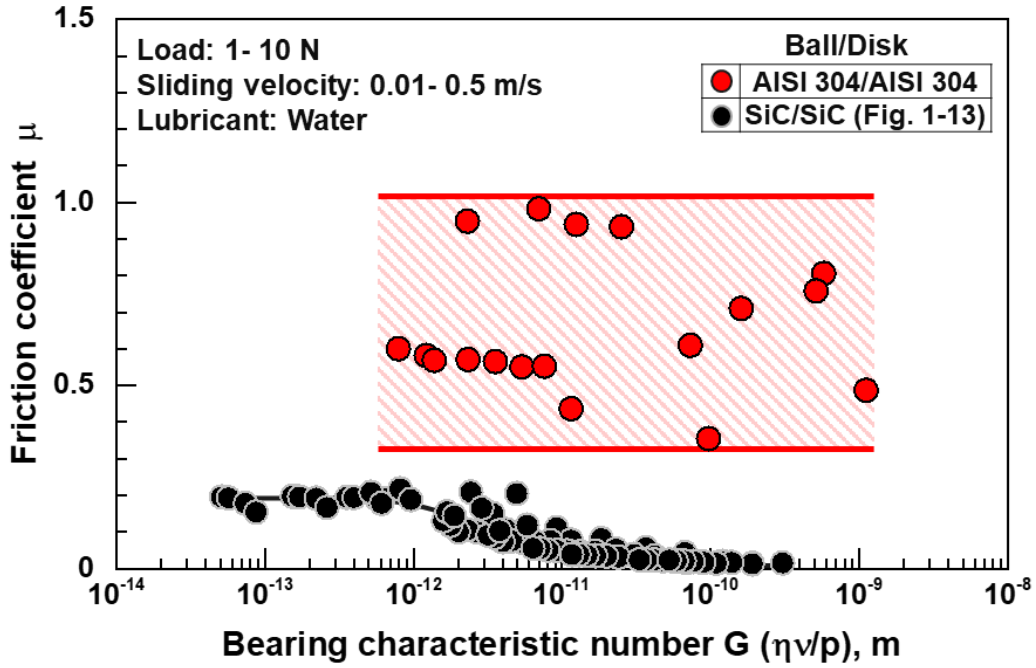

Fig. 2-13 Relationship between bearing characteristic number and average friction coefficient of AISI 304/AISI 304 in water.

2.3.2 Wear modes of stainless steel sliding against itself in water

Figure 2-14 shows distribution of wear modes of AISI 304/AISI 304 as a function of sliding velocity a by initial contact pressure and specific wear rate of ball. This result indicates that wear mode of AISI 304 sliding against itself in water is determined by initial contact pressure multiplied by sliding velocity. When sorted out using the constant $P_i \cdot V$ value line, it becomes as shown in the Fig. 2-15. This figure indicates that as the $P_i \cdot V$ value increases, that is, as the amount of input energy given to the friction surface increases, the specific wear rate increases too.

Figures 2-16 and 2-17 show the topography of the wear surface of the wear scar on AISI 304 ball and the wear track on AISI 304 disk in load of 10 N and sliding velocity of 0.5 m/s. It can be seen that the wear scar is formed by adhering several layers. Figure 2-18 shows the profile curves of wear scar and wear track in the same condition. From this profile curve, it can be seen that both surfaces have shape with a peak of several ten micrometer.

In constant, Figures 2-19 and 2-20 show the SEM image of the wear scar on ball specimen and the wear track on disk specimen in load of 1 N and sliding velocity of 0.01 m/s. It can be seen that the wear surface is formed by scratch of a mating material. Figure 2-21 shows the profile curves of wear scar and wear track in the same condition. From Fig. 2-21, the wear surfaces with a height of about 10 μm or less and it is understood that it forms a relatively flat plane as compared with the surface of Fig. 2-18.

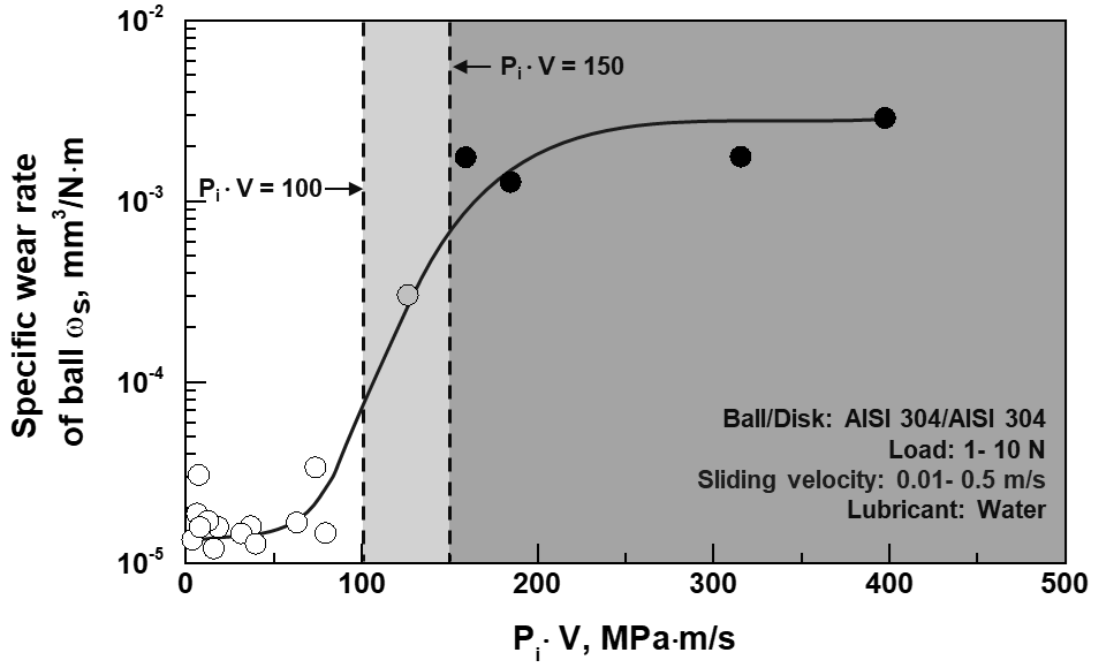

Fig. 2-14 Relationship among the product of initial contact pressure, sliding velocity and specific wear rate of AISI 304/AISI 304 in water.

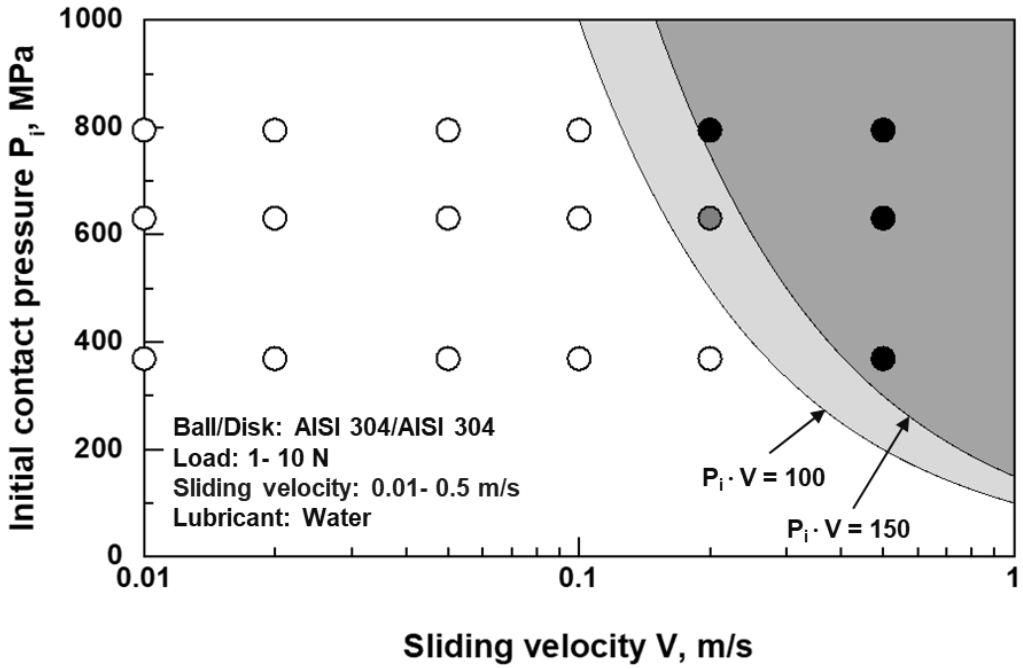

Fig. 2-15 Distribution of wear mode of AISI 304/AISI 304 in water as function hertz contact pressure and sliding velocity.

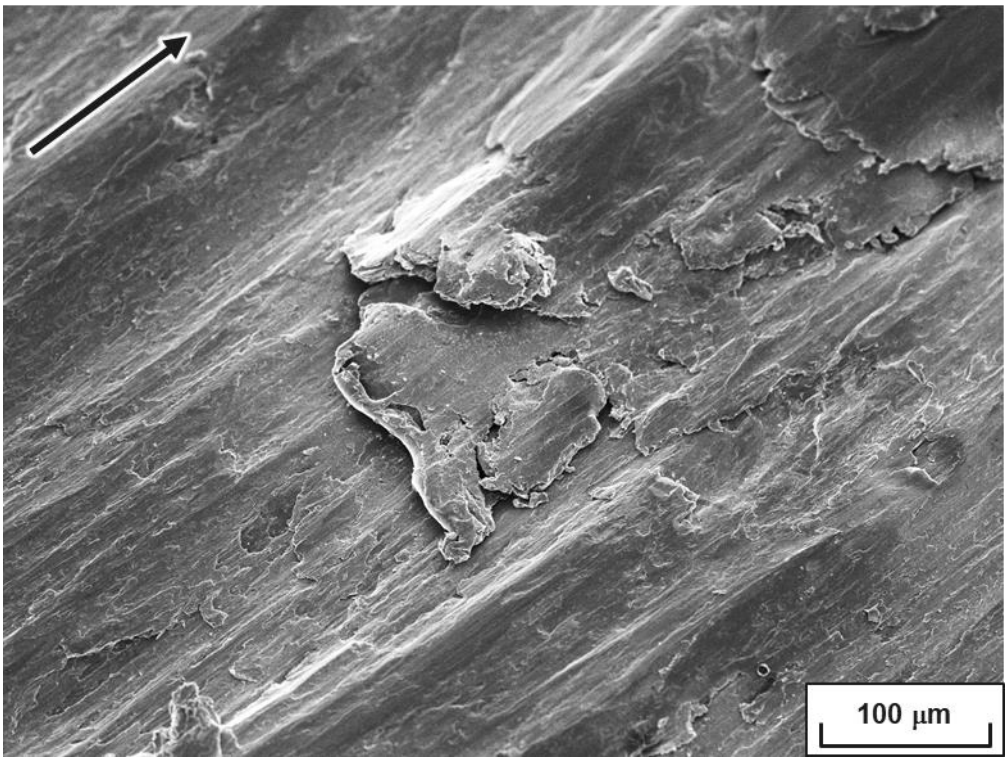

Fig. 2-16 SEM image of the wear scar on AISI 304 ball specimen (load 10 N, sliding velocity 0.5 m/s). Black arrow indicates the sliding direction of disk material.

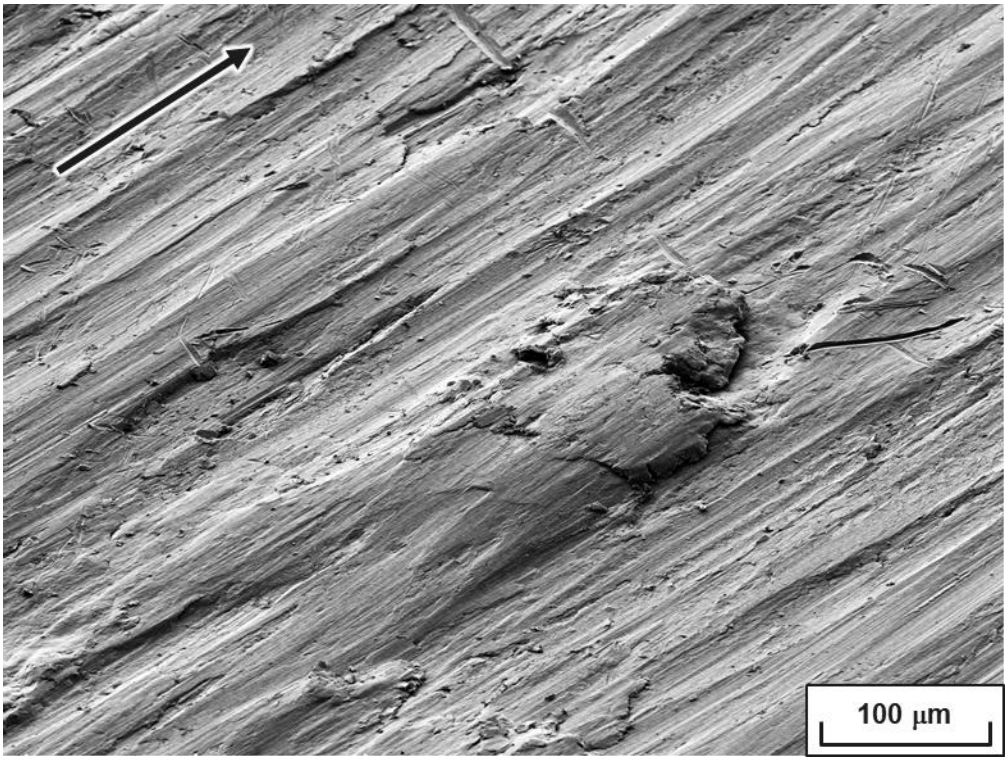

Fig. 2-17 SEM image of the wear track on AISI 304 disk specimen (load 10 N, sliding velocity 0.5 m/s). Black arrow indicates the sliding direction of disk material.

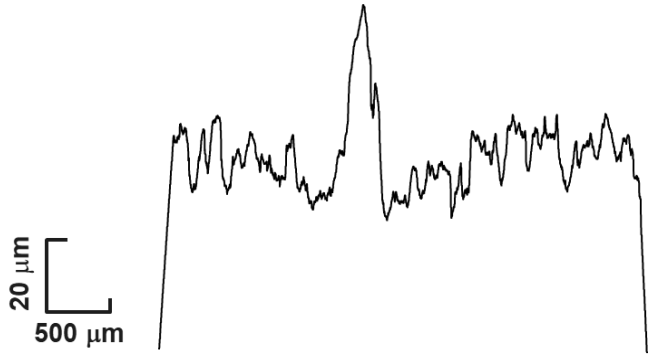

(a) Wear scar on the ball

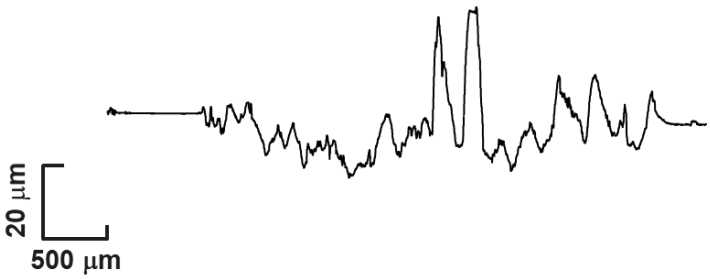

(b) Wear track on the disk

Fig. 2-18 Surface profile curves of (a) wear scar on AISI 304 ball and (b) wear track on AISI 304 disk (load 10 N, sliding velocity 0.5 m/s).

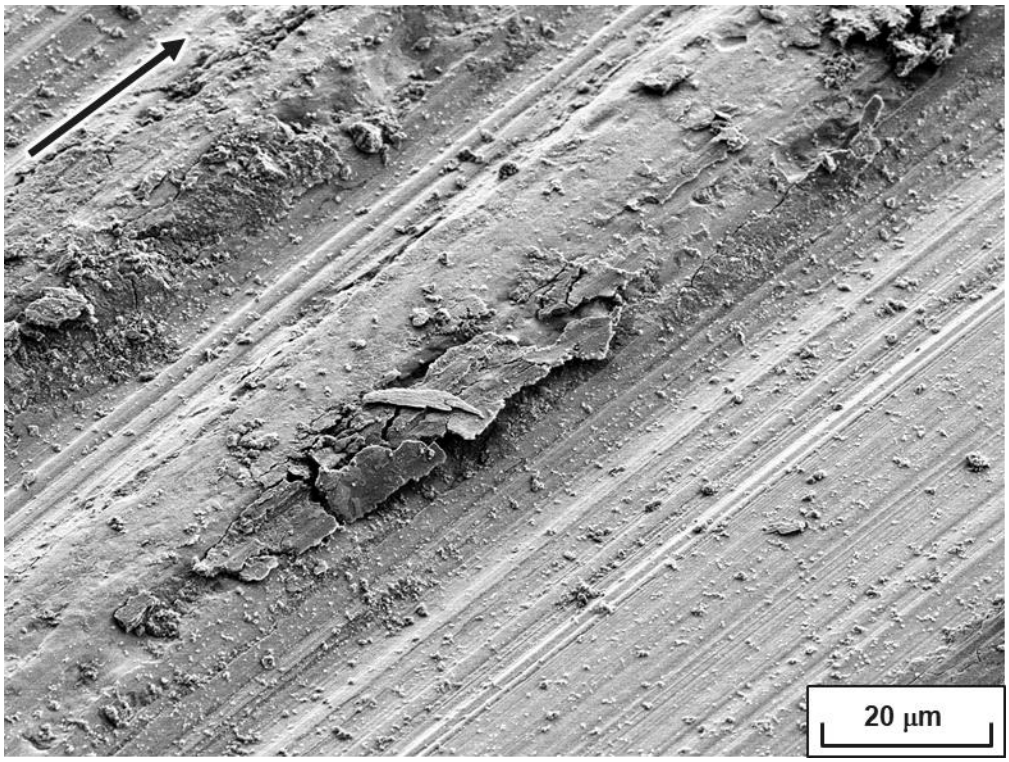

Fig. 2-19 SEM image of the wear scar on AISI 304 ball (load 1 N, sliding velocity 0.01 m/s). Black arrow indicates the sliding direction of counter material.

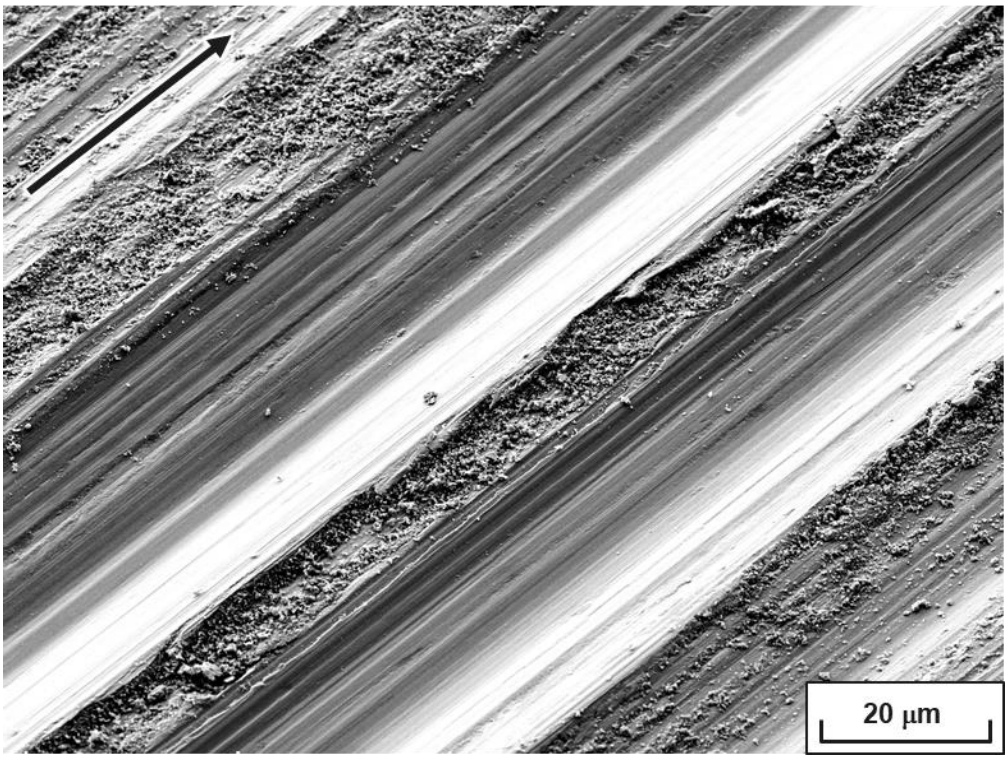

Fig. 2-20 SEM image of the wear track on AISI 304 disk (load 1 N, sliding velocity 0.01 m/s). Black arrow indicates the sliding direction of counter material.

(a) Wear scar on the ball

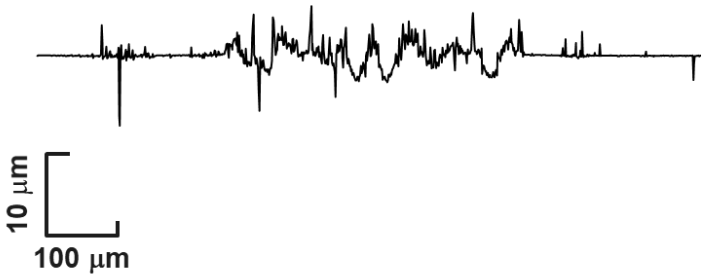

(b) Wear track on the disk

Fig. 2-21 Surface profile curves of (a) wear scar on AISI 304 ball and (b) wear track on AISI 304 disk (load 1 N, sliding velocity 0.01 m/s).

2.4 Conclusions

In this chapter, friction tests using a stainless steel ball slid against stainless steel disk were conducted under various sliding conditions in water. As a result, the following conclusions were achieved.

(1) The combination of AISI 304/AISI 304 shows friction coefficient in water varied from 0.3 to 1.0 under various sliding conditions.

(2) The specific wear rate of the ball in AISI 304/AISI 304 increases from 10^{-5} $mm^3/N{\cdot}m$ to 10^{-2} $mm^3/N{\cdot}m$ as the sliding velocity and initial contact pressure increases.

(3) Seizure occurred on both surfaces even under the lowest sliding velocity and the lowest initial contact pressure. Thus adhesion of stainless steel is found to be main cause of high friction and severe wear.

References

[1] V. Maurice, W. P. Yang, P. Marcus, XPS and STM investigation of the passive film formed on Cr(110) single-crystal surfaces, Journal of the Electrochemical Society, 141, 11 (1994) 3016–3027.

[2] V. Maurice, W. P. Yang, P. Marcus, XPS and STM study of passive films formed on Fe-22Cr(110) single-crystal surfaces, Journal of the Electrochemical Society, 143, 4 (1996) 1182–1200.

[3] V. Maurice, W. P. Yang, P. Marcus, X-ray photoelectron spectroscopy and scanning tunneling microscopy study of passive films formed on (100) Fe-18Cr-13Ni single-crystal surfaces, Journal of the Electrochemical Society, 145, 3 (1998) 909–920.

[4] R. Jung, H. Tsuchiya, S. Fujimoto, XPS characterization of passive films formed on type 304 stainless steel in humid atmosphere, Corrosion Science, 58 (2012) 62–68.

[5] J. Chen, Q. Zhang, Q. Li, S. Fu, J. Wang, Corrosion and tribocorrosion behaviors of AISI 316 stainless steel and Ti6Al4V alloys in artificial seawater, Transactions of Nonferrous Metals Society of China, 24, 4 (2014) 1022–1031.

[6] Y. Zhang, J. Z. Wang, X. Y. Yin, F. Y. Yan, Tribocorrosion behaviour of 304 stainless steel in different corrosive solutions, Materials and Corrosion, 67, 7 (2016) 769–777.

Chapter 3

Silicon-based Ceramics as Mating Material of Stainless Steel in Water

3.1 Introduction

In chapter 2, it was revealed that friction between the AISI 304 in water shows a high coefficient of friction of 0.3 to 1.0 without depending on the lubrication region (Fig. 2-13) and the specific wear rate increases with increase in the $P_i \cdot V$ value (Fig. 2-14). It was found that water can not play as a role of lubricant and behaves like friction behavior in an unlubricated state. The role of water as lubricant is desired to improve the water lubrication properties using stainless steel. Therefore, silicon-based ceramics materials were introduced as the mating material in order to suppress the adhesion of stainless steel.

Si_3N_4 and SiC which are materials expected to become the friction surface smoothness and hydrophilic by tribochemical reaction with water as follow [1-5].

$$Si_3N_4 + 6H_2O \rightarrow 3SiO_2 + 4NH_3 \quad (3.1)$$

$$SiC + 2H_2O \rightarrow SiO_2 + CH_4 \quad (3.2)$$

$$SiO_2 + 2H_2O \rightarrow Si(OH)_4 \quad (3.3)$$

$$SiO_2 + nH_2O \rightarrow SiO_2 \cdot n(H_2O) \quad (3.4)$$

The combination of silicon-based ceramics and steel has been studied by many researchers [6-15]. Silicon-based ceramics are expected to react with water and have advantages such as high strength and hardness, but many severe brittle fractures occur due to existing pores, grain boundaries, and cracks near the surface. Due to low fracture toughness, ceramic materials are not widely used in the manufacture of mechanical parts.

For engineering applications, stress relaxation is required to avoid brittle fracture in ceramic materials. Therefore, a combination of ceramic and metal materials is expected to exhibit an excellent balance between fracture toughness and strength [16].

In the present chapter, silicon-based ceramics materials are introduced as counter material of AISI 304 in order to discuss the possibilities to obtain low friction and low wear in water. The effect of

hydrophilization process on frictional behavior due to tribochemical reaction between silicon-based ceramics and water is focused.

3.2 Experimental details

3.2.1 Specimens

AISI 304 ball (8 mm in diameter) and Si_3N_4 and SiC disk (30 mm in diameter, 4 mm in height) were used as specimens. Overview of the Si_3N_4 and SiC disk are shown in Fig. 3-1. Optical microscope image of initial Si_3N_4 and SiC disk is shown in Fig. 3-2. A surface profile curve of Si_3N_4 and SiC disk are shown in Fig. 3-3. These disks were 30 mm in diameter, 4 mm in thickness. Arithmetic mean roughness are 6.8 nm and 19.0 nm, respectively.

Table 3-1 shows mechanical properties of Si_3N_4 and SiC. All specimens were sonicated by acetone and ethanol before the friction tests.

3.2.2 Friction test conditions

Friction tests were conducted in water as shown in Fig. 2-4. Friction tests were performed in purified water and sliding distance was set as 100 m. Load and sliding velocity were varied from 1 N to 10 N and from 0.01 to 0.5 m/s respectively. The water temperature was kept constant at 20°C. In order to investigate chemical changes of worn surface, contact angle of water droplet on the worn surface was measured. Microscopic contact angle meter (MCA-3, Kyowa Interface Science) was used. Purified water was used as test liquid. Water droplet is generated through a grass capillary. Volume of droplet was controlled within the range of 100 to 200 μm. Specimens after the friction tests were rinsed in purified water to avoid contamination owing to wear particles. Specimens were picked up from water and then dried with a blower immediately before measurements. Measurements were finished at least within 30 minutes after pickup from water. After first measurement, the specimen is wiped by acetone in order to remove a tribo-chemical reaction product from worn surface and measurement is performed again.

(a) Si_3N_4 (b) SiC

Fig. 3-1 Overviews of (a) Si3N4 and (b) SiC disk

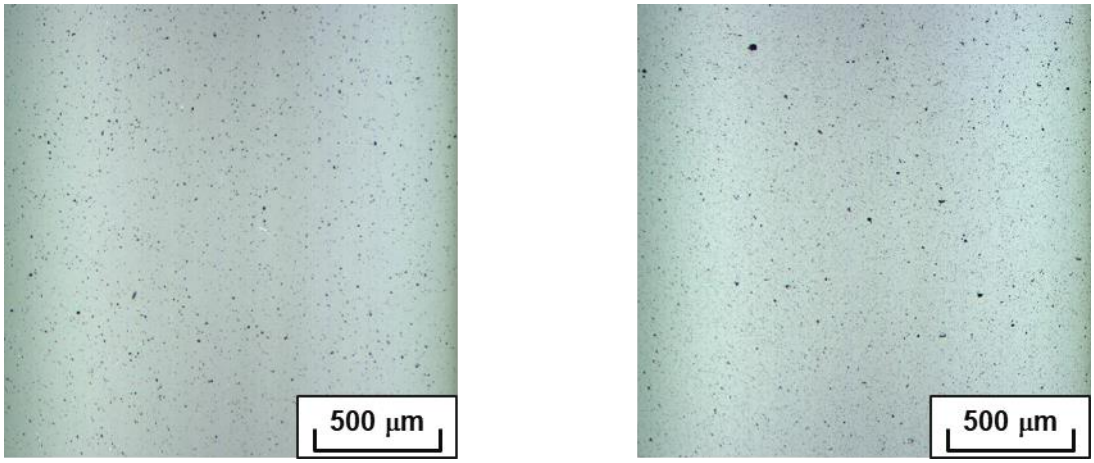

(a) Si_3N_4 (b) SiC

Fig. 3-2 Optical microscope images of initial surface of (a) Si_3N_4 and (b) SiC disk.

(a) Si_3N_4 disk

(b) SiC disk

Fig. 3-3 Surface profile curves of (a) Si_3N_4 and (b) SiC disk.

Table 3-1 Mechanical properties of Si3N4 and SiC.

	Si_3N_4	SiC
Density, kg/m^3	3200	3100
Young's modulus, GPa	290	430
Poisson's ratio	0.29	0.18
Bending strength, MPa	800	490
Vickers hardness Hv, GPa	15	25
Thermal conductivity, W/m·K	24	158
Specific heat, kJ/(kg·K)	0.64	0.67

3.3 Experimental results and discussion

3.3.1 Friction and wear behaviors of silicon-based ceramics sliding against stainless steel

Figure 3-4 shows friction properties of AISI 304/Si_3N_4 in water at normal load of 1 N and sliding velocity varied from 0.01 to 0.5 m/s. Figure 3-5 shows friction properties of AISI 304/Si_3N_4 in water at normal load of 5 N and sliding velocity varied from 0.01 to 0.5 m/s. Figure 3-6 shows friction properties of AISI 304/Si_3N_4 in water at normal load of 10 N and sliding velocity varied from 0.01 to 0.5 m/s. Under many sliding conditions, the friction coefficient rises from the beginning and stabilizes at a high level. On the other hand, it is noteworthy that under the sliding conditions of low load and low sliding velocity, the tribo-pair of AISI 304/Si_3N_4 shows friction behavior with large amplitude.

Figure 3-7 shows optical microscope images of wear scar on AISI 304 ball slid against Si_3N_4 in water at normal load of 1 N and sliding velocity varied from 0.01 to 0.5 m/s. Figure 3-8 shows optical microscope images of wear scar on AISI 304 ball slid against Si_3N_4 in water at normal load of 5 N and sliding velocity varied from 0.01 to 0.5 m/s. Figure 3-9 shows optical microscope images of wear scar on AISI 304 ball slid against Si_3N_4 in water at normal load of 10 N and sliding velocity varied from 0.01 to 0.5 m/s. The wear scar diameter increases as the load increases. Many wear scars were formed parallel to the sliding direction, but the scaly transfer films were formed on the wear scars under conditions where frictional behavior has a large amplitude such as a sliding speed of 0.2-0.5 m/s occurs. All wear scars basically had a metallic luster. A black transfer film tends to be formed on wear scar on AISI 304 ball under high load conditions.

Figure 3-10 shows friction properties of AISI 304/SiC in water at normal load of 1 N and sliding velocity varied from 0.01 to 0.5 m/s. Figure 3-11 shows friction properties of AISI 304/SiC in water at normal load of 5 N and sliding velocity varied from 0.01 to 0.5 m/s. Figure 3-12 shows friction properties of AISI 304/SiC in water at normal load of 10 N and sliding velocity varied from 0.01 to 0.5 m/s. This combination didn’t show running-in behavior and stabilize at a lower level than AISI 304/Si_3N_4.

Figure 3-13 shows optical microscope images of wear scar on AISI 304 ball slid against SiC in water at normal load of 1 N and sliding velocity varied from 0.01 to 0.5 m/s. Figure 3-14 shows optical microscope images of wear scar on AISI 304 ball slid against SiC in water at normal load of 5 N and sliding velocity varied from 0.01 to 0.5 m/s. Figure 3-15 shows optical microscope images of wear scar on AISI 304 ball slid against SiC in water at normal load of 10 N and sliding velocity varied from 0.01 to 0.5 m/s. The diameter of wear scar on AISI 304 slid against SiC tends to be smaller than that on AISI 304 slid against Si_3N_4.

Relationship between friction coefficient and bearing characteristic number are shown in Fig. 3-16 . AISI 304/Si_3N_4 and AISI 304/SiC show a tendency to decrease friction coefficient in water as the number of bearing characteristics increases. This means that the friction coefficient decreases in a lubricated state where it is easy to form a water film relatively. AISI 304/Si_3N_4 shows friction coefficient in water varied from 0.4 to 0.8 and AISI 304/SiC shows friction coefficient in water varied from 0.2 to 0.4, which shows the effect of reducing friction in water using AISI 304 by silicon-based ceramics.

Thus, it was clarified that selection of the mating material of AISI 304 leads to improve the water lubrication properties of AISI 304. However, these combinations have not been reached to the friction between silicon carbides in water.

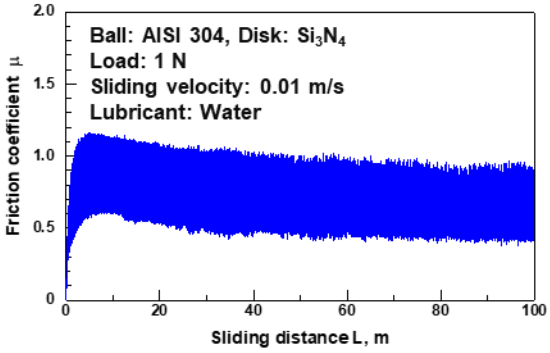

(a) 0.01 m/s

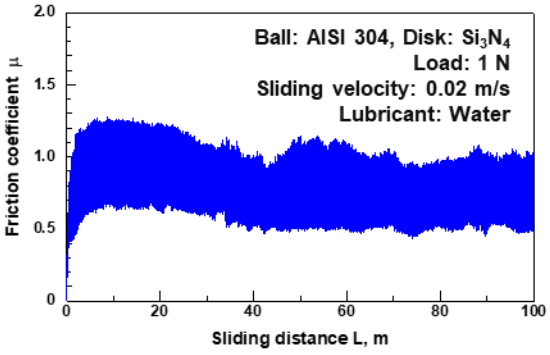

(b) 0.02 m/s

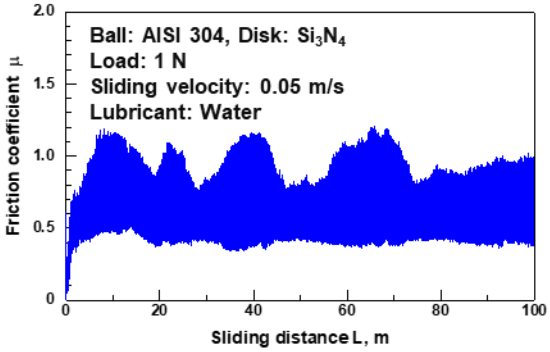

(c) 0.05 m/s

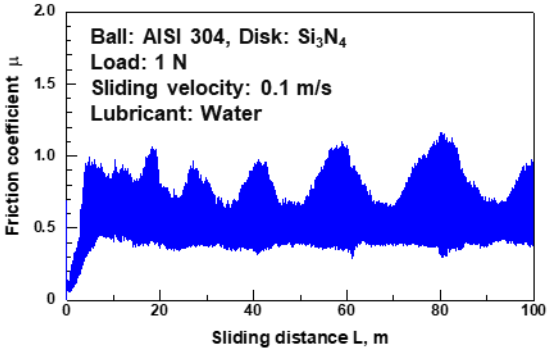

(d) 0.1 m/s

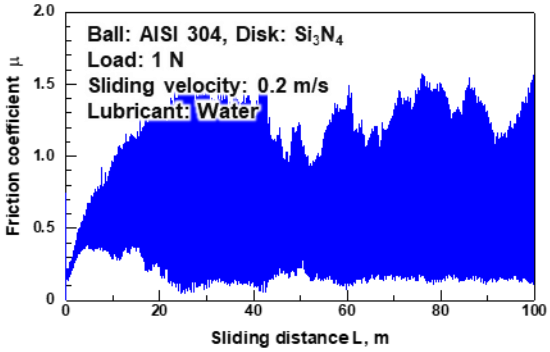

(e) 0.2 m/s

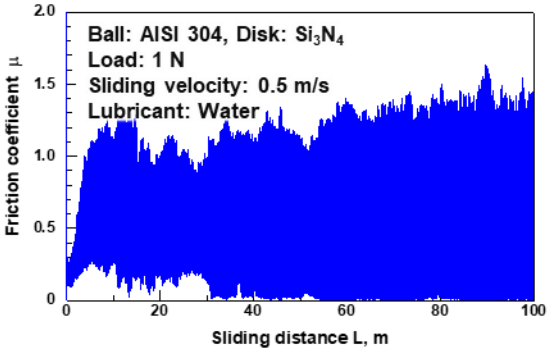

(f) 0.5 m/s

Fig. 3-4 Friction properties of AISI 304 sliding against Si_3N_4 in water at load 1 N and sliding velocity (a) 0.01 m/s, (b) 0.02 m/s, (c) 0.05 m/s, (d) 0.1 m/s, (e) 0.2 m/s and (f) 0.5 m/s.

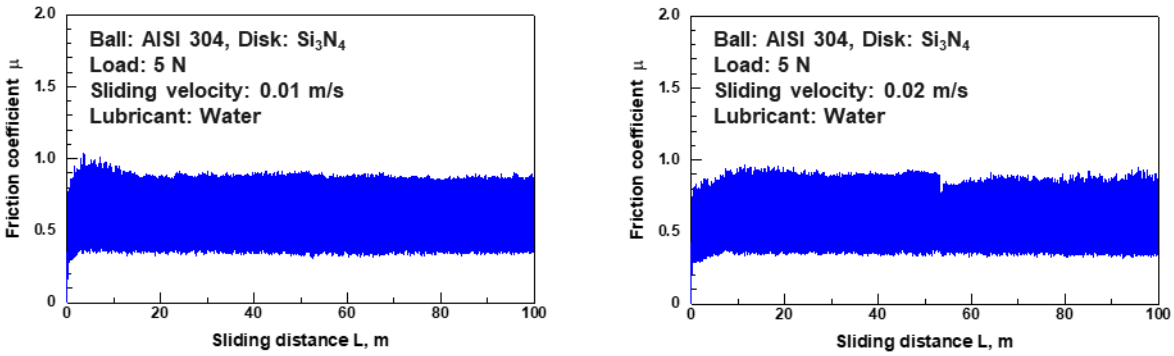

(a) 0.01 m/s

(b) 0.02 m/s

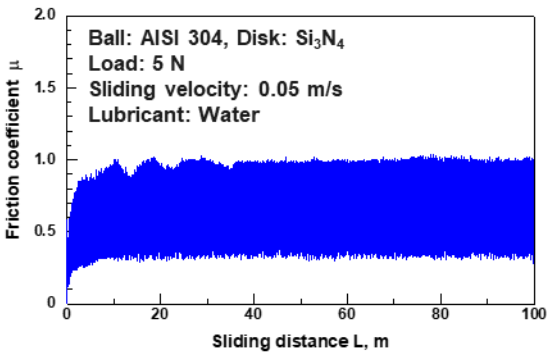

(c) 0.05 m/s

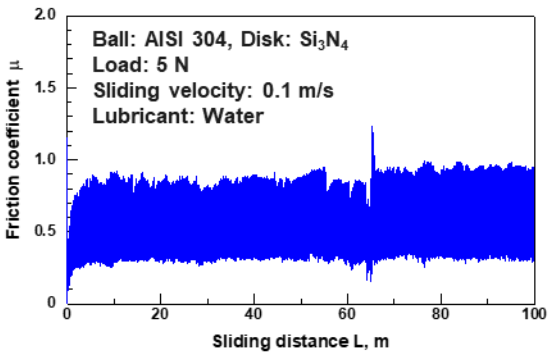

(d) 0.1 m/s

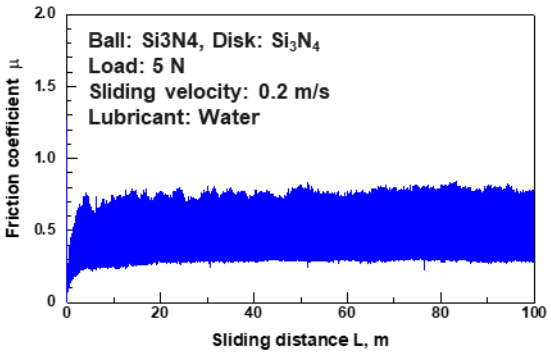

(e) 0.2 m/s

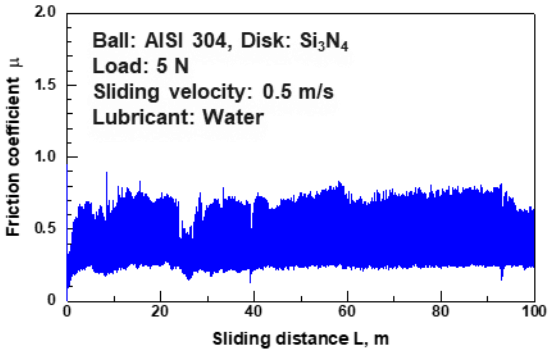

(f) 0.5 m/s

Fig. 3-5 Friction properties of AISI 304 sliding against Si_3N_4 in water at load 5 N and sliding velocity (a) 0.01 m/s, (b) 0.02 m/s, (c) 0.05 m/s, (d) 0.1 m/s, (e) 0.2 m/s and (f) 0.5 m/s.

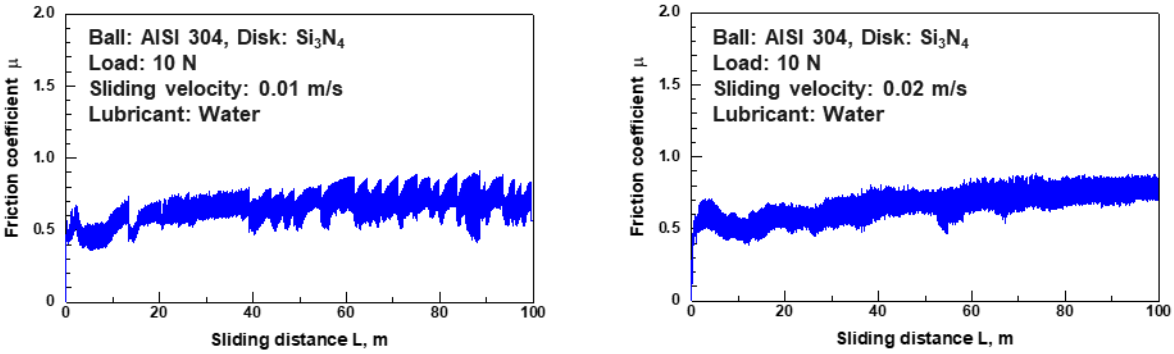

(a) 0.01 m/s

(b) 0.02 m/s

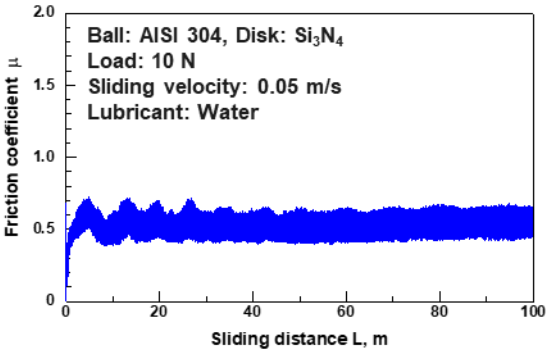

(c) 0.05 m/s

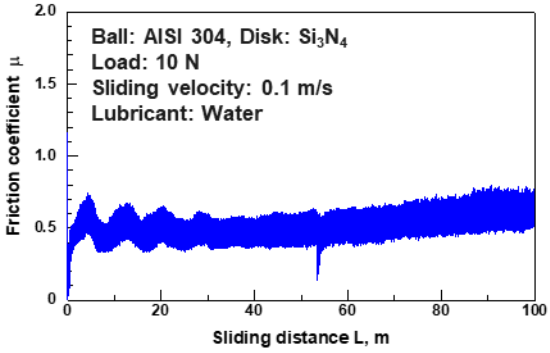

(d) 0.1 m/s

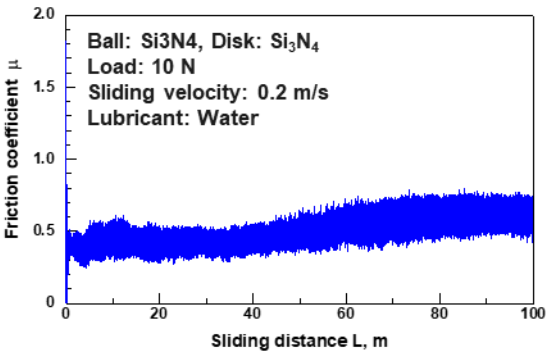

(e) 0.2 m/s

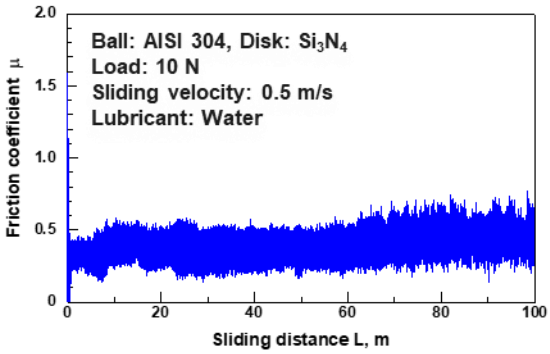

(f) 0.5 m/s

Fig. 3-6 Friction properties of AISI 304 sliding against Si_3N_4 in water at load 10 N and sliding velocity (a) 0.01 m/s, (b) 0.02 m/s, (c) 0.05 m/s, (d) 0.1 m/s, (e) 0.2 m/s and (f) 0.5 m/s.

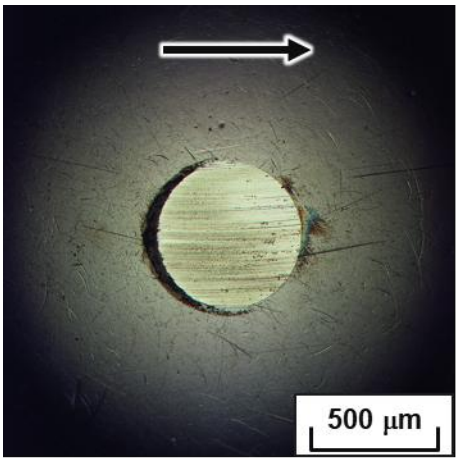

(a) 0.01 m/s

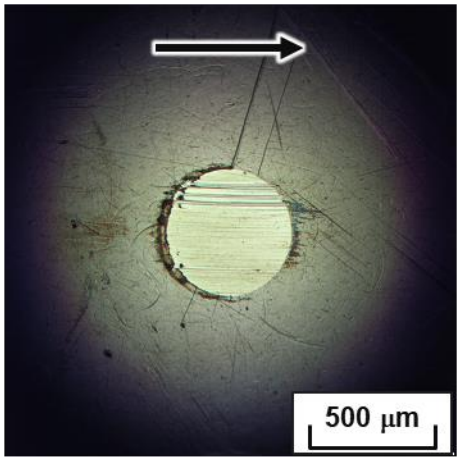

(b) 0.02 m/s

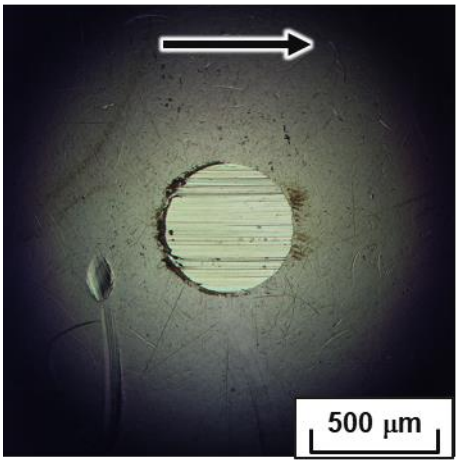

(c) 0.05 m/s

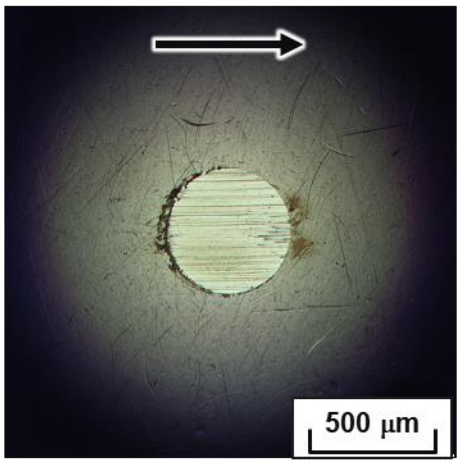

(d) 0.1 m/s

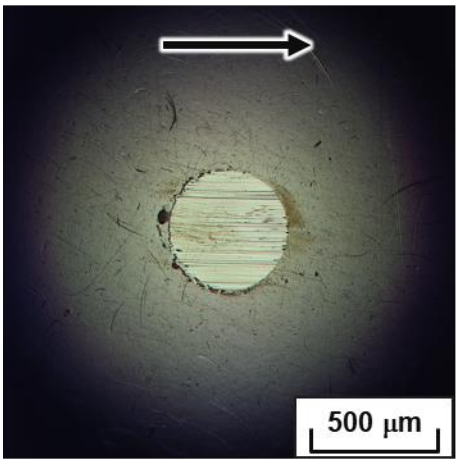

(e) 0.2 m/s

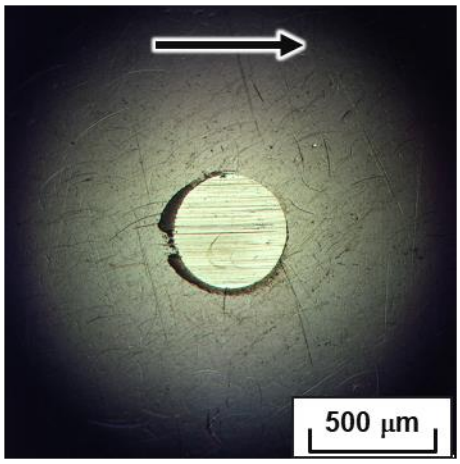

(f) 0.5 m/s

Fig. 3-7 Optical microscope images of wear scar on AISI 304 ball sliding against Si_3N_4 in water at load 1 N and sliding velocity (a) 0.01 m/s, (b) 0.02 m/s, (c) 0.05 m/s, (d) 0.1 m/s, (e) 0.2 m/s and (f) 0.5 m/s. Blacks arrow indicate the sliding direction of disk material.

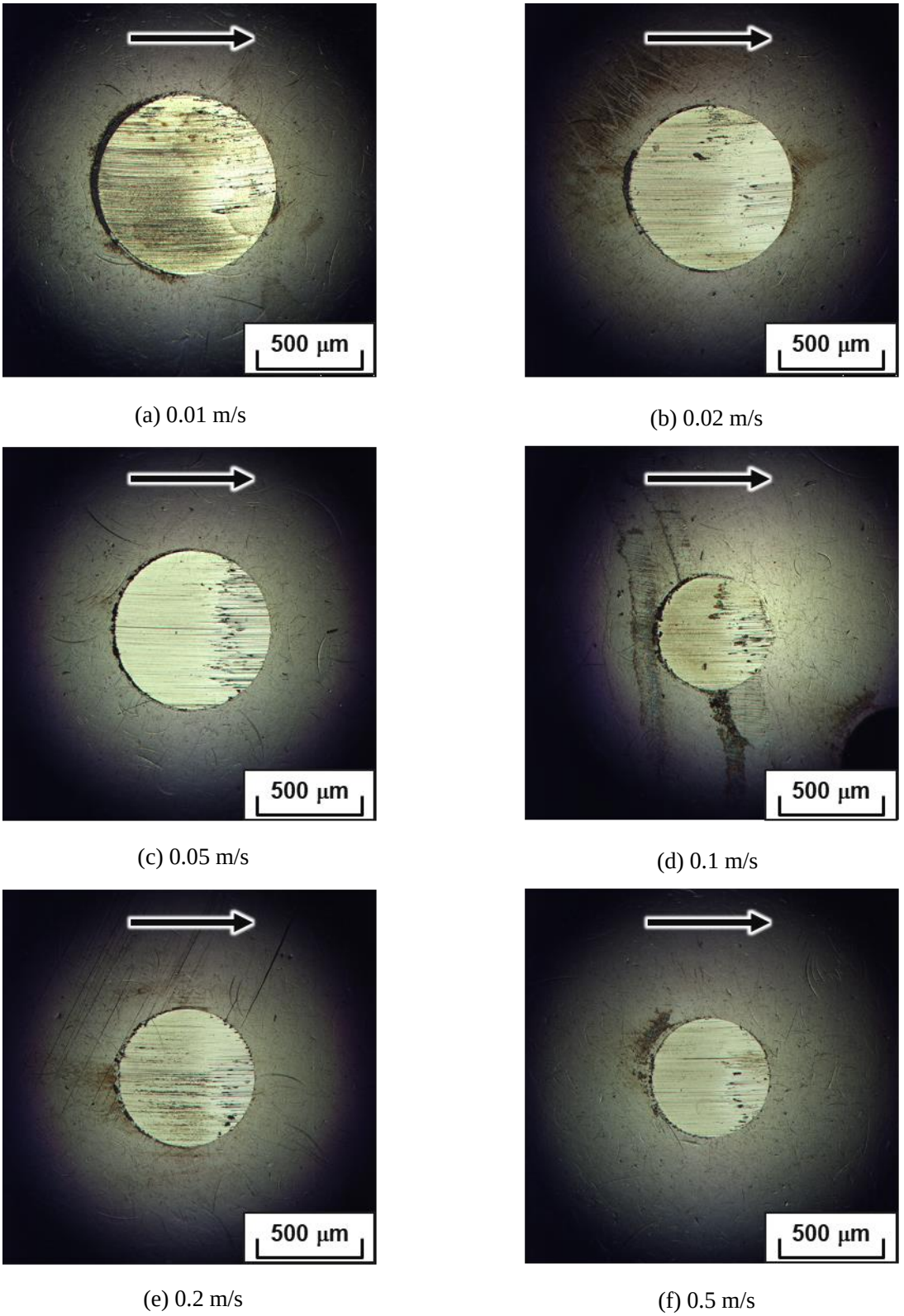

(a) 0.01 m/s (b) 0.02 m/s

(c) 0.05 m/s (d) 0.1 m/s

(e) 0.2 m/s (f) 0.5 m/s

Fig. 3-8 Optical microscope images of wear scar on AISI 304 ball sliding against Si_3N_4 in water at load 5 N and sliding velocity (a) 0.01 m/s, (b) 0.02 m/s, (c) 0.05 m/s, (d) 0.1 m/s, (e) 0.2 m/s and (f) 0.5 m/s. Blacks arrow indicate the sliding direction of disk material.

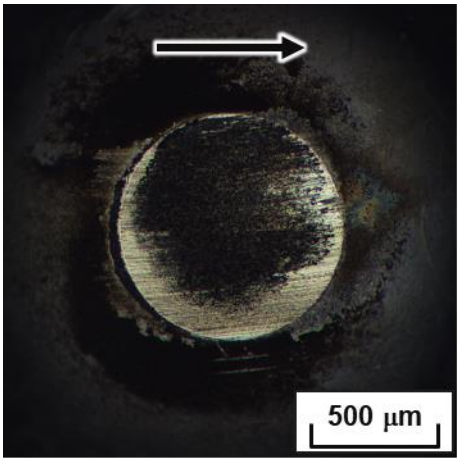

(a) 0.01 m/s

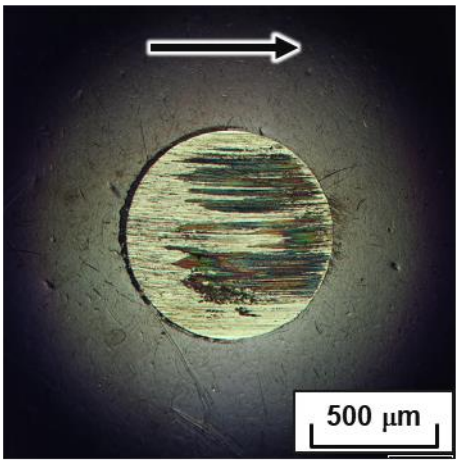

(b) 0.02 m/s

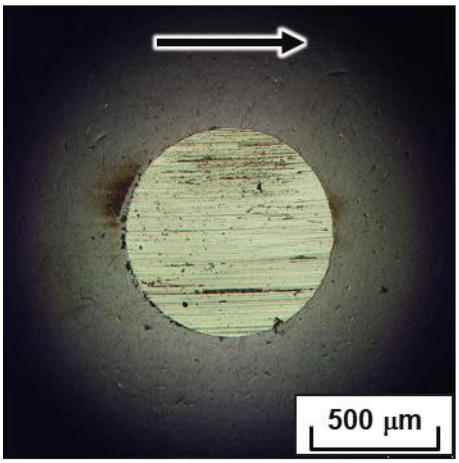

(c) 0.05 m/s

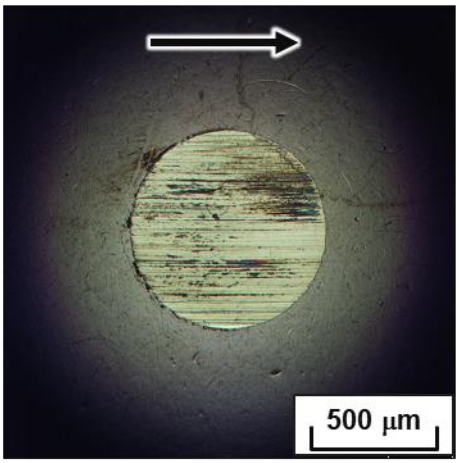

(d) 0.1 m/s

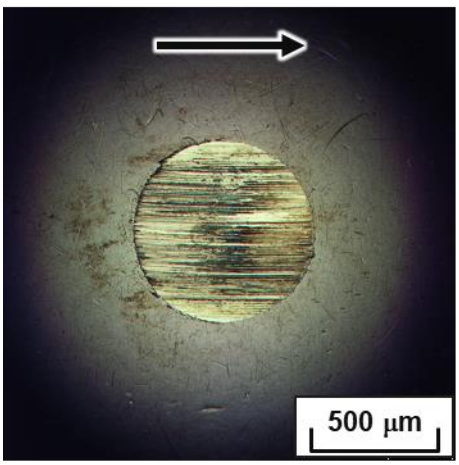

(e) 0.2 m/s

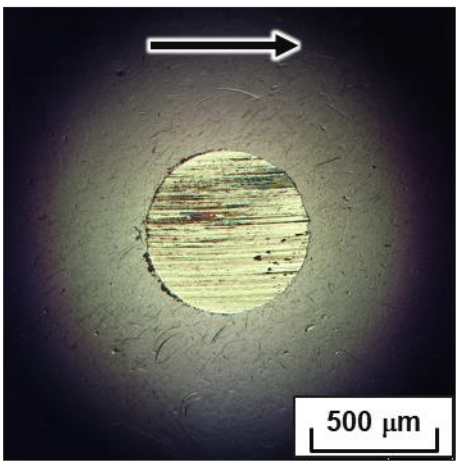

(f) 0.5 m/s

Fig. 3-9 Optical microscope images of wear scar on AISI 304 ball sliding against Si_3N_4 in water at load 10 N and sliding velocity (a) 0.01 m/s, (b) 0.02 m/s, (c) 0.05 m/s, (d) 0.1 m/s, (e) 0.2 m/s and (f) 0.5 m/s. Blacks arrow indicate the sliding direction of disk material.

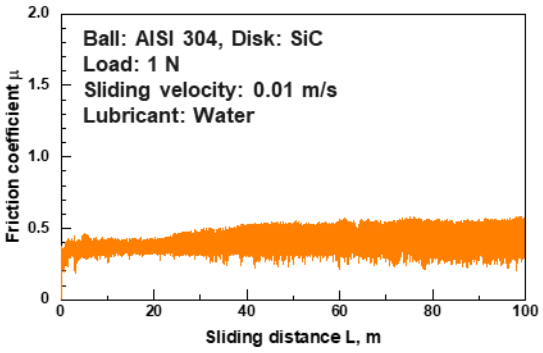

(a) 0.01 m/s

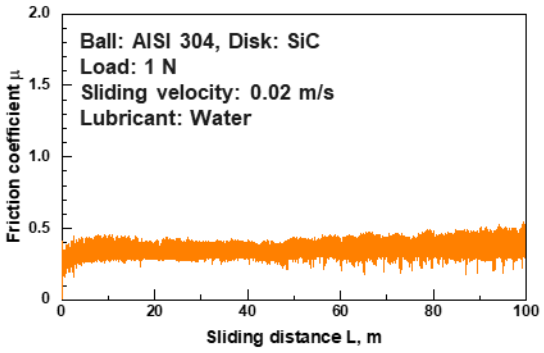

(b) 0.02 m/s

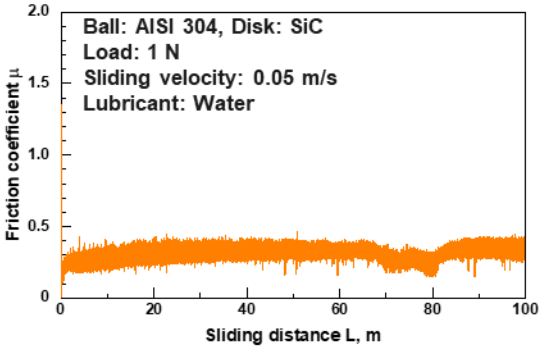

(c) 0.05 m/s

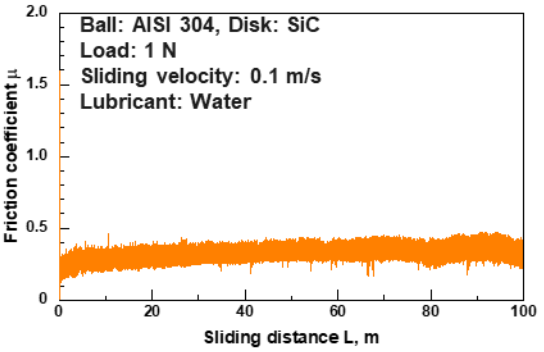

(d) 0.1 m/s

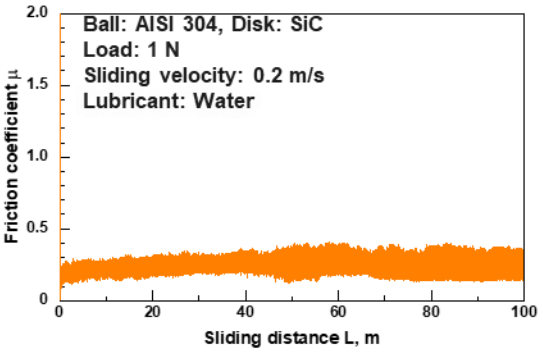

(e) 0.2 m/s

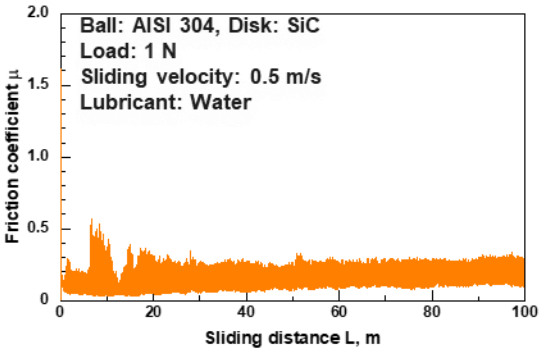

(f) 0.5 m/s

Fig. 3-10 Friction properties of AISI 304 sliding against SiC in water at load 1 N and sliding velocity (a) 0.01 m/s, (b) 0.02 m/s, (c) 0.05 m/s, (d) 0.1 m/s, (e) 0.2 m/s and (f) 0.5 m/s.

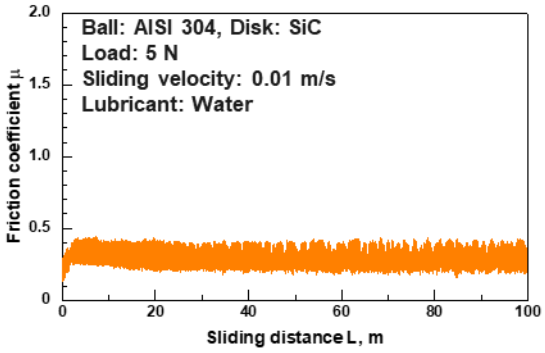

(a) 0.01 m/s

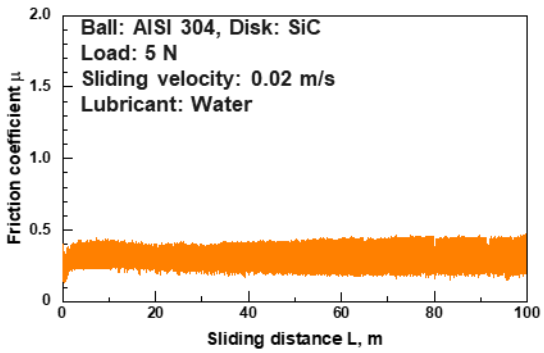

(b) 0.02 m/s

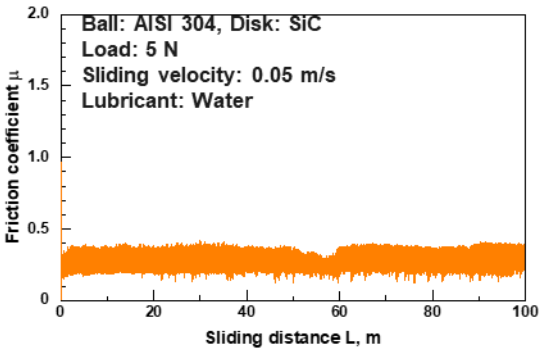

(c) 0.05 m/s

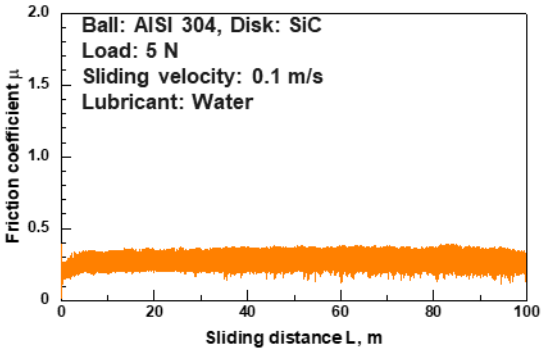

(d) 0.1 m/s

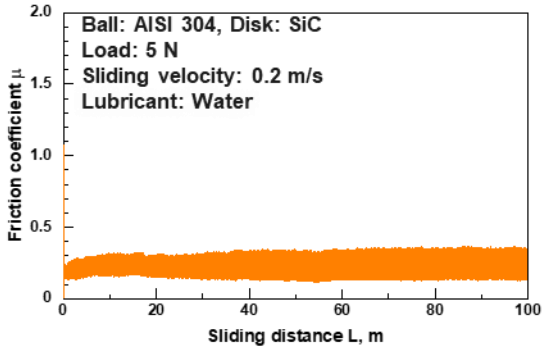

(e) 0.2 m/s

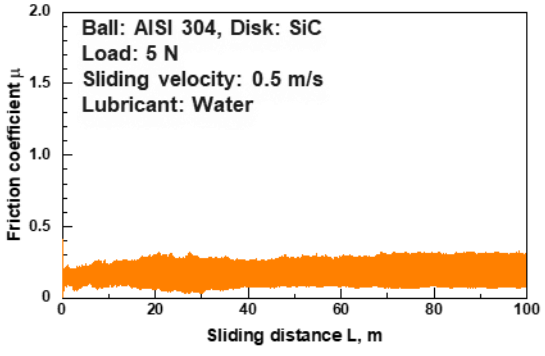

(f) 0.5 m/s

Fig. 3-11 Friction properties of AISI 304 sliding against SiC in water at load 5 N and sliding velocity (a) 0.01 m/s, (b) 0.02 m/s, (c) 0.05 m/s, (d) 0.1 m/s, (e) 0.2 m/s and (f) 0.5 m/s.

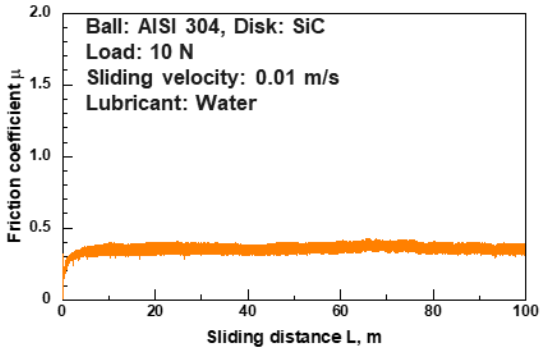

(a) 0.01 m/s

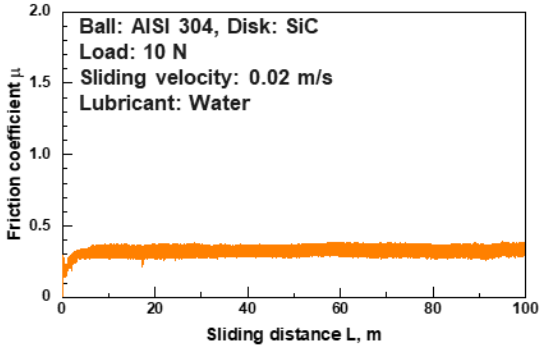

(b) 0.02 m/s

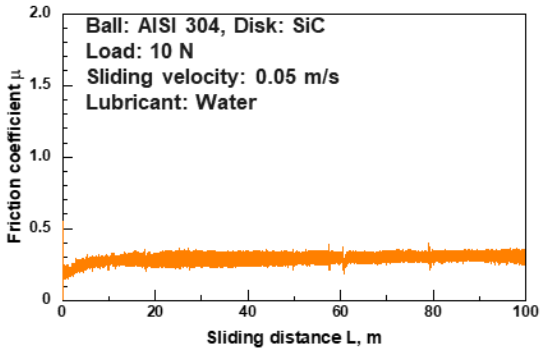

(c) 0.05 m/s

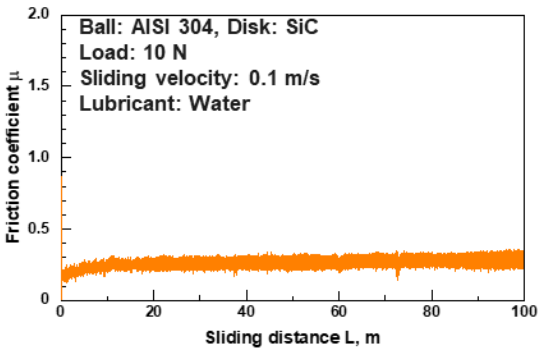

(d) 0.1 m/s

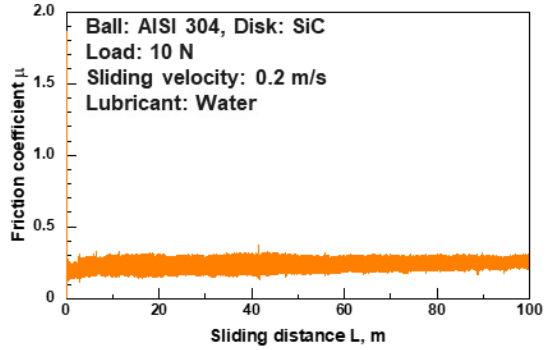

(e) 0.2 m/s

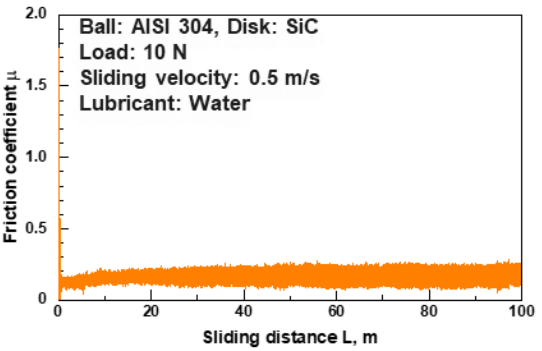

(f) 0.5 m/s

Fig. 3-12 Friction properties of AISI 304 sliding against SiC in water at load 10 N and sliding velocity (a) 0.01 m/s, (b) 0.02 m/s, (c) 0.05 m/s, (d) 0.1 m/s, (e) 0.2 m/s and (f) 0.5 m/s.

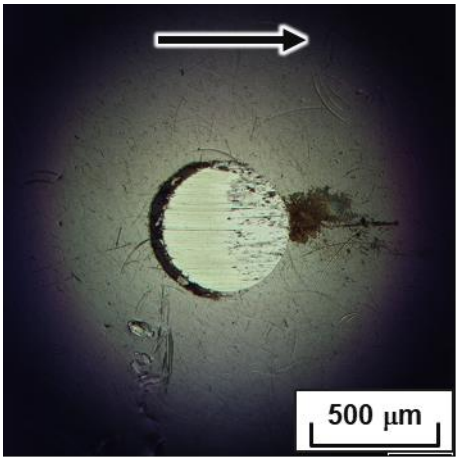

(a) 0.01 m/s

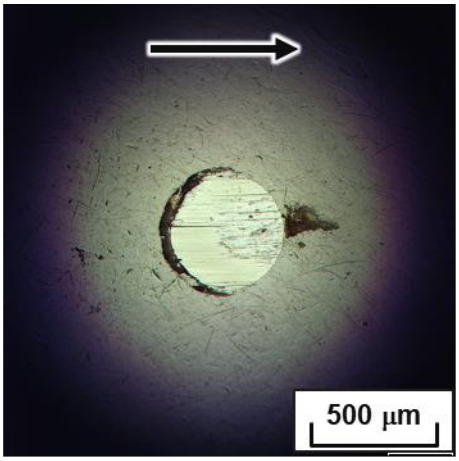

(b) 0.02 m/s

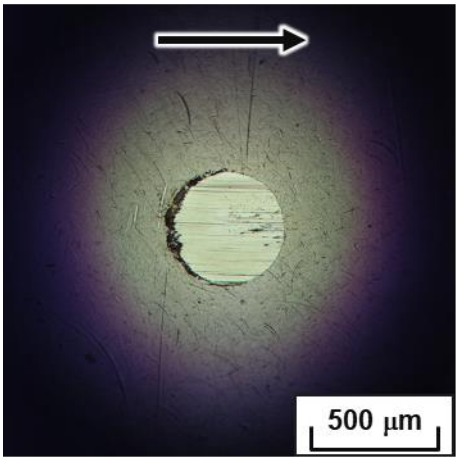

(c) 0.05 m/s

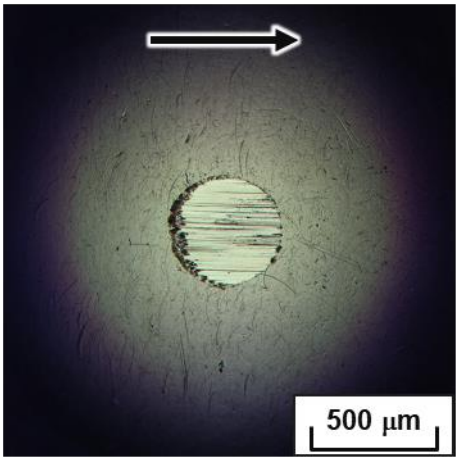

(d) 0.1 m/s

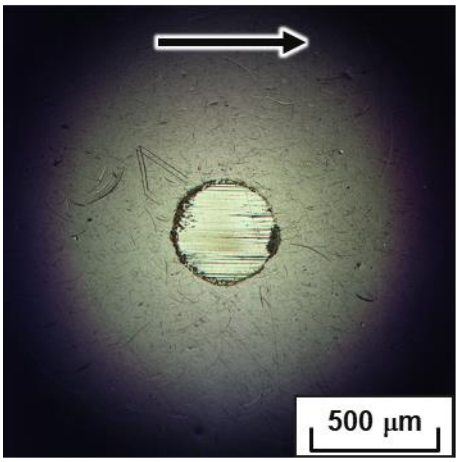

(e) 0.2 m/s

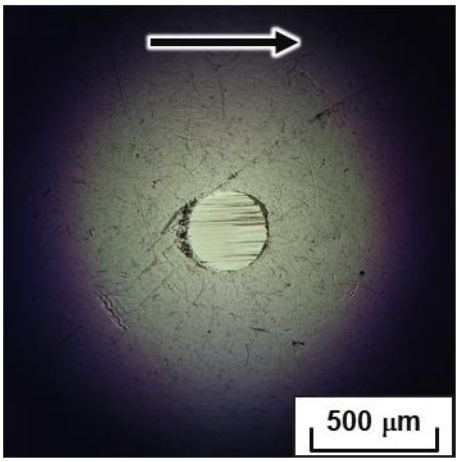

(f) 0.5 m/s

Fig. 3-13 Optical microscope images of wear scar on AISI 304 ball sliding against SiC in water at load 1 N and sliding velocity(a) 0.01 m/s, (b) 0.02 m/s, (c) 0.05 m/s, (d) 0.1 m/s, (e) 0.2 m/s and (f) 0.5 m/s. Blacks arrow indicate the sliding direction of disk material.

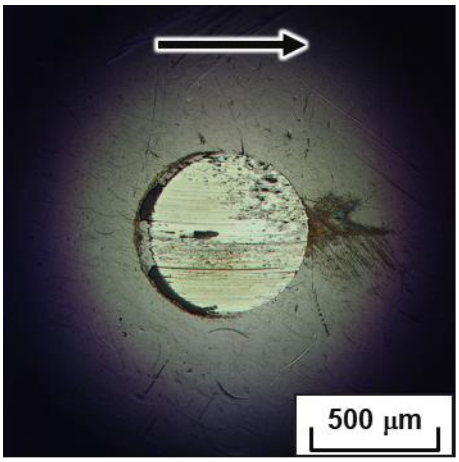

(a) 0.01 m/s

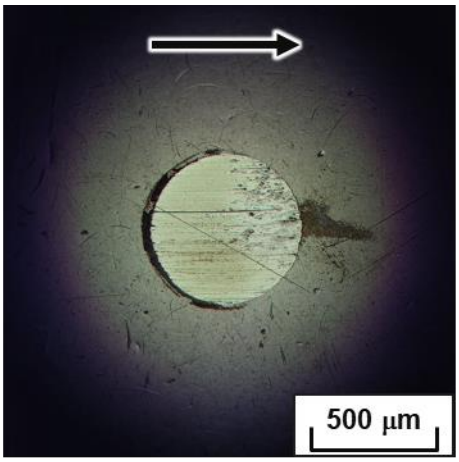

(b) 0.02 m/s

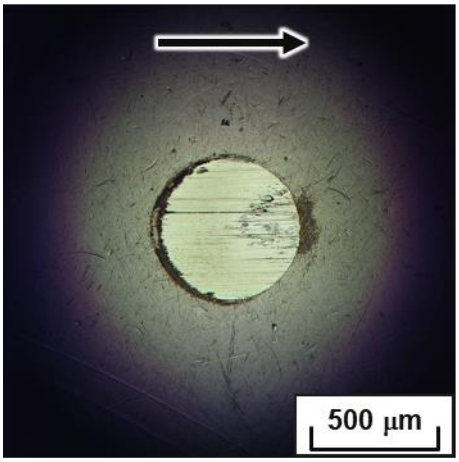

(c) 0.05 m/s

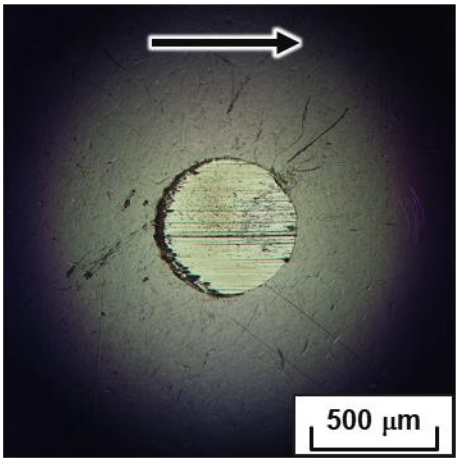

(d) 0.1 m/s

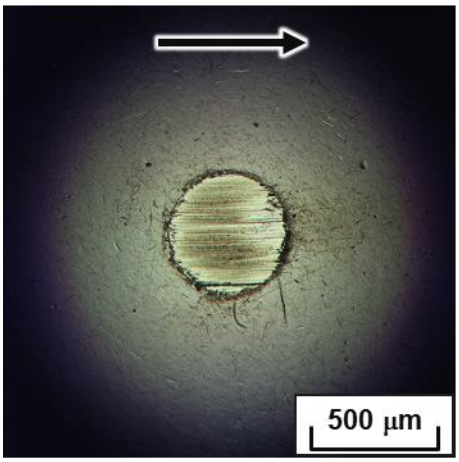

(e) 0.2 m/s

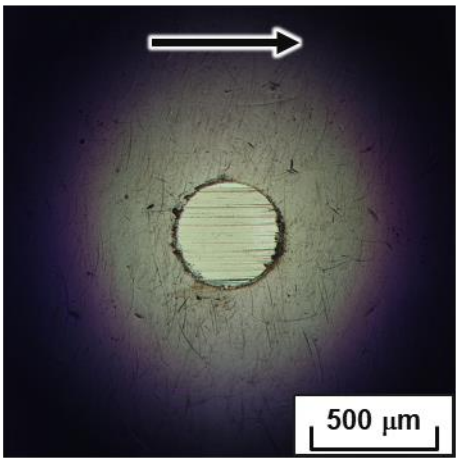

(f) 0.5 m/s

Fig. 3-14 Optical microscope images of wear scar on AISI 304 ball sliding against SiC in water at load 5 N and sliding velocity(a) 0.01 m/s, (b) 0.02 m/s, (c) 0.05 m/s, (d) 0.1 m/s, (e) 0.2 m/s and (f) 0.5 m/s. Blacks arrow indicate the sliding direction of disk material.

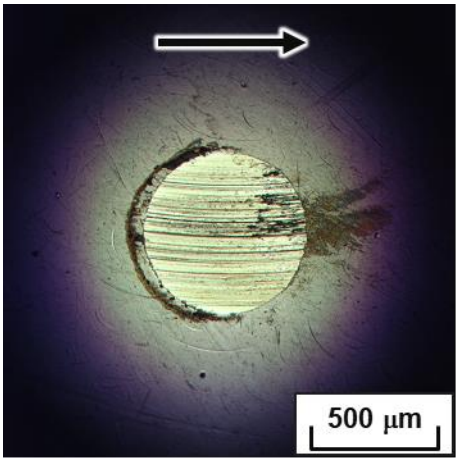

(a) 0.01 m/s

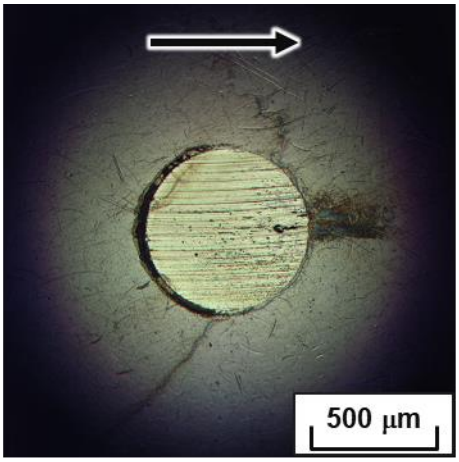

(b) 0.02 m/s

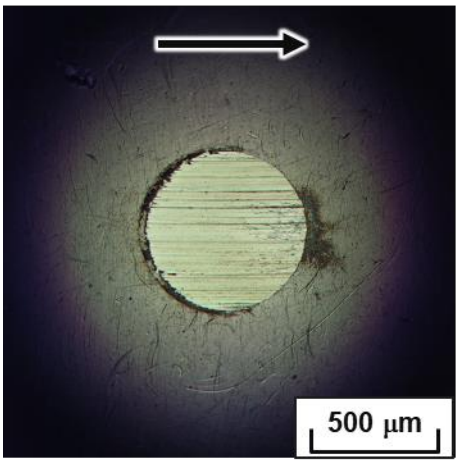

(c) 0.05 m/s

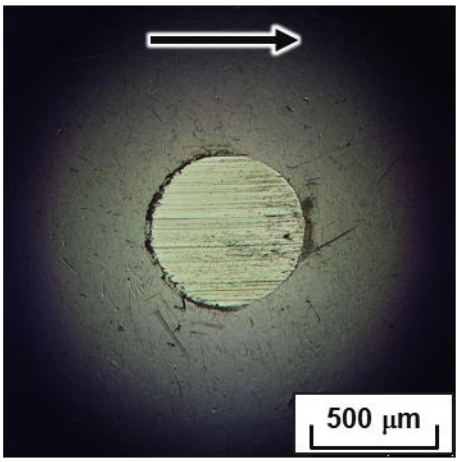

(d) 0.1 m/s

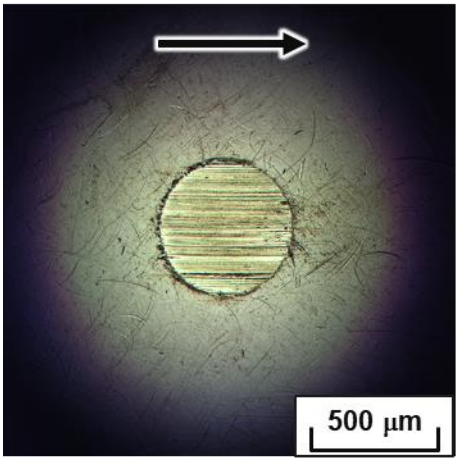

(e) 0.2 m/s

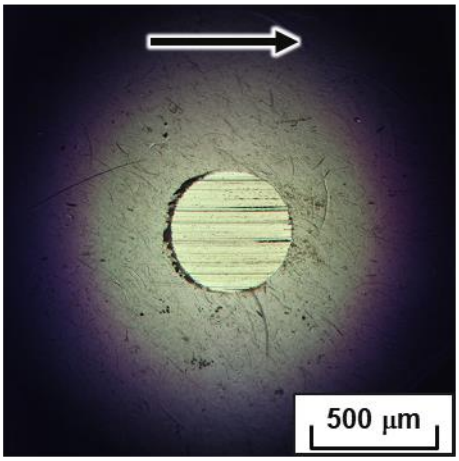

(f) 0.5 m/s

Fig. 3-15 Optical microscope images of wear scar on AISI 304 ball sliding against SiC in water at load 10 N and sliding velocity(a) 0.01 m/s, (b) 0.02 m/s, (c) 0.05 m/s, (d) 0.1 m/s, (e) 0.2 m/s and (f) 0.5 m/s. Blacks arrow indicate the sliding direction of disk material.

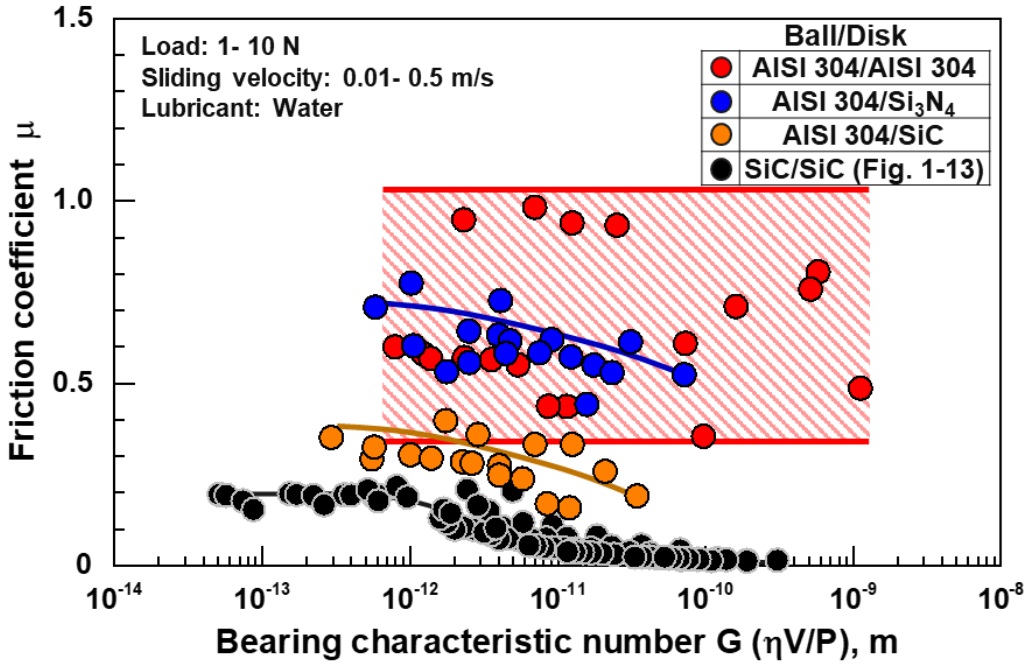

Fig. 3-16 Relationship between bearing characteristic number and average friction coefficient of AISI 304/AISI 304, AISI 304/Si_3N_4 and AISI 304/SiC in water.

3.3.2 Wear modes of stainless steel sliding against silicon-based ceramics in water

Figure. 3-17 shows the specific wear rate of ball calculated from the all wear scar after the friction test under AISI 304/AISI 304, AISI 304/Si_3N_4 and AISI 304/SiC combinations in water as a function of products of initial contact pressure P_i and sliding velocity V, which is proportional to the initial input energy. When AISI 304 disk was used as mating material of AISI 304 ball, the specific wear rate increased with increase of $P_i \cdot V$ value. The specific wear rate of ball under AISI 304/AISI 304 varied from 10^{-5} $mm^3/N \cdot m$ to 10^{-2} $mm^3/N \cdot m$. By contrast, when silicon-based ceramics were used as mating material against AISI 304, the specific wear rate of ball decreases with increasing $P_i \cdot V$ values. The specific wear rate of ball under AISI 304/Si_3N_4 and AISI 304/SiC combinations decreased from 10^{-5} $mm^3/N \cdot m$ to 10^{-6} $mm^3/N \cdot m$ and from 10^{-6} $mm^3/N \cdot m$ to 10^{-7} $mm^3/N \cdot m$ as the sliding velocity and initial contact pressure increase.

Figures 3-18 and 3-19 show distribution of wear modes of AISI 304/Si_3N_4 and AISI 304/SiC as a function of sliding velocity a by hertz contact pressure and specific wear rate of ball specimen. Either friction pairs differ from AISI 304/AISI 304 in that they exhibit less specific wear rate at higher load and higher sliding velocity. Figure 3-20 shows the tomography of the worn surfaces of AISI 304/SiC which shows the smallest specific wear rate. Looking at the wear scar on the ball specimen in Fig. 3-20 (a), it can be seen that there is almost no transferred material on the wear scar and the shape is flat. While, when looking at the sliding trace on the disk in Fig. 3-20 (b), although the transferred material derived from AISI 304 is seen in part, this also shows a flat shape similar to the wear scar on the ball. From the cross-sectional profile of Fig. 3-21, the peak of the order of several micrometers as like Fig. 2-18 and Fig. 2-21 was not confirmed, and it was found that a smooth worn surface could be formed on AISI 304 by using SiC as the counter material. These results suggest that the input energy may promote the tribochemical reaction between silicon and water. Therefore, in the next section, the evaluation is performed using the contact angle of water droplet, which indicates the involvement of the tribochemical reaction.

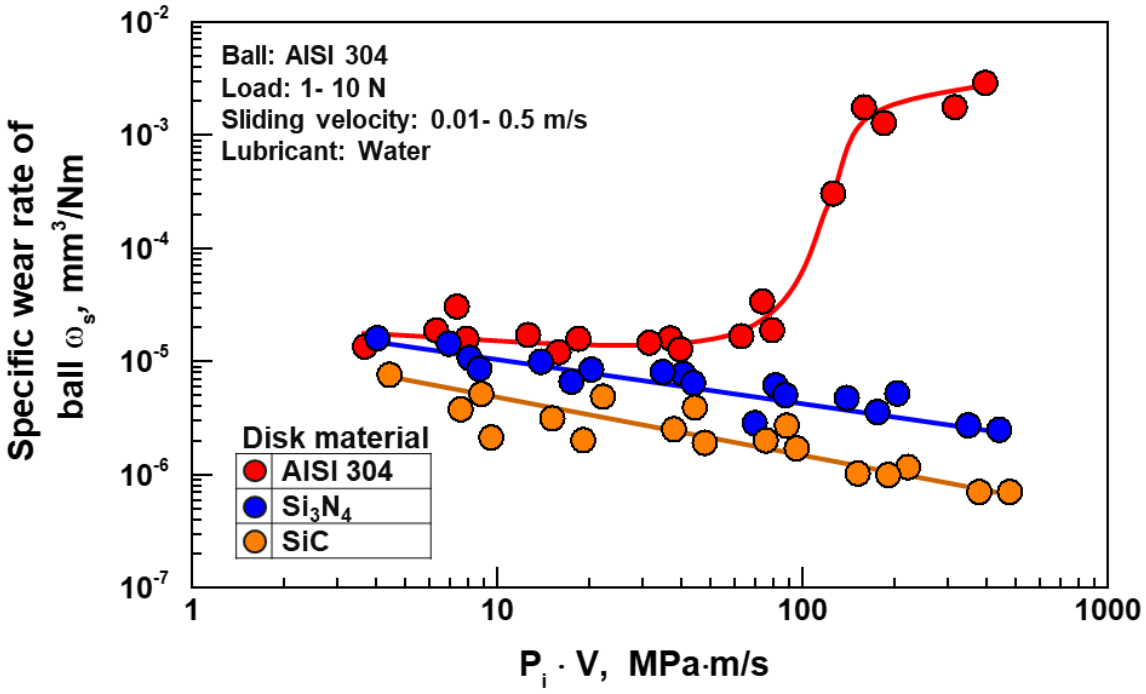

Fig. 3-17 Relationship between the product of initial contact pressure and sliding velocity and the specific wear rate of AISI 304 ball slid against itself, Si_3N_4 and SiC in water.

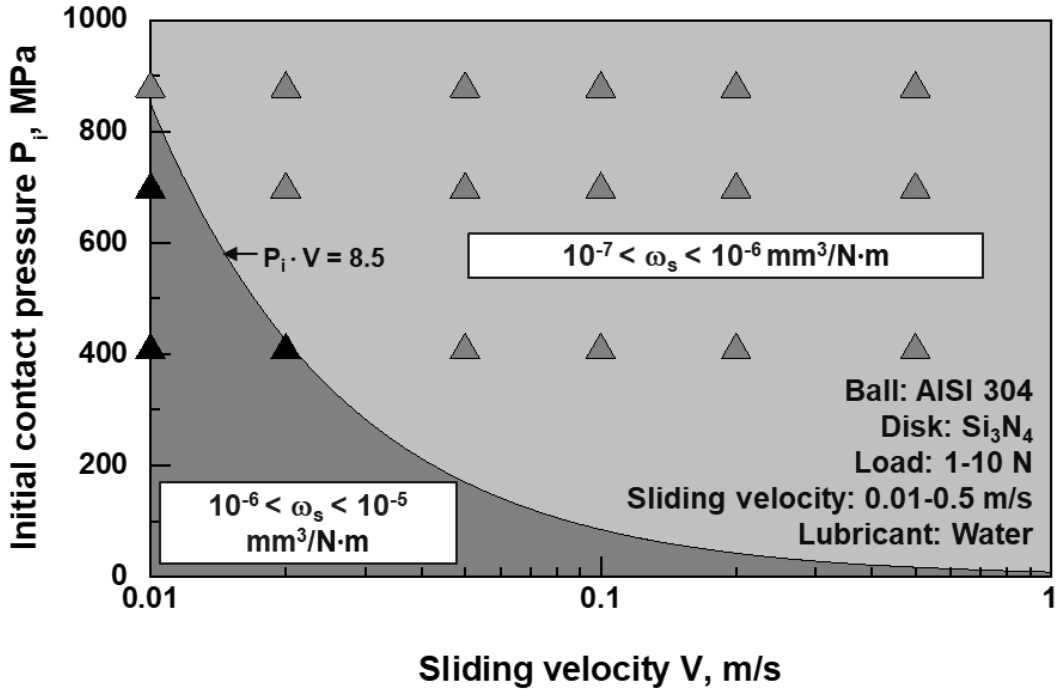

Fig. 3-18 Distribution of wear mode of AISI 304/Si_3N_4 in water as function hertz contact pressure and sliding velocity.

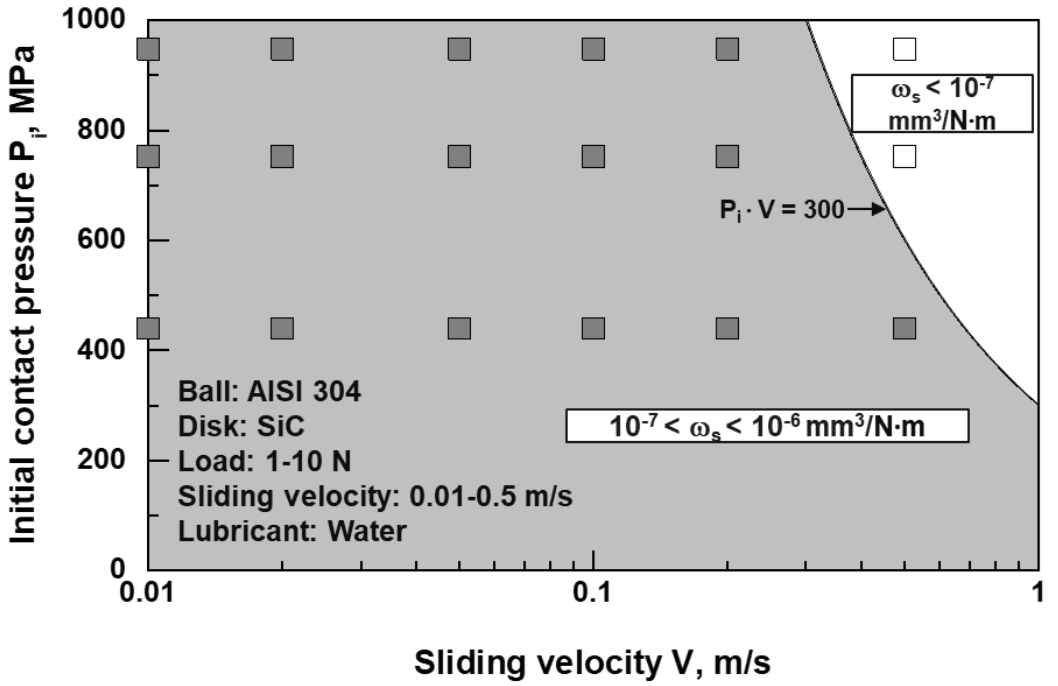

Fig. 3-19 Distribution of wear mode of AISI 304/SiC in water as function hertz contact pressure and sliding velocity.

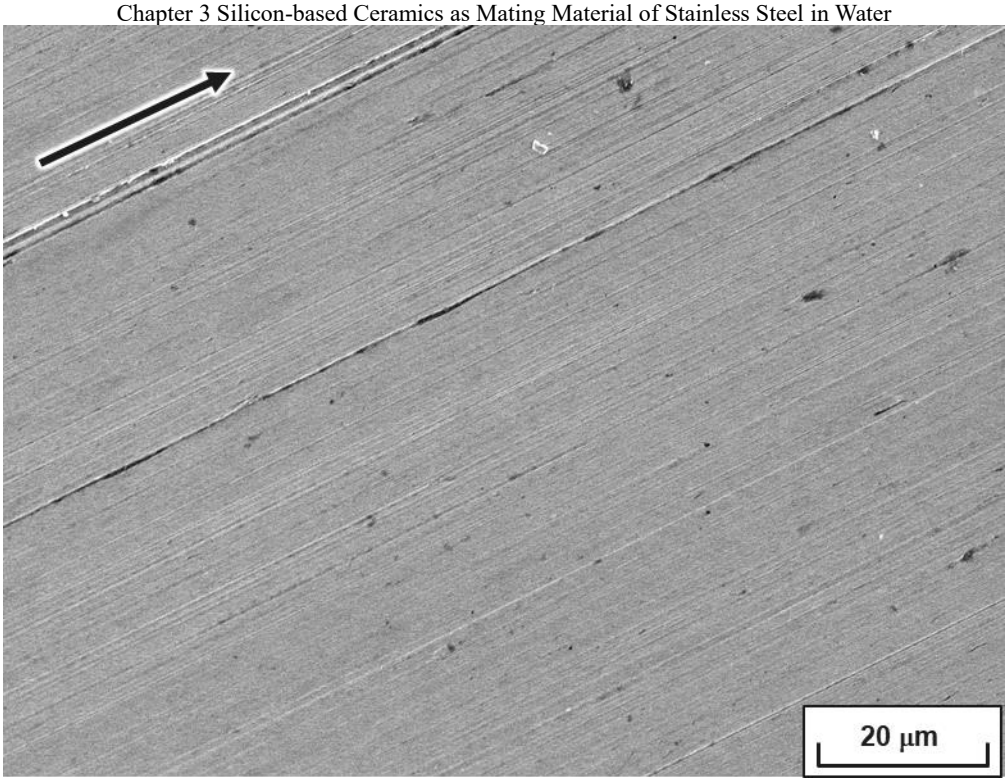

(a) SEM image of the wear scar on AISI 304 ball

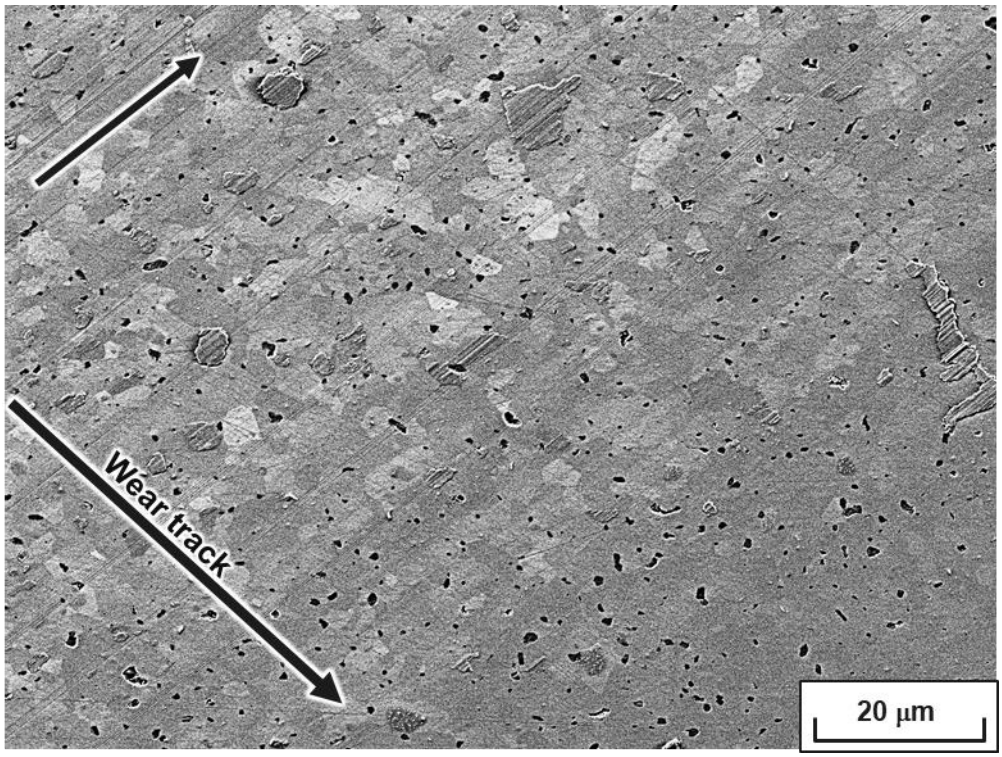

(b) SEM image of the wear track on SiC disk

Fig. 3-20 Topography of the wear surface of (a) the wear scar on AISI 304 ball and (b) the wear track on SiC disk (load 10 N, sliding velocity 0.5 m/s). Black arrow indicates the sliding direction of disk.

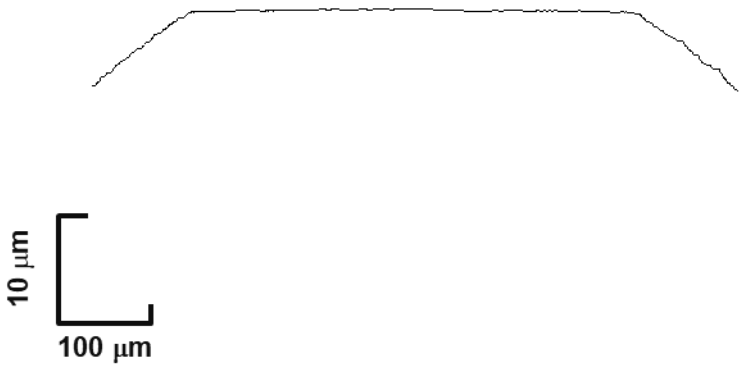

(a) Wear scar on AISI 304 ball

(b) Wear track on SiC disk

Fig. 3-21 Surface profile curves of (a) wear scar on AISI 304 ball and (b) wear track on SiC disk.

3.3.3 Possible low friction due to hydrophilic surface formation on stainless steel

To understand the reason why the differences of stability of friction behavior between AISI 304/Si_3N_4 and AISI 304/SiC in water are exhibited, the distribution of contact angle of water droplet on Si_3N_4 disk and SiC disk after sliding test is obtained.

Figure 3-22 shows the distribution of the contact angle for water droplet on a Si_3N_4 disk slid against AISI 304 ball in water. Fig. 3-22 (a) indicates that the hydrophilicity on the wear track sliding against AISI 304 ball improved. However, there are places where the change of the contact angle with the initial surface is about 10 degrees, as represented by the position of 60 to 180 degrees. Fig. 3-22 (b) indicates that the contact angle on the initial surface on Si_3N_4 disk is distributed from 70 to 80^o (the average contact angle: 73.9^o), while the contact angle in the wear track is distributed from 30 to 70^o (the average contact angle: 56.9^o).

Figure 3-23 shows the distribution of the contact angle for water droplet on a SiC disk slid against AISI 304 ball in water. Fig. 3-23 (a) shows that the hydrophilicity on the wear track sliding against AISI 304 ball improved as like to Fig. 3-22 (a). Fig. 3-23 (b) shows the contact angle at the initial surface on the SiC disk is distributed from 60 to 90^o (the average contact angle: 67.7^o), while the contact angle in the wear track is distributed from 30 to 60^o (the average contact angle: 41.5^o). This indicates that the hydrophilicity of the surface is improved.

Thus, in order to consider the effect of tribo-chemical reaction between silicon-based ceramics on the wear scar on AISI 304 ball, the contact angle of water droplet on the wear scar on AISI 304 ball after friction test was obtained. To remove the effect of the friction products like wear particles, cleaning the surface of wear scar with acetone was performed. The result of comparing the contact angle before and after cleaning with acetone is Fig. 3-24.

In order to evaluate the wettability of the wear scar slid against SiC, the measurement of contact angle of water droplet on the wear scar on AISI 304 ball was performed as shown in Fig. 3-24. The contact angle of the wear scar rubbed with SiC was 33.8^o, which are greatly reduced compared to the contact angle of the initial surface of AISI 304, and the hydrophilicity is improved. And, the contact angles after cleaning with acetone was 74.1^o, which were worse than the contact angles after sliding, but still maintained a hydrophilic surface compared to the initial surface. Considering the meaning of the contact angle after cleaning, it is understood that it suggests the chemical state of the solid friction surface, not the tribo-chemical reaction products that can be easily removed with acetone.

Cross-sectional image and distribution of related elements on worn surface of AISI 304 ball slid against SiC at load 10 N and sliding velocity 0.5 m/s in water is shown in Fig. 3-25. These images indicate that the transferred film, approximate thickness is 10 nm, is mainly comprised of nickel and iron. Even in this system, no distribution of chromium is seen in the nanolayer, and a clear distribution of silicon can't be seen. Uchidate et al. reported that the specific wear rate of AISI 304 and the ratio of nickel in the wear scar are correlated [12], and that the ratio of nickel increases as the wear decreases. The reason for this is that only the inert nickel remains in the wear scar because the dissolution rate varies depending on the material type due to the difference in the standard potential of iron, chromium and nickel. Wang et al. measured the contact angles of micro water droplet by with an atomic force microscope on pure chromium, pure nickel, and AISI 304, which were immersed in distilled water after wet polishing [17]. Each contact angle was 23º, 17º and 26º, respectively. This indicated that pure nickel showed a tendency to have hydrophilicity although the difference was slight.

In summary, the wear surface consisting of nickel and iron on AISI 304, which was slid against SiC in water showed hydrophilic. However, there is the challenge to show higher friction than the tribo-pair of SiC/SiC.

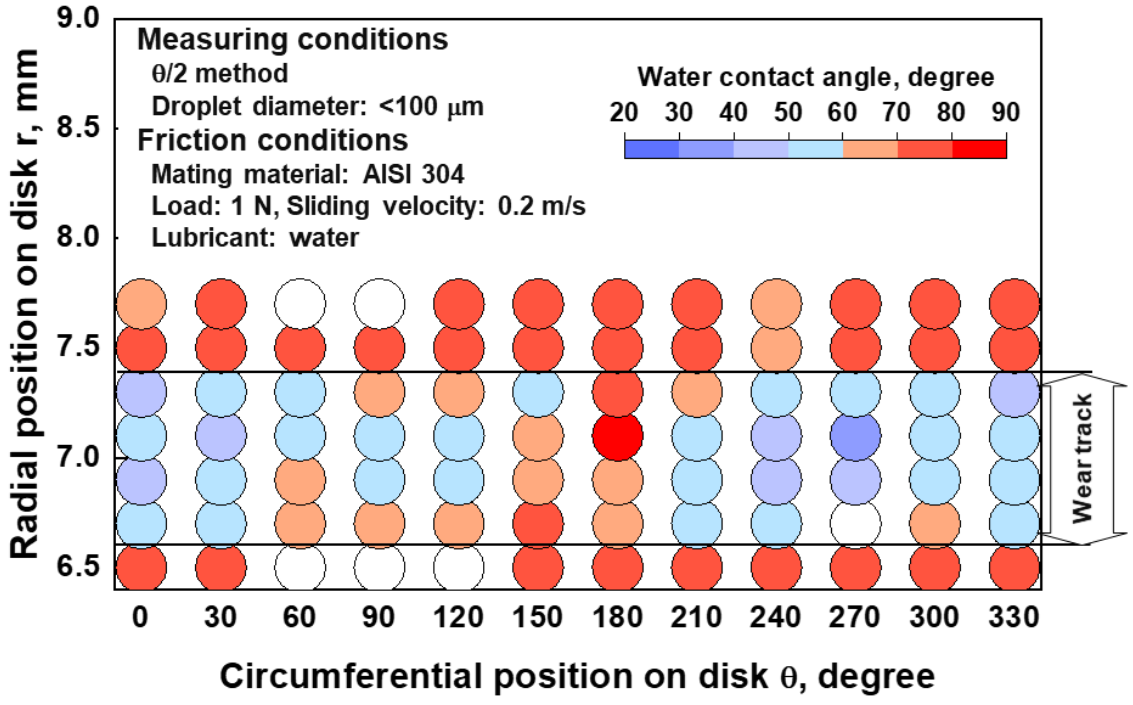

(a) Distribution of contact angle of water droplet on SiC disk after sliding test.

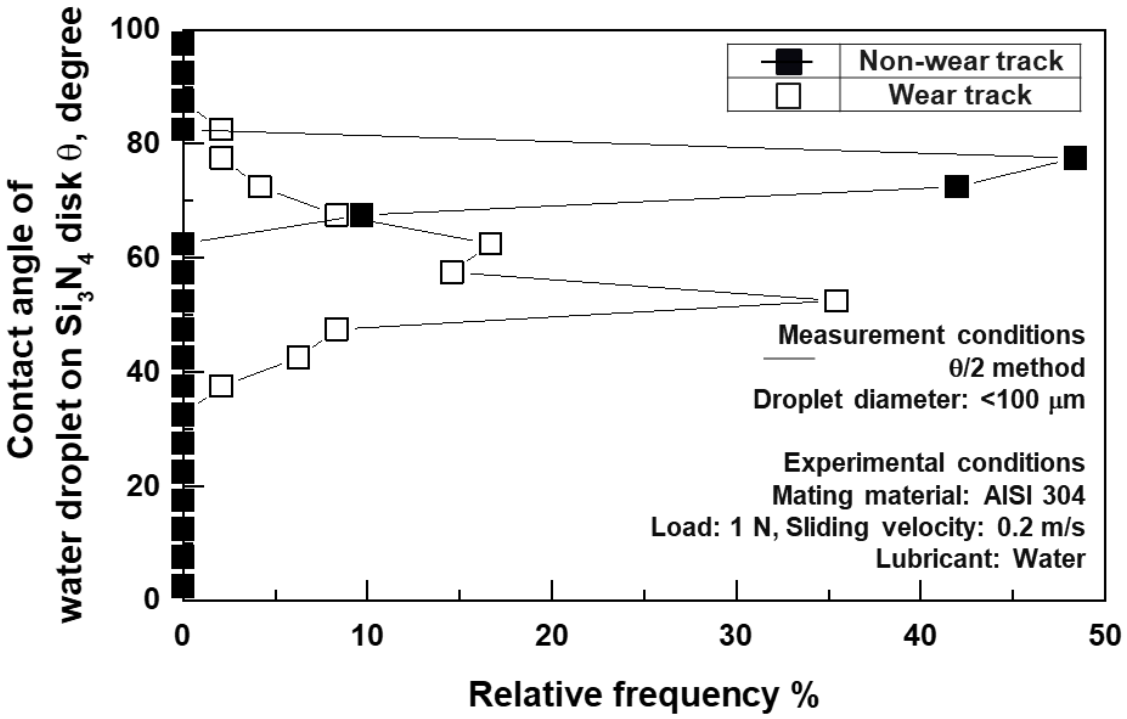

(b) Distribution of contact angle of water droplet on SiC disk after sliding test taken from (a).

Fig. 3-22 Change of contact angle of water droplet on Si_3N_4 disk after sliding test.

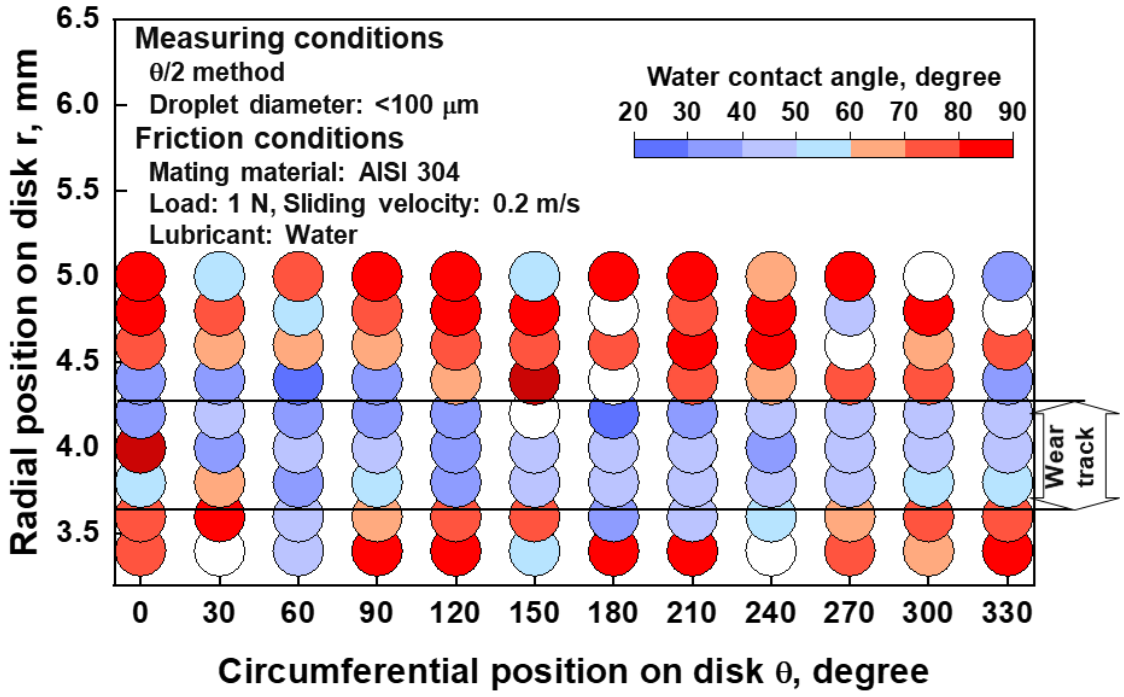

(a) Distribution of contact angle of water droplet on SiC disk after sliding test.

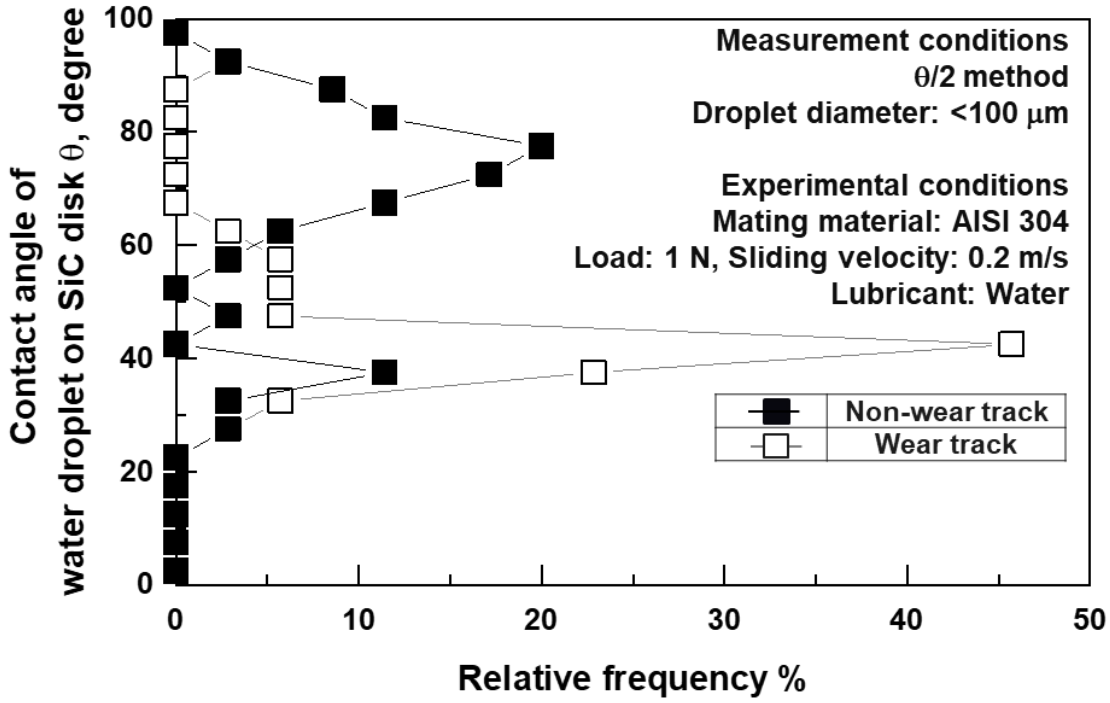

(b) Distribution of contact angle of water droplet on SiC disk after sliding test taken from (a).

Fig. 3-23 Change of contact angle of water droplet on SiC disk after sliding test.

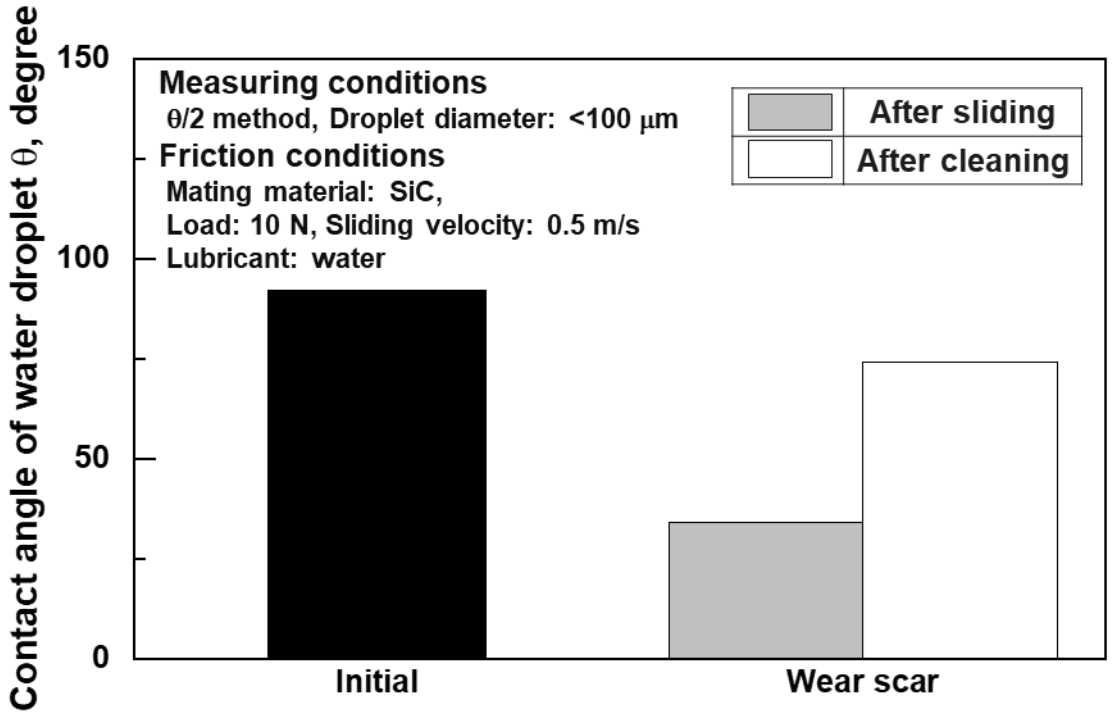

Fig. 3-24 Difference of contact angle of water droplet on initial AISI 304 ball and the wear scar on AISI 304 ball slid against SiC disk in water.

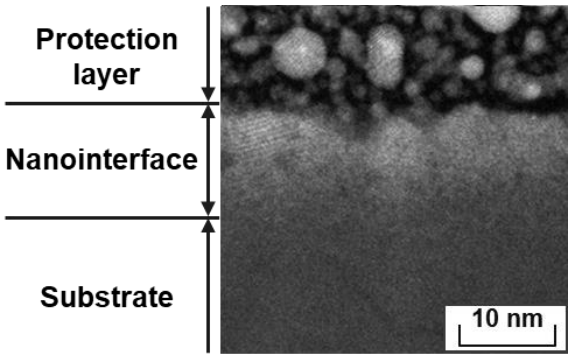

(a) Cross sectional image

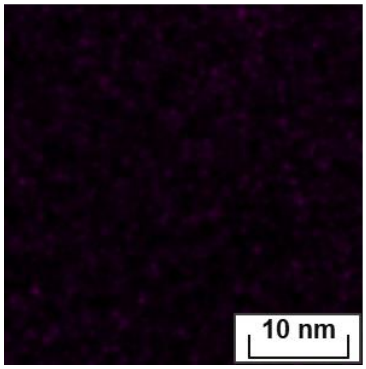

(b) Silicon

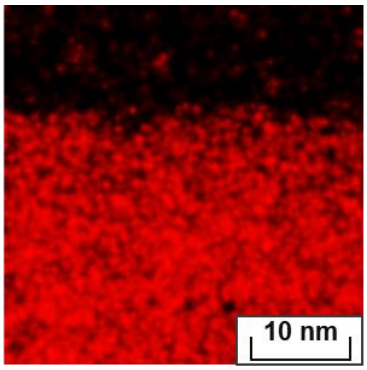

(c) Iron

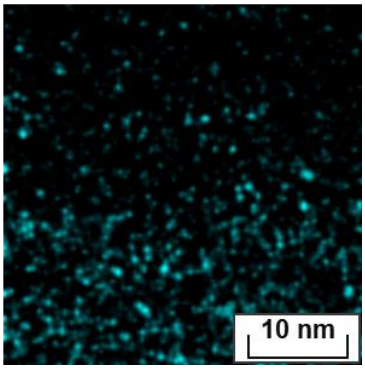

(d) Oxygen

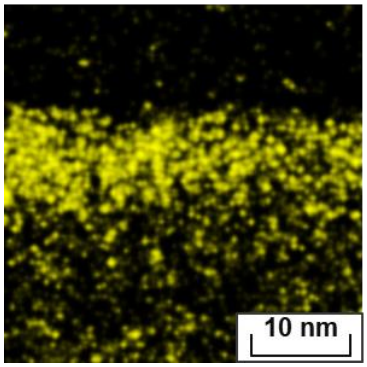

(e) Nickel

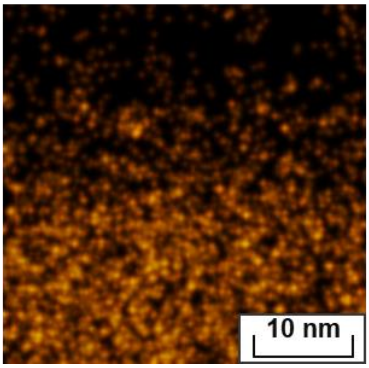

(f) Chromium

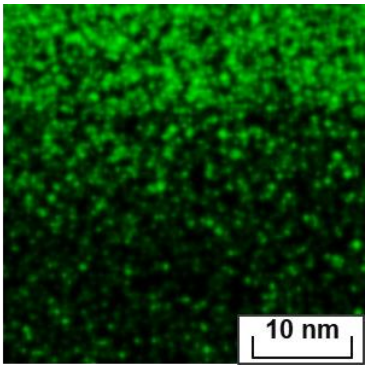

(g) Carbon

Fig. 3-25 (a) TEM image and distribution of (b) silicon, (c) iron, (d) oxygen, (e) nickel (f) chromium and (g) carbon of the worn surface on wear scar on AISI 304 ball slid against SiC at load 10 N and sliding velocity 0.5 m/s in water.

.

3.4 Conclusions

In this chapter, friction tests using a stainless steel ball slid against silicon-based ceramics such as silicon nitride and silicon carbide disk were conducted under various sliding conditions in water. As a result, the following conclusions were achieved.

(1) When silicon-based ceramics was used as a counter material against AISI 304, AISI 304/Si_3N_4 shows friction coefficient varied from 0.4 to 0.8 and AISI 304/SiC shows friction coefficient around 0.2 to 0.4. The specific wear rate of ball of AISI 304/Si_3N_4 and AISI 304/SiC combinations decreased from 10^{-5} $mm^3/N{\cdot}m$ to 10^{-6} $mm^3/N{\cdot}m$ and from 10^{-6} $mm^3/N{\cdot}m$ to 10^{-7} $mm^3/N{\cdot}m$ as the sliding velocity and initial contact pressure increase..

(2) The contact angle of water droplet in the wear track on the SiC disk is found to be 67.7° while that on non-wear track is 41.5°. This clearly indicates tribochemical reaction between SiC and water occurred due to sliding with stainless steel.

(3) The contact angles in the wear scars after sliding against SiC disk was 33.8° while the contact angles after cleaning with acetone was 74.1 °, which indicates that the hydrophilic surface on stainless steel is formed by sliding against SiC in water. In addition, nanolayer, approximate thickness is 10 nm and mainly consists of nickel and iron is self-formed on wear scar on stainless steel ball.

References

[1] T. E. Fischer, H. Tomizawa, Interaction of tribochemistry and microfracture in the friction and wear of silicon Nitride, Wear, 105, 1 (1985) 29–45.

[2] H. Tomizawa, T. E. Fischer, Friction and wear of silicon nitride and silicon carbide in water: hydrodynamic lubrication at low sliding speed obtained by tribochemical wear, ASLE Transactions, 30, 1 (1987) 41–46.

[3] T. Sugita, U. Kanji, Material removal rubbing in water, Wear, 97 (1984) 1–8.

[4] S. Sasaki, The effects of water on friction and wear of ceramics, Journal of Japanese Society of Lubrication Engineering, 33, 8, (1988) 620-628 (in Japanese).

[5] H. Yuko, Studies of tribochemical reactions of silicon based ceramics in water and alcohols and its applications to sliding and machining, National Institute of Advanced Industrial Science and Technology Mechanical Engineering Laboratory Report, 177 (1998) 1-74 (in Japanese).

[6] H. Czichos, S. Becker, J. Lexow, International multilaboratory sliding wear tests with ceramics and steel, Wear, 135, 1 (1989) 171–191.

[7] K. Adachi, U. Cho, S. K. Sinha, K. Kato, Self-lubrication by formation of graphite films in the sliding of silicon nitride against cast iron, Tribology Transactions, 44, 1 (2001) 41–46.

[8] X. Zhao, J. Liu, B. Zhu, H. Miao, Z. Luo, Tribological characteristics of Si_3N_4 ceramic sliding on stainless steel, Wear, 206, 1–2 (1997) 76–82.

[9] Y.-M. Gao, L. Fang, J.-Y. Su, Z.-G. Xie, Investigation on the components and the formation of a tribochemical film in the Si3N4–gray iron sliding pair lubricated with distilled water, Wear, 206, 1 (1997) 87–93.

[10] A. Iwabuchi, T. Tsukamoto, T. Shimizu, H. Yashiro, The mechanism of corrosive wear of an austenitic stainless steel in an aqueous electrolyte solution, Tribology Transactions, 41, 1 (1998) 96–102.

[11] L. Fang, Y. Gao, Z. Zhang, Tribology of Si_3N_4 with different glassy phase content sliding against grey cast iron lubricated with water, Wear, 225–229, (1999) 896–904.

[12] M. Uchidate, A. Iwabuchi, H. Liu, T. Shimizu, SEM observation and EPMA analysis of tribochemical products under water lubircated conditions, Journal of Japanese Society of Tribologists, 49, 2 (2004) 181-188 (in Japanese).

[13] N. Liu, J. Wang, B. Chen, F. Yan, Tribology international tribochemical aspects of silicon nitride ceramic sliding against stainless steel under the lubrication of seawater, Tribiology International, 61, (2013) 205–213.

[14] A. J. Winn, D. Dowson, J. C. Bell, The lubricated wear of ceramics, Tribology International, 28, 6 (1995) 395–402.

[15] B. Dumont, P. J. Blau, G. M. Crosbie, Reciprocating friction and wear of two silicon nitride-based ceramics against type 316 stainless steel, Wear, 238, 2 (2000) 93–109.

[16] M. F. Ashby, Materials selection in mechanical design second edition, Butterworth-Heinemann (1999) 430–431.

[17] R. Wang, N. Morihiro, T. Tokuda and M. Kido, Water Micro-Wettability Evalution of Several Metal Surfaces by Atomic Force Microscopy, Journal of the Japan Institute of Metals and Materials, 66, 8, (2002) 808–815 (In Japanese).

Chapter 4

Formation of Low Frictional Nanointerface on AISI 304 Sliding against DLC Coating in Water

4.1 Introduction

In this chapter, a Diamond-like carbon (DLC) coating is introduced as a mating material of stainless steel to suppress the adhesion of stainless steel as in Chapter 3. DLC is used as a material that has the potential to prevent the adhesion of stainless steel as well as silicon-based ceramics because of its chemical stability. Therefore, DLC coating is coated on processing tools as a methods to prevent adhesion of metal material such as an aluminum [1-2]. Aluminum is known as a material that easily adheres due to its low melting point of 660 degrees and its activity. If aluminum adheres to the cutting tool, the processing accuracy will decrease and the life of the tool will be shortened. Therefore, in order to prevent the adhesion of aluminum, DLC coating is actually deposited on the tool.

Recently, it has been reported that combination of stainless steel and DLC coating shows about 0.07 as friction coefficient in water due to formation of carbon-rich tribo-film [3-6] which react with water to form CH and OH groups on stainless steel surface [5]. On the other hands, it has also been reported that the hydrophilicity of DLC itself is improved by terminating of oxygen and hydroxyl groups on the surface during friction in water [7]. And the result of SiC/SiC shows the possibility of increasing the load supported by water between the two surfaces by improving the hydrophilicity of the friction surface [8]. If we focus on the hydrophilicity of the friction surface, it is expected that the friction coefficient between the stainless steel and the DLC coating in water will be even lower.

In this chapter, DLC coating, one of the materials to prevent adhesion is introduced as mating material of AISI 304 in water to improve tribological characteristics of AISI 304/DLC in water.

4.2 Experimental details

4.2.1 Deposition of DLC coating

Schematic of deposition apparatus is shown in Fig. 4-1.. DLC coating was produced by a plasma-enhanced chemical vapor deposition (denoted as PE-CVD) method. Table 4-1 shows deposition

conditions of DLC coating. Optical microscope image of initial DLC disk is shown in Fig. 4-2.. A surface profile curve of DLC disk is shown in Fig. 4-3. Arithmetic mean roughness is 16.8 nm. The indentation hardness of DLC coating on the SiC disk was 17.8 GPa. The indentation hardness of the disk substrate was 38.8 GPa and the surface roughness of the disk was 14.5 nm in average roughness. In order to remove the contamination, the substrate was sonicated by semiconductor cleaning solution (Semicoclean, Furuuchi Chemical Corporation) and ethanol before deposition procedures. The SiC disk was cleaned by argon (Ar) ion sputtering for 20 min to remove any adsorbed materials on the surface. The total coating thickness of DLC composite on the SiC disk surface was set as 400 nm, approximately.

4.2.2 Friction test conditions

Friction tests were conducted in water as shown in Fig. 2-1. AISI 304 ball and DLC coated SiC disk were used as specimens. All specimens were sonicated by acetone and ethanol before the friction tests. Friction tests were performed in purified water and sliding distance was set as 100 m. Load and sliding velocity were varied from 1 N to 20 N and from 0.001 m/s to 0.5 m/s, respectively. The water temperature was kept at 20ºC constantly. Contact surface pressure was calculated from the dimeter of wear scar on ball specimen after friction test.

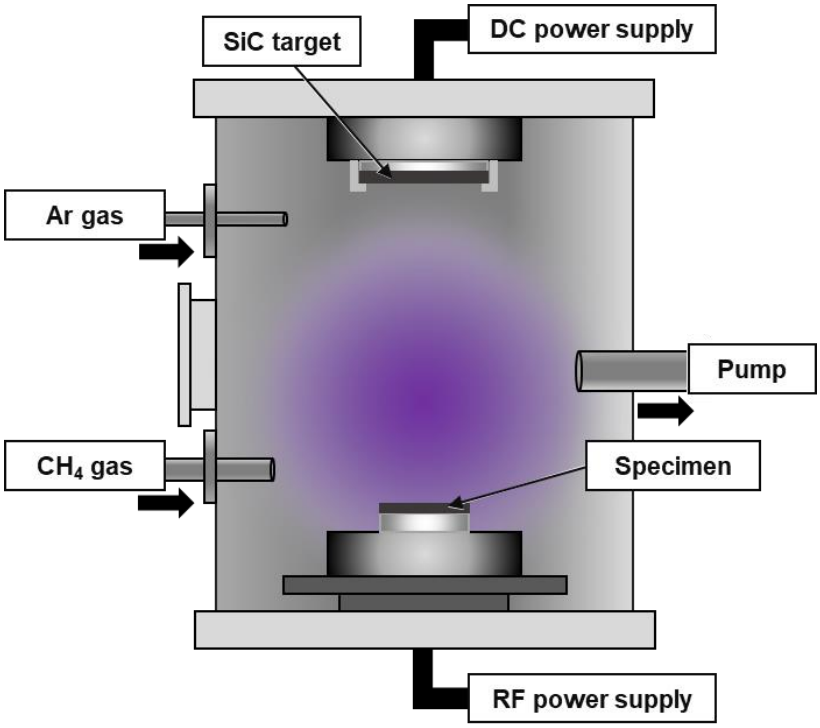

Fig. 4-1 Schematic illustration of deposition vapor deposition system.

Table 4-1 Deposition conditions of DLC coating.

Pressure	**Background**	**$< 1.0 \times 10^{-4}$ Pa**
	Operating	**10 Pa**
Sputter cleaning	**Self bias voltage**	**-520 V**
	Gas flow rate	**Ar: 10 sccm**
	Process time	**20 minutes**
Chemical vapor deposition	**Self bias voltage**	**-420 V**
	Gas flow rate	**Ar: 10 sccm CH_4: 2 sccm**
	Deposition time	**40 min.**

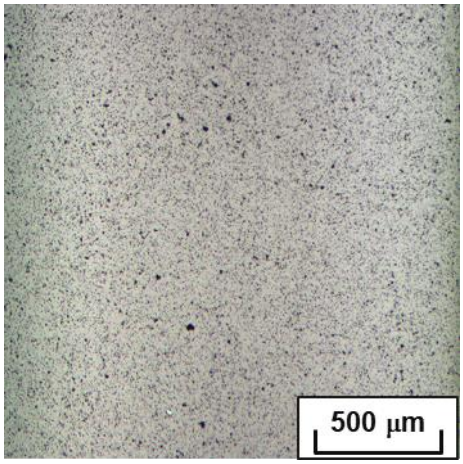

Fig. 4-2 Optical microscope image of initial surface of DLC coated SiC disk specimen.

Fig. 4-3 Surface profile curve of DLC coated SiC disk specimen.

4.3 Experimental results and discussion

4.3.1 Friction property of stainless steel slid against DLC coating in water

Figure 4-4 shows friction properties of AISI 304/DLC in water at normal load of 1 N and sliding velocity varied from 0.001 to 0.5 m/s. Figure 4-5 shows friction properties of AISI 304/DLC in water at normal load of 5 N and sliding velocity varied from 0.001 to 0.5 m/s. Figure 4-6 shows friction properties of AISI 304/DLC in water at normal load of 10 N and sliding velocity varied from 0.001 to 0.5 m/s. Figure 4-7 shows friction properties of AISI 304/DLC in water at normal load of 20 N and sliding velocity varied from 0.001 to 0.5 m/s. From these results, that the introduction of DLC coating as a mating material of AISI 304 caused the running-in under certain conditions was clarified. Figure 4-8 shows optical microscope images of wear scar on AISI 304 ball slid against DLC coating in water at normal load of 1 N and sliding velocity varied from 0.001 to 0.5 m/s. Figure 4-9 shows optical microscope images of wear scar on AISI 304 ball slid against DLC coating in water at normal load of 5 N and sliding velocity varied from 0.001 to 0.5 m/s. Figure 4-10 shows optical microscope images of wear scar on AISI 304 ball slid against DLC coating in water at normal load of 10 N and sliding velocity varied from 0.001 to 0.5 m/s. Figure 4-11 shows optical microscope images of wear scar on AISI 304 ball slid against DLC coating in water at normal load of 20 N and sliding velocity varied from 0.001 to 0.5 m/s. The overall characteristic of wear scar on AISI 304 slid against DLC is that a black transfer film is formed on the wear scar.

Relationship between friction coefficient and bearing characteristic number is summarized in Fig. 4-12. In the region where the bearing characteristic number is smaller than 10^{-14}, when using a tribo-pair such as AISI 304/AISI 304, AISI 304/Si_3N_4, AISI 304/SiC, the friction coefficient shows 0.2 or more and it is thought that it is a boundary lubrication region. On the other hand, it was found that low friction with a friction coefficient of 0.1 or less is exhibited in the boundary lubrication region by introducing DLC coating as the mating material of AISI 304.

Figure 4-13 is an enlarged graph of the y axis in Fig. 4-12. SiC/SiC combination, which is currently used as a water lubrication system, exhibits a friction coefficient of 0.2 or more when the value of G is less than 10^{-12}, whereas AISI 304/DLC coating combination exhibits a friction coefficient of 0.1 or less . This contributed to the improvement of boundary lubrication characteristics in water lubrication, which was the original purpose.

Figure 4-14 shows the specific wear rate of ball calculated from the all wear scar after the friction test under AISI 304/AISI 304, AISI 304/Si_3N_4, AISI 304/SiC and AISI 304/DLC coating combinations in water as a function of products of initial contact pressure P_i and sliding velocity V, which is proportional

to the initial input energy. When DLC coating was used as mating material of AISI 304 ball, the AISI 304/DLC coating combination succeeded in significantly reducing specific wear rate of AISI 304 ball. The specific wear rate of ball under AISI 304/DLC coating varied from 10^{-8} $mm^3/N{\cdot}m$ to 10^{-6} $mm^3/N{\cdot}m$. This specific wear amount is equivalent to around 1/10 or 1/100 of the specific wear rate using Si_3N_4 or SiC as the mating material of AISI 304.

These results demonstrate that DLC coating has a potential to improve friction property of AISI 304 in water.

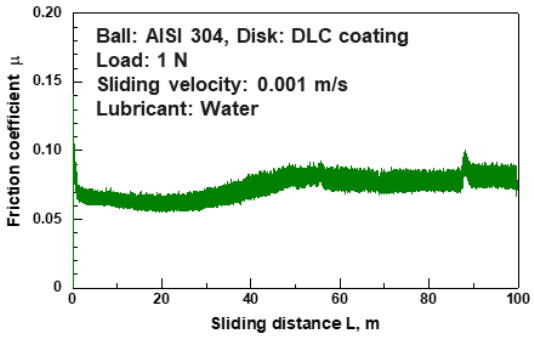

(a) 0.001 m/s

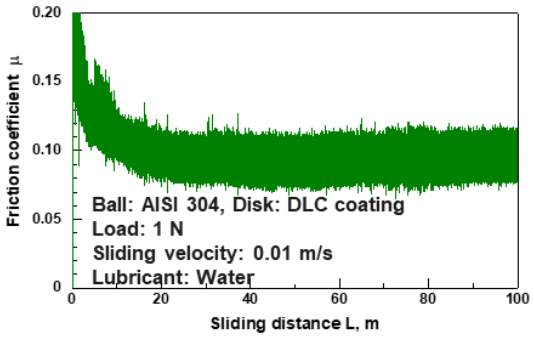

(b) 0.01 m/s

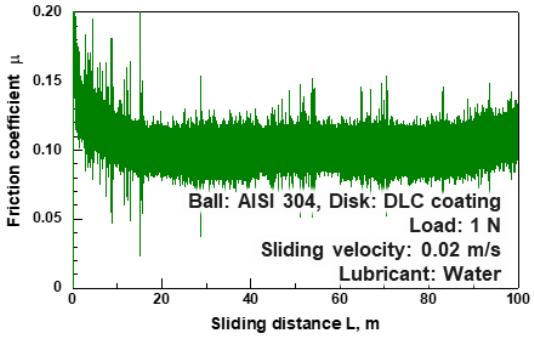

(c) 0.02 m/s

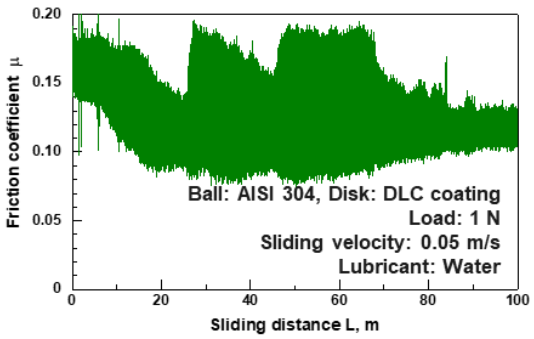

(d) 0.05 m/s

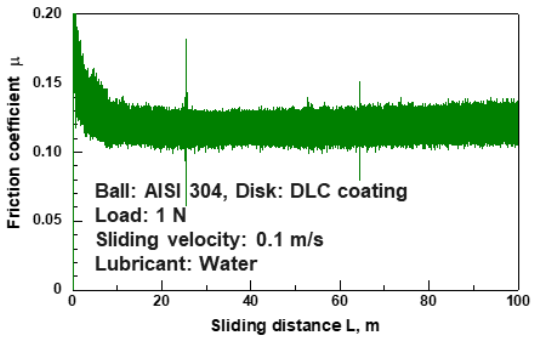

(e) 0.1 m/s

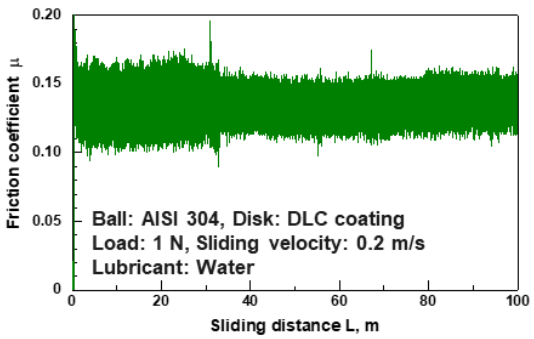

(f) 0.2 m/s

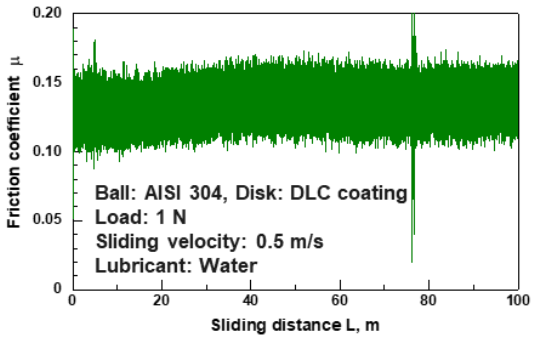

(g) 0.5 m/s

Fig. 4-4 Friction properties of AISI 304 sliding against DLC in water at load 1 N and sliding velocity (a) 0.001 m/s, (b) 0.01 m/s, (c) 0.02 m/s, (d) 0.05 m/s, (e) 0.1 m/s, (f) 0.2 m/s and (g) 0.5 m/s.

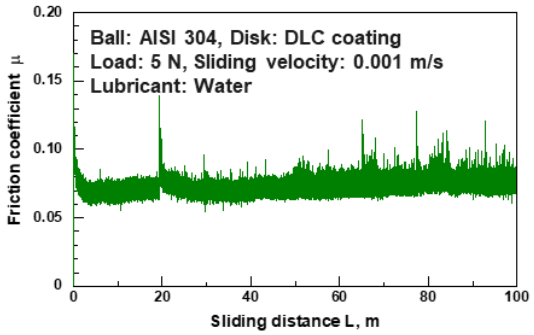

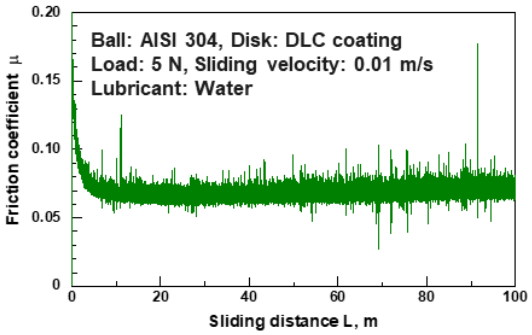

(a) 0.001 m/s

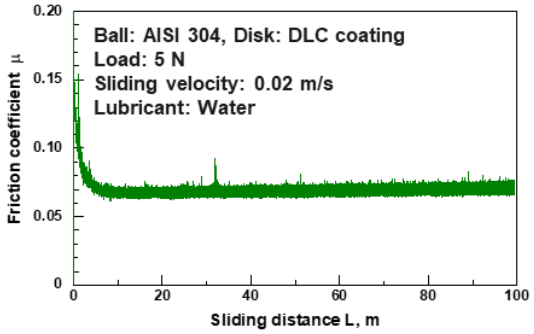

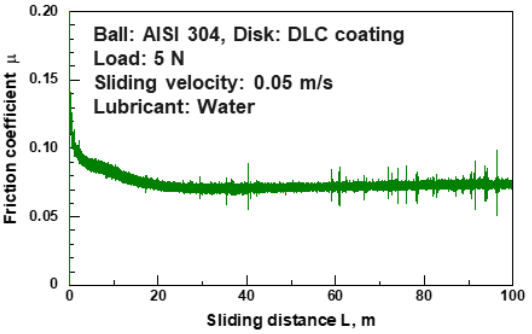

(c) 0.02 m/s

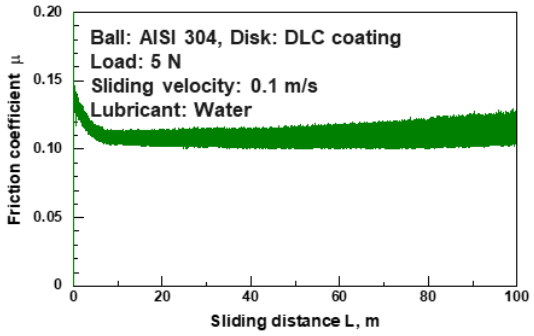

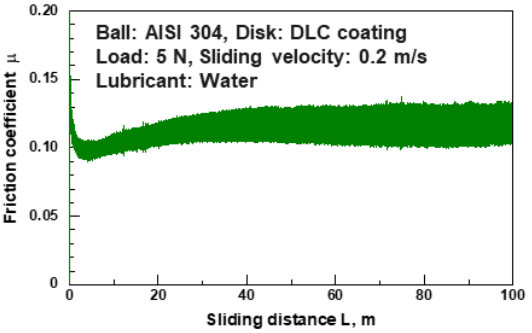

(e) 0.1 m/s

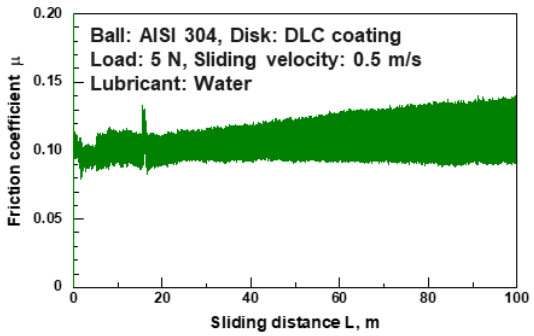

(g) 0.5 m/s

Fig. 4-5 Friction properties of AISI 304 sliding against DLC in water at load 5 N and sliding velocity (a) 0.001 m/s, (b) 0.01 m/s, (c) 0.02 m/s, (d) 0.05 m/s, (e) 0.1 m/s, (f) 0.2 m/s and (g) 0.5 m/s.

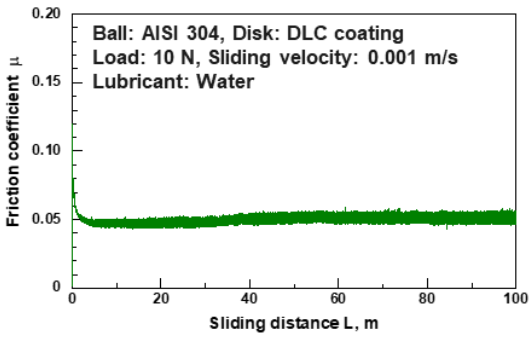

(a) 0.001 m/s

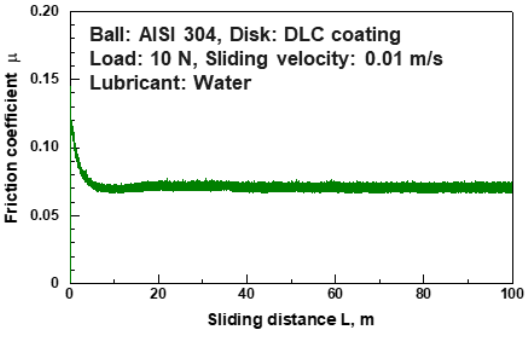

(b) 0.01 m/s

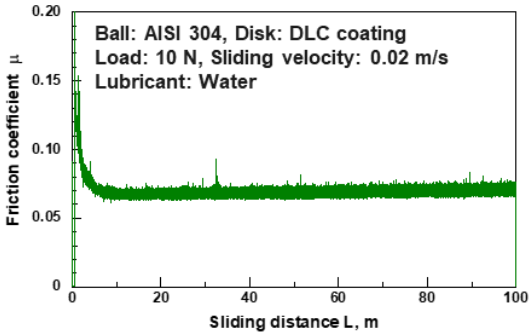

(c) 0.02 m/s

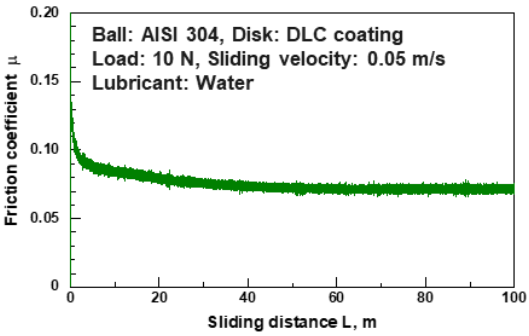

(d) 0.05 m/s

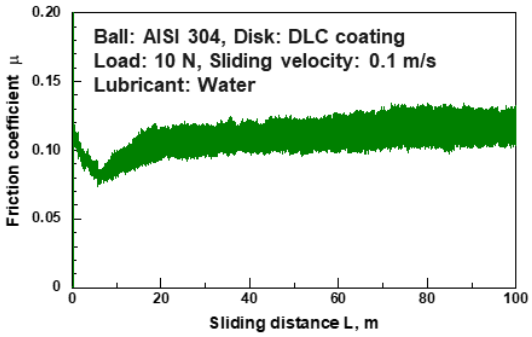

(e) 0.1 m/s

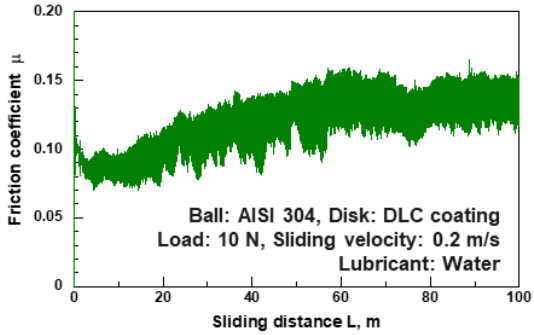

(f) 0.2 m/s

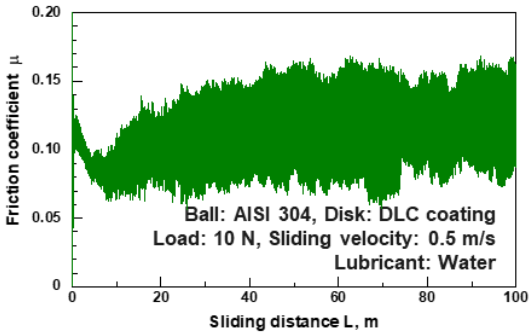

(g) 0.5 m/s

Fig. 4-6 Friction properties of AISI 304 sliding against DLC in water at load 10 N and sliding velocity (a) 0.001 m/s, (b) 0.01 m/s, (c) 0.02 m/s, (d) 0.05 m/s, (e) 0.1 m/s, (f) 0.2 m/s and (g) 0.5 m/s.

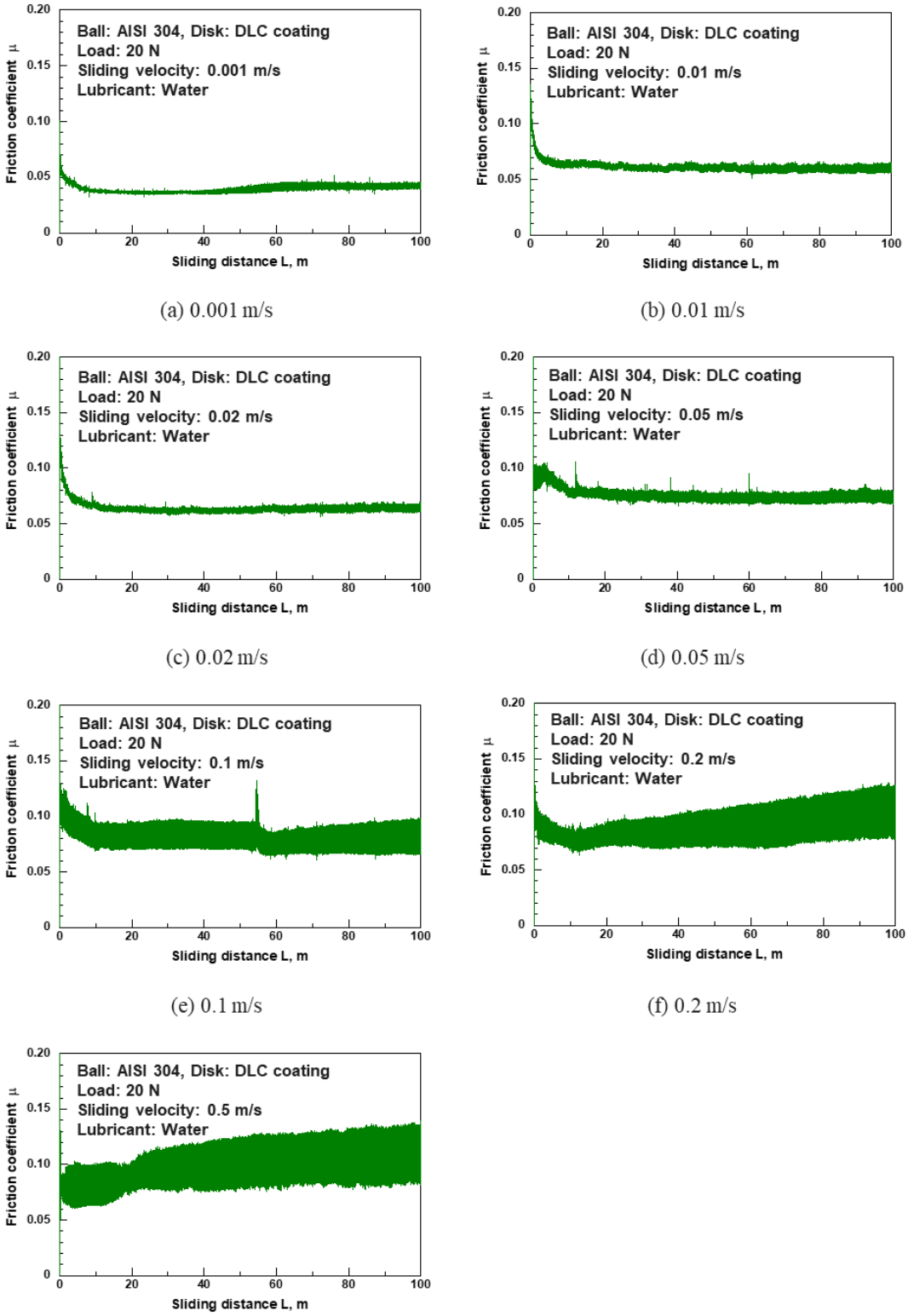

Fig. 4-7 Friction properties of AISI 304 sliding against DLC in water at load 20 N and sliding velocity (a) 0.001 m/s, (b) 0.01 m/s, (c) 0.02 m/s, (d) 0.05 m/s, (e) 0.1 m/s, (f) 0.2 m/s and (g) 0.5 m/s.

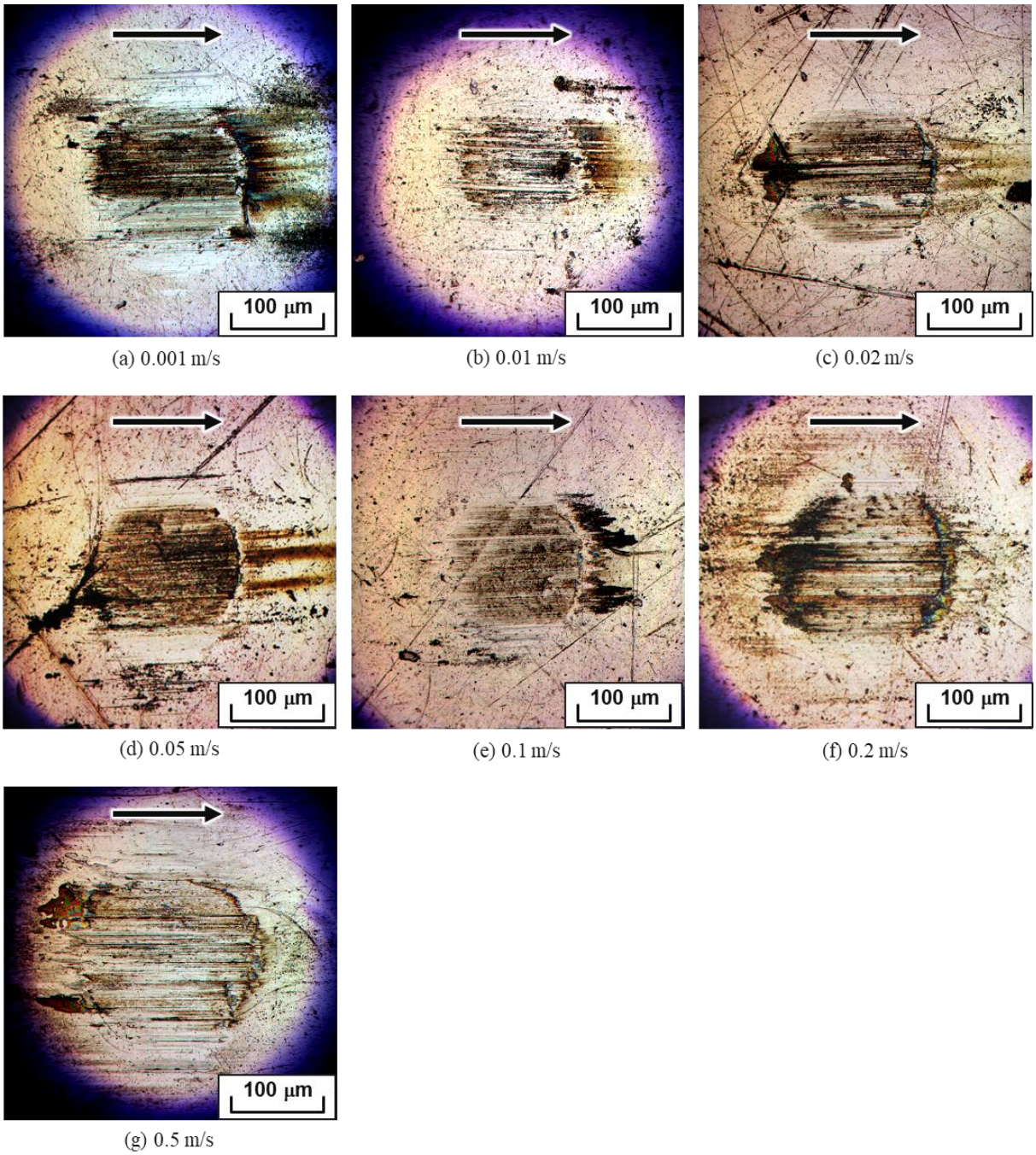

(a) 0.001 m/s (b) 0.01 m/s (c) 0.02 m/s

(d) 0.05 m/s (e) 0.1 m/s (f) 0.2 m/s

(g) 0.5 m/s

Fig. 4-8 Optical microscope images of wear scar on AISI 304 ball sliding against DLC in water at load 1 N and sliding velocity (a) 0.001 m/s, (b) 0.01 m/s, (c) 0.02 m/s, (d) 0.05 m/s, (e) 0.1 m/s, (f) 0.2 m/s and (g) 0.5 m/s.

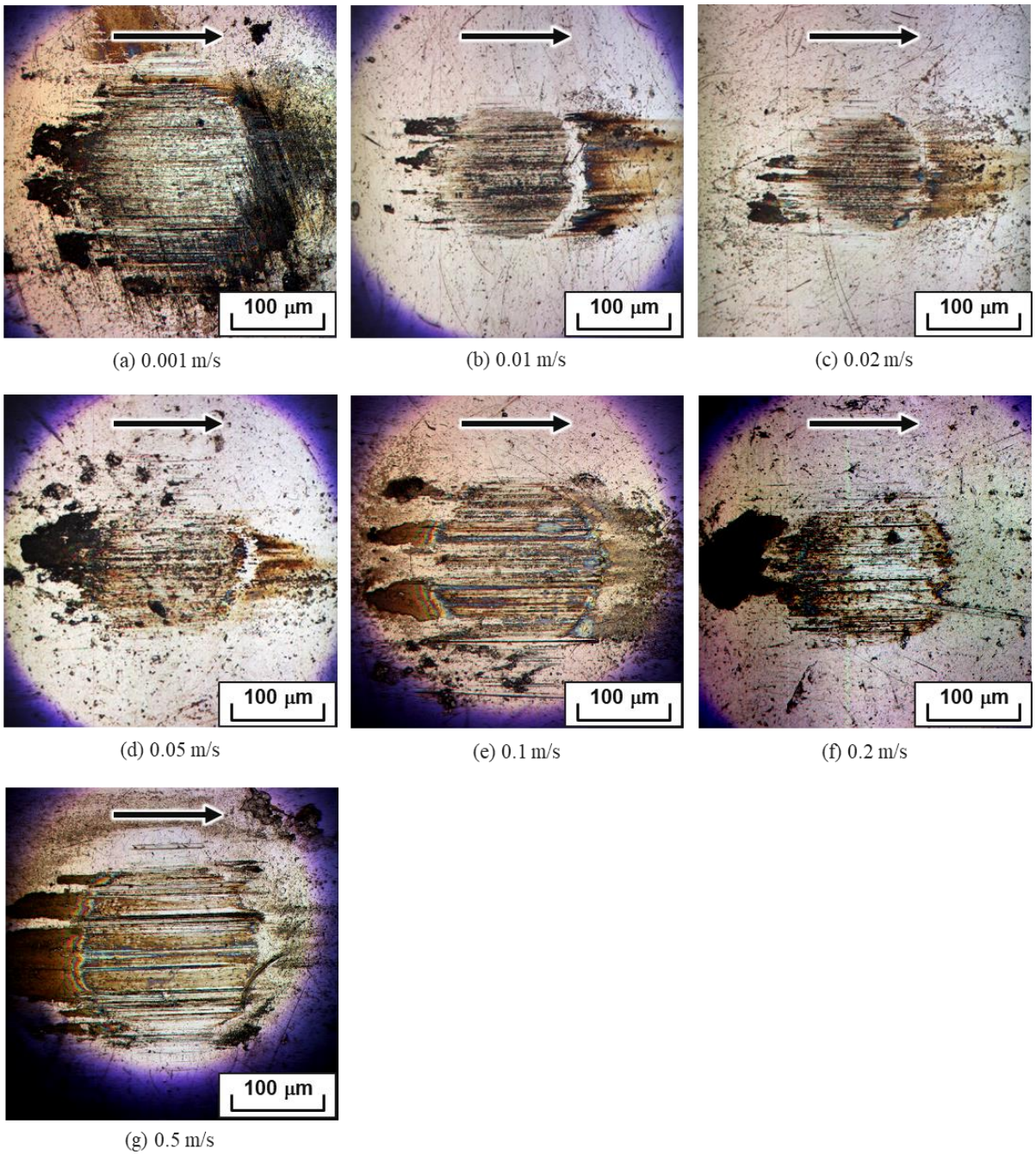

(a) 0.001 m/s (b) 0.01 m/s (c) 0.02 m/s

(d) 0.05 m/s (e) 0.1 m/s (f) 0.2 m/s

(g) 0.5 m/s

Fig. 4-9 Optical microscope images of wear scar on AISI 304 ball sliding against DLC in water at load 5 N and sliding velocity (a) 0.001 m/s, (b) 0.01 m/s, (c) 0.02 m/s, (d) 0.05 m/s, (e) 0.1 m/s, (f) 0.2 m/s and (g) 0.5 m/s.

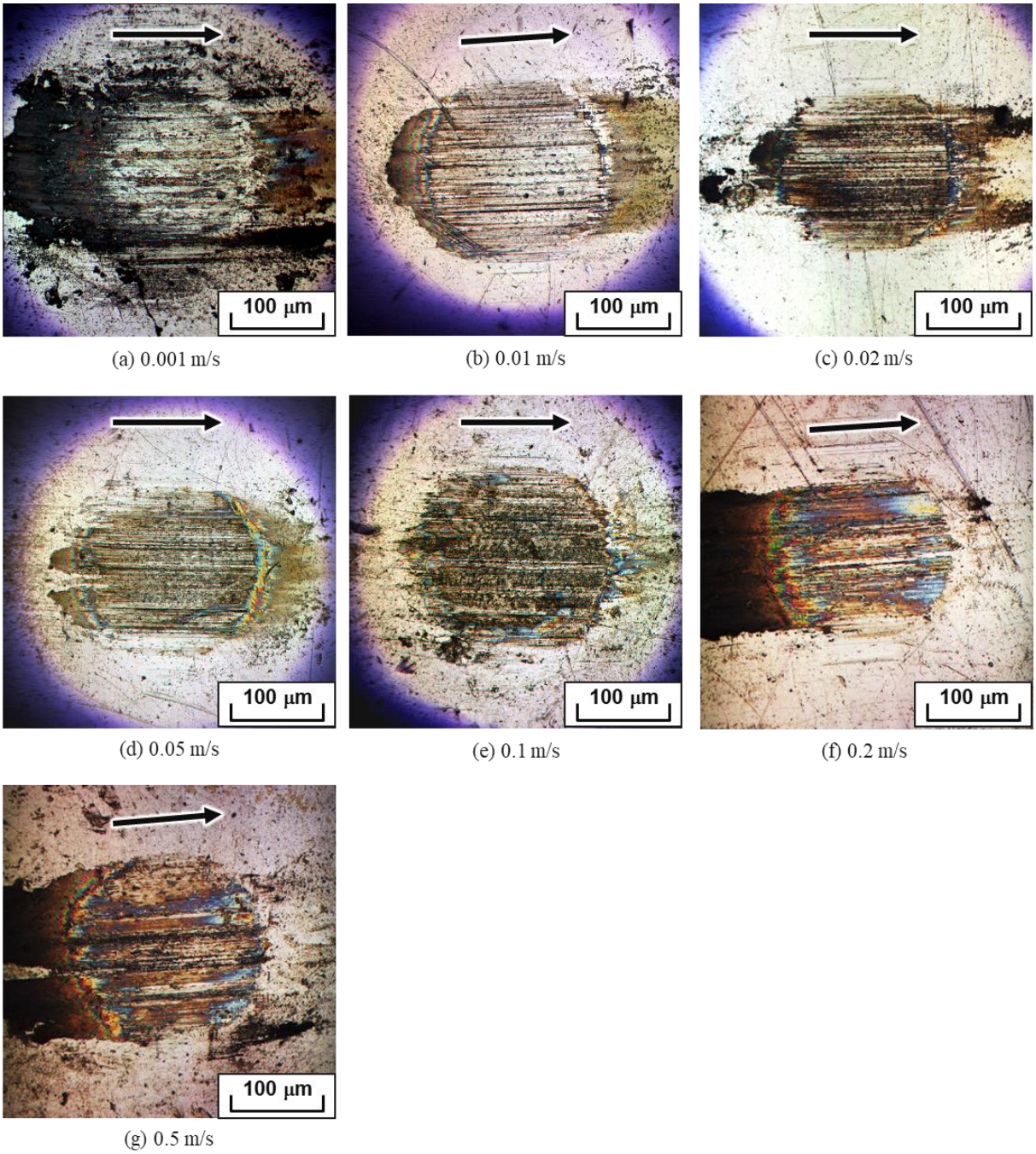

(a) 0.001 m/s (b) 0.01 m/s (c) 0.02 m/s

(d) 0.05 m/s (e) 0.1 m/s (f) 0.2 m/s

(g) 0.5 m/s

Fig. 4-10 Optical microscope images of wear scar on AISI 304 ball sliding against DLC in water at load 10 N and sliding velocity (a) 0.001 m/s, (b) 0.01 m/s, (c) 0.02 m/s, (d) 0.05 m/s, (e) 0.1 m/s, (f) 0.2 m/s and (g) 0.5 m/s.

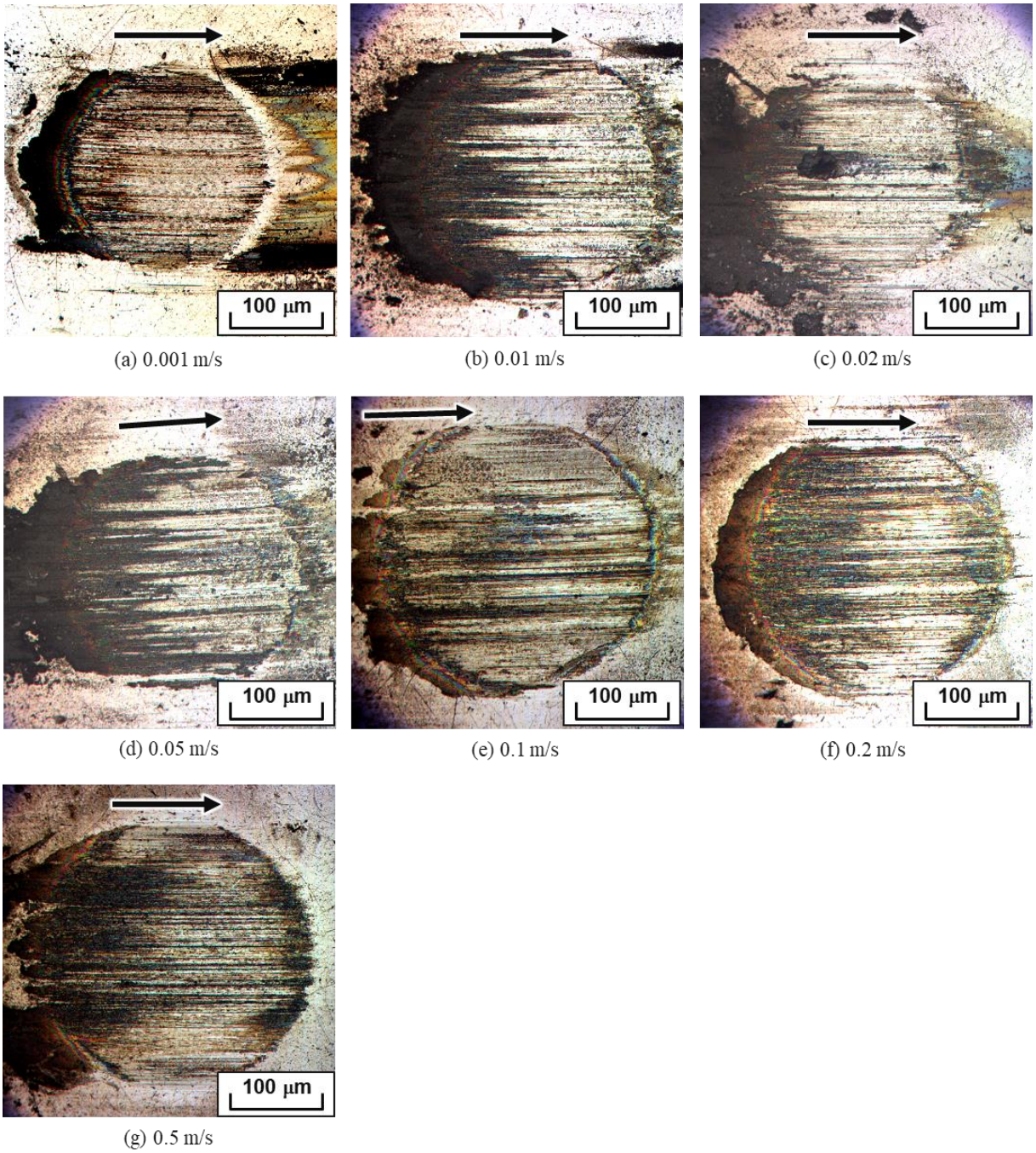

(a) 0.001 m/s (b) 0.01 m/s (c) 0.02 m/s

(d) 0.05 m/s (e) 0.1 m/s (f) 0.2 m/s

(g) 0.5 m/s

Fig. 4-11 Optical microscope images of wear scar on AISI 304 ball sliding against DLC in water at load 20 N and sliding velocity (a) 0.001 m/s, (b) 0.01 m/s, (c) 0.02 m/s, (d) 0.05 m/s, (e) 0.1 m/s, (f) 0.2 m/s and (g) 0.5 m/s.

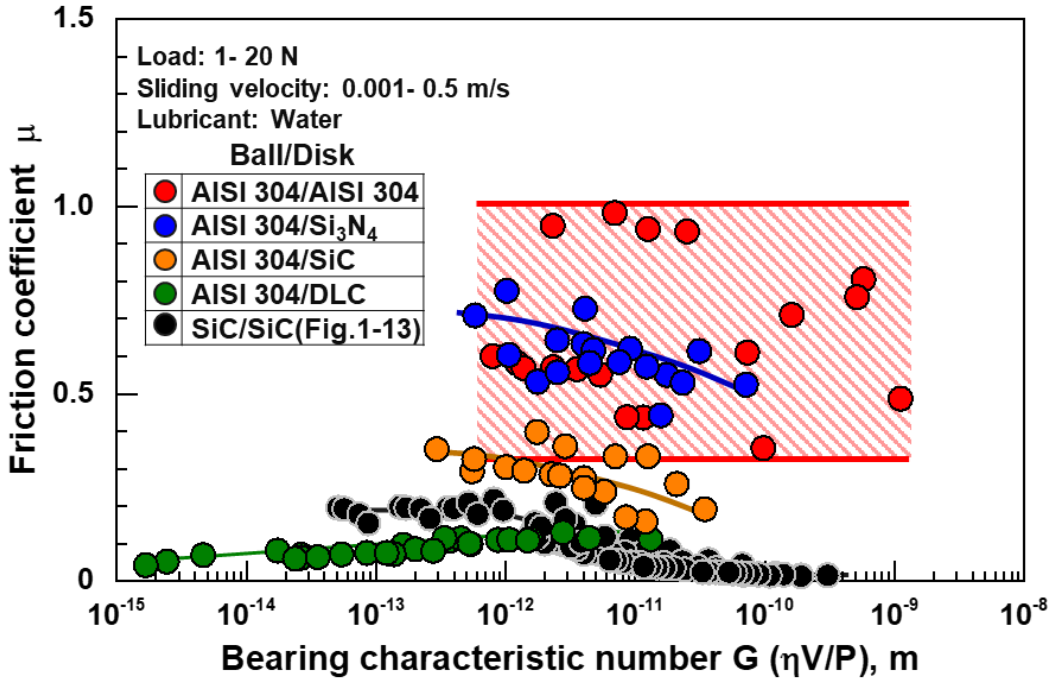

Fig. 4-12 Relationship between bearing characteristic number and average friction coefficient of AISI 304/AISI 304, AISI 304/Si_3N_4, AISI 304/SiC and AISI 304/DLC coating in water.

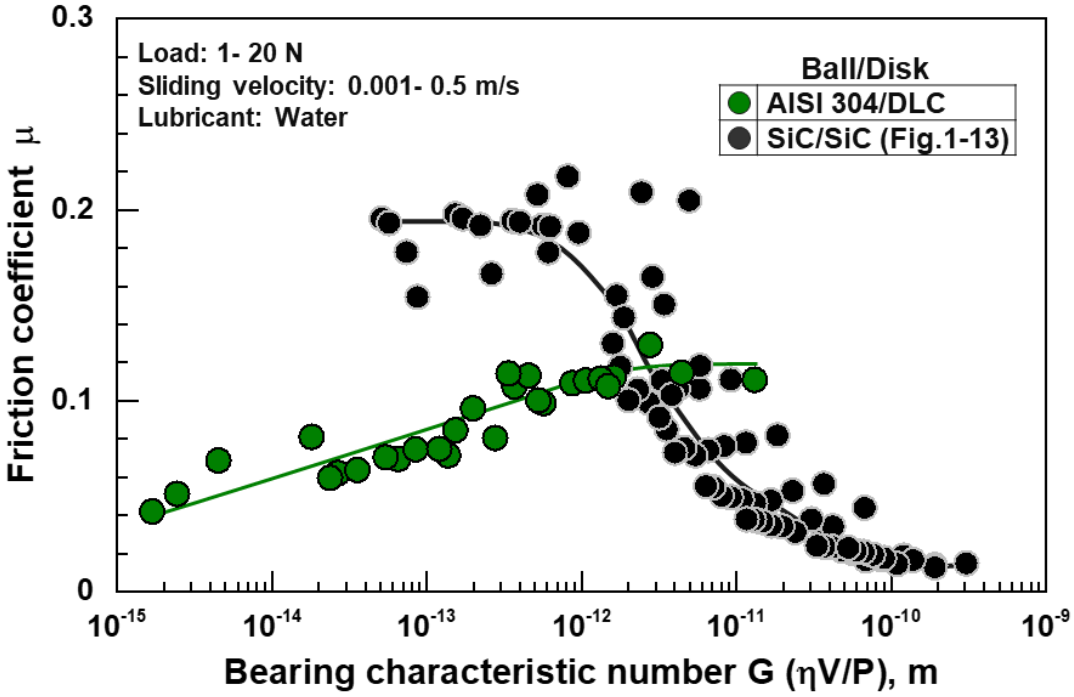

Fig. 4-13 Relationship between bearing characteristic number and average friction coefficient of AISI 304/DLC coating and SiC/SiC in water.

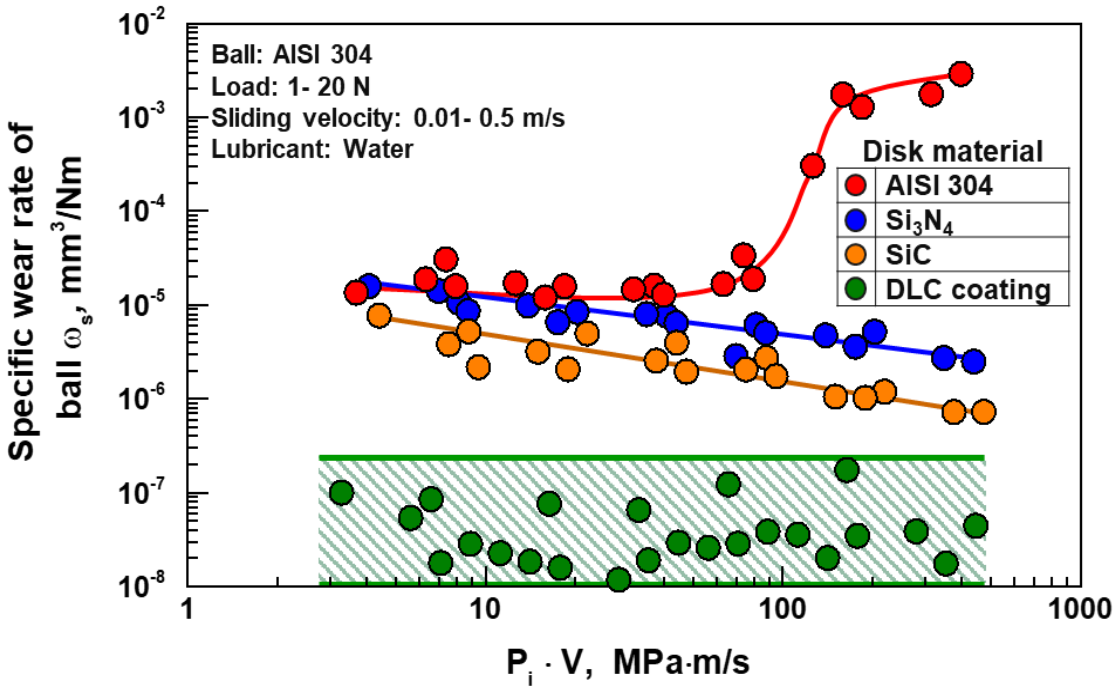

Fig. 4-14 Relationship between the value of P_iV and the specific wear rate of AISI 304 ball sliding against AISI 304, Si_3N_4, SiC and DLC coating in water.

4.3.2 Generation of low friction under boundary lubrication regime

Friction properties between AISI 304 and DLC coating in water are classified into friction modes from the viewpoint of wear scars on AISI 304 ball and running-in in order to understand the friction behaviors in detail. Friction properties of AISI 304/DLC coating in water are classified into two modes as follows:

Mode I; no running-in or increasing the friction coefficient after running-in (4.1)

Mode II; running-in behavior and showing the stable friction coefficient (4.2)

The distribution of these friction modes is shown in Fig. 4-15. As shown in Fig. 4-15, it can be seen that Mode II exhibits at high contact pressure and low sliding velocity. In other words, it indicates that it is a friction mode dependent on the value sliding velocity divided by contact pressure (V/P). The quotient is around 3000 and Mode I and Mode II occurrences are organized by this value.

Figure 4-16 shows Stribeck curve which shows friction coefficient as a function of bearing characteristic number G in the case of AISI 304/DLC coating in water. The friction coefficient varied from 0.04 to 0.14 The value of G indicates the thickness of water film relatively. In general, when the value of G increases, the water film that can be retained becomes thicker, so that direct contact between the two surfaces is prevented and the friction coefficient is consequently reduced. On the other hands, the friction couple of AISI 304/DLC coating in water exhibits lower friction in areas where it is difficult to form a water film and it is easy to occur the direct contact.

Optical microscope images of the wear scar on AISI 304 ball sliding against DLC coating in water are shown in Fig. 4-17. As shown in Fig. 4-17, the wear scar on AISI 304 ball are divided into two types. Those in which a transfer film is formed on the wear scar entirely (Fig. 4-17 (a)) and those in which a transfer film is formed only partially (Fig. 4-17 (b)). Therefore, the area ratio where the transfer film is not seen on the wear scar was calculated by binarization processing in order to clarify the relationship between the transfer film and the friction properties of AISI 304/DLC coating in water. As shown in Fig. 4-17, the binarization process was performed in the red circle area of radius 40 μm at the center of the wear scar on AISI 304 ball, and the threshold value for areas was set to a gradation value of 165 or higher. Areas without transfer film is converted to yellow color. Figure 4-18 shows the relationship the area ratio without transfer film and the friction coefficient. The friction coefficient decreases from 0.07 when the area ratio exceeds 37% from Fig. 4-18. And even with the same Mode II, it was found that there were

conditions that could not show low friction depending on the amount of transfer film. Moreover, Mode II are classified into two modes as follows:

Mode II-I; the ratio of the wear scar without transfer film < 37% (4.3)

Mode II-II; the ratio of the wear scar without transfer film ≥37% (4.4)

XPS analysis was performed to clarify the difference between Mode I and Mode II-II, differences were found between the Fe 2p spectrum and the C 1s spectrum. The ratio of Fe_2O_3 in the distribution of chemical bond of Fe 2p spectrums achieved on initial AISI 304 surface, wear scar on modes I and II-II are shown in Fig. 4-19. The ratio of Fe_2O_3 is higher highest in Mode I than in the other samples. These results indicate that the formation of Fe_2O_3 on the wear of AISI 304 ball is prevented in Mode II-II. The ratio of Sp^3 carbon in the distribution of C 1s spectrums of initial surface of AISI 304 ball, in case of Mode I and II-II are shown in Fig. 4-20. The sp^3 component derived from DLC coating was detected only in Mode II-II. The transfer film on AISI 304 ball sliding against DLC coating was analyzed by Raman spectroscopy (Fig. 4-21). Raman analysis was performed at two points where transfer film and transfer film were not observed (Fig. 4-21 (a)) and as-deposited DLC coating. It is not possible to distinguish the carbon-derived peak from Points 1 and 2 where transfer film was not observed. On the other hand, Point 3 indicates that a peak derived from $Fe_{2.2}Cr_{0.8}O_3$[9] in addition to the peak derived from carbon. The transfer film is meant to be a mixture of wear particle of DLC coating and AISI 304. Mode II-I and Mode I-II are divided according to the area ratio of the transfer film derived from DLC and AISI 304 on the wear scar.

Cross-sectional image and distribution of related elements on worn surface without transfer film on AISI 304 ball slid against DLC coating is shown in Fig. 4-22. The images indicate that the nanolayer, approximate thickness is 20 nm, is mainly comprised of oxygen, chromium, iron and carbon. Based on these results, it is considered that the wear scar without transfer film on AISI 304 is dominated, and the surface is formed of a nanolayer composed of oxygen, chromium, iron and carbon, when AISI 304/DLC coating generates low friction in Mode II-II. Based on the fact that the passive film of ordinary stainless steel has a thickness of 1 to 3 nm, that this passive film was self-formed during friction is clarified.

In order to clarify the reason why the friction coefficient tends to decrease as the sliding velocity decreases, in other words, the value of G decreases in Fig. 4-16, the contact angle of water droplet on the wear scars slid against DLC coating for each sliding velocity under a constant load was measured (Fig.

4-23). The contact angle on the wear scar after cleaning with acetone was measured to remove influence of friction products such as wear particles. Friction products that can be removed by cleaning with acetone are considered to be easily removed during friction. Therefore, the friction phenomenon is governed by the contact angle after cleaning with acetone. Considering that the contact angle on the initial AISI 304 ball is 92°, it can be said that the hydrophilicity improved at any sliding velocity. Corresponding to each contact angle and friction modes, Mode I had an average contact angle of 67° after cleaning, but it decreased to 52° in Mode II-I and 43° in Mode II-II, respectively. From the above, it is suggested that the chemical properties of the friction surface formed in each mode are different due to the difference of wettability.

Figure 4-24 shows the contact angle of water droplet after sliding. This figure shows the hydrophilicity on DLC coating by sliding. However, the reduction of contact angle is limited. This is a point that should be improved to further improve the lubrication characteristics.

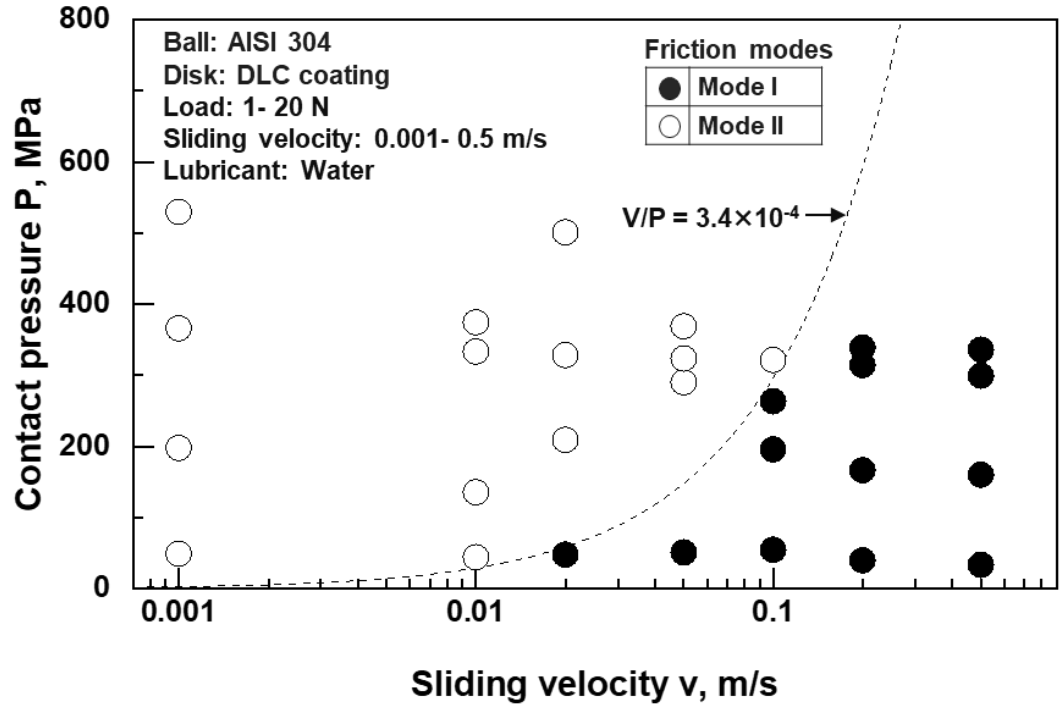

Fig. 4-15 Distribution of friction modes of AISI 304/DLC in water as function of sliding velocity and contact pressure.

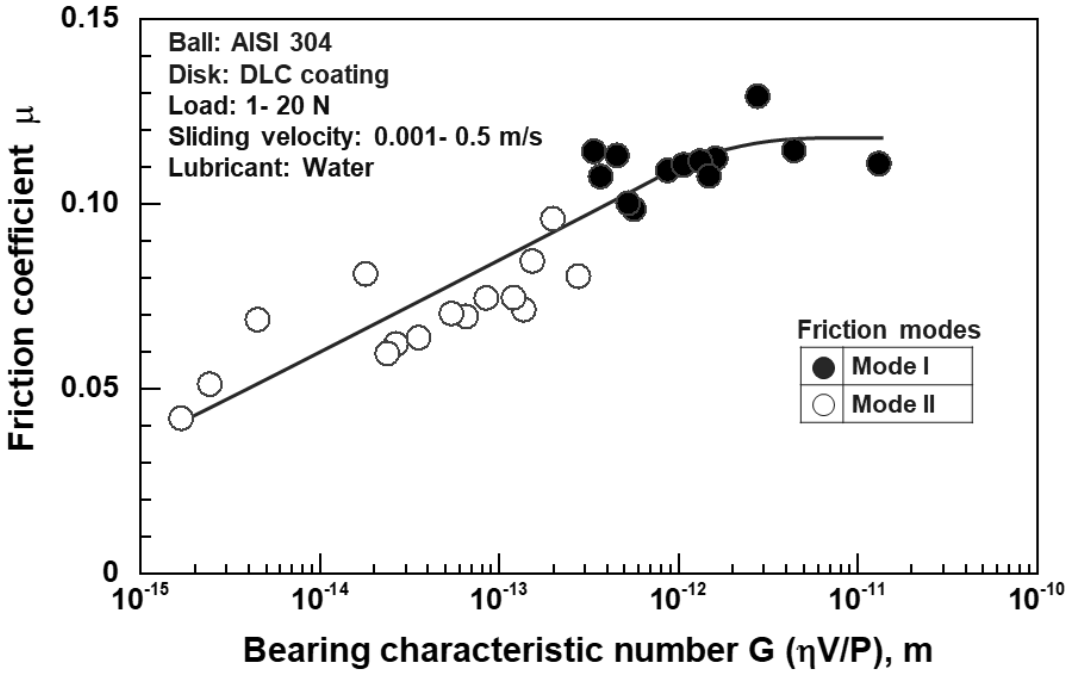

Fig. 4-16 Distribution of friction modes of AISI 304/DLC in water as function of bearing characteristic number and average friction coefficient.

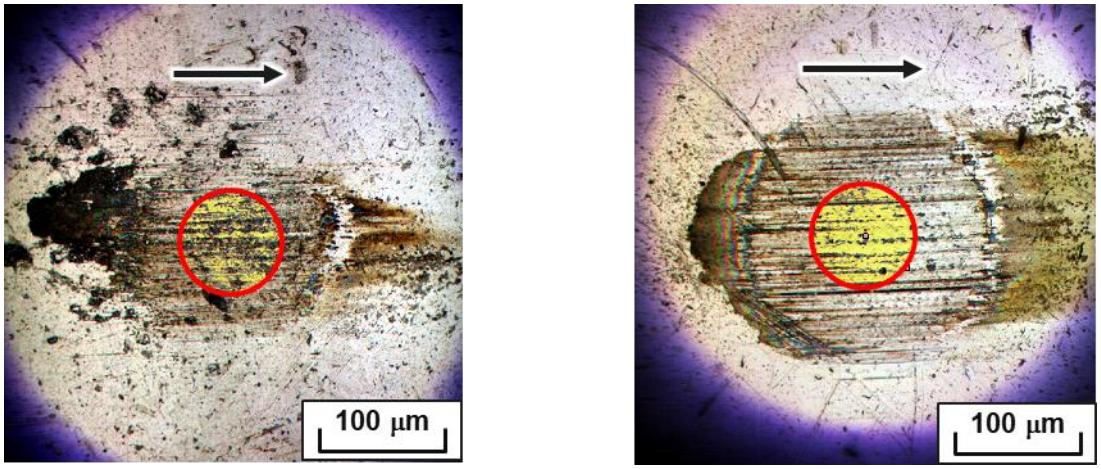

(a) Mode II-I (b) Mode II-II

Fig. 4-17 Optical microscope images of the wear scar on AISI 304 balls sliding against DLC coating in water; (a) Mode II-I (Load: 5 N, sliding velocity: 0.05 m/s) and (b) Mode II-II (Load: 10 N, sliding velocity: 0.01 m/s). Yellow area shows the wear scar without transferred-film. Arrows show the sliding direction of the counter material.

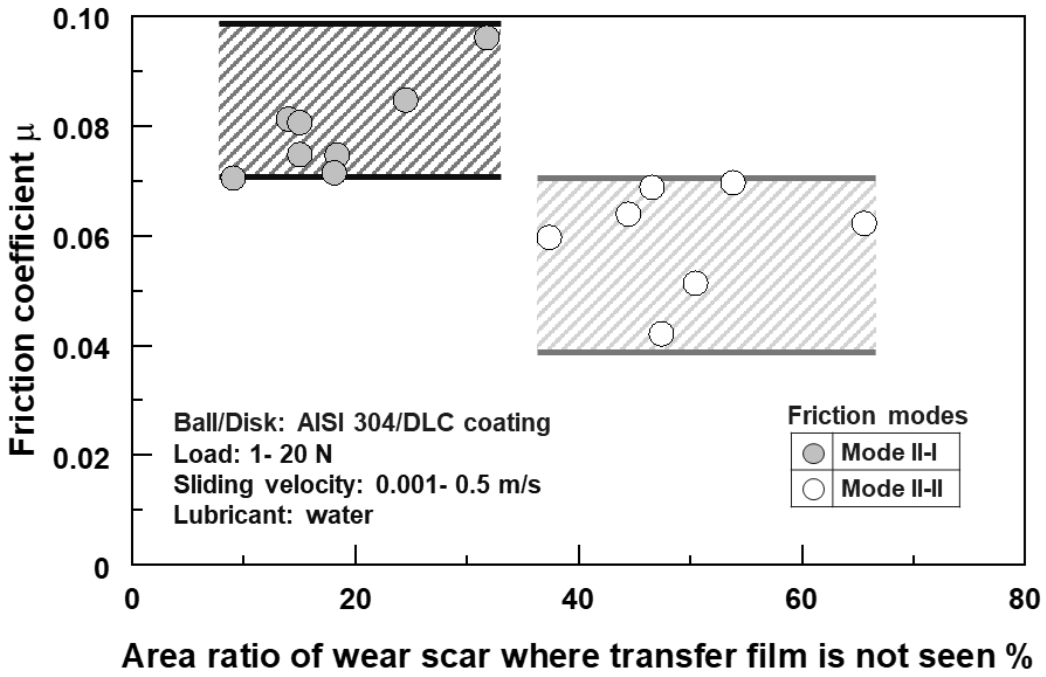

Fig. 4-18 Distribution of the friction modes of AISI 304/DLC coating in water as function of friction coefficient and rate of wear scar without transfer film.

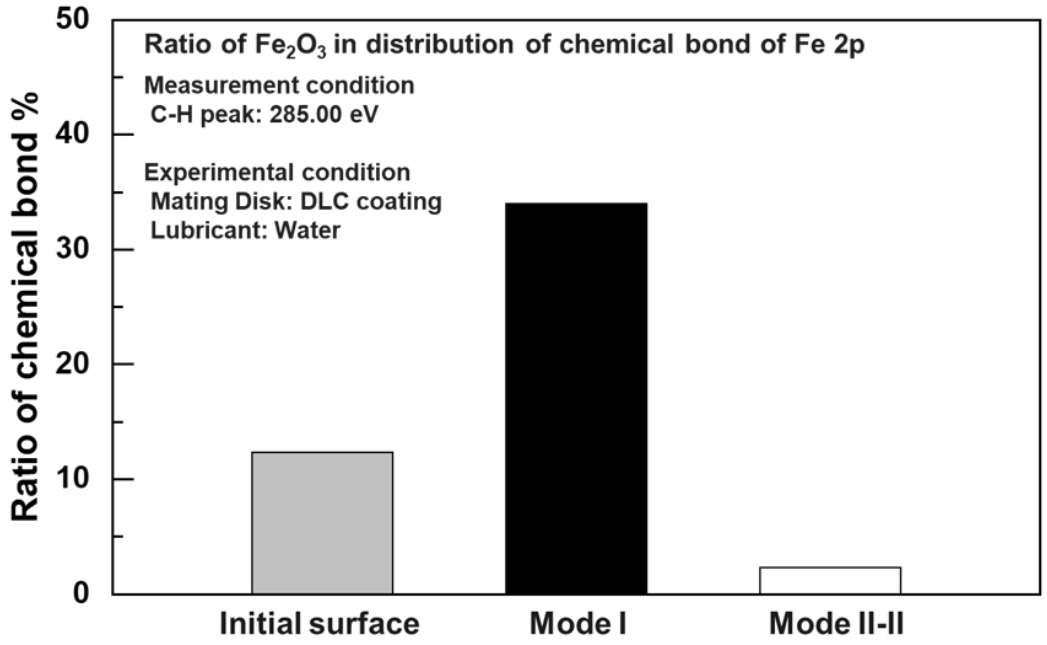

Fig. 4-19 Ratio of Fe_2O_3 in the distribution of chemical bond of Fe 2p in the initial surface, the worn surface in Mode I and Mode II-II on AISI 304 ball.

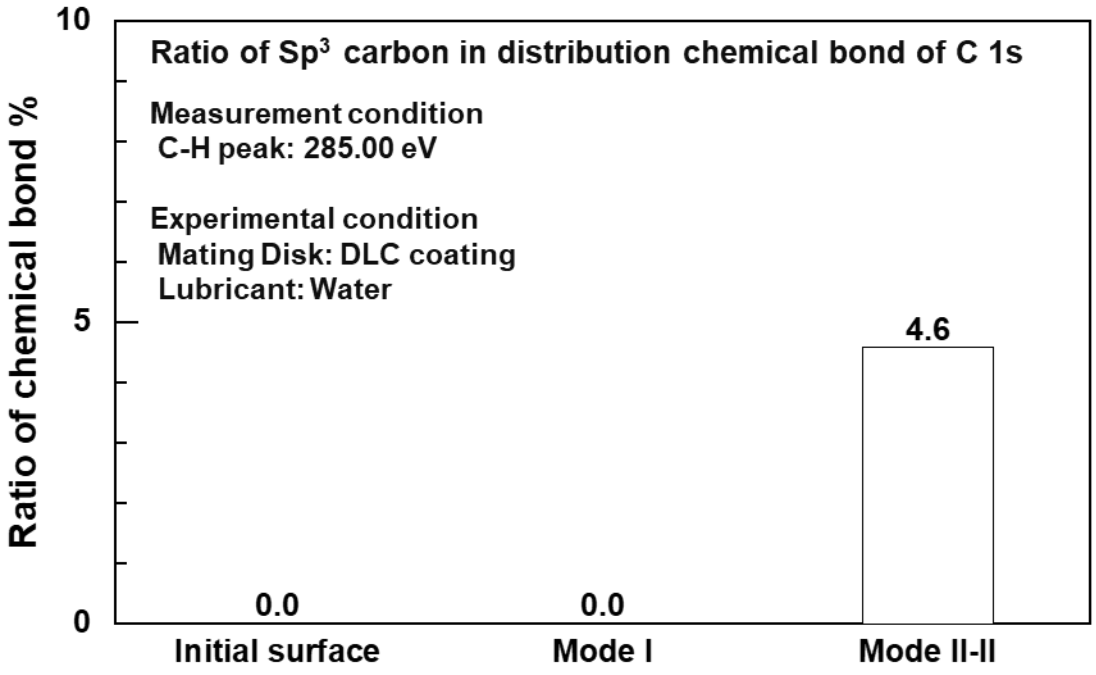

Fig. 4-20 Distribution of chemical bond of C 1s 2p in the initial surface, the worn surface in Mode I and Mode II-II on AISI 304 ball.

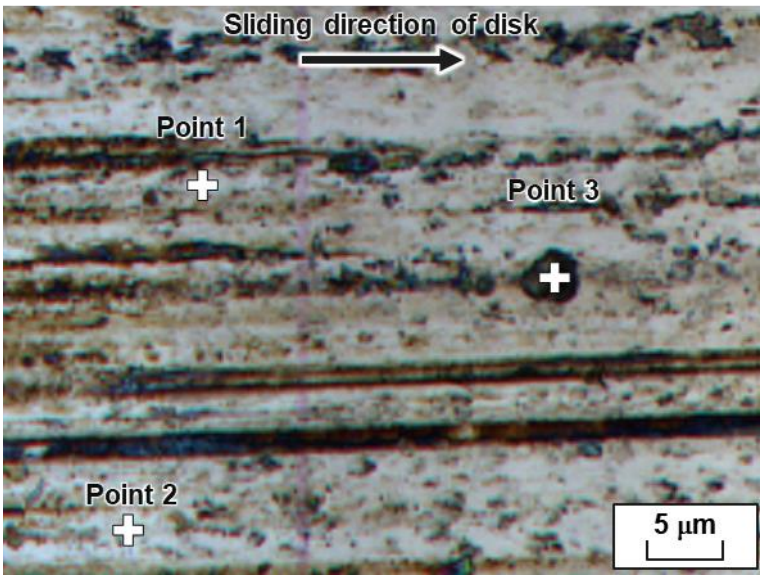

(a) Optical microscope image of wear scar

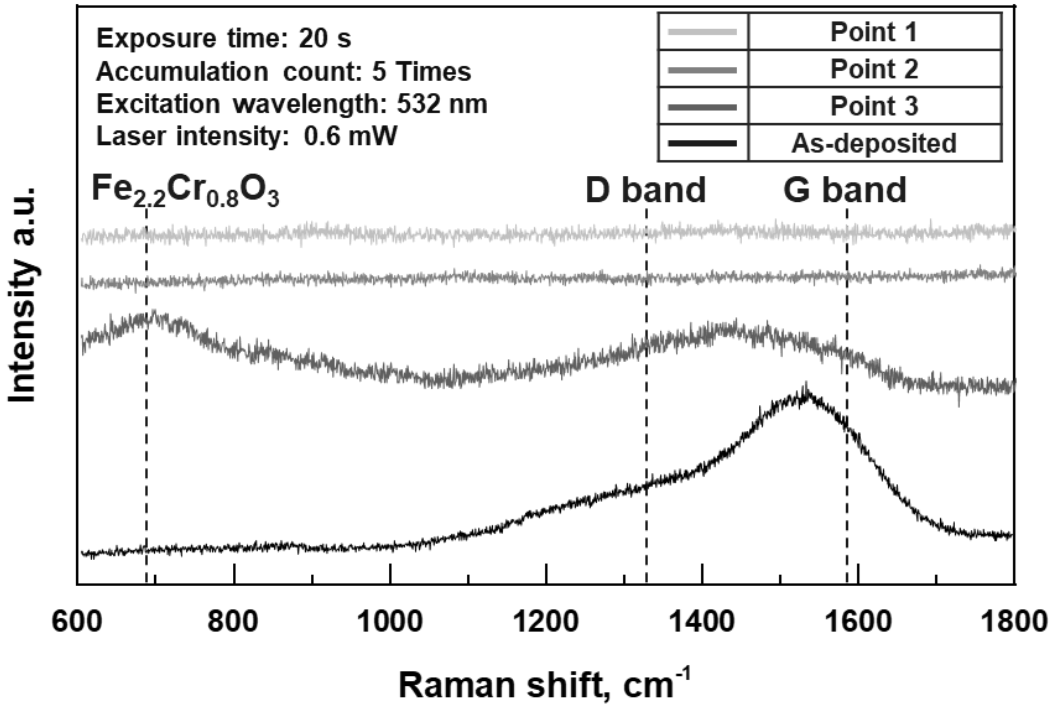

(b) Spectrums obtained by Raman spectroscopy

Fig. 4-21 (a) Optical image of the swear scar on AISI 304 ball sliding against DLC coating in Mode II and (b) Raman spectrums of points which was taken from Fig. 4-21 (a).

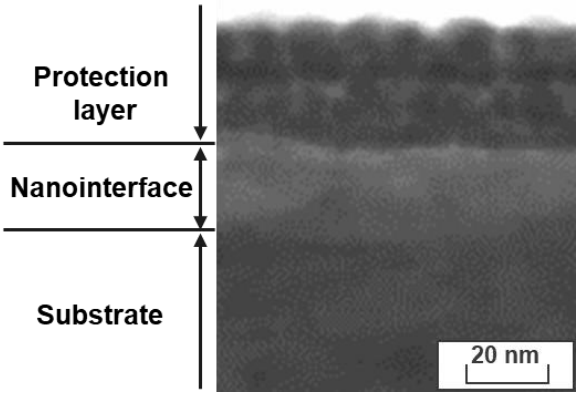

(a) Cross sectional image

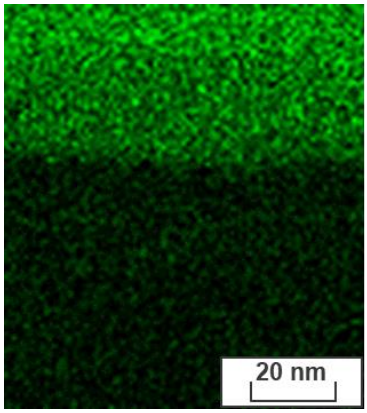

(b) Carbon

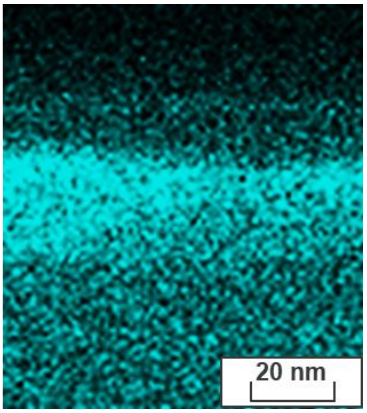

(c) Oxygen

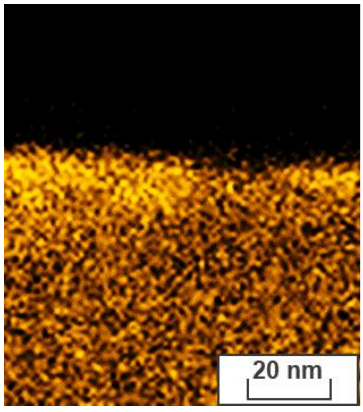

(d) Chromium

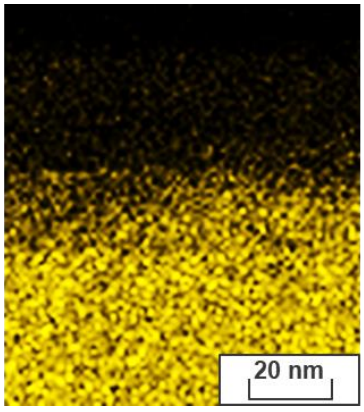

(e) Nickel

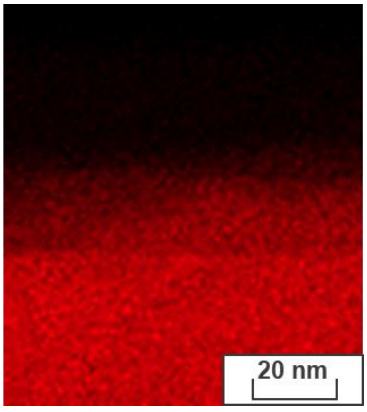

(f) Iron

Fig. 4-22 (a) TEM image and distribution of (b) carbon, (c) oxygen, (d) chromium, (e) nickel and (f) iron of the wear scar without transferred film on AISI 304 slid against DLC coating.

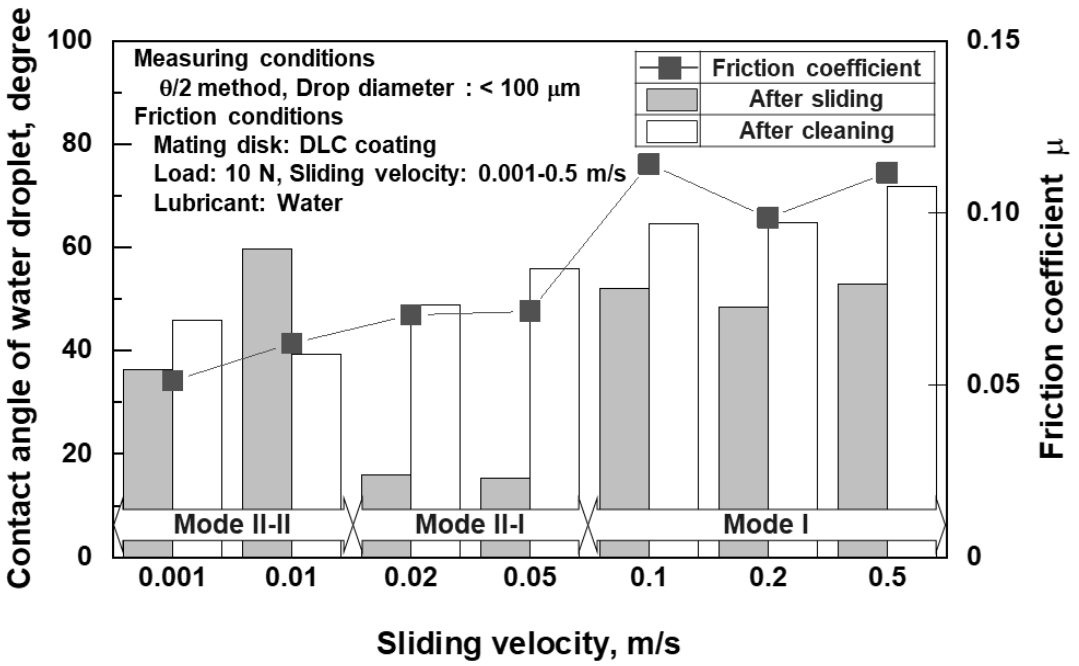

Fig. 4-23 Relationship sliding velocity, contact angle of water droplet on the wear scar sliding against DLC coating and friction coefficient in water. Initial contact angle on AISI 304 ball is 92 degree.

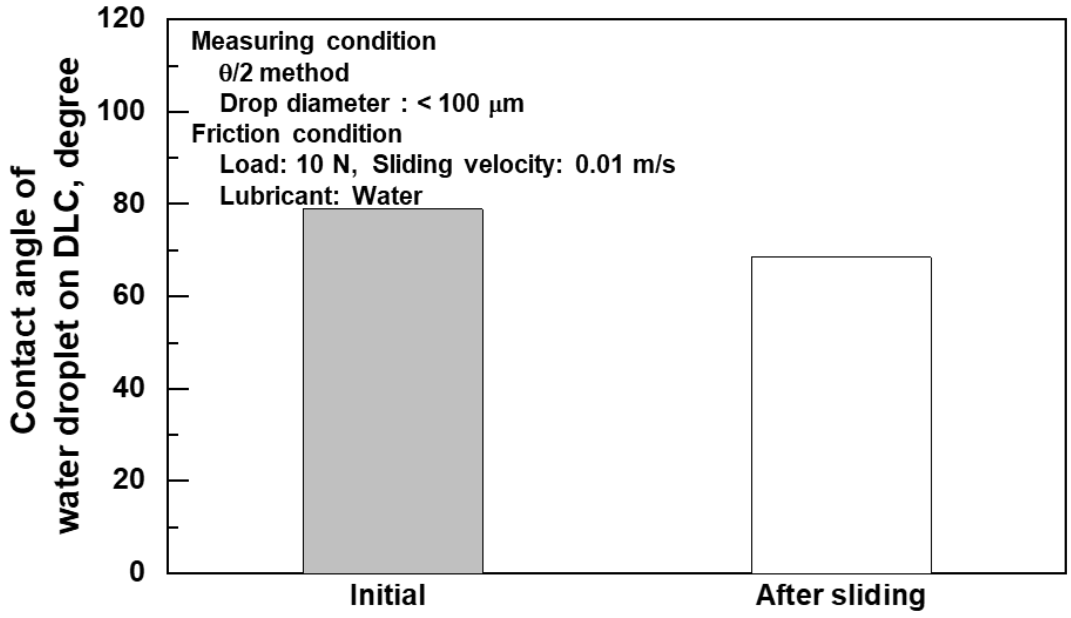

Fig. 4-24 Contact angle of water droplet on DLC coating after sliding.

.

4.3.3 Formation Process of Low Frictional Interface

Figure 4-25 shows the friction property of AISI 304/DLC coating in Mode II-II and the geometrical transition of wear scar on AISI 304 ball. This figure can be confirmed that the carbon transfer film formed initially on the ball wear scar, gradually wears as the running-in process progresses, and the transfer film becomes thinner and the stainless steel surface is exposed. This metal surface is thought to be equivalent to the surface where the nanolayer was confirmed. From this figure, Mode II undergoes carbon transfer on the wear scar at the initial stage of friction, and changes to Mode II-I or Mode II-II depends on the progress of wear of the transfer film. From the results of Stribeck curves, the friction modes depend on the lubrication state. In the initial stage of friction, carbon becomes a worn surface.

Although the exact mechanism is unclear, the role of the transfer of carbon is to prevent the formation of iron oxide on the wear scar on stainless steel and to help the formation of a passive film consisting chromium oxide from these facts.

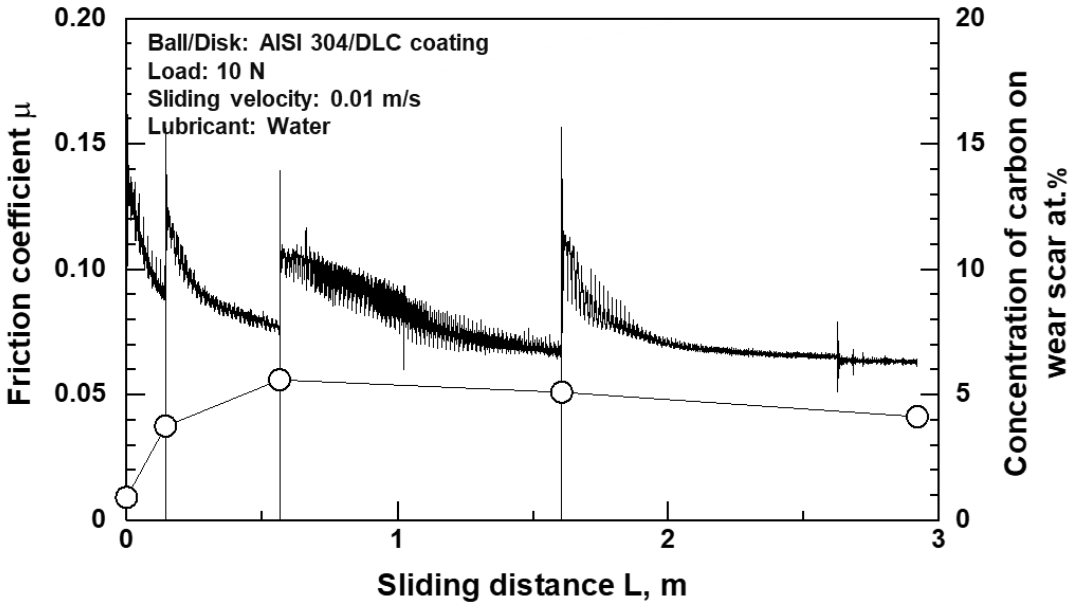

(a) Friction properties and transition of DLC-derived carbon on the wear scar of AISI 304 ball

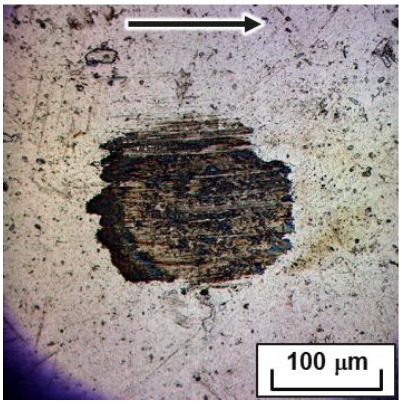

(b1)

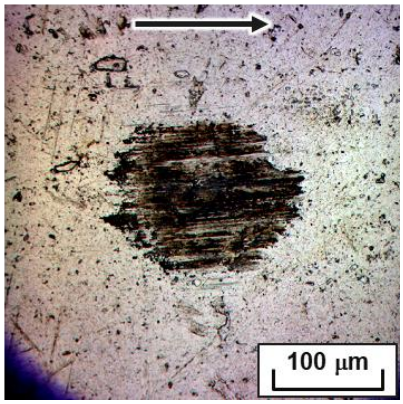

(b2)

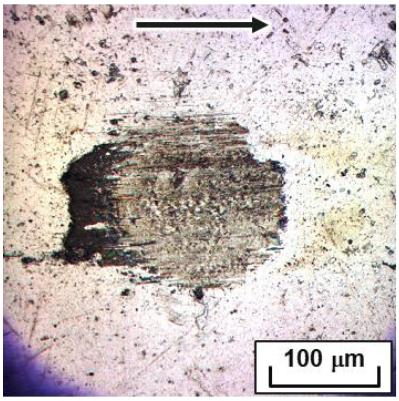

(b3)

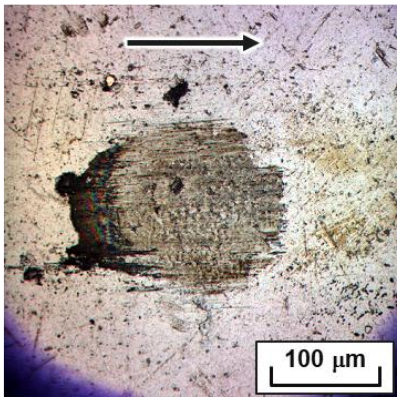

(b4)

(b) Optical microscope images of the wear scar on AISI 304

Fig. 4-25 Friction properties and transition of wear scar on AISI 304 slid against DLC coating in water.

4.4 Conclusions

In this chapter, friction tests using stainless steel ball sliding against DLC coated silicon carbide disk were conducted in water under various sliding conditions. As a result, following conclusions were achieved. Introduction of DLC coating, the water lubrication property of AISI 304 was improved.

(1) The friction coefficient of AISI 304/DLC coating varied from 0.04 to 0.14.

(2) Friction properties of AISI 304/DLC coating in water are classified into two modes as follows:

Mode I; no running-in or increasing the friction coefficient after running-in

Mode II; running-in and showing the stable friction

In Mode II, the wear scar without transfer film on stainless steel ball is dominates and nanolayer, approximate thickness is 20 nm, composed of oxygen, chromium, iron and carbon is self-formed. This indicates passive chromium oxide film is self-formed and possibility of low friction and low wear is shown.

(3) Transfer of carbon on AISI 304 is dound to be important to prevent oxidation of steel. Also, formation of hydrophilic passive film is enhanced and lower friction is generated at severe sliding condition where water film is hardly made between sliding surfaces.

References

[1] H. Fukui, J. Okida, N. Omori, H. Moriguchi, K. Tsuda, Cutting performance of DLC coated tools in dry machining aluminum alloys, Surface and Coatings Technology, 187, 1 (2004) 70–76.

[2] J. Heinrichs, M. Olsson, S. Jacobson, Initiation of galling in metal forming: differences between aluminium and austenitic stainless steel studied in situ in the SEM, Tribology Letters, 50, 3 (2013) 431–438.

[3] M. Suzuki, T. Ohana, A. Tanaka, M. Suzuki, Tribological properties of DLC films with different hydrogen contents in water environment, Diamond & Related Materials, 13, 11–12 (2004) 2216–2220.

[4] K. Yamamoto, K. Matsukado, Effect of hydrogenated DLC coating hardness on the tribological properties under water lubrication, Tribology International, 39, 12 (2006) 1609–1614.

[5] X. Wu, T. Ohana, A. Tanaka, T. Kubo, H. Nanao, I. Minami, S. Mori, Tribochemical investigation of DLC coating tested against steel in water using a stable isotopic tracer, Diamond and Related Materials, 16, 9 (2007) 1760–1764.

[6] T. Ohana, M. Suzuki, T. Nakamura, A. Tanaka, Y. Koga, Low-friction behaviour of diamond-like carbon films in a water environment, Diamond and Related Materials, 15, 4–8 (2006) 962–966.

[7] Y. Niiyama, Effect of sliding history on super-low friction of diamond-like carbon coating in water lubrication, Tribology Letters, 65, 2 (2017) 1–14.

[8] K. Noguchi, M. Kasuya, M. Mizukami, K. Kurihara, K. Adachi, Control of solid-liquid interface for increasing load-carrying capacity of water lubrication system with silicon carbide, Proceedings of the Tribology Conference 2012 Spring Tokyo, B4 (2012) 73-74 (in Japanese).

[9] K. F. McCarty, D. R. Boehme, A raman study of the systems Fe3-xCrxO4 and Fe2-xCrxO3, Journal of Solid State Chemistry, 79, 1 (1989) 19–27.

Chapter 5

Running-in Process of AISI 304 Sliding against DLC Coating

5.1 Introduction

It is said that 75% of the cause of failure or life of the mechanical device is due to wear between contact surfaces and 30% of the consumption of energy loss in automobile is caused by friction. Therefore, the control of friction and wear is recognized as an important technology directly linked to the construction of a low-carbon society. In order to clarify the mechanism of friction and wear which can not be directly viewed from the outside, it is mainly focused on estimating friction and wear mechanism based on observation and analysis of the worn surface after friction. One of the friction phenomena to be clear is the running-in behavior of friction. Figure 5-1 shows the friction behavior when indium of soft metal is supplied as a lubricant [1]. Depending on the tribo-pairs, different transfer films were formed on wear scar on ball specimen and the friction coefficient were also changed, respectively (Fig. 5-2). An example of the wear surface formed corresponds to the friction behavior. Controlling the friction behavior is equal to controlling the wear surface formed, understanding of the friction process including running-in process is an understanding of formation process of the wear surface. In-situ technique is one of the strong tools for this purpose. In-situ Raman tribometry [2] and triboscopy [3] have been proposed until now and powerful for analyzing carbon-based materials and conductive materials, respectively. Recent investigations have demonstrated that friction tester is installed into scanning electron microscope (SEM) to understand the wear of materials by observation of formation process of wear scar and generation of wear particle [4-7]. Akagami et al. made it possible to perform repeated friction tests while observing the wear scar on ball specimen shown in Fig. 5-3. Because this system is equipped with EDX analyzer, it can obtain not only the change of geometrical shape of the sample but also the changes of the elemental composition. Of course, it can obtain the value of friction force, beam which composes leaf springs which has strain gauge for friction axis is introduced.

Moreover, a positioning mechanism enabling repeatable observation and friction test is introduced (Fig. 5-4).[7]. On the other hand, since SEM is normally observed under a high vacuum environment, the environment of the friction test is limited in the in-situ SEM tribo-system. In order to clarify the effect of the atmosphere on the running-in process in detail, we newly developed in-situ ESEM tribo-system in

which a friction tester is introduced in an environment scanning electron microscope (ESEM) capable of purging water vapor into the chamber.

In the previous chapter, it was clarified that low friction was developed in a wide lubrication region by using DLC coating as the counterpart material of stainless steel. When low friction is exhibited, it can be seen that a hydrophilic nano-interface comprised of chromium, oxygen, iron and carbon is formed on stainless steel, and it is important for water lubrication of AISI 304/DLC coating combination to transfer the carbon film on the wear scar on AISI 304 at initial friction state. However, it is unclear the formation process of the wear surface on AISI 304 consisting a nanolayer in the boundary lubrication region where water films are difficult to form. Therefore, the initial period between stainless steel and DLC coating is focused by ESEM tribo-system, which can repeatedly analyze the geometry and elemental composition of the wear surface on the ball in this chapter, and the effectiveness of the ESEM tribo-system is clarified.

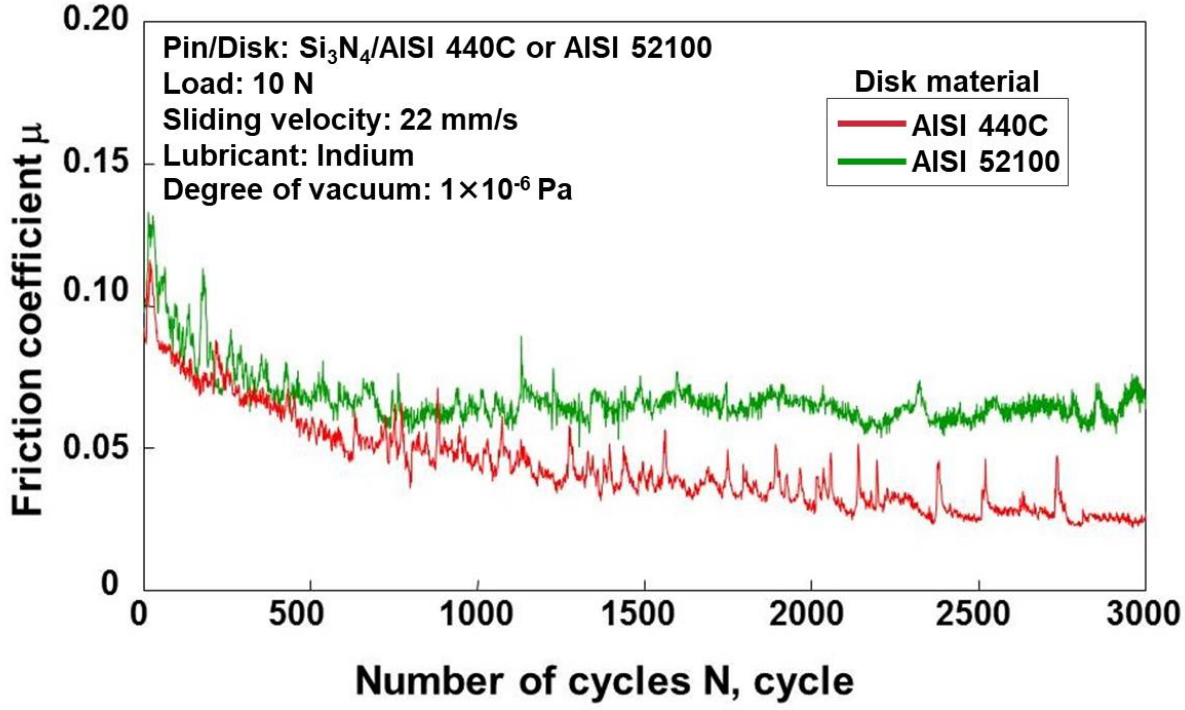

Fig. 5-1 Effect of disk material on friction properties of Si_3N_4/AISI 440C or AISI 52100 with indium [1].

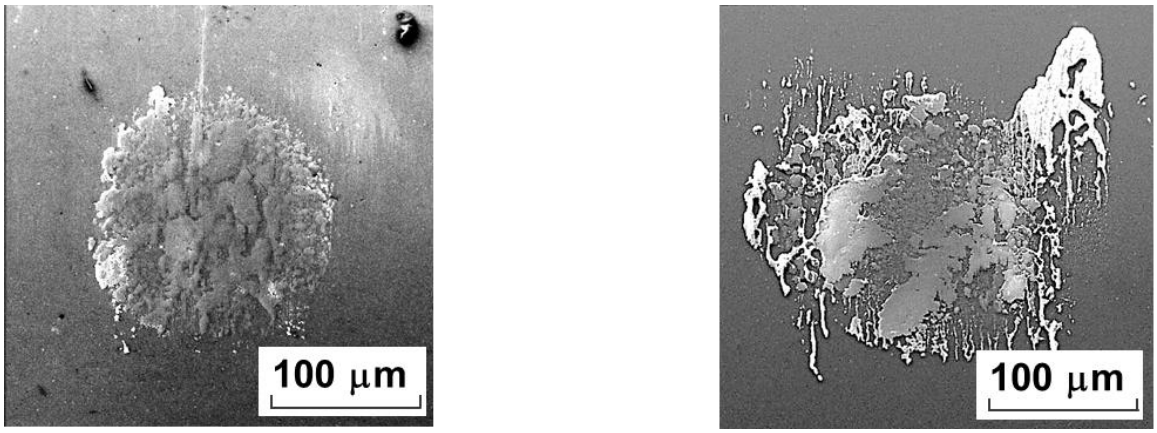

(a) Slid against AISI 440C

(a) Slid against AISI 52100

Fig. 5-2 SEM images of the Si3N4 pin (a), (b) showing the formation of transfer film after sliding against AISI 440C and AISI 52100 [1].

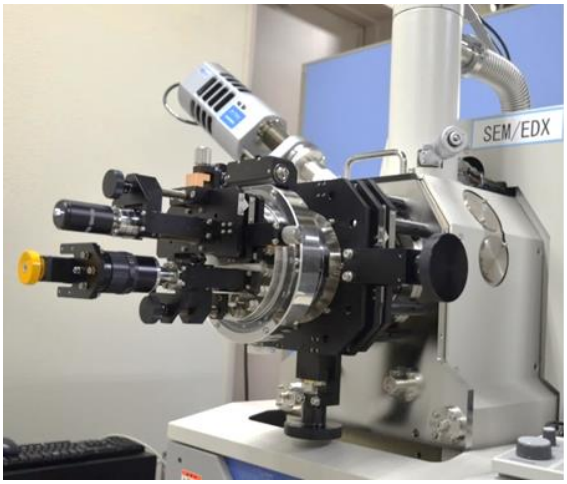

(a) Appearance

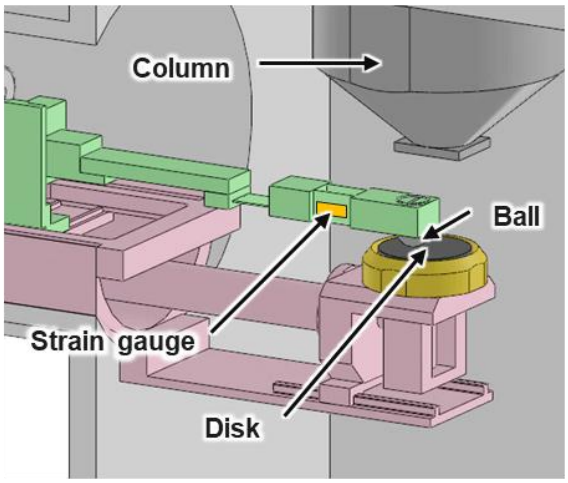

(b) Schematic illustration image of inside view

Fig. 5-3 In-situ SEM tribo-system

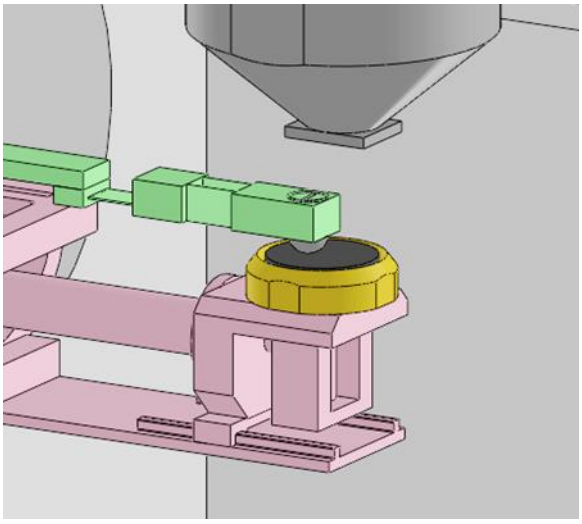

(a) Friction test position

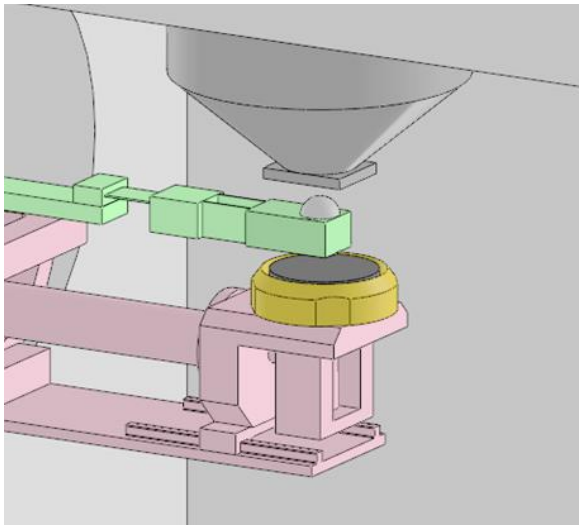

(b) Observation position

Fig. 5-4 Mechanism of semi in-situ observation of the wear scar on ball specimen.

5.2 Development of ESEM tribo-system

5.2.1 Environmental scanning electron microscope (ESEM)

The authors developed the tribo-system based ESEM (Quanta 650 FEG, Thermo Fisher SCIENTIFIC). The type of the electron gun is a Schottky gun, which is characterized by being suitable for analysis because its probe current is high, and its probe diameter is stable. A degree of vacuum ($<10^{-4}$-1000 Pa) was controlled by vacuuming using turbo molecular pomp and rotary pomp and supplying water vapor into the specimen chamber. An energy dispersive X-ray spectroscopy (EDX; EDAX Octane Plus, AMETEK Co., Ltd) was equipped with the ESEM to analyze the surface of specimen. A hygrometer (Hygroclip S, Rotronic AG) was employed to monitor the relative humidity in the chamber. The hygrometer cannot measure humidity below 0.5 %RH.

5.2.2 Ball-on-disk friction tester

Schematic illustrations of ESEM tribo-system are shown in Figs. 5-5 and 5-6. Sliding friction is generated by pressing a ball specimen against a disk specimen mounted on the rotation stage of ESEM. Rotation of the stage is performed by a speed control motor (SCM425GV-JA, ORIENTAL MOTOR Co., Ltd.) with speed reducer (4GV300B, ORIENTAL MOTOR Co., Ltd.) outside the chamber. The rotation frequency of disk was set from 0.01 to 0.03 rpm adjusted by gear ration of gearbox. A rotary encoder (K3HB-C, OMRON Co.) was employed to measure the rotation angle of stage. The rotation direction of the stage can switch between the one-way and the reciprocating rotation. The reciprocating rotation angle can be set arbitrarily. The load is applied by the tension spring (Spring constant: 0.49 N/mm) in order to increase repeatability. The load is controlled by changing the number of spacers mounted ESEM tribo-system. The frictional force is obtained by measuring the force in the tangential direction of the disk specimen with the beam type load cell（1002-0.5K, Tokyo Measuring Instruments Laboratory Co., Ltd.）.

5.2.3 Mechanism of semi in-situ observation for wear scar on ball specimen

In the case of ball-on-disk test, it is potential that ball specimen has more information about friction than disk specimen because ball specimen is longer friction time than disk specimen. In order to carry out detailed analysis of wear surface continuously, it is necessary to accurately return to the position where the friction test is finished while maintaining the wear surface after the analysis. In this apparatus, the mechanism of semi in-situ observation for wear scar on ball specimen shown in Fig. 5-7. During friction test, these parts are point contacted with each other by the spring force of the tension spring to maintain a stationary state (Fig. 5-7 (a) and (b)). When the wear scar is observed, unloading and rotating with respect to the center axis of the load cell are performed by winding wire for controlling position and load

(Fig. 5-7 (c)). When SEM observation is over, the beam with ball specimen is rotated and loading to disk specimen by unwinding these wires. By repeating these steps, the wear scar on the ball specimen can be repeatedly slid against disk specimen and observed by SEM. In previous chapter, it is clarified that the wear scar without transfer film on stainless steel ball in Mode II-II is dominated and the surface is formed of a nanolayer composed of oxygen, chromium, iron and carbon. In this chapter, it is investigated that the formation process of the wear scar on stainless steel in environments with varying humidity in order to clarify the role of water in nanolayer formation. ESEM tribo-system is a powerful tool for tracking the formation process of wear surface because it allows repeated friction testing, observation and analysis. ESEM tribo-system was used to simulate friction under boundary lubrication with almost no lubricant.

5.3 Experimental details

A ball-on-disk friction tests were conducted by ESEM tribo-system. The type of friction test was the reciprocating rotation. Load and average sliding velocity were 1.8 N and 30 μm/s, respectively. The distance of one stroke was set as 6000 μm. The degree of vacuum in the specimen chamber was set to 10 Pa, 100 Pa and 1000 Pa by purging water vapor into the chamber. Water vapor was generated from tap water. The humidity in each vacuum environment is <0.5 %RH, 0.5 %RH, 30 %RH, respectively. In addition, each value of humidity is actually measured using a hygrometer which cannot measure humidity below 0.5 %RH. AISI 304 ball (8 mm in diameter) and DLC coated SiC disk (30 mm in diameter, 4 mm in height) were used as specimens. Deposition of DLC coating is same method in section 4-2-1. All specimens were sonicated by acetone and ethanol before the friction tests. SEM observation and EDX analysis of wear scar on AISI 304 ball were carried out on sliding distance 0.01 m, 0.02 m, 0.05 m, 0.08 m and 0.12 m, respectively to focus on the initial state of friction between AISI 304 ball and DLC coating. In order to obtain the wear volume of ball specimen, the diameter of wear scar was measured by SEM image of wear scar and the calculation was applied to the formula in section 2-2-3. In calculating the friction coefficient, the raw value is converted to an absolute value and 300 points are decimated to 1 point.

.

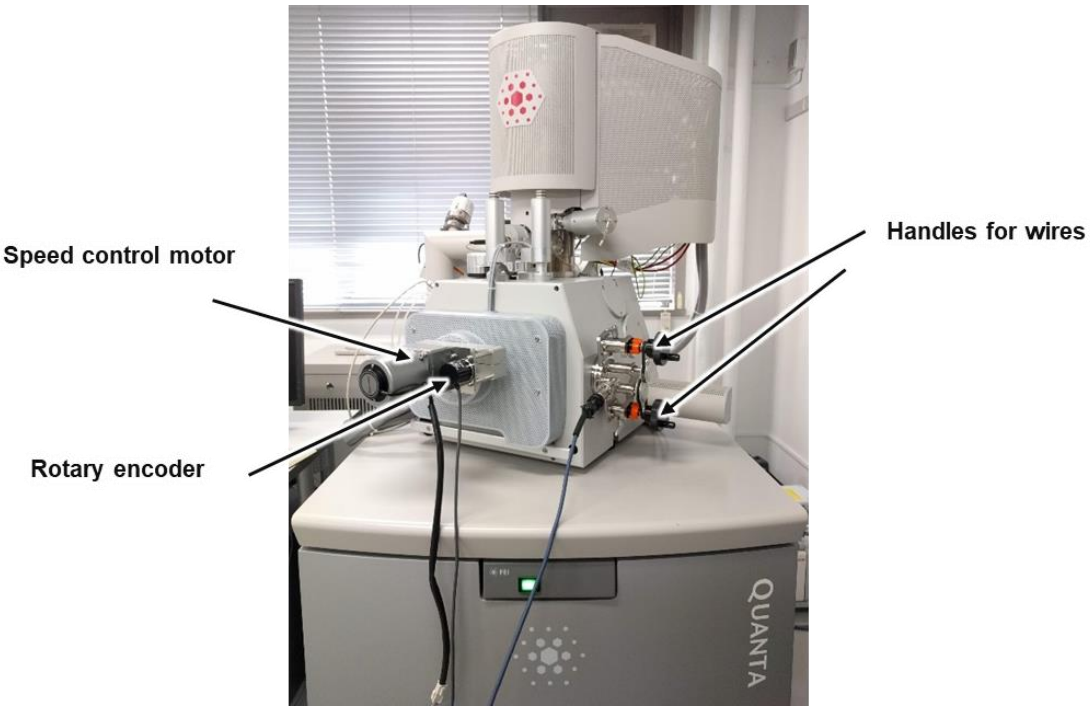

Fig. 5-5 Appearance of in-situ ESEM tribo-system.

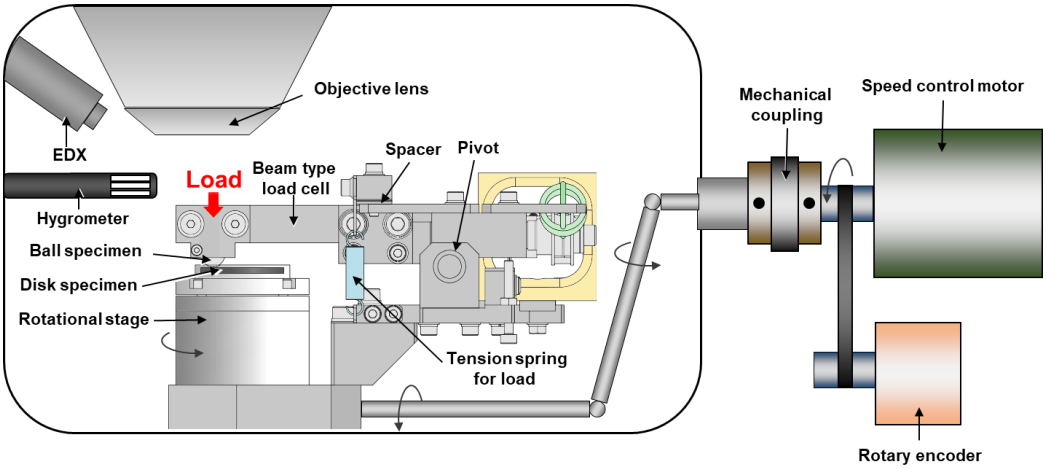

Fig. 5-6 Schematic of in-situ ESEM tribo-system.

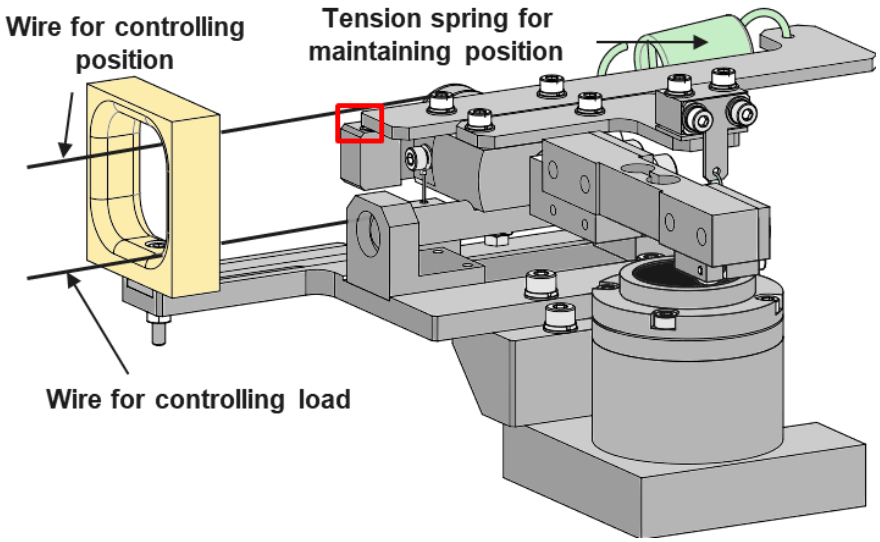

(a) Friction test state

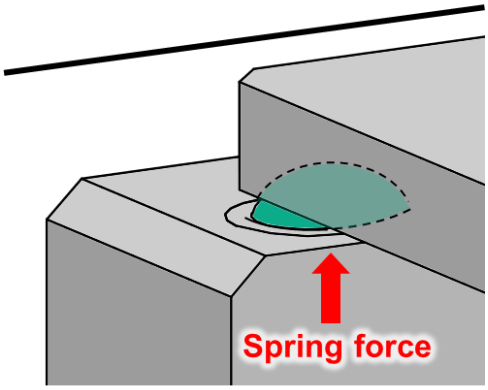

(b) Point contact of parts

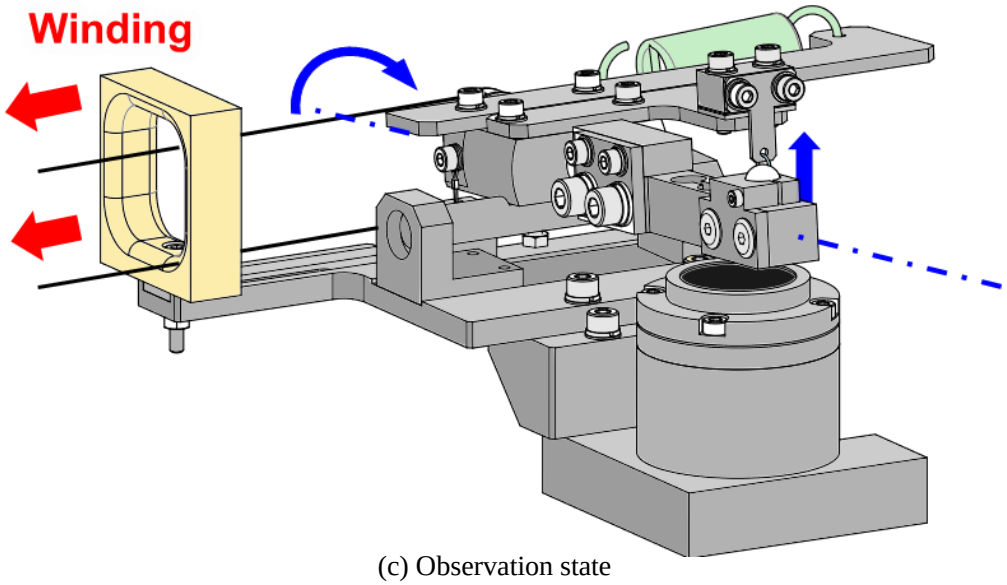

(c) Observation state

Fig. 5-7 (a) Schematic illustration of mechanism of semi in-situ observation for wear scar on ball.
(b) Magnified schematic illustration is taken from the rectangle enclosed area in Fig. 5-7 (a).
(c) Schematic illustration of observation state for wear scar on ball.

5.4 Experimental results and discussion

Figure 5-8 shows friction behavior of AISI 304/DLC coating in relative humidity of 0.5 %RH. In this condition, there is no significant change of friction coefficient. The ratio of carbon decreased from initial friction to a friction distance of 0.01 m, but then tended to increase slightly. This result indicates that carbon derived from DLC coating was transferred. In Fig. 5-9, SEM images show that the generated wear particles gradually accumulate outside the wear scar and form a smooth surface on the wear scar. Figure 5-10 shows the transition of distribution of carbon on the wear scar. This figure shows that the wear particles seen in Fig. 5-9 are carbon derived from DLC and there is a thin carbon film in the wear scar.

Figure 5-11 shows friction behavior of AISI 304/DLC coating in relative humidity of 30 %RH. The friction behavior showed a decreasing tendency of the friction coefficient up to a friction distance of 0.01 m, but after that it kept stable at a constant value. The difference from the relative humidity of 0.5% RH is that the ratio of carbon did not show an increasing tendency. In Fig. 5-12, SEM images show that the wear particles were not seen in the wear scar and form a smooth surface on the wear scar. Figs. 5-8 and 5-11 indicate that forming a smooth friction surface is one of the characteristics when DLC is used as a mating material. Form Fig. 5-13 it was possible to confirm the wear powder deposited outside the wear scar, but no clear transfer film was found on the wear scar.

Figure 5-14 shows the relationship between the relative humidity and the rate of change of carbon in the wear scar. The rate of change was obtained by fitting the atomic concentration at each point and obtaining the slope. This graph indicates that the presence of a small amount of water inhibits the transfer of carbon onto stainless steel. However, the fact that carbon is transferred in water suggests that even in water, water film was broken out and carbon was transferred at the order of the real contact point.

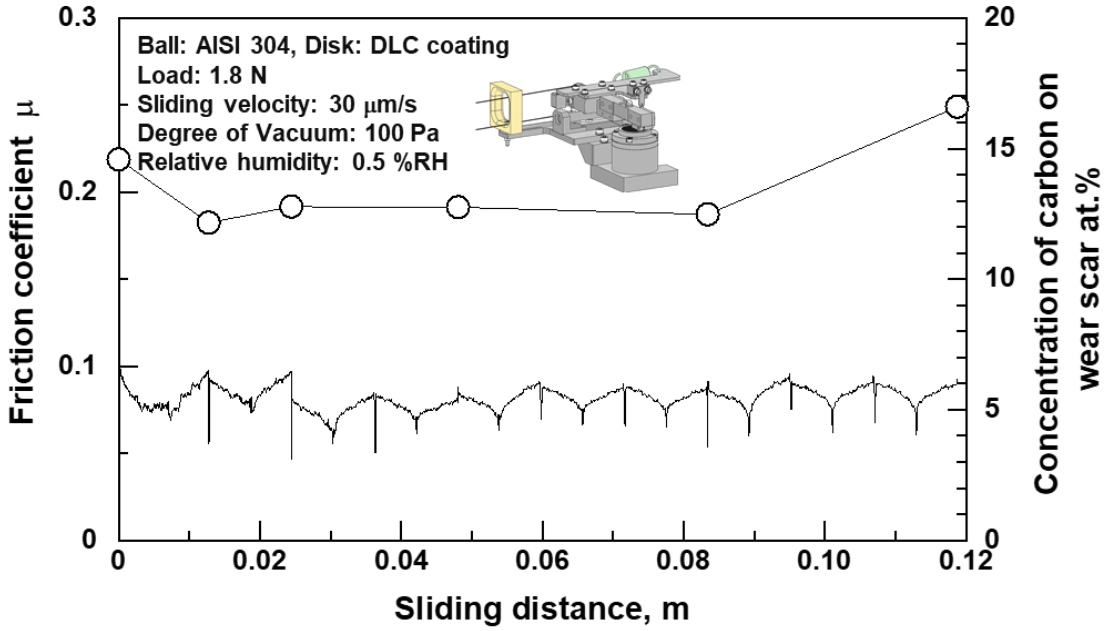

Fig. 5-8 Friction properties between AISI 304/DLC coating in vacuum of 100 Pa and change of carbon on the wear scar.

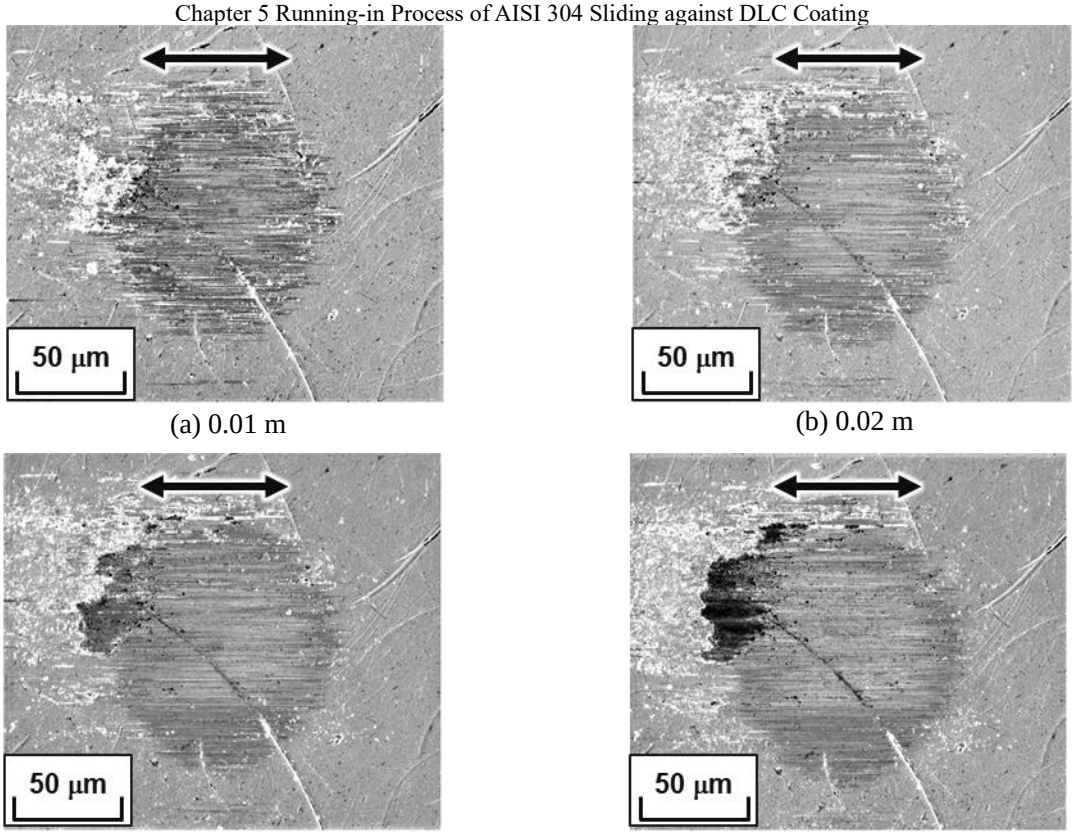

(a) 0.01 m (b) 0.02 m

(c) 0.05 m (d) 0.12 m

Fig. 5-9 Transition of wear scar on AISI 304 slid against DLC coating in vacuum of 100 Pa. Arrows show sliding direction of disk specimen.

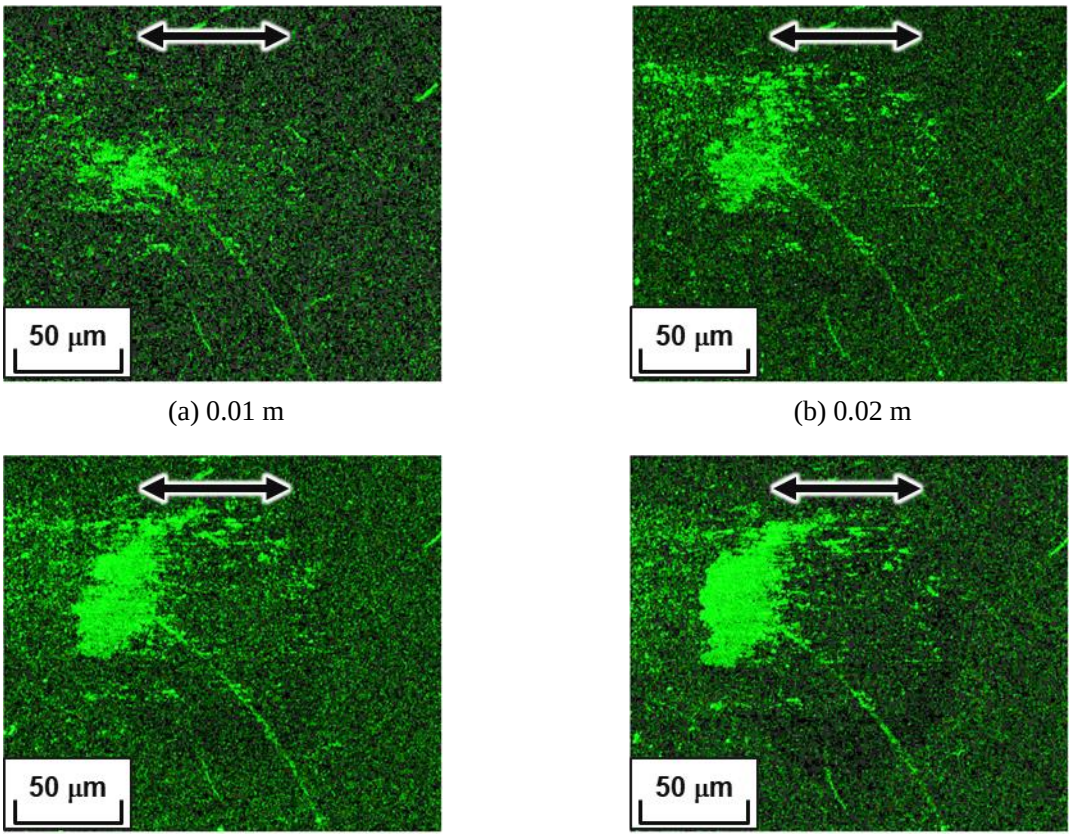

(a) 0.01 m (b) 0.02 m

(c) 0.05 m (d) 0.12 m

Fig. 5-10 Transition of distribution of carbon in wear scar on AISI 304 slid against DLC coating in vacuum of 100 Pa. Arrows show sliding direction of disk specimen.

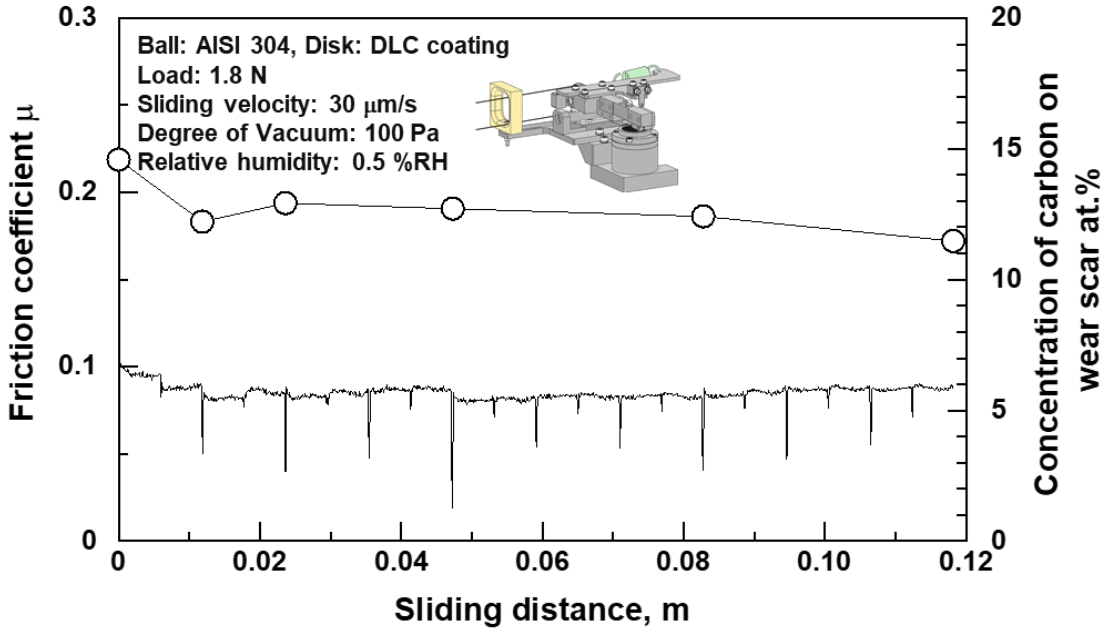

Fig. 5-11 Friction properties between AISI 304/DLC coating in vacuum of 100 Pa and change of carbon on the wear scar.

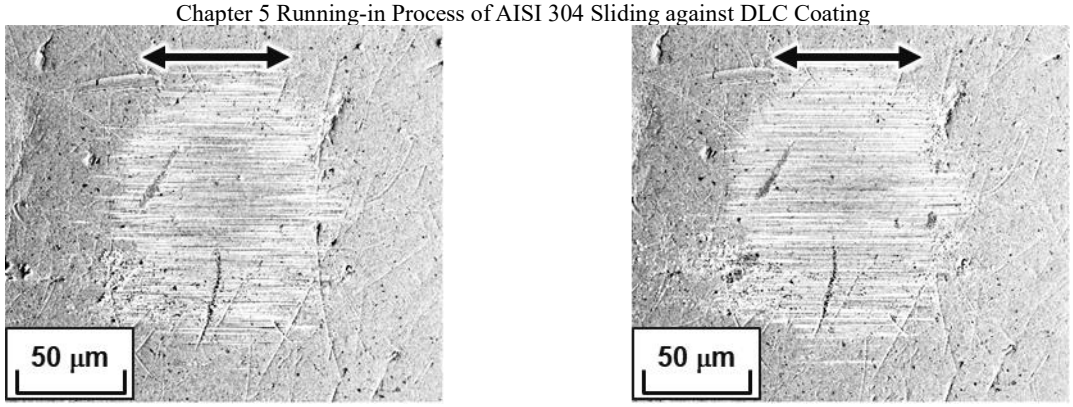

(a) 0.01 m (b) 0.02 m

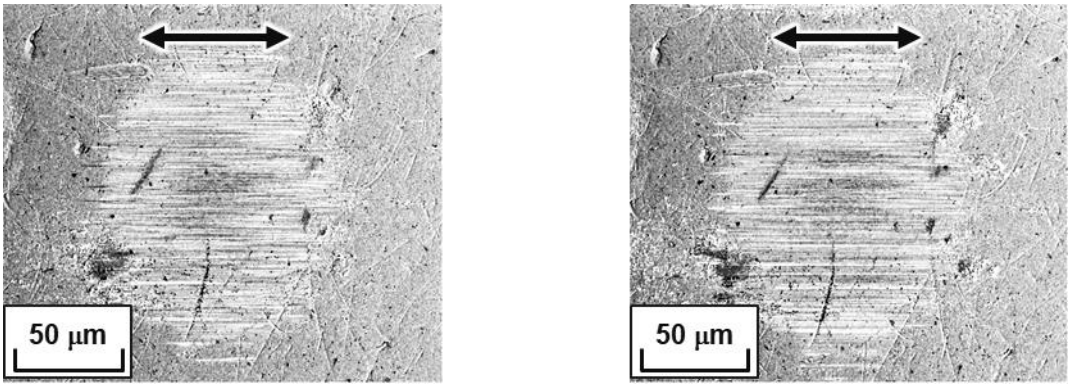

(c) 0.05 m (d) 0.12 m

Fig. 5-12 Transition of wear scar on AISI 304 slid against DLC coating in vacuum of 1000 Pa. Arrows show sliding direction of disk specimen.

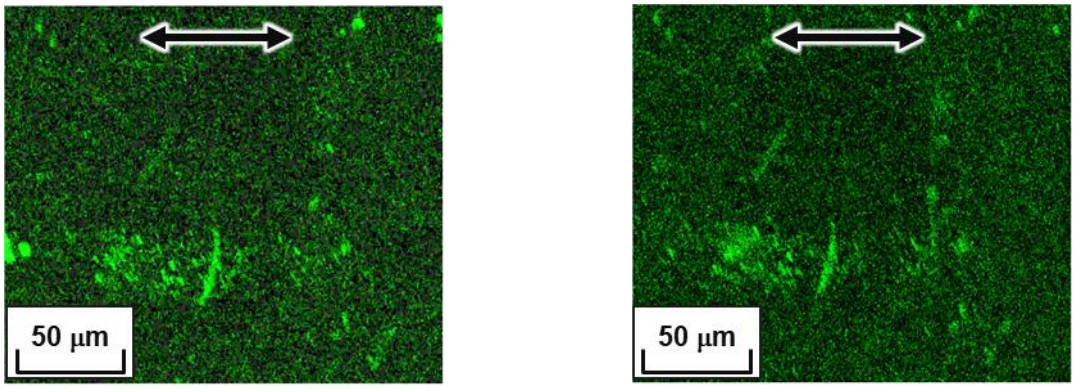

(a) 0.01 m (b) 0.02 m

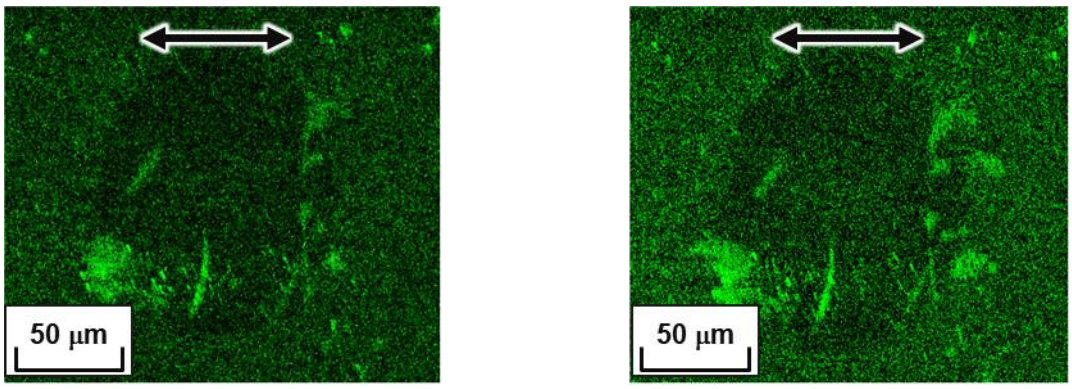

(c) 0.05 m (d) 0.12 m

Fig. 5-13 Transition of distribution of carbon in wear scar on AISI 304 slid against DLC coating in vacuum of 1000 Pa. Arrows show sliding direction of disk specimen.

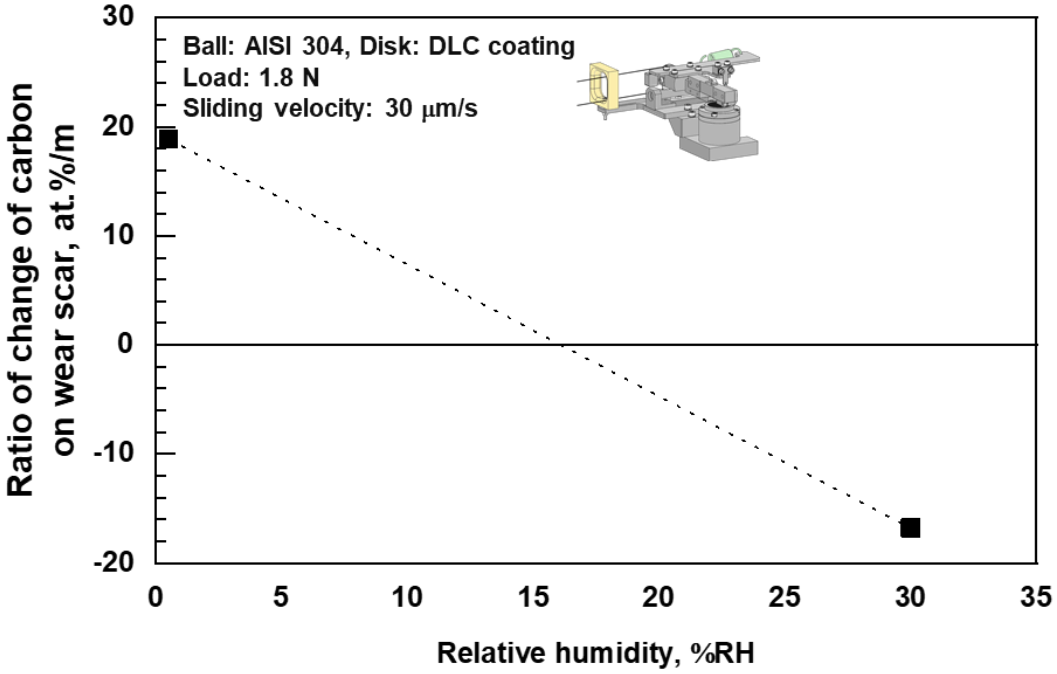

Fig. 5-14 Effect of relative humidity on wear curve of AISI 304 slid against DLC coating.

5.5 Conclusions

In this chapter, friction tests using stainless steel ball sliding against DLC coated silicon carbide disk were conducted by newly developed an ESEM-tribo system. As a result, following conclusions were achieved.

(1) We developed an ESEM tribo-system that allows in-situ observation of wear scar formed on ball specimens under controlled humidity.

(2) Small amount of water inhibits the transfer of carbon onto stainless steel.

References

[1] K. Adachi, K. Kato, In situ and on-demand lubrication by tribo-coating for space applications, Proceedings of the Institution of Mechanical Engineers, Part J: Journal of Engineering Tribology, 222, (2008) 1031–1039.

[2] T. W. Scharf, I.L. Singer, Monitoring transfer films and friction instabilities with in situ raman tribometry, Tribology Letters, 14, 1 (2003) 3–8.

[3] M. Belin, J.M. Martin, Triboscopy, a new approach to surface degradations of thin films, Wear, 156, 1 (1992) 151–160.

[4] N. Gane, F.P. Bowden, Microdeformation of solids, Journal of Applied Physics, 39, 3 (1968) 1432–1435.

[5] W. Holzhauer, F.F. Ling, In-situ SEM study of boundary lubricated contacts, Tribology Transactions, 31, 3 (1988) 360–369.

[6] W. Holzhauer, S.J. Calabrese, Steel hardness effects in boundary lubricated sliding. An in-situ SEM study, Tribology Transactions, 33, 1 (1990) 1–10.

[7] K. Akagami, T. Takeno, K. Adachi, In-situ SEM Tribosystem for analyses of running-in process, Proceedings of International Tribology Conference, Tokyo 2015, 17P–01 (2015).

Chapter 6

Formation of Low Frictional Nanointerface on AISI 304 Sliding by SiC-DLC Coating in Water

6.1 Introduction

In chapter 3, although the introduction of silicon-based ceramics as a mating material did not improve the friction characteristics, the formation of a hydrophilic nanolayer of nickel and iron on stainless steel and the improvement of the hydrophilicity on the disk side were confirmed.

In chapter 4, it was clarified that DLC coating has the potential as a mating material of stainless steel in water and that the nanolayer composed of oxygen, chromium, iron and carbon is formed on wear scar on AISI 304 ball. Therefore, it is proposed that the self-formation of nanolayer on stainless steel is the key of realizing low friction in water. The hydrophilicity on DLC coating after sliding against AISI 304 ball was improved slightly.

Based on these findings, silicon-based ceramics contributed to the improvement of the hydrophilicity of the material itself, so a new SiC-DLC coating with SiC introduced into the DLC coating was newly developed.

In previous researches, Si-DLC (a-C:Si:H) has been studied from the viewpoints of relaxation of residual stress [1] and thermal stability [2], [3] and in water it is necessary to develop lower friction when increasing silicon content in DLC has been reported Among the doped DLC coatings, The ELID grinding method is one of the methods to thicken the passive film of stainless steel [4], [5]. A positive potential is applied to the grinding wheel, and a negative potential is applied to the electrodes, and during machining, the conductive alkaline coolant is electrolytically decomposed by the potential to generate hydroxide ions (OH^-). Also in this processing method, silicon or carbon considered to be derived from the SiO_2 or diamond wheel used for the thickening passive film is included [5].

Water lubrication system using self-mated SiC is known to form amorphous nano-thick layer which consists of silicon, carbon and oxygen when low friction appears in water [6], [7]. Since this nanolayer is believed to be chemically active due to its amorphous structure, formation of amorphous silicon carbide

coating is effective to enhance chemical reaction via friction in water. Furthermore, DLC coating is believed to work as matrix to support amorphous SiC structure.

In this chapter, the aim of this study is to clarify potential of water lubrication system with stainless steel by introducing SiC-DLC coating. Besides, we discussed to propose the formation process of low frictional nanolayer in water using stainless steel and SiC-DLC coating.

6.1.1 Deposition process of SiC-DLC coating

Schematic of deposition apparatus is shown in Fig. 6-1. SiC-DLC coating was produced by PE-CVD method and DC magnetron co-sputtering of SiC target. Table 6-1 shows deposition conditions of SiC-DLC coating. Overview of the SiC-DLC disk is shown in Fig. 6-2. A surface profile curve of SiC-DLC disk is shown in Fig. 6-3. Arithmetic mean roughness is 25.9 nm. The indentation hardness of SiC-DLC coating on the SiC disk was 15.6 GPa. In order to remove the contamination, the substrate was sonicated by semiconductor cleaning solution (Semicoclean, Furuuchi Chemical Corporation) and ethanol before deposition procedures. The SiC disk was cleaned by argon ion sputtering for 20 min to remove any adsorbed materials on the surface. The total coating thickness of DLC composite on the SiC disk surface was set as 400 nm, approximately.

Figure 6-4 shows a cross-sectional image of SiC-DLC coating. SiC-DLC coating has an amorphous structure different from SiC bulk substrate.

6.1.2 Friction test conditions

Friction tests were conducted in water as shown in Fig. 2-1. AISI 304 ball and SiC-DLC coated SiC disk were used as specimens. Friction tests were performed in purified water and sliding distance was set as 100 m. Load and sliding velocity were varied from 1 N to 20 N and from 0.001 m/s to 0.5 m/s, respectively. The water temperature was kept at 20^{o}C constantly. Contact surface pressure was calculated from the dimeter of wear scar on ball specimen after friction test.

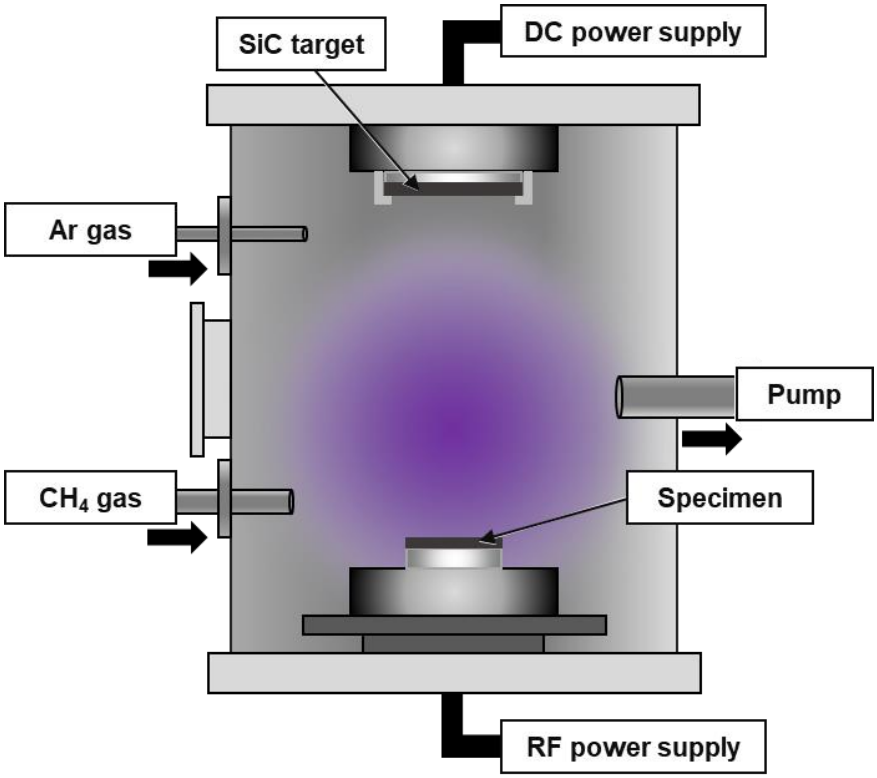

Fig. 6-1 Schematic illustration of deposition vapor deposition system.

Table 6-1 Deposition conditions of SiC-DLC coating.

Substrate cleaning	**Self bias voltage**	**-520 V**
	Gas	**Ar**
	Gas flow rate	**Ar: 10 sccm**
	Pressure	**10 Pa**
	Process time	**20 minutes**
Target cleaning	**Gas**	**Ar**
	Gas flow rate	**Ar: 10 sccm**
	Pressure	**0.9 Pa**
	Input DC	**200 W**
	Process time	**10 minutes**
Deposition of coating	**Self bias voltage**	**-420 V**
	Gas	**Ar, CH_4**
	Gas flow rate	**Ar: 10 sccm** **CH_4: 2 sccm**
	Pressure	**0.9 Pa**
	Target material	**SiC**
	Sputtering power	**200 W**
	Deposition time	**40 min.**

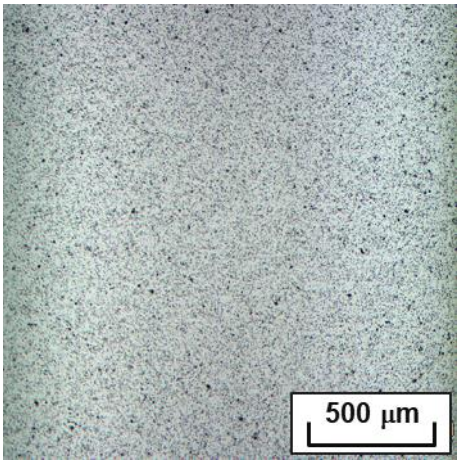

Fig. 6-2 Optical microscope images of initial surface of SiC-DLC coated SiC disk.

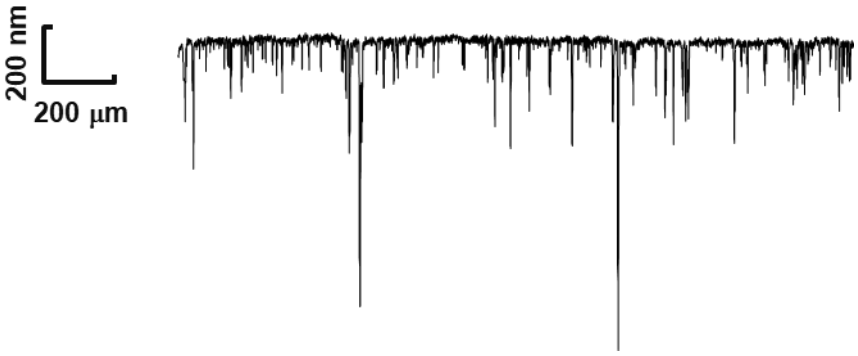

Fig. 6-3 Surface profile curve of SiC-DLC coated SiC disk.

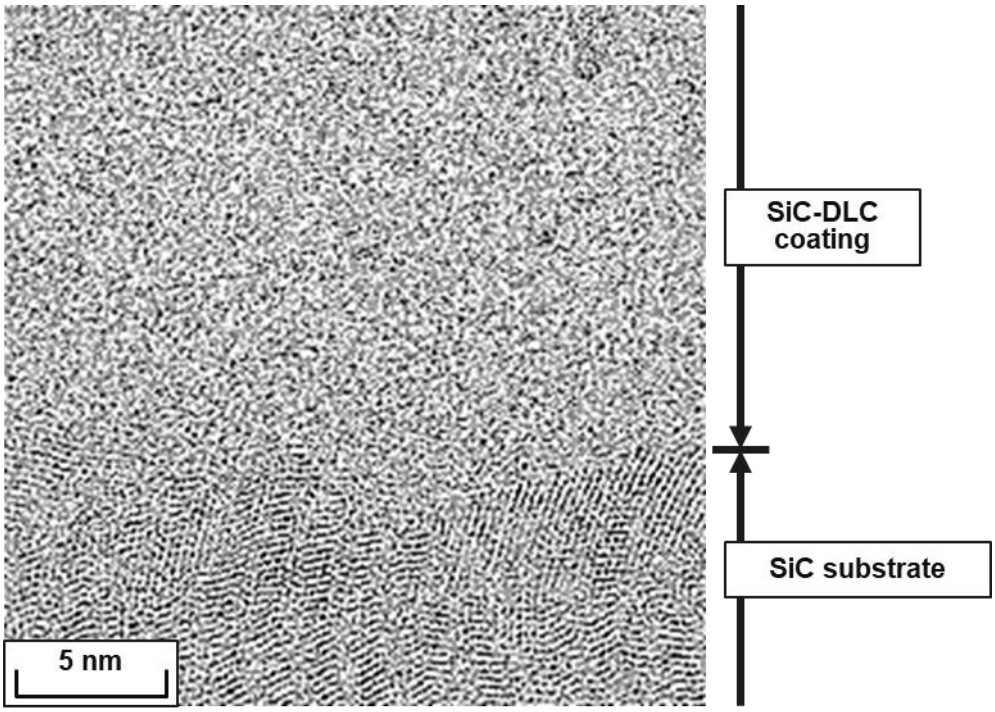

Fig. 6-4 Cross-sectional TEM image of SiC-DLC coating.

6.2 Experimental results and discussion

6.2.1 Friction property of SiC-DLC coating sliding against stainless steel

Figure 6-5 shows friction properties of AISI 304/SiC-DLC coating in water at normal load of 1 N and sliding velocity varied from 0.001 to 0.5 m/s. Figure 6-6 shows friction properties of AISI 304/SiC-DLC coating in water at normal load of 5 N and sliding velocity varied from 0.001 to 0.5 m/s. Figure 6-7 shows friction properties of AISI 304/SiC-DLC coating in water at normal load of 10 N and sliding velocity varied from 0.001 to 0.5 m/s. Figure 6-8 shows friction properties of AISI 304/SiC-DLC coating in water at normal load of 20 N and sliding velocity varied from 0.001 to 0.5 m/s. From these results, the friction test between stainless steel and SiC-DLC coating proved to show running-in under most of the conditions used in this study.

Figure 6-9 shows optical microscope images of wear scar on AISI 304 ball slid against SiC-DLC coating in water at normal load of 1 N and sliding velocity varied from 0.001 to 0.5 m/s. Figure 6-10 shows optical microscope images of wear scar on AISI 304 ball slid against SiC-DLC coating in water at normal load of 5 N and sliding velocity varied from 0.001 to 0.5 m/s. Figure 6-11 shows optical microscope images of wear scar on AISI 304 ball slid against SiC-DLC coating in water at normal load of 10 N and sliding velocity varied from 0.001 to 0.5 m/s. Figure 6-12 shows optical microscope images of wear scar on AISI 304 ball slid against SiC-DLC coating in water at normal load of 5 N and sliding velocity varied from 0.001 to 0.5 m/s. There were few transfer films on AISI 304 sliding against SiC-DLC coating compared to sliding against DLC coating, and there were many conditions with metallic luster on wear scars.

Relationship between friction coefficient and bearing characteristic number is summarized in Fig. 6-13. In the region where the bearing characteristic number is smaller than 10^{-14}, tribo-pair of AISI 304/SiC-DLC coating exhibits lower friction coefficient than tribo-pairs such as AISI 304/AISI 304, AISI 304/Si_3N_4, AISI 304/SiC, which shows the same tendency as AISI 304/DLC.

Figure 6-14 is an enlarged graph of the y axis in Fig. 6-13. AISI 304/SiC-DLC coating combination shows the lower friction than SiC/SiC combination when the value of G is less than 10^{-12}. This tendency is same as AISI 304/DLC coating combination. In addition, the friction coefficient of AISI 304/SiC-DLC coating combination exhibits lower friction slightly than AISI 304/DLC coating. This contributed to the improvement of boundary lubrication characteristics rather than DLC coating in water lubrication.

Figure 6-15 shows the specific wear rate of ball calculated from the all wear scar after the friction test under AISI 304/AISI 304, AISI 304/Si_3N_4, AISI 304/SiC, AISI 304/DLC coating and AISI 304/SiC-DLC

coating combinations in water as a function of products of initial contact pressure P_i and sliding velocity V, which is proportional to the initial input energy. When SiC-DLC coating was used as mating material of AISI 304 ball, the AISI 304/SiC- DLC coating combination succeeded in significantly reducing specific wear rate of AISI 304 ball as same level to AISI 304/DLC coating. The specific wear rate of ball under AISI 304/DLC coating varied from 10^{-8} $mm^3/N{\cdot}m$ to 10^{-6} $mm^3/N{\cdot}m$.

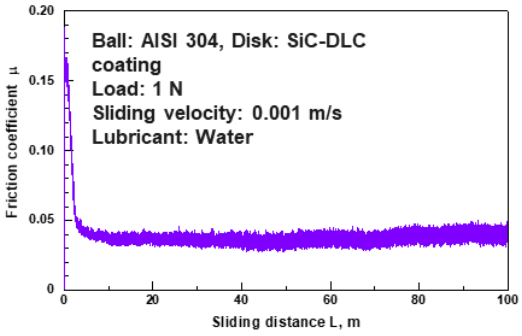

(a) 0.001 m/s

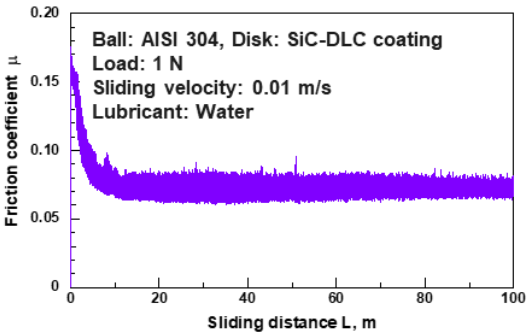

(b) 0.01 m/s

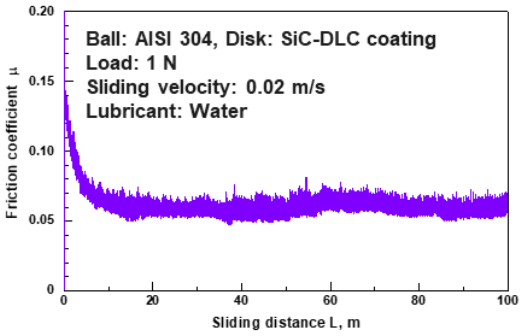

(c) 0.02 m/s

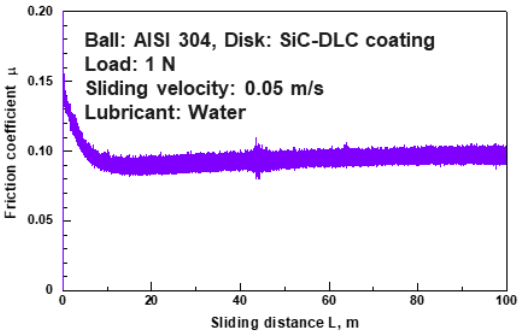

(d) 0.05 m/s

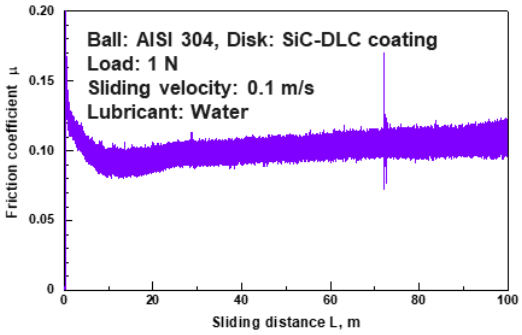

(e) 0.1 m/s

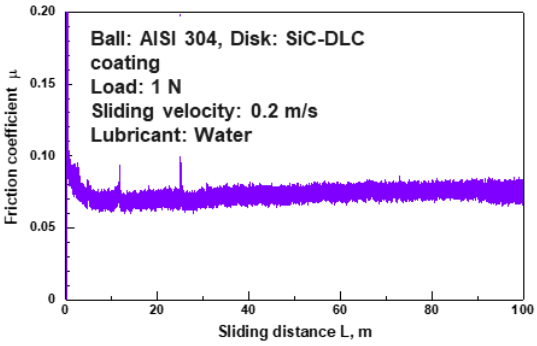

(f) 0.2 m/s

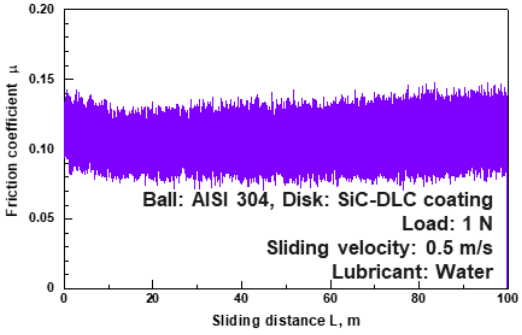

(g) 0.5 m/s

Fig. 6-5 Friction properties of AISI 304 sliding against SiC-DLC in water at load 1 N and sliding velocity (a) 0.001 m/s, (b) 0.01 m/s, (c) 0.02 m/s, (d) 0.05 m/s, (e) 0.1 m/s, (f) 0.2 m/s and (g) 0.5 m/s.

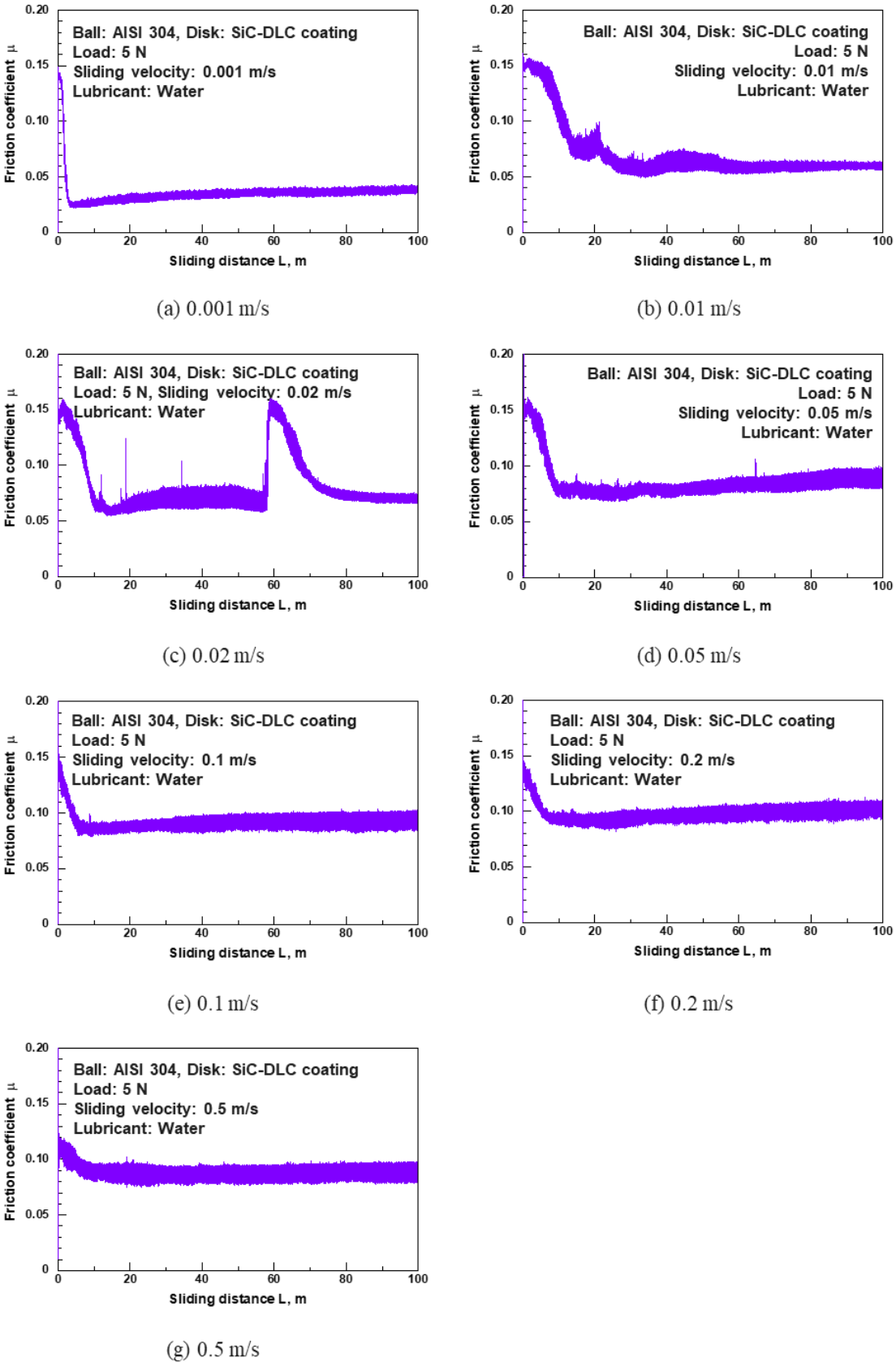

Fig. 6-6 Friction properties of AISI 304 sliding against SiC-DLC in water at load 5 N and sliding velocity (a) 0.001 m/s, (b) 0.01 m/s, (c) 0.02 m/s, (d) 0.05 m/s, (e) 0.1 m/s, (f) 0.2 m/s and (g) 0.5 m/s.

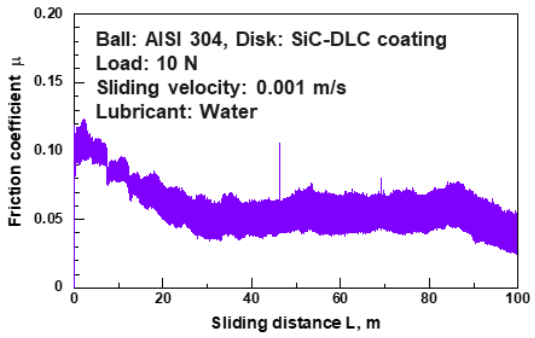

(a) 0.001 m/s

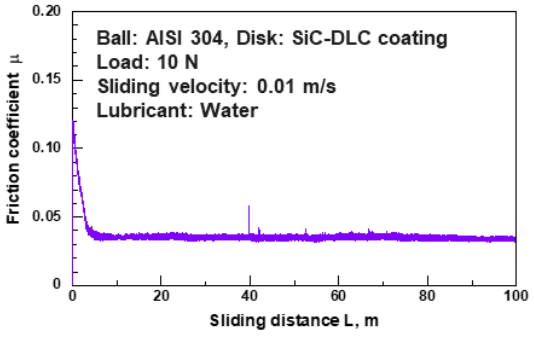

(b) 0.01 m/s

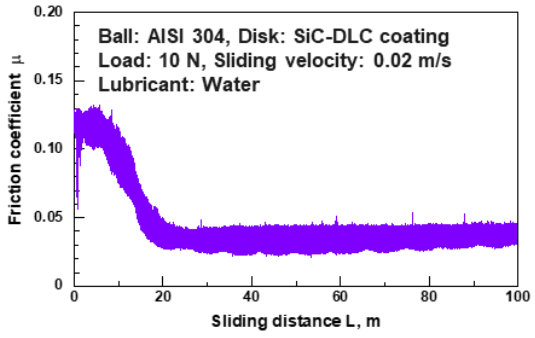

(c) 0.02 m/s

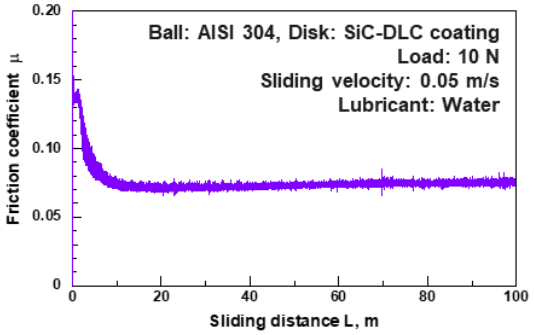

(d) 0.05 m/s

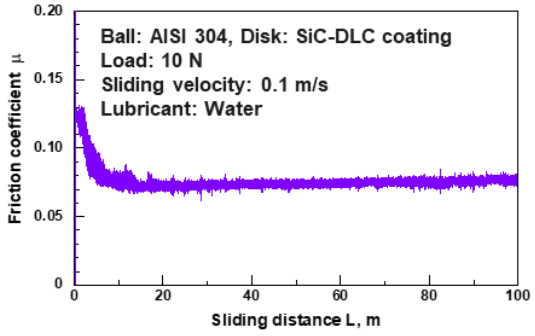

(e) 0.1 m/s

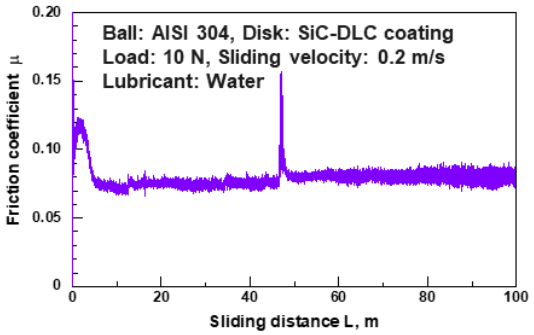

(f) 0.2 m/s

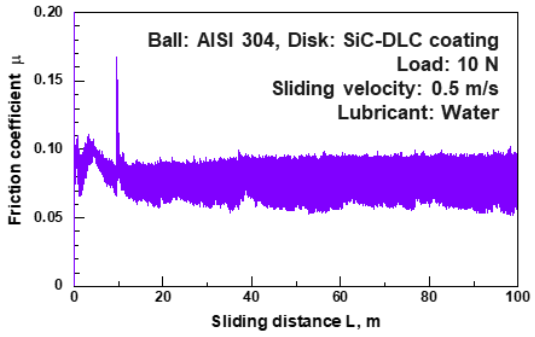

(g) 0.5 m/s

Fig. 6-7 Friction properties of AISI 304 sliding against SiC-DLC in water at load 10 N and sliding velocity (a) 0.001 m/s, (b) 0.01 m/s, (c) 0.02 m/s, (d) 0.05 m/s, (e) 0.1 m/s, (f) 0.2 m/s and (g) 0.5 m/s.

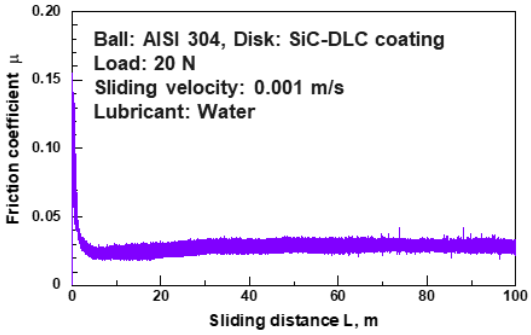

(a) 0.001 m/s

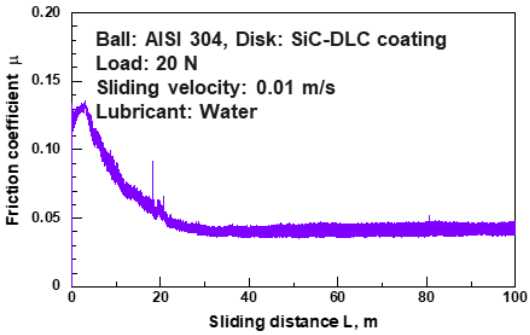

(b) 0.01 m/s

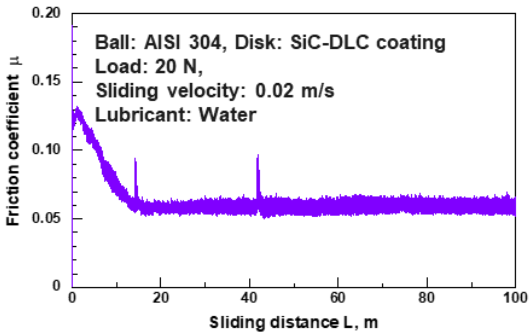

(c) 0.02 m/s

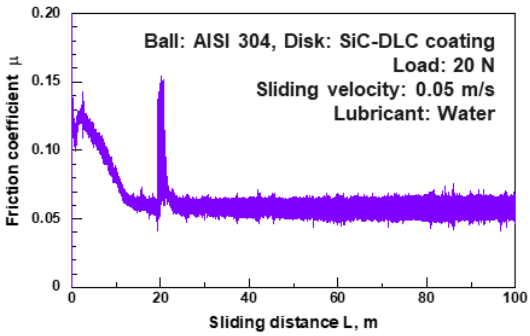

(d) 0.05 m/s

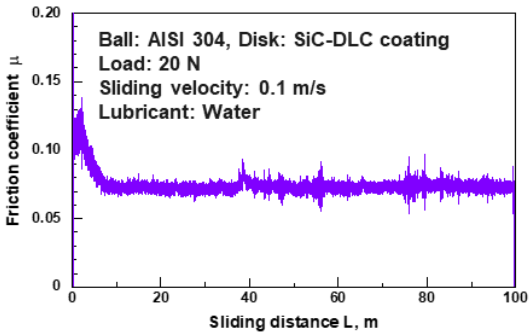

(e) 0.1 m/s

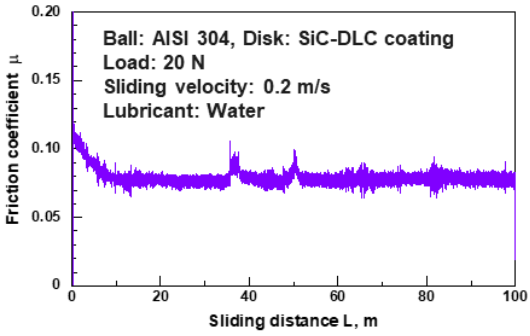

(f) 0.2 m/s

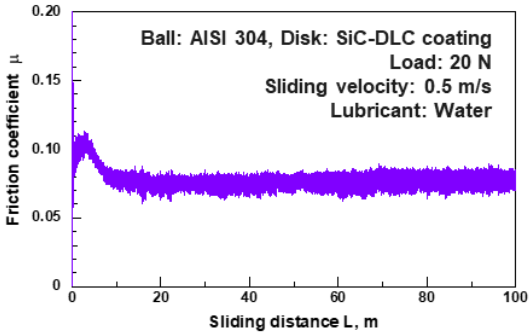

(g) 0.5 m/s

Fig. 6-8 Friction properties of AISI 304 sliding against SiC-DLC in water at load 20 N and sliding velocity (a) 0.001 m/s, (b) 0.01 m/s, (c) 0.02 m/s, (d) 0.05 m/s, (e) 0.1 m/s, (f) 0.2 m/s and (g) 0.5 m/s.

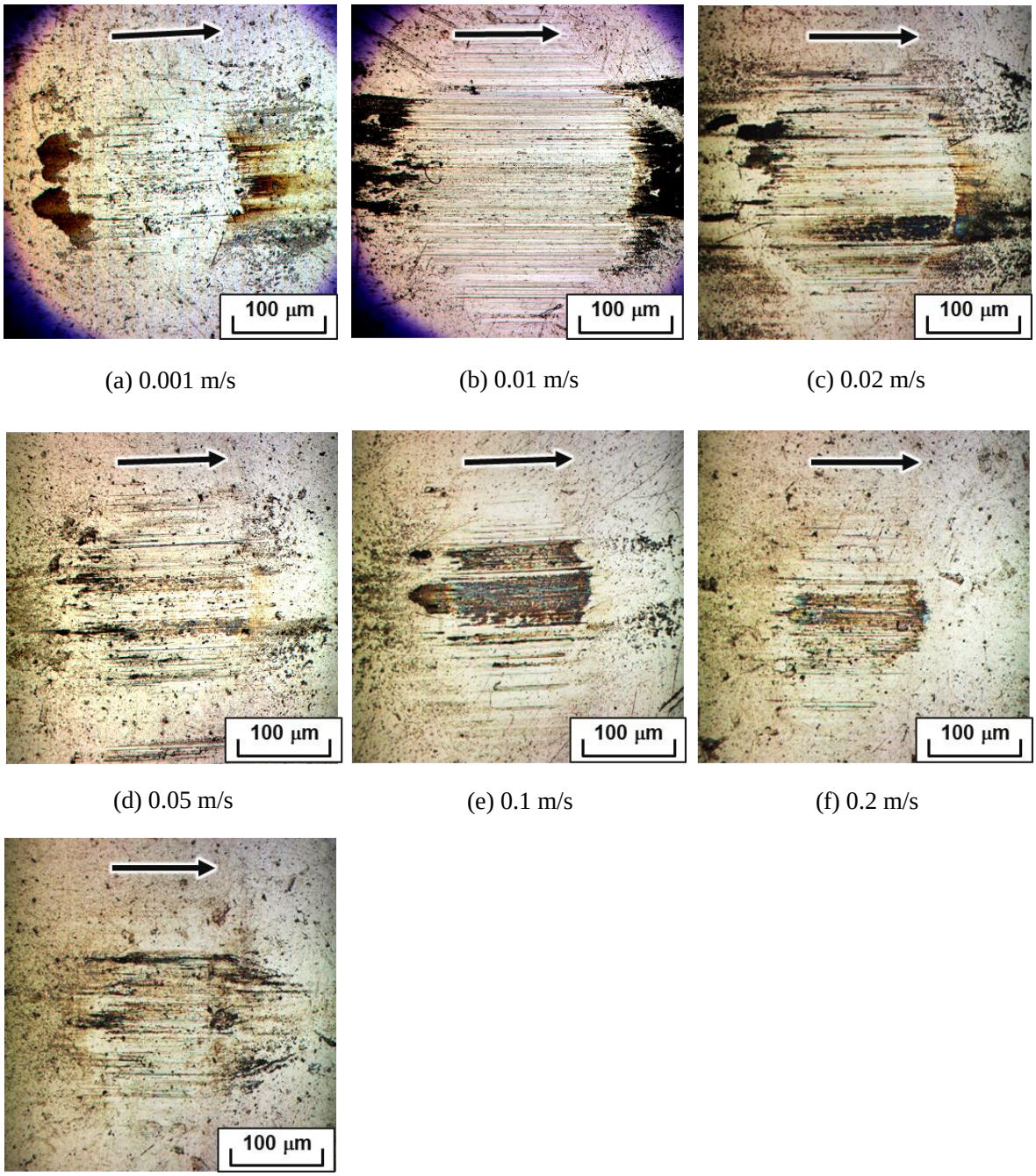

(a) 0.001 m/s (b) 0.01 m/s (c) 0.02 m/s

(d) 0.05 m/s (e) 0.1 m/s (f) 0.2 m/s

(g) 0.5 m/s

Fig. 6-9 Optical microscope images of wear scar on AISI 304 ball sliding against SiC-DLC in water at load 1 N and sliding velocity (a) 0.001 m/s, (b) 0.01 m/s, (c) 0.02 m/s, (d) 0.05 m/s, (e) 0.1 m/s, (f) 0.2 m/s and

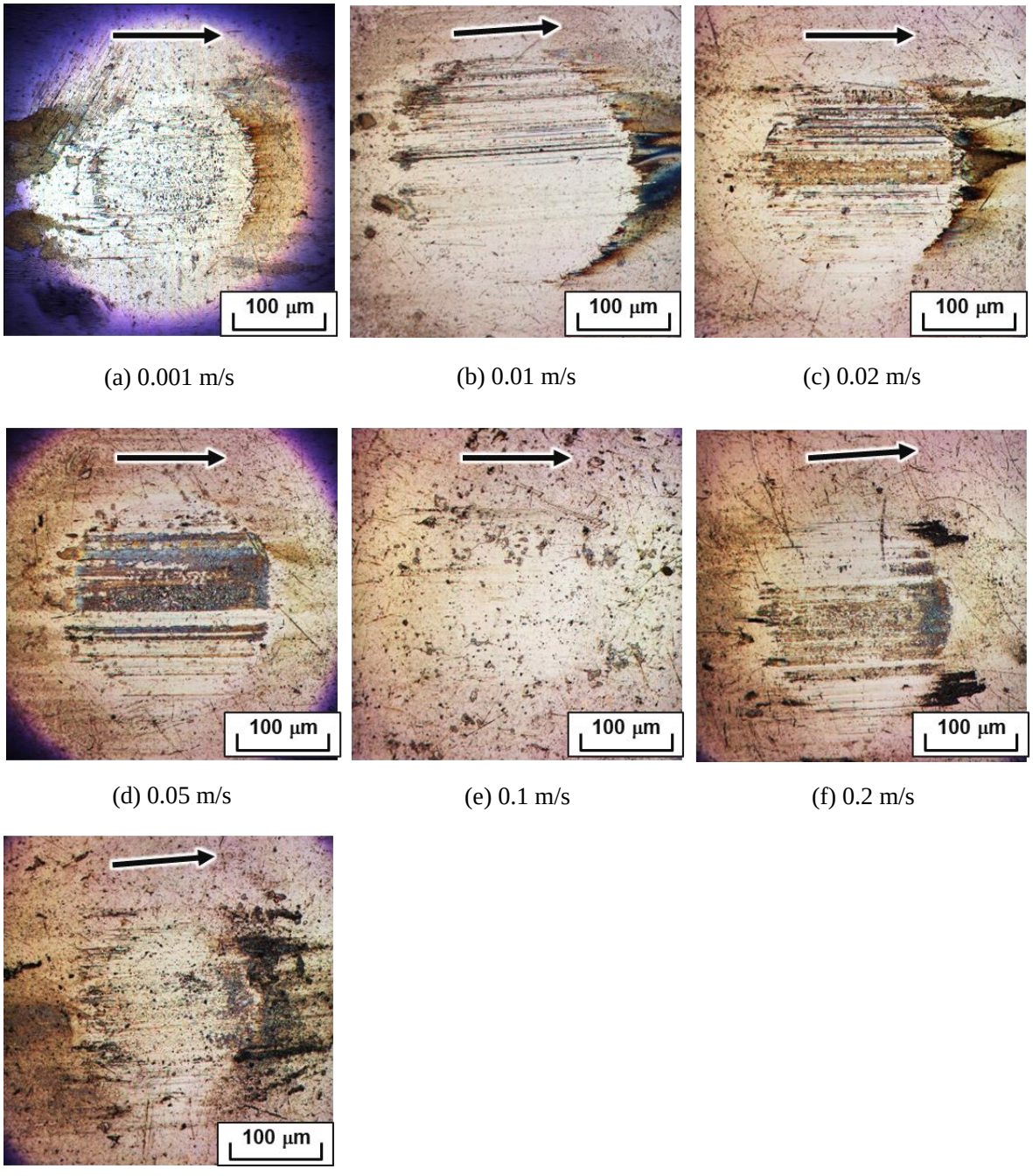

(a) 0.001 m/s (b) 0.01 m/s (c) 0.02 m/s

(d) 0.05 m/s (e) 0.1 m/s (f) 0.2 m/s

(g) 0.5 m/s

Fig. 6-10 Optical microscope images of wear scar on AISI 304 ball sliding against SiC-DLC in water at load 5 N and sliding velocity (a) 0.001 m/s, (b) 0.01 m/s, (c) 0.02 m/s, (d) 0.05 m/s, (e) 0.1 m/s, (f) 0.2 m/s and (g) 0.5 m/s.

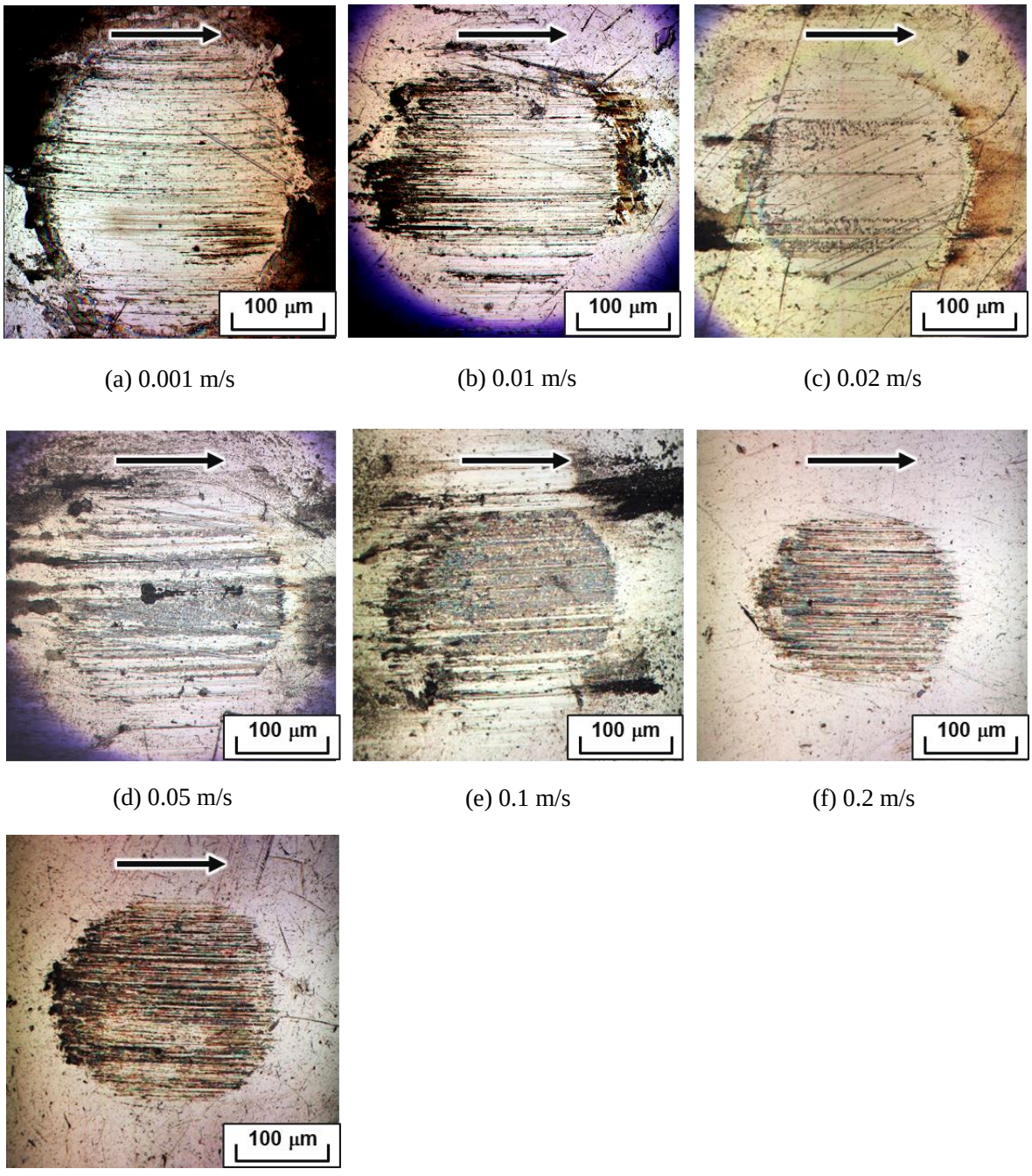

(a) 0.001 m/s (b) 0.01 m/s (c) 0.02 m/s

(d) 0.05 m/s (e) 0.1 m/s (f) 0.2 m/s

(g) 0.5 m/s

Fig. 6-11 Optical microscope images of wear scar on AISI 304 ball sliding against SiC-DLC in water at load 10 N and sliding velocity (a) 0.001 m/s, (b) 0.01 m/s, (c) 0.02 m/s, (d) 0.05 m/s, (e) 0.1 m/s, (f) 0.2 m/s and (g) 0.5 m/s.

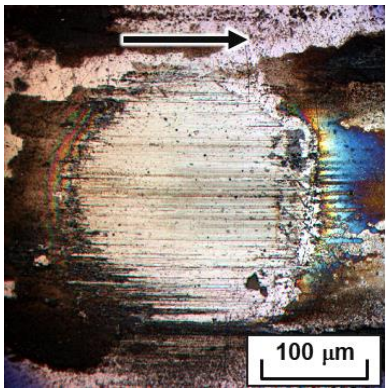

(a) 0.001 m/s

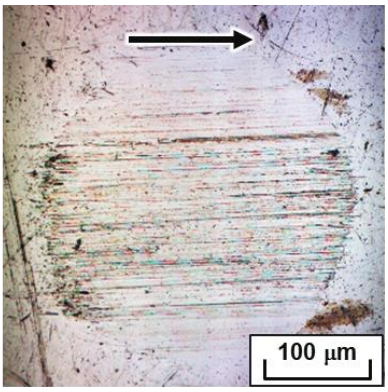

(b) 0.01 m/s

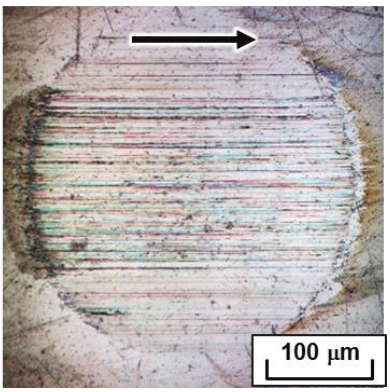

(c) 0.02 m/s

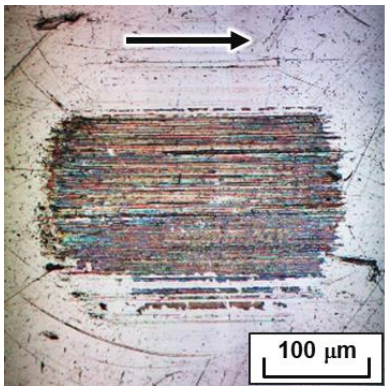

(d) 0.05 m/s

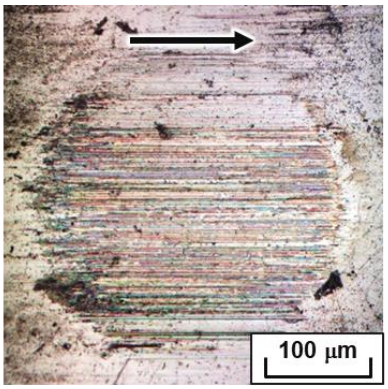

(e) 0.1 m/s

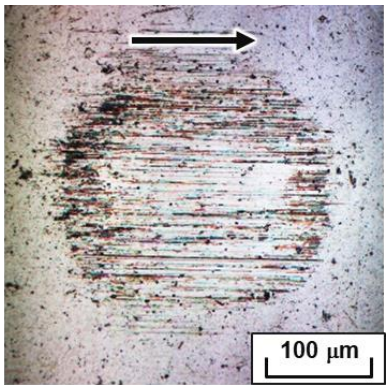

(f) 0.2 m/s

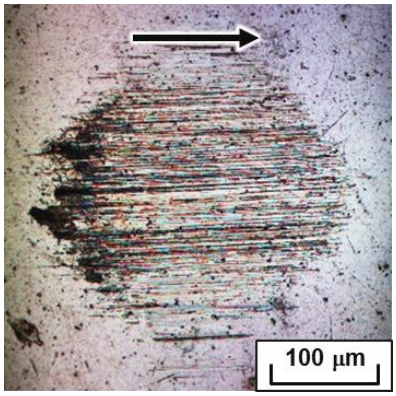

(g) 0.5 m/s

Fig. 6-12 Optical microscope images of wear scar on AISI 304 ball sliding against SiC-DLC in water at load 20 N and sliding velocity (a) 0.001 m/s, (b) 0.01 m/s, (c) 0.02 m/s, (d) 0.05 m/s, (e) 0.1 m/s, (f) 0.2 m/s and (g) 0.5 m/s.

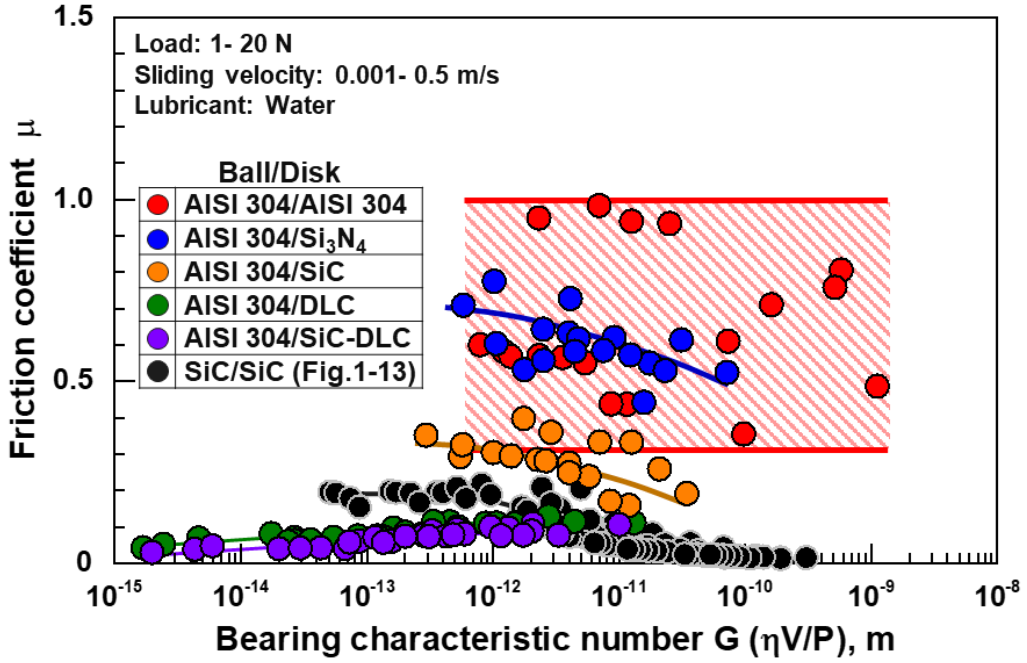

Fig. 6-13 Relationship between bearing characteristic number and average friction coefficient of AISI 304/AISI 304, AISI 304/Si3N4, AISI 304/DLC coating and AISI 304/SiC-DLC coating in water.

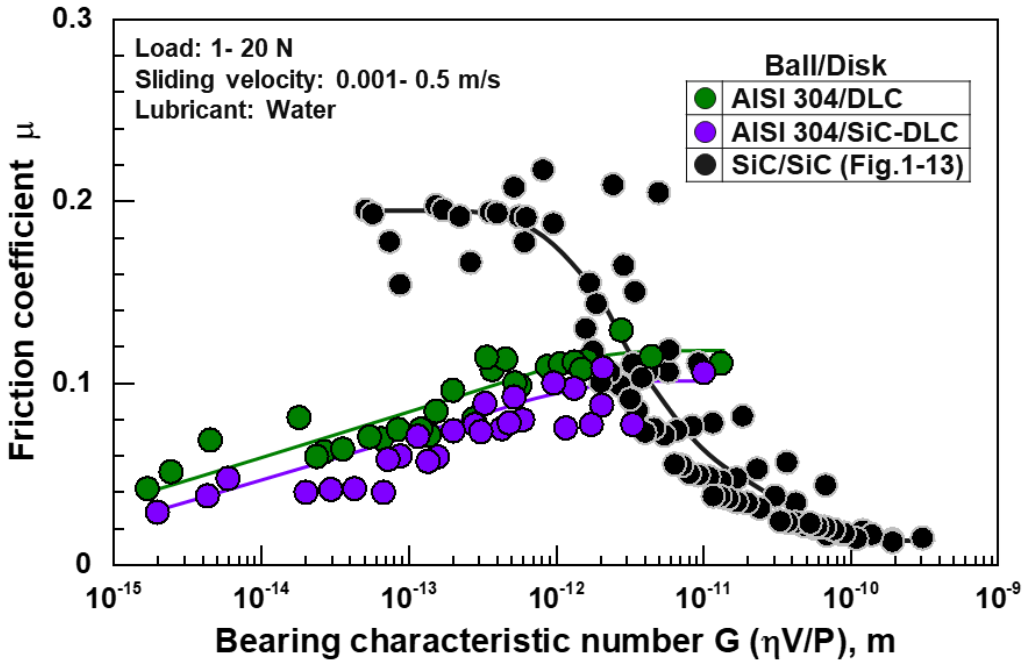

Fig. 6-14 Relationship between bearing characteristic number and average friction coefficient of AISI 304/DLC coating and AISI 304/SiC-DLC coating in water.

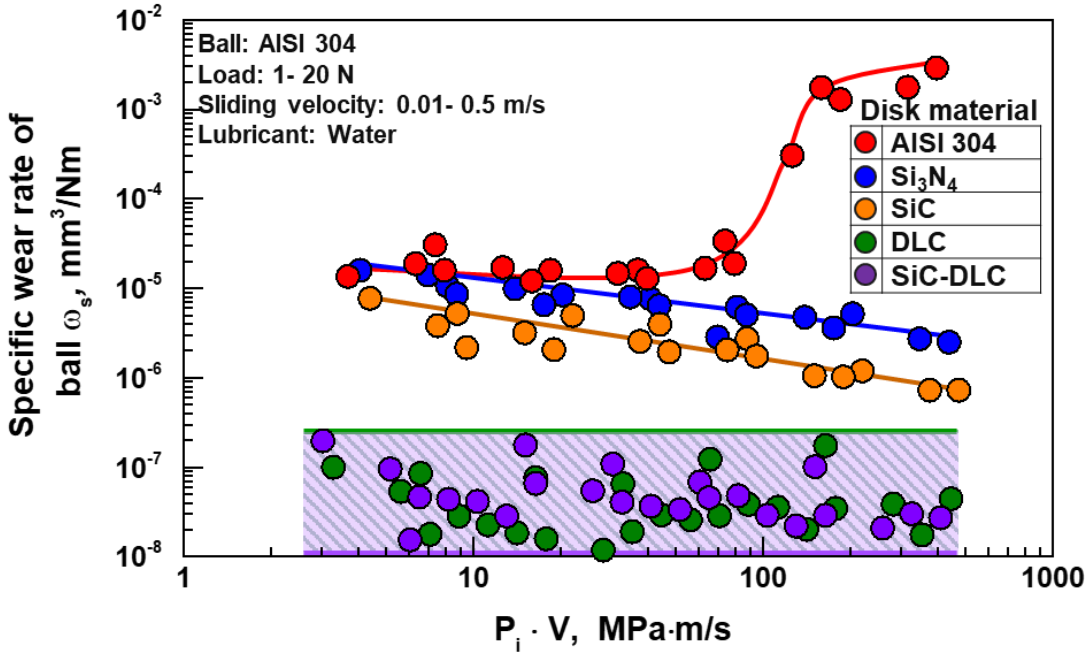

Fig. 6-15 Relationship between the value of P_iV and the specific wear rate of AISI 304 ball sliding against AISI 304, Si_3N_4, SiC, DLC coating and SiC-DLC coating in water.

6.2.2 Friction modes of stainless steel sliding against SiC-DLC coating in water

Friction properties of AISI 304/SiC-DLC coating are classified into two modes as follows:

Mode I; no running-in or increasing the friction coefficient after running-in (6.1)

Mode II; running-in behavior and showing the stable friction coefficient (6.2)

The arrangement of these friction modes is shown in Fig. 6-16. As shown in Fig. 6-16, it can be seen that Mode II exhibits at high contact pressure and low sliding velocity conditions. In other words, it indicates that it is a friction mode dependent on the function of v/P. By introducing SiC-DLC coating as counter material of AISI 304, the region of running-in behavior is expanded compared to tribo-pair of AISI 304/DLC coating.

Optical microscope images of the wear scar on AISI 304 ball sliding against SiC-DLC coating in water are shown in Fig. 6-17. All of wear scars after friction tests were classified according to the amount of transfer film inside the contact area. Binarization was performed in the circle area of radius 40 μm on a side at the center of the wear scar on AISI 304 ball, and the area of threshold 165 or more was made the area without transfer film. In Mode II, there are cases where the transfer film is formed on the wear scar (Fig. 6-17 (a)) and where it is difficult to form (Fig. 6-17 (b)). Figure 6-18 shows the relationship between the area ratio without transfer film and the coefficient of friction. The friction coefficient shows below 0.07 when the area ratio exceeds 60%.

Moreover, Mode II are classified into two modes as follows:

Mode I; no running-in or increasing the friction coefficient after running-in (6.3)

Mode II; running-in behavior and showing the stable friction coefficient (6.4)

From these results, it is important for developing a low friction in water that the wear scar like Mode II-II is formed in the case of AISI 304/SiC-DLC coating.

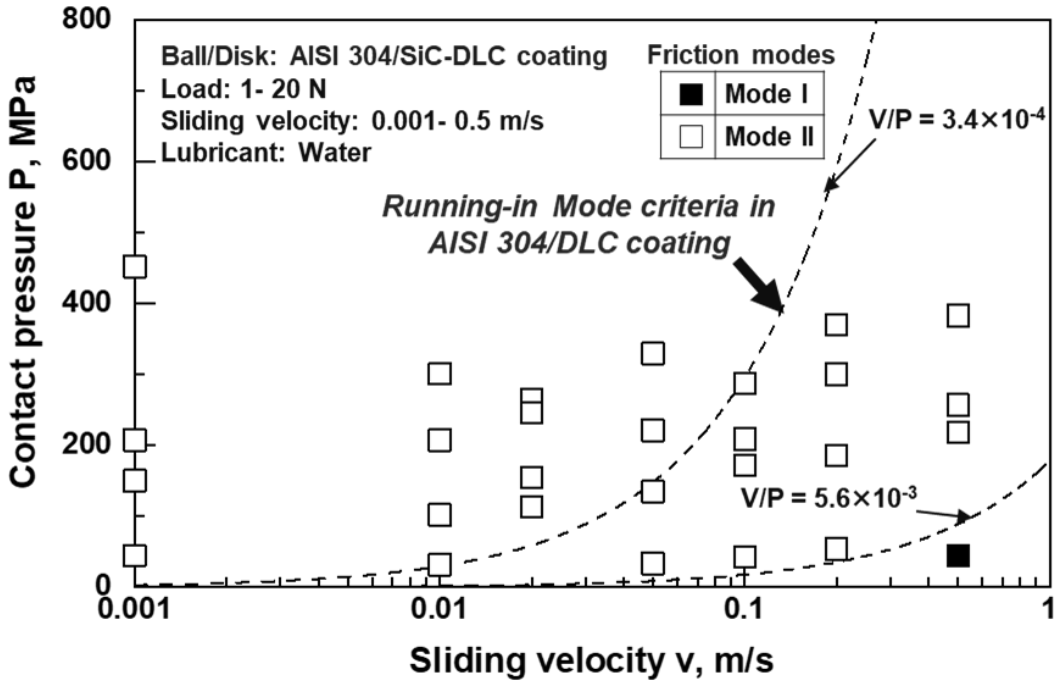

Fig. 6-16 Distributions of the friction modes of AISI 304/SiC-DLC coating in water of Mode I and Mode II as functions of sliding velocity and contact pressure. Dashed line shows the friction mode boundary in AISI 304/DLC coating in water.

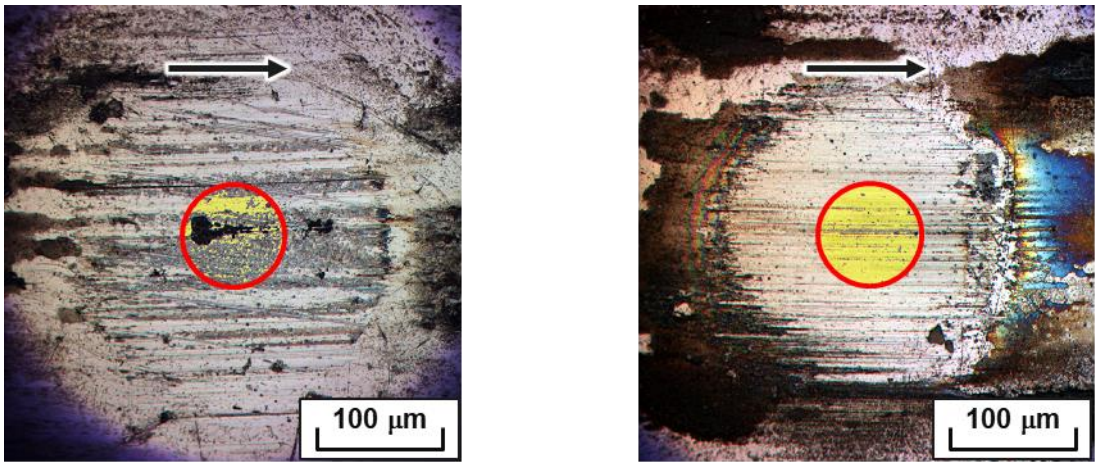

(a) (b)

Fig. 6-17 Optical microscope images of the wear scar on AISI 304 balls sliding against SiC-DLC coating in water in Mode II; (a) Load: 10 N, sliding velocity: 0.05 m/s and (b) Load: 20 N, sliding velocity: 0.001 m/s. Yellow area shows the wear scar without transferred-film. Arrows show the sliding direction of the counter material.

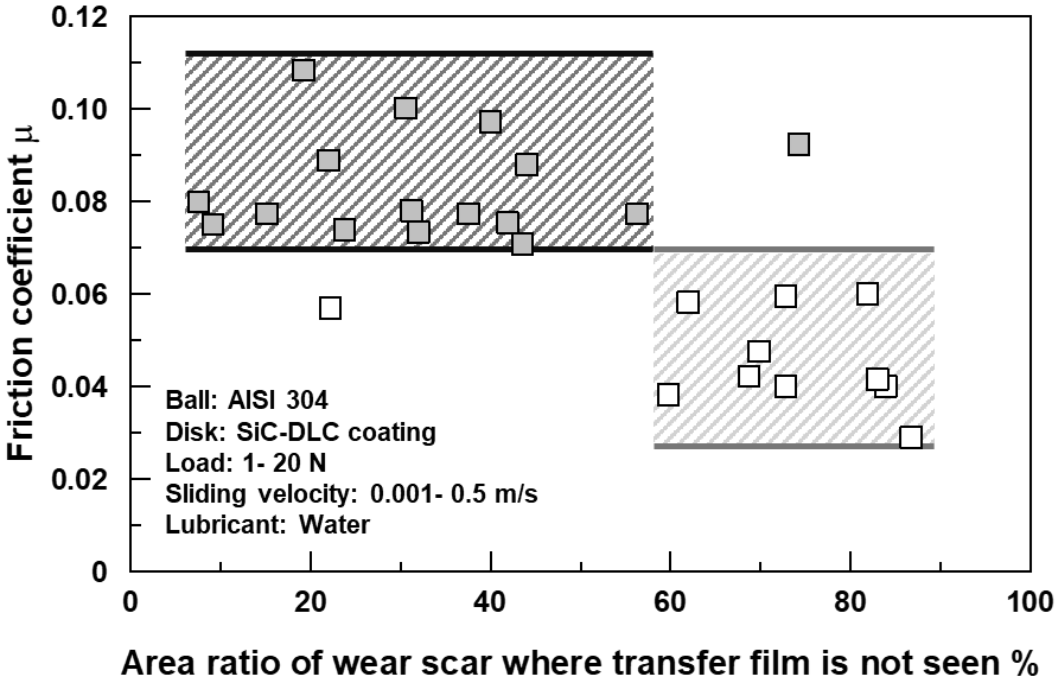

Fig. 6-18 Distribution of the Mode II of AISI 304/SiC-DLC coating in water as function of friction coefficient and the rate of wear scar without transfer film.

6.2.3 Generation of low friction in water under boundary lubrication regime

Figure 6-19 shows Stribeck curve which shows friction coefficient as a function of bearing characteristic number G in the cases of AISI 304/DLC coating and AISI 304/SiC-DLC coating in water. G indicates the thickness of water film relatively. In other words, the friction couple of AISI 304/SiC-DLC coating in water exhibits lower friction in areas where it is difficult to form a water film. And, in any regime where the experiment was conducted, it is possible to express lower friction than AISI 304/DLC coating in water.

Thus, in order to consider the reason for low friction in the boundary region where water film is difficult to form, the contact angle of water droplet on the wear scar on AISI 304 ball after friction test was obtained. To remove the effect of the friction products like wear particles, cleaning the surface of wear scar with acetone was performed. The result of comparing the contact angle before and after cleaning with acetone is Fig. 6-20. The average contact angle of Mode II-I is 53 degrees, but the average contact angle of Mode II-II, which shows a friction coefficient of 0.07 or less, is 42 degrees, indicating that the hydrophilization is progressing further in Mode II-II. Considering the meaning of the contact angle after cleaning, it is understood that it suggests the chemical state of the solid friction surface, not the friction product that can be easily removed with acetone. And it can be seen that such a solid hydrophilic friction surface is easy to form under sliding conditions with a low sliding velocity. Figure 6-21 shows the contact angle of water droplet after sliding. This figure shows the hydrophilicity on SiC-DLC coating itself by sliding. Compared to Fig. 4-24, the effect of SiC-doping is improvement of hydrophilicity of DLC material itself.

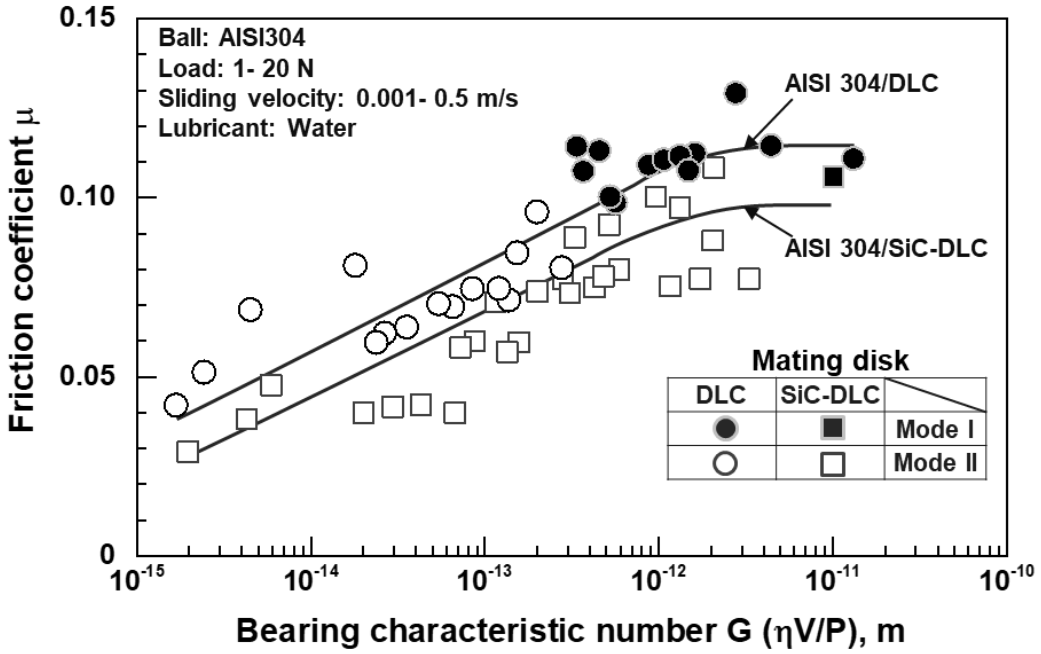

Fig. 6-19 Distributions of the friction modes of AISI 304/DLC coating and AISI 304/SiC-DLC coating in water of Mode I and Mode II as functions of bearing characteristic number and friction coefficient.

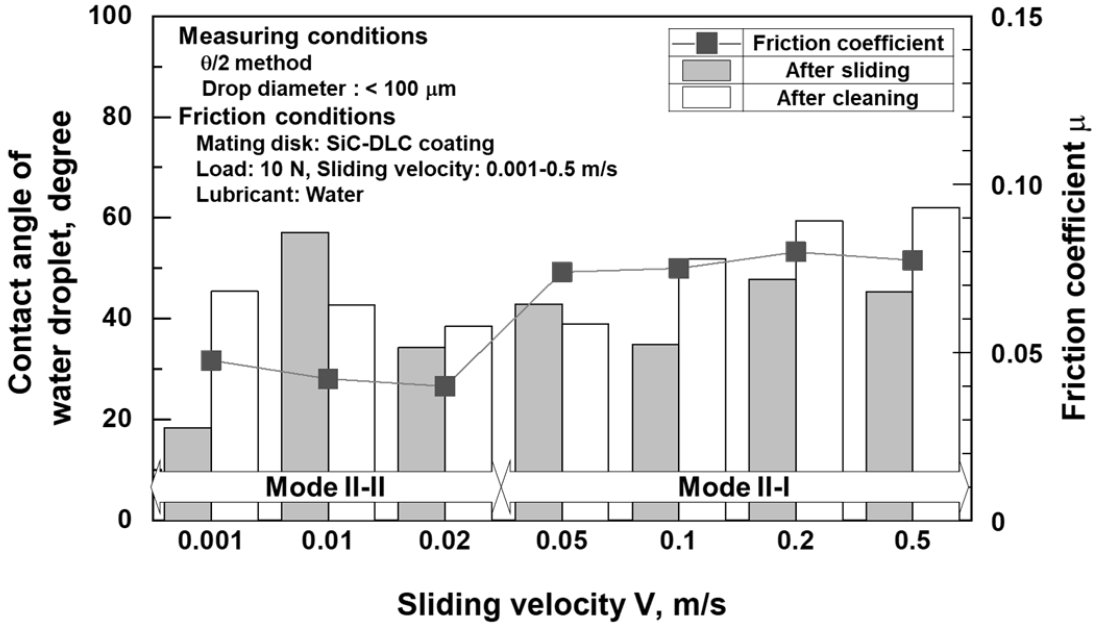

Fig. 6-20 Relationship sliding velocity, contact angle of water droplet on the wear scar sliding against SiC-DLC coating and friction coefficient in water.

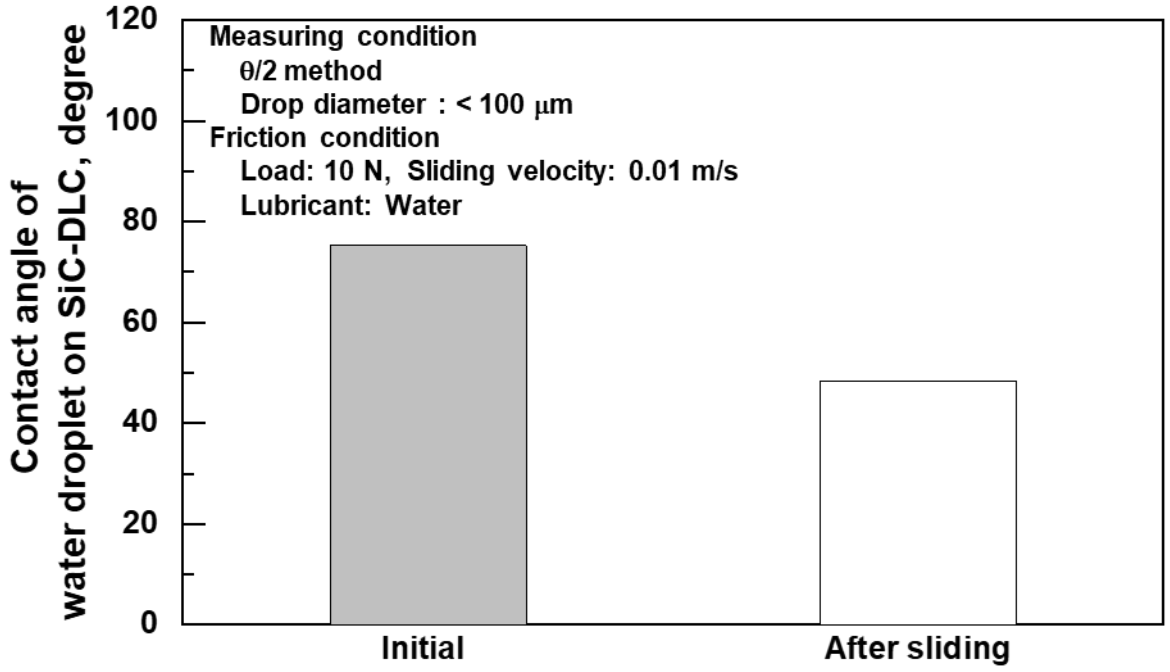

Fig. 6-21 Contact angle of water droplet on SiC-DLC coating after sliding in water.

6.2.4 Formation of low frictional interface on stainless steel in water

Cross-sectional image and distribution of related elements of transfer film on AISI 304 ball slid against SiC-DLC coating is shown in Fig. 6-22. The images where vacancies are seen indicate that the transfer film, approximate thickness is 150 nm, is mainly comprised of carbon, silicon, oxygen, chromium, and nickel. It is considered that the transfer film having the structure as described above is dominant in Mode II-I.

Figure 6-23 shows the cross-sectional image and distribution of related elements on worn surface without transfer film on AISI 304 ball slid against SiC-DLC coating. The images indicate that the nanolayer, approximate thickness is 20 nm, is mainly comprised of oxygen, chromium, iron and silicon. Based on these results, it is considered that the wear scar without transfer film on AISI 304 is dominated, and the surface is formed of a nanolayer composed of carbon, silicon, oxygen, chromium, nickel and iron, when AISI 304/SiC-DLC coating generates low friction in the boundary lubrication regime. Since the passive film contains silicon and is thicker than the passive film existing on the stainless steel on the initial surface, the passive film is self-formed during friction.

It is noteworthy that the wear scar slid against SiC-DLC coating is that the nanolayer has a passive film of chromium oxide containing silicon. It is known that the surface of chromium oxide has a hydrophilic [8]. In addition, the wear scar slid against SiC-DLC coting is more hydrophilic than the wear scar slid against DLC coating. Kajita et al. reveal that the Si-OH bond of silicon doped in the DLC coating fixes the water molecule in the water film with hydrogen bond, and this bond is maintained even under severe sliding conditions and the retained water It shows that the film plays a role of lubricant in the boundary lubrication regime [9]. In other words, the inclusion of silicon in the nanolayer leads to the promotion of the retention of the water film, which is considered to have developed low friction in the boundary lubrication regime.

Summarizing the above results, it was found that the contact angle of water droplet on the wear scar after cleaning in Fig. 6-20 is nothing but the measurement of the contact angle on the nanolayer itself, and that the nanolayer having the above structure is formed in the boundary lubrication region.

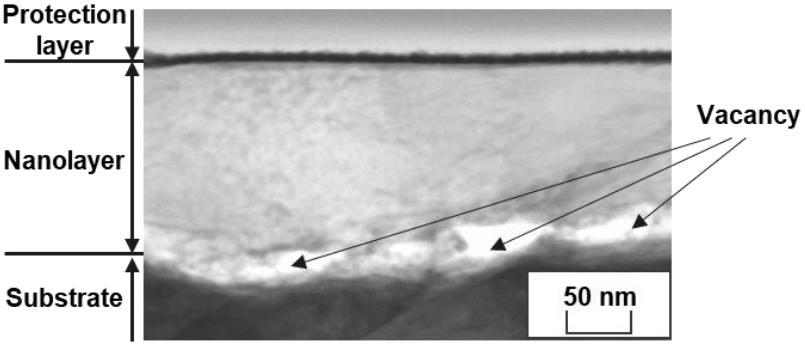

(a) Cross sectional image

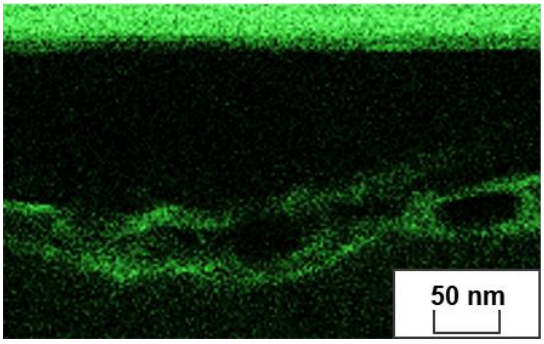

(b) Carbon

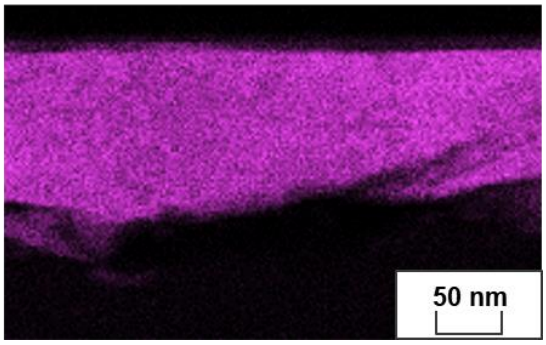

(c) Silicon

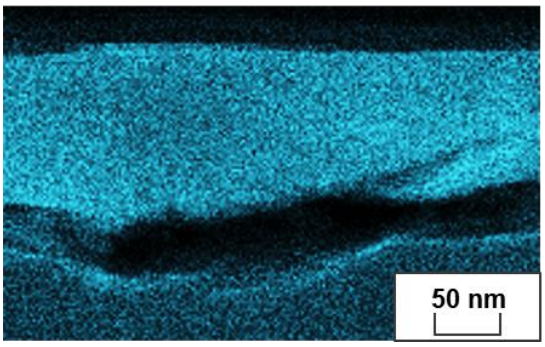

(e) Oxygen

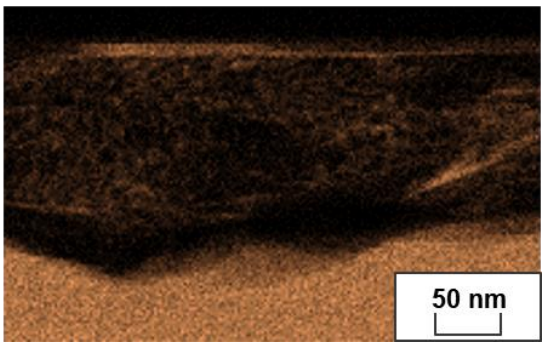

(e) Chromium

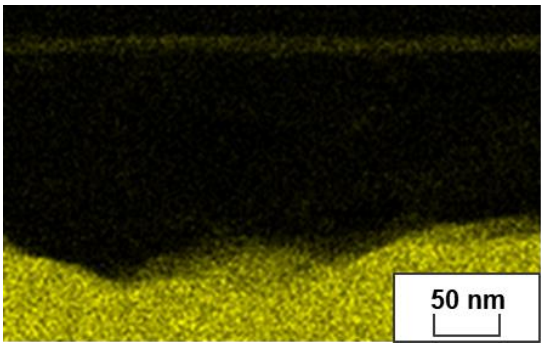

(f) Nickel

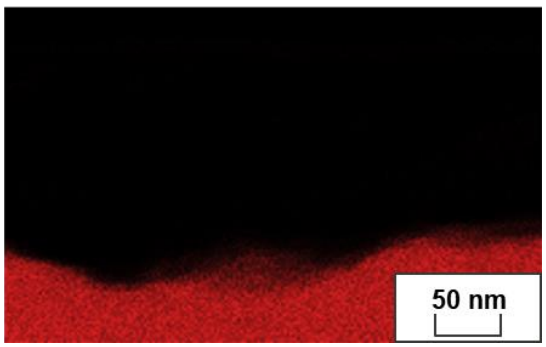

(g) Iron

Fig. 6-22 (a) TEM image and distribution of (b) carbon, (c) silicon, (d) oxygen, (e) chromium, (f) nickel and (g) iron of the transfer film on wear scar on AISI 304 ball slid against SiC-DLC coating.

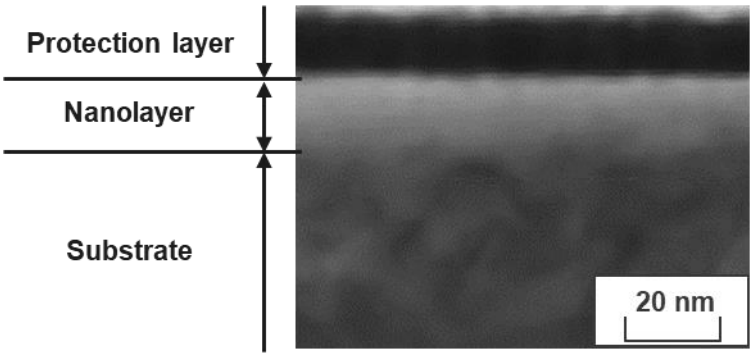

(a) Cross sectional image

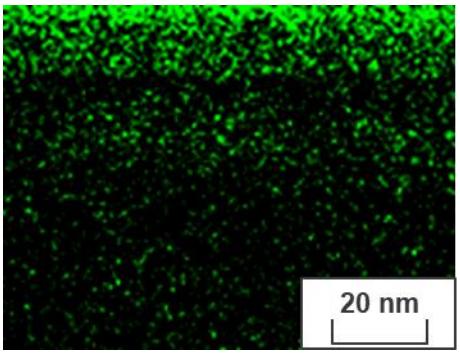

(b) Carbon

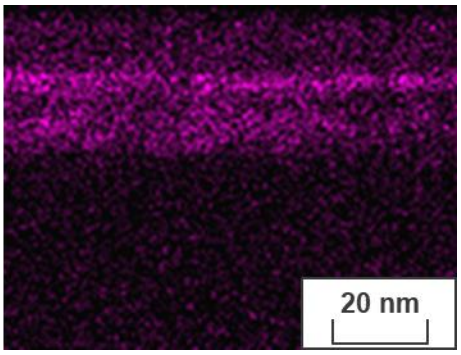

(c) Silicon

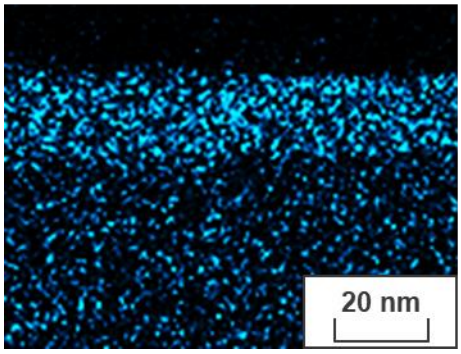

(e) Oxygen

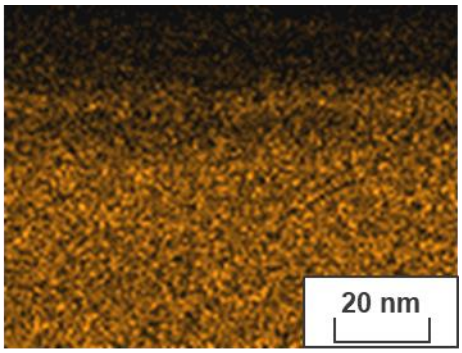

(e) Chromium

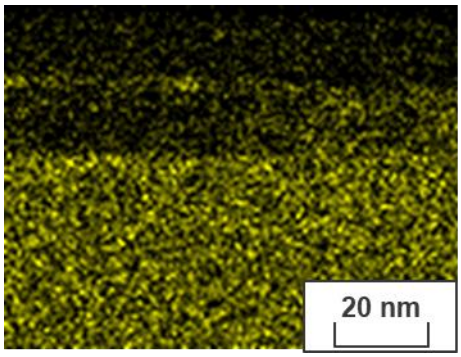

(f) Nickel

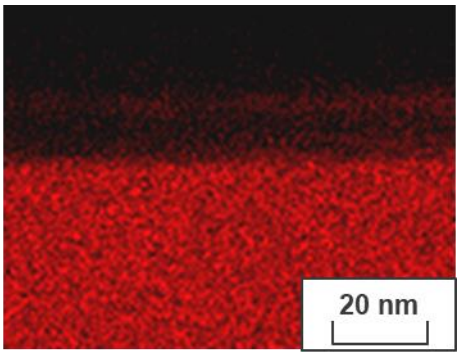

(g) Iron

Fig. 6-23 (a) TEM image and distribution of (b) carbon, (c) silicon, (d) oxygen, (e) chromium, (f) nickel and (g) iron of the worn surface on wear scar on AISI 304 ball slid against SiC-DLC coating.

6.3 Conclusions

In this chapter, friction for using stainless steel sliding against the newly developed SiC-DLC coating were conducted under various sliding conditions in water. As a result, following conclusions were achieved.

(1) The SiC-DLC coating newly introduced using the PE-CVD method and the DC magnetron co-sputtering of the SiC target simultaneously contributes to improve the water lubrication properties of AISI 304.

(2) Friction properties of AISI 304/SiC-DLC coating in water are classified into two modes as follows:

Mode I; no running-in

Mode II; running-in behavior and showing the friction coefficient

SiC-DLC coating enables to generate Mode II under wider sliding conditions than AISI 304/DLC coating.

(3) Mode II tends to show lower friction coefficient as the bearing characteristic number decreases. In Mode II, when the contact angle of water droplet on the wear scar after cleaning is compared, the contact angel in Mode II-II with a non-transferred area ratio on the wear scar of 60% or more is lower than that in Mode II-I with a non-transferred area ratio on the wear scar less than 60%.

(4) Mode II, the wear scar without transfer film on stainless steel ball is dominates nanolayer, approximate thickness is 20 nm, composed of carbon, silicon, oxygen, chromium, nickel and iron is self-formed continuously. Formed nanolayer is more hydrophilic than the initial surface of AISI 304.

(5) By introducing SiC into DLC coating, the coating itself becomes hydrophilic than DLC coating.

References

[1] J. C. Damasceno, S. S. Camargo, F. L. Freire, R. Carius, Deposition of Si-DLC films with high hardness, low stress and high deposition rates, Surface and Coatings Technology, 133–134, (2000) 247–252.

[2] X. Deng, H. Kousaka, T. Tokoroyama, N. Umehara, Thermal stability and high-temperature tribological properties of a-C:H and Si-DLC deposited by microwave sheath voltage Combination Plasma, Tribology Online, 8, 4 (2013) 257–264.

[3] R. Hatada, K. Baba, S. Flege, W. Ensinger, Long-term thermal stability of Si-containing diamond-like carbon films prepared by plasma source ion implantation, Surface and Coatings Technology, 305, (2016) 93–98.

[4] H. Ohmori, K. Katahira, J. Nagata, M. Mizutani, J. Komotori, Improvement of corrosion resistance in metallic biomaterials using a new electrical grinding technique, CIRP Annals - Manufacturing Technology, 51, 1 (2002) 491–494.

[5] H. Ohmori, K. Katahira, J. Komotori, M. Mizutani, F. Maehama, M. Iwaki, Investigation of substrate finishing conditions to improve adhesive strength of DLC films, CIRP Annals - Manufacturing Technology, 54, 1 (2005) 511–514.

[6] H. Sato, K. Adachi, Formation of nanointerface during running-in for low friction of silicon carbide in water, Proceedings of ITS-IFToMM 2017 & K-TIS 2017, Jeiu, Korea (2017) 151.

[7] V. Presser, O. Krummhauer, A. Kailer, K. G. Nickel, In situ monitoring and depth-resolved characterization of wet wear of silicon carbide, Wear, 271, 9–10 (2011) 2665–2672.

[8] R. Wang, Using atomic force microscope to observe nano-size water droplets on everal materials surfaces and evaluate their wettabilities, Science Technology and Education of Microscopy: An Overview, December (2006) 10–16.

[9] S. Kajita, M. C. Righi, A fundamental mechanism for carbon-film lubricity identified by means of ab initio molecular dynamics, Carbon, 103, (2016) 193–199.

[10] J. S. Dunning, D. E. Alman, J. C. Rawers, Influence of silicon and aluminum additions on the oxidation resistance of a lean-chromium stainless Steel, Oxidation of Metals, 57, 5–6 (2002) 409–425.

[11] Y. Wouters, G. Bamba, A. Galerie, M. Mermoux, J. P. Petit, Oxygen and water vapour oxidation of 15Cr ferritic stainless steels with different silicon contents, Materials Science Forum, 461–464, II (2004) 839–846.

[12] A. Paúl, R. Sánchez, O. M. Montes, J. A. Odriozola, The role of silicon in the reactive-elements effect on the oxidation of conventional austenitic stainless steel, Oxidation of Metals, 67, 1 (2007) 87–105.

Chapter 7

General Conclusions

Water lubrication system has a possibility to reduce the friction loss for next-generation technology. However, the sliding-material of conventional water lubrication system is mainly limited to silicon-based ceramics. Silicon-based ceramics is known to react with water and have advantages such as high strength and hardness, but these materials are difficult to process due to fractures dependent on pores, grain boundaries, and cracks near the surface. Also ceramic materials are not widely used in the manufacture of mechanical parts due to high processing cost.

Metal materials are easy to process and widely used as conventional mechanical materials. Therefore, use of metal material as sliding materials for water lubrication systems is expected to extend further applications of water lubrication systems. In particular, stainless steel is expected to be used in water lubrication systems because of its corrosion resistance to water. In this thesis, the aim is to create the low frictional interface on stainless steel which has for widespread of water lubrication system and to achieve design guidelines for water lubrication system using stainless steel.

In chapter 2, basic friction property of stainless steel in water is evaluated. Stainless steel and itself shows the friction coefficient varied from 0.3 to 1.0 under various sliding conditions and does not depend on the relative thickness of the lubricant film. The specific wear rate of stainless steel ball increases from 10^{-5} $mm^3/N{\cdot}m$ to 10^{-2} $mm^3/N{\cdot}m$ as the $P_i{\cdot}V$ value which indicates the initial contact pressure multiplied by sliding velocity increases. Adhesion between sliding counterpart occurs and high friction and severe wear occurs.

In chapter 3, the role of silicon-based ceramics as a mating material of stainless steel in water is clarified. Silicon-based ceramics with high chemical stability are expected to prevent the adhesion and seizure of stainless steel itself. As a result, the introduction of a silicon-based ceramic successfully prevented seizing of the stainless steel itself. However, no running-in which shows the decrease of friction coefficient from the initial stage of friction test was observed under any conditions. Furthermore, the improvement of hydrophilicity of the ceramic material side due to the tribochemical reaction between the silicon ceramic and water was confirmed.

In chapter 4, the role of DLC coating as a mating material of stainless steel in water is clarified.

DLC coating with high chemical stability are expected to prevent the adhesion of stainless steel and prevent seizure, similar to silicon-based ceramics. As a result, the introduction of DLC coating prevents seizure as well as exhibits for running-in under certain sliding conditions and lower friction in the boundary lubrication region than the conventional combination of SiC. In order to exhibit running-in, carbon from DLC coating needs to transfer onto stainless steel and the suppression of the oxidation of iron, which is the bulk material of stainless steel. Furthermore, a passive film of chromium oxide with a thickness of 20 nm was formed on the area where the transfer film did not cover and the improvement of hydrophilicity showed as this area became more dominant. Based on the fact that the passive film of ordinary stainless steel has a thickness of 1 to 3 nm, this passive film was self-formed continuously during friction is clarified.

In chapter 5, in order to clarify the transfer mechanism of carbon from DLC coating onto stainless steel in the initial stage of friction, test apparatus in ESEM was newly designed which can control the relative humidity of the chamber. Experiments in dry conditions clarified that the presence of a small amount of water inhibits the transfer of carbon onto stainless steel. However, transferred carbon in water suggests that water film was broken out and carbon was transferred at actual contact point between sliding interface.

In chapter 6, in order to demonstrate the possibility of further low friction in a water lubrication system using stainless steel, a SiC-DLC coating with introduced SiC into the DLC matrix was introduced as a mating material for stainless steel since SiC enhances its hydrophilicity by tribochemical reaction with water as shown in chapter 3. The introduction of SiC-DLC coating has succeeded to extend the sliding conditions that shows running-in compared to DLC coating. When the combination between stainless steel and SiC-DLC coating showed low friction in the boundary lubrication regime, a passive film containing chromium and oxygen in addition to silicon was self-formed on stainless steel, and the film was hydrophilic. Furthermore, by introducing SiC into DLC coating, the hydrophilicity of the coating itself due to friction was improved compared to DLC coating.

The main conclusions in this thesis were as follows:

(1) In the case of stainless steels, seizure occurs on both surfaces even under the conditions of the lowest sliding velocity and the lowest initial contact pressure in this experiment, thus high friction and severe wear is induced.

(2) The combination between stainless steel and silicon nitride shows friction coefficient varied from 0.4 to 0.8 and the combination between stainless steel and silicon carbide shows friction coefficient varied from 0.2 to 0.4. Under any the sliding conditions, these combinations do not show running-in and higher friction than the combination of SiC was exhibited.

(3) Silicon-based ceramics becomes hydrophilic after slid against stainless steel in water.

(4) The friction coefficient of the combination between stainless steel and DLC coating decreased from 0.14 to 0.04 as direct contact dominates. In the boundary lubrication regime, lower friction was exhibited than the combination of SiCs with a friction coefficient around 0.2. These results demonstrate that DLC coating has a potential to realize low friction in boundary regime.

(5) A passive film of chromium oxide with a thickness of 20 nm on the stainless steel sliding against DLC coating in water was self-formed during friction. This film shows more hydrophilic than initial stainless steel.

(6) An ESEM-tribo system that can repeatedly analyze changes in the ball at extremely short sliding distances was newly developed and its effectiveness was shown.

(7) In the case of tribo-pair between stainless steel and DLC coating, a critical relative humidity for the transfer of carbon was clarified.

(8) The friction coefficient of the combination between stainless steel and SiC-DLC coating that newly introduced decreased from 0.11 to 0.03 as direct contact dominates. In the boundary lubrication regime, lower friction occurs than the combination between stainless steel and DLC coating.

(9) A passive film of chromium and oxygen in addition to silicon with a thickness of 20 nm was self-formed on the stainless steel ball sliding against SiC-DLC coating in water. This film is more hydrophilic than initial stainless steel.

(10) By introducing SiC into DLC coating, the hydrophilicity of the coating itself due to friction was

improved compared to DLC coating.

(11) Design concepts for water lubrication system using stainless steel are proposed as follows.

(a) In order to suppress the adhesion of stainless steel, a material with excellent chemical stability such as silicon-based ceramics and DLC coating must be used as the mating material of stainless steel.

(b) In order to realize self-formation of a passive film on the stainless steel surface during friction, carbon transfer to the friction surface is required to suppress the formation of iron oxide.

(c) In order to maintain a water film on both surfaces of the friction, hydrophilicity of the mating material of stainless steel must be improved by friction.

Acknowledgement

This thesis was arranged the results of four-year Ph. D. course in Tohoku University.

First, I would like to show my greatest appreciation to Professor Koshi Adachi who supervised me. I am grateful for his continuous support and encouragement with his passion for research. I have learned his philosophy through daily life in Adachi-Kanda laboratory. I have the highest respect for him.

I would like to thank Professor Hitoshi Soyama and Professor Kazuhiro Ogawa for their review and discussions for improvement of this thesis.

I would like to thank Mr. Tetuji Tsuru, Eagle Industry Co., Ltd. President and CEO for giving me the opportunity to continue this research and summarize this thesis, despite the research while studying at Tohoku University.

I would like to thank the people in the Engineering Research Department at Eagle Industry for their great cooperation so that I can concentrate on this research. In particular, I would like to express my deep appreciation to Dr. Norio Uemura, Senior Managing Director and General Manager of Development, Mr. Naohisa Ikegami, Section Senior General Manager of Engineering Research Department, Mr. Takuto Fukuhara, Senior Engineer and Dr. Masao Oka, Senior Engineer.

I would like to thank Assistant Professor Koki Kanda for careful review of this thesis and support of the submitted papers. He gave me valuable comments, suggestions and helpings at weekly seminar. I have learned logical and simple thinking from him.

I would like to thank Dr. Takanori Takeno, Advanced Research and Innovation Center at DENSO Corporation for his powerful support about SiC-DLC coating, excellent comments and suggestions throughout the four years in Adachi/Takeno laboratory.

I would like to thank Dr. Ryo Koike, Joint laboratory of Tribological Material Research for Advanced Automobile at Toyota Motor East Japan, Inc. for daily discussion and his advice. He constantly encouraged me in my research work.

I would like to thank Professor Momoji Kubo, Tohoku University, Professor Joichi Sugimura, of Kyushu University, Professor Yoshinori Sawae, Kyushu University, Professor Hiroyuki Kosaka, Gifu University, Assistant Professor Hiroyoshi Tanaka, Kyushu University, Assistant Professor Yusuke Ootani,

Tohoku University and Assistant Professor Yang Wang, Tohoku University giving the chance to make discussion during CREST team meetings.

I would like to thank Mr. Noboru Akao and Ms. Yukie Oohira Organization for Technical Division in Tohoku University. Thanks to their technical support according to XPS analysis.

I would like to thank Associate Professor Masahiko Nishijima, Organization for Electron Microscopy Center in Tohoku University. Thanks to his technical support according to TEM analysis.

I would like to thank all members in Adachi-Kanda Laboratory for lots of discussions and supports. In particular, I express grateful appreciation to Mr. Kenta Shirai, Mr. Kento Ihara, Mr. Yuki Konomi, Mr. Tsubasa Takahashi, Mr. Yoshiyuki Ueno, Mr. Masaya Yoshida, Mr. Kazuya Kuriyagawa, Mr. Yasuhisa Yamamoto, Mr. Satoshi Sakaki and Ms. Runa Suzuki.

I would like to acknowledge financial support from Tohoku University School of Engineering.

At last, I would like to thank my wife Mina, my parents and my brother giving me the continuous support for my research work at Ph. D. course.

January 14, 2020

Kenta Akagami